# Investigation of Flexural Plate Wave Devices for Sensing Applications in Liquid Media

A thesis submitted in fulfilment of the requirements
of the degree of Doctor of Philosophy

Glenn I. Matthews
B.Eng (Hons)

School of Electrical and Computer Engineering
Science, Engineering and Technology Portfolio
RMIT University
August, 2007

[ This page has intentionally been left blank. ]

# Declaration

I certify that except where due acknowledgement has been made, the work is that of the author alone; the work has not been submitted previously, in whole or in part, to qualify for any other academic award; the content of the thesis is the result of work which has been carried out since the official commencement date of the approved research program; and, any editorial work, paid or unpaid, carried out by a third party is acknowledged.

Glenn Matthews

# Acknowledgement

I would like the thank the following people and organisations for their assistance in my research and in writing this thesis:

- My senior supervisor Prof. Wojtek Wlodarski for his continual support, advice and constructive feedback during my time with the RMIT University Sensor Technology Group.
- My secondary supervisor Dr. Kourosh Kalantar-zadeh for his experience in fabrication of acoustic wave devices.
- Dr. Anthony Holland for his expertise in vacuum technology and microfabrication techniques.
- Dr. David Powell and Dr. Samuel Ippolito for their friendship, technical knowledge and their continual willingness to explain the finer points of acoustic wave devices.
- The technical staff at RMIT University, School of Electrical and Computer Engineering. In particular, I am grateful for the knowledge imparted to me by Mr. Paul Jones, Mr. Yuxun Cao, Mr. Bob Kealy, Mr. Chris Arthur and Mr. David Welch.
- Past and present colleagues of the RMIT Sensor Technology Group for their continuing friendship and advice: Dr. Adrian Trinchi, Mr. Alex Fechete, Mr. Sasikaran Kandasamy, Mr. Abu Sadek, Ms. Joy Tan and Ms. Rashidah Arsat.
- Special thanks to my parents Denise and Ian and my sister Lauren, as well as all my other friends for their support and encouragement. A heartfelt thanks to Ms.

Katrina Neville for her continual support, optimism and understanding during the final stages of this thesis.

- The IEEE UFFC Society who provided travel support to enable me to present a paper at the 2006 IEEE International Ultrasonics Symposium in Vancouver, Canada.

[ This page has intentionally been left blank. ]

# Abstract

In this thesis, the author proposes and presents a novel simulation technique for the analysis of multilayered Flexural Plate Wave (FPW) devices based on the convergence of the Finite Element method (FEM) with classical Surface Acoustic Wave (SAW) analysis techniques and related procedures. Excellent agreement has been obtained between the author's approach and other more conventional modelling techniques. Utilisation of the FEM allows the performance characteristics of a FPW structure to be critically investigated and refined before undertaking the costly task of fabrication. Based on a series of guidelines developed by the author, it is believed the proposed technique can also be applied to other acoustic wave devices. The modelling process developed is quite unique as it is independent of the problem geometry as verified by both two and three dimensional simulations. A critical review of FEM simulation parameters is presented and their effect on the frequency domain response of a FPW transducer given. The technique is also capable of simultaneously modelling various second-order effects, such as triple transit, diffraction and electromagnetic feedthrough, which often requires the application of several different analysis methodologies.

To verify the results obtained by the author's novel approach, several commonly used numerical techniques are discussed and their limitations investigated. The author initially considers the Transmission Matrix method, where it is shown that an inherent numerical instability prevents solution convergence when applied to large frequency-thickness products and complex material properties which are characteristic of liquids. In addition the Stiffness Matrix method, is investigated, which is shown to be unconditionally stable. Based on this technique, particle displacement profiles and mass sensitivity are presented for multilayered FPW structures and compared against simpler single layer devices commonly quoted in literature. Significant differences are

found in mass sensitivity between single layer and multilayered structures, which to the best of the author's knowledge, is the first time that such characteristics have been discussed for FPW devices. Frequency response characteristics of a FPW device are then explored via a spectral domain Green's function, which serves as a further verification technique of the author's novel analysis procedure. Modifications to the spectral domain Green's function are discussed and implemented due to the change in solution geometry from SAW to FPW structures.

Using the developed techniques, an analysis is undertaken on the applicability of FPW devices for sensing applications in liquid media. Additions are made to both the Stiffness Matrix method and FEM to allow these techniques to accurately incorporate the influence of a liquid layer. The FEM based approach is then applied to obtain the frequency domain characteristics of a liquid loaded FPW structure, where promising results have been obtained. Displacement profiles are considered in liquid media, where it is shown that a tightly coupled Scholte wave exists that is deemed responsible for most reported liquid sensing results. The author concludes the theoretical analysis with an in-depth analysis of a FPW device when applied to density, viscosity and mass sensing applications in liquid media. It is shown that a single FPW device is potentially capable of discriminating between density and viscosity effects, which is typically a task that requires a complex and costly sensor array.

Finally, the author presents preliminary results pertaining to the fabrication of a simulated FPW structure used within this thesis. A brief description of the fabrication techniques, including the design, development and characterisation of a reactive d.c. sputtering system constructed by the author is given. X-ray Photoelectron Spectroscopy (XPS) has confirmed that the deposited aluminium nitride films are stoichiometric, with the orientation of the film determined by Atomic Force Microscopy (AFM). The piezoelectric coupling coefficient $d_{33}$ has been measured by a standard AFM, with the results and a detailed explanation of the technique accepted for publication by an international journal.

# Contents

# List of Figures

# List of Tables

[ This page has intentionally been left blank. ]

# Chapter 1

# Introduction

This chapter provides an introduction to the author's novel work in modelling Flexural Plate Wave structures for sensing applications. A brief overview of acoustic wave devices is presented allowing the basic concepts to be understood, with an emphasis placed on the application of these structures to sensing applications. Section 1.1 discusses the rationale and necessity of the author's research program. A brief discussion of current modelling limitations is presented, illustrating the proposed direction of the author's research. The objectives of the author's PhD program are given in Section 1.2, with the key achievements discussed in Section 1.3. This chapter concludes with a summary of thesis layout and organisation in Section 1.4.

## 1.1 Research Rationale

The use of acoustic wave devices for signal processing applications is a well studied area [1, 2]. Surface Acoustic Wave (SAW) devices are routinely applied as high frequency filters in wireless communication systems and more recently have been utilised for sensing applications [3]. To qualify as a sensor, a measurable property of the device must vary as a function of input stimulus. In terms of acoustic wave sensors, deviation in wave velocity, and hence resonant frequency, or changes in attenuation form the basis of most experimental measurements.

In their simplest form, an acoustic wave device can be considered to be comprised of a structure along which a time varying mechanical wave propagates. Depending

on the orientation, dimensions and type of materials employed, alternative acoustic modes can be excited, each with vastly different properties and potential applications. Furthermore, if a piezoelectric material is utilised, a layer of bound charge also travels with the mechanical wave. Perturbation of the device boundaries, whether by electrical or mechanical stimulus, causes the phase velocity, attenuation or both parameters of the propagating electro-acoustic wave to be altered. Therefore, for the purpose of this thesis, an acoustic wave sensor is defined as a structure along which an electro-mechanical wave propagates whose characteristics can be altered by changes in boundary conditions. The acoustic wave can be perturbed by changes in temperature, electric field, material properties, mass, pressure, density and viscosity, just to name a few. In some applications, the aforementioned parameters may be the quantities under scrutiny, or could potentially be undesired measurands of whose effect can be minimised by careful simulation and material selection.

Two main configurations exist for the excitation and detection of acoustic waves in piezoelectric media. Both techniques rely on the piezoelectric effect to convert an applied electrical signal into a mechanical deformation and vice-versa. This particular study focuses on the commonly used delay line technique, Figure 1.1. Here, a series of metallic interwoven comb like structures, known as Interdigital Transducers (IDTs), are deposited on the surface of the device with an electrode period defined by $\lambda$. The IDT width, indicated by the term $W$ in Figure 1.1, is termed the acoustic aperture. The IDTs are separated by a known distance along which the electro-acoustic wave propagates, which is typically several times the electrode period. Perturbation of the wave propagation path, as previously mentioned, induces changes in the travelling acoustic wave, which is detected at the output transducer and converted back into a usable electrical signal. The second IDT configuration is known as a resonator structure, which relies on the in-phase reflections of the acoustic wave. This layout is typically not applied to sensing applications and will not be discussed here.

Flexural Plate Wave (FPW) devices meet the criteria for acoustic wave sensors, where two distinct acoustic modes, known as Lamb waves, propagate along the structure with vastly different phase velocities and particle displacements. The existence of two unique primary modes suggest that a FPW structure can be used to simulta-

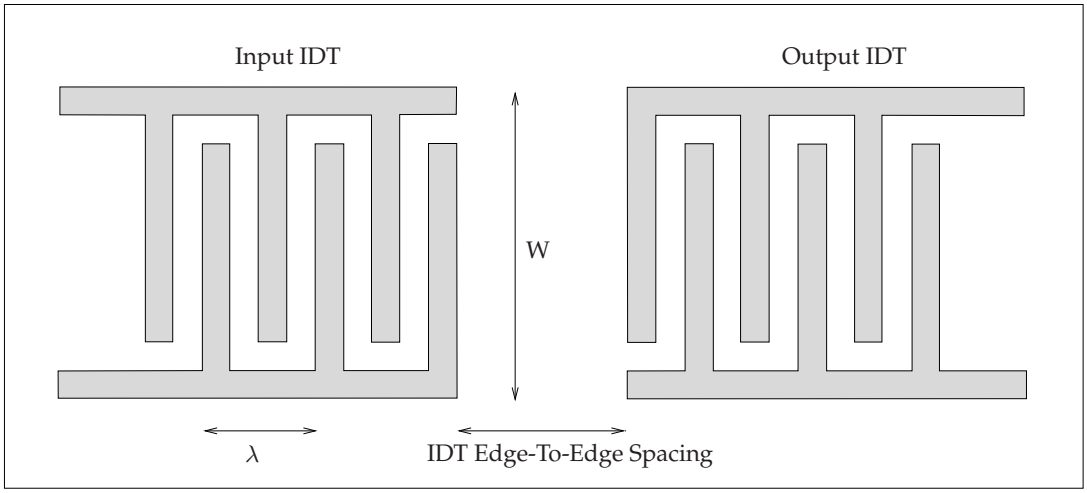


Figure 1.1: Delay Line FPW Device

neously evaluate alternative properties of a given medium. This will be examined in more detail throughout this thesis.

Although other sensing platforms exist to detect biological, chemical and physical quantities, acoustic wave structures, and in particular FPW devices, offer distinct advantages [4]. The benefits of FPW devices over other acoustic wave structures can be partially attributed to their physical construction. A FPW device essentially consists of an acoustically thin membrane, which defines the active area of the device. The thin membrane, or plate, is typically formed by bulk micromachining of a specifically orientated silicon (Si) wafer. Silicon is a well understood, inexpensive and readily available material that has been utilised without the Integrated Circuit industry for many years. In addition to the underlying silicon substrate, silicon nitride ($Si_3N_4$) is used as an etch stop and to form the underlying membrane of the device. A metallic ground plane of either gold (Au) or aluminium (Al) is then deposited, followed by a piezoelectric material such as zinc oxide (ZnO) or aluminium nitride (AlN) which when used in conjunction with the final patterned IDT aluminium layer generates and detects the propagating acoustic waves. More details on the physical layout of a FPW device can be found in Section 2.2.1. As FPW structures are typically fabricated on silicon substrates, the necessary signal processing electronics can also be fabricated on the same die. This implies that FPW devices can potentially be configured for 'lab-on-chip' applications with a simple digital output indicating the concentration of a particular analyte.

The overall thickness and composition of the membrane defines the resonant frequency for the two primary modes, denoted $A_0$ and $S_0$ for antisymmetric and symmetric displacements about the device mid-plane respectively. The primary $A_0$ mode has the unique characteristic of a low resonant frequency when the plate thickness is small compared to the acoustic wavelength. As an example, it is common to fabricate devices with an $A_0$ mode resonant frequency less than $20$MHz [5]. Conversely, the $S_0$ mode has a significantly higher resonant frequency, typically between $50$ and $100$MHz. As the plate structure is further thinned, the phase velocity, and hence resonant frequency, of the $A_0$ mode further decreases. It is this phenomenon that allows FPW structures to be applied to sensing applications in liquid media [6]. For small thickness-wavelength ratios $(h/\lambda << 1)$, the relatively low phase velocity and particle displacement profiles allow the $A_0$ mode to be used for liquid media sensing applications with minimal loss due to viscous loading.

FPW structures are quite unique, as they can be applied to sensing applications in both gas and liquid media. For gas phase sensing applications, a multilayered structure can be employed [7], where an additional metal oxide layer is deposited on the device surface. The introduction of a target gas causes conductivity changes in the metal oxide layer, thereby perturbing the electrical boundary conditions of the acoustic wave, which manifests as a measurable change in resonant frequency. In terms of biosensing applications, the selectivity of a FPW device can be improved by the immobilisation of a biorecognition element [8]. These layers are configured to detect specific biomolecules, thereby also decreasing the minimum detectable concentration of a given analyte. However, FPW structures are not strictly limited to sensing applications. Recently, FPW devices have been employed as liquid delivery systems and micro actuators [9]. In terms of micromachined sensors, which is the focus of this study, FPW devices have successfully been applied to sense pressure [10], humidity [11], protein concentration [12], liquid density and viscosity [13]. Although the sensitivity of an FPW device can be potentially enhanced by the addition of various layers, the structure can also be used without. In particular, for pressure, density and viscosity sensing the additional layer is not required.

The mass sensitivity of FPW structures comprised of a single isotropic layer, in

both gas and liquid media, is inversely proportional to the overall thickness of the active area of the device. Therefore, for high sensitivity, the membrane should be as thin as possible. It is common to achieve an overall thickness of under $3\mu m$, whilst still maintaining a sturdy and reliable sensing platform [8]. In comparison to other acoustic wave devices, such as the widely used Quartz Crystal Microbalance (QCM), a FPW structure exhibits a sensitivity of up to $31$ times greater, whilst operating at approximately the same frequency [14].

Numerous simulation techniques exist for the analysis of acoustic wave structures when configured as sensors [13, 15]. However, for all currently available methods, a series of underlying assumptions and approximations are made that ultimately limit the accuracy of these approaches. The most common simplifying assumption for FPW devices relates to the materials used to realise the structure. In most published results, particularly in the earlier stages of development, FPW devices were approximated as an acoustically thin isotropic plate, where the influence of the supporting silicon substrate was neglected. The author addresses many of these simplifications by applying numerical techniques which consider the anisotropic nature of the individual device layers are well as the membrane silicon support structure. In particular, significant differences are found when considering the mass sensitivity of FPW structures when comparing the isotropic approximation to the results obtained by the employed anisotropic analysis technique.

Another current deficiency with conventional modelling techniques is the inability to simultaneously model various second order phenomena such as triple transit, diffraction and electromagnetic feedthough. Whilst in some structures these effects can be safely ignored [16], as substrate dimensions are reduced to provide cost benefits, these effects must be included. The author intends to investigate potential methods to incorporate the aforementioned phenomena into the simulation process developed for FPW structures.

Of particular interest is the modelling of FPW structures using the Finite Element Method (FEM). Although a well established technique for the analysis of mechanical structures such as beams, trusses and bridges, the process is typically not applied to acoustic wave devices. One common issue with this technique is the computational

resources required to obtain an accurate solution within a relatively small timeframe. As computers have become significantly more powerful over the last few years, the reluctance to use the FEM for complex tasks such as acoustic wave propagation is decreasing [17, 18]. The second deficiency with the application of the FEM for the study of acoustic wave devices is a set of clear and concise guidelines on how various structures should be modelled. The author intends to address these concerns with a discussion on the influence of FEM parameters such as simulated structure dimensions, simulation time, timestep and node density. Furthermore, routines will be established to convert the data obtained from the FEM simulations to commonly quoted parameters, such as admittance and therefore insertion loss, used within the Ultrasonics community.

The FEM provides significant benefits over other analysis techniques. When correctly applied, the technique is independent of problem geometry, whereas other more conventional methods may require complete redefinition of basis equations [19]. In many current models of FPW structures, the device is assumed to consist solely of an acoustically thin plate, typically less than a few tens of microns. As mentioned previously, the effect of the silicon support structure is often neglected, which can cause inaccuracies in the frequency response characteristics. Using the FEM, a complete three dimensional FPW device can be simulated, thereby providing a more accurate representation of the physical device. Using the same methodology, it is also suggested that the FEM can be applied to determine the frequency domain characteristics of liquid loaded FPW structures. It is envisaged that liquid layers can be incorporated with the addition of an appropriate finite element, whereas other techniques require significant modifications to account for viscous damping [20].

The FEM is also capable of modelling the physical and electrical effects of the IDTs, which until recently was ignored in the analysis of SAW structures [21]. This is particular important for FPW structures as the electrode thicknesses can be a significant percentage of the overall plate thickness. This task was not undertaken by the author, however is a topic of ongoing research. It is believed that the work conducted in this thesis will serve as a benchmark for future development and analysis of FPW structures, as well as other acoustic wave devices, using the combination of the FEM with author's modified SAW analysis techniques.

With respect to other more conventional techniques, most of the available literature focuses on the analysis of more established acoustic wave structures. SAW and QCM devices have been available for over 50 years, and as such the device physics are well understood, leading to well defined analysis procedures. Whilst analogies can be drawn from the SAW case, many techniques have to be re-evaluated to determine their applicability to FPW devices. The author also addresses these concerns, particularly when considering the spectral domain Green's function to evaluate the frequency domain characteristics of FPW structures in the gas phase. The calculated results from these more conventional techniques will be used to verify solutions obtained from the author's novel analysis of FPW structures based on the FEM.

Throughout the development of this thesis, the commercially available FEM package ANSYS 8.0 was utilised. Whilst other groups have focused on writing proprietary FEM computation routines, the application of commercially available software allows other researchers, without the necessary programming skills, to apply the same techniques to other acoustic wave devices and structures. To the best of the author's knowledge the simulation guidelines presented are generic and thus are still suitable for other FEM packages.

## 1.2 Objectives

The aim of this thesis is to provide a comprehensive theoretical analysis of Flexural Plate Wave devices for sensing applications. Using a variety of analytical and numerical techniques, the operating parameters of these structures will be investigated and described in detail. The main objectives of the author's research include:

- Discussion of current modelling techniques and their applicability to the analysis of multilayered FPW structures. The limitations of current techniques will be investigated and a thorough description of underlying assumptions given. Based on this review, the author's novel approach to modelling FPW structures will be developed.

- Development of a unified approach for the simulation and evaluation of multilayered FPW structures, applied to sensing applications in both gas and liq-

uid media, that can readily adapt to changes in geometry and device layout. As a minimum, the simulation procedures developed must be capable of accurately determining key electrical and mechanical performance parameters such as phase velocity, electromechanical coupling, particle displacement and of prime importance, frequency response characteristics in both gas and liquid media. To achieve this objective, an array of both numerical and analytical techniques will be considered and the appropriate methods employed. Preliminary investigations into modelling techniques suggest that the FEM, combined with alternative techniques used in the analysis of other acoustic wave devices, can be applied to this task. It is envisaged that analogies drawn from modelling techniques applied to SAW structures can be adapted to suit FPW devices, provided that all underlying assumptions are fully explored and the appropriate modifications implemented. Furthermore, the results obtained from the author's approach will be verified against routinely applied existing techniques used within the Ultrasonics community.

- To comprehensively investigate the differences in mass sensitivity and particle displacement profiles between commonly quoted single layer FPW devices and significantly more complex multilayered structures. A study will also be undertaken on the influence of the device layers with respect to mass sensitivity. Based on this information, the author intends to fabricate a highly sensitive FPW structure that can be applied to sensing applications in both gas and liquid media.

- Develop an understanding of acoustic wave devices that can be potentially applied to sensing applications in liquid media. In particular, the limitations of alternative devices will be considered and potential methods to prevent the same issues with FPW structures will be considered.

- Evaluation of FPW device performance in liquid media. Of particular interest is the ability of these structures to be applied to density, viscosity and mass sensing tasks in liquid media. An investigation will be performed on the applicability of the primary antisymmetric and symmetric modes for sensing applications. Whereas the antisymmetric mode is typically applied in liquid media, the au-

thor will investigate whether the symmetric mode can be used simultaneously to obtain more detailed information.

- Design, development and fabrication of a functional FPW device based on the findings of the author's novel analysis technique. It is envisaged that this process will serve as a further validation of the author's findings.

## 1.3 Authors Achievements and Outcomes

Throughout the course of the author's PhD program, several significant achievements were obtained of which a majority are contained within this thesis. The most notable aspects of the author's research include:

- Development of a novel analysis technique for the simulation and evaluation of multilayered FPW devices based on the convergence of the FEM with classical analysis techniques and procedures typically applied to SAW structures. The necessary modifications to the SAW analysis techniques have been undertaken to suit the FPW case by critically examining the underlying principals and assumptions of these methods.

- Development of a three dimensional (3D) FEM simulation for the analysis of multilayered FPW structures. Electrostatic and dynamic transient simulations were successfully conducted on a 3D FPW structure to obtain key electrical and mechanical performance criteria such as electrode charge density and mechanical displacement. The two simulations performed further demonstrated that the FEM approach used by the author is capable of simultaneously evaluating various second-order effects, such as electromagnetic feedthrough and diffraction, which typically can not be achieved using alternative numerical techniques. Furthermore, the dynamic transient analysis has demonstrated that the displacement in a multilayered FPW structure in predominantly in the longitudinal and transverse directions, indicating a less computationally intensive two dimensional FEM analysis can be applied without significantly influencing the simulation results.

- Development of a comprehensive two dimensional (2D) FEM simulation for the analysis of multilayered FPW structures. Various FPW devices have been simulated with and without the underlying silicon support structure, which is typically ignored with more conventional modelling techniques. It was found that the support structure influences both the resonant frequency and insertion loss values of the two primary acoustic modes, thereby providing a significantly more accurate representation of physical FPW structures. Various signal processing techniques have been applied to the FEM derived data to improve the resolution of the frequency domain results. A clear link has been established between the frequency domain data and the FEM simulation parameters, which allows the desired frequency resolution to be obtained.

- To determine the theoretical frequency response of a FPW device, a two dimensional dynamic transient FEM analysis was performed. A modified impulse function was applied at the input IDT and the corresponding charge density determined at the input and output transducers over the complete simulation time. By appropriately modifying SAW analysis techniques to suit FPW structures, the complete admittance characteristics of the device was calculated from the FEM results. The admittance data was then converted to equivalent scattering matrix parameters, widely used within the Ultrasonics community, allowing the insertion loss to be evaluated. This approach improves on existing techniques by allowing the complete frequency response spectra to be obtained concurrently instead of applying discrete frequencies and evaluating the transducer response. Other researchers have focused on the modal analysis of FPW structures, which does not take the excitation source, nor the piezoelectric nature of the device into account. The techniques demonstrated by the author fully account for the electrical influence of the IDTs as well as the anisotropic and piezoelectric properties of the individual layers. Furthermore, the author's approach is independent of geometry and device layout, which is typically not the case with more conventional techniques.

- Based on the results obtained via the FEM simulations, the author has successfully determined key electrical and mechanical parameters of various FPW struc-

tures. In particular, input capacitance, electromechanical coupling coefficient, admittance, and hence insertion loss, have all been successfully evaluated, where excellent agreement has been obtained when compared against other more conventional techniques. To verify the overall simulation method presented by the author, a diverse range of routinely applied modelling techniques, such as the stiffness matrix method and spectral domain Green's function were applied to the same theoretical FPW device. Via the stiffness matrix method, basic parameters such as phase velocity and electromechanical coupling were calculated, whereas a spectral domain Green's function was applied to verify the FEM derived frequency response characteristics. A full investigation has been performed on the impact of various simulation parameters within the FEM package and a general set of guidelines established for the use of this technique when modelling acoustic wave devices in both gas and liquid media.

- An detailed discussion has been given on the necessary modifications to both the stiffness matrix method and FEM to apply both techniques to the analysis of liquid loaded FPW structures. It was shown that the FEM requires the addition of a dedicated fluid element, whereas the stiffness matrix method requires significant modification. In particular, for the stiffness matrix method, the additional liquid layer is modelled as semi-infinite, whereas for the FEM, the optimum liquid thickness was found to be 1.5 times the IDT edge-to-edge spacing. The frequency response of a liquid loaded FPW structure was obtained via the techniques presented by the author and the spectral domain Green's function. It was found the FEM based techniques provided a more correct representation of the influence of the additional liquid layer when compared against experimental results presented in literature. The spectral domain Green's function, in its current form, was unable to correctly calculate the required characteristics, and in some cases, provided insertion loss characteristics superior to that of an unloaded FPW structure.

- The author has developed a series of guidelines for the analysis of multilayered FPW structures based on the presented FEM techniques. Although the author's analysis focuses directly on FPW devices, it is believed that the same technique

could be applied to other acoustic wave structures. To the best of the author's knowledge, this is the first time a critical discussion has been held on the influence of FEM simulation parameters, such as node density, simulation time, timestep and structure length for the analysis of acoustic wave devices in gas media. A discussion has also been held on the influence of the assumed liquid thickness and node density when modelling liquid loaded FPW structures via the FEM.

- Density, viscosity and mass sensitivity of multilayered FPW structures in liquid media has been discussed and compared against commonly quoted single layer equivalents. To the best of the author's knowledge, this is the first time that theoretical density, viscosity and mass sensing results have been calculated for multilayered FPW structures. Evaluation of the density-viscosity product has shown that a single FPW structure is theoretically capable of discriminating between these two parameters. Potential guidelines to increase the density, viscosity and mass sensitivity, such as the substitution of the piezoelectric layer, have been investigated. For a liquid loaded FPW structure, it was found that the substitution of the ZnO layer with a higher velocity material, such as AlN, resulted in an increase of all three quoted sensitivities.

- A thorough review of modelling techniques for the study of acoustic wave structures has been conducted and their suitability to FPW device analysis discussed. Of the reviewed techniques, it was found that none of the existing approaches considered were capable of solving for key electrical and mechanical properties simultaneously. To verify the author's novel approach to modelling FPW devices, three different, routinely applied, numerical techniques were implemented. The first technique, known as the transmission matrix method, allowed the basic properties of a FPW structures, such as phase velocity and electromechanical coupling coefficient to be obtained. Although relatively simplistic to implement, the transmission matrix method suffered from numerical instability when applied to structures with large frequency-thickness products and lossy material parameters such as those used to describe liquids. The cause of the instability was discussed and a suitable replacement technique, the stiffness matrix method, was

considered. This technique was applied in conjunction with a spectral domain Green's function to determine the frequency response characteristics of a FPW structure in the gas phase. Furthermore, these two techniques served as a benchmark for the author's approach to modelling FPW devices primarily based on the FEM. The necessary modifications to both the stiffness matrix method and the spectral domain Green's function to suit FPW structures were thoroughly described and implemented.

- Particle displacement profiles for multilayered FPW structures in both gas and liquid phases have been obtained and compared against the more commonly quoted single layer structures. It was found that particle displacement in multilayered FPW devices could no longer be categorised as antisymmetric or symmetric due to the alternative materials used throughout the layered structure. When placed in contact with liquid, a tightly coupled surface mode was identified, termed a Scholte mode, with a phase velocity approximately equal to the compressional velocity of the liquid. This particular mode was deemed responsible for most liquid sensing results presented in literature. A simple computational technique was also presented on acoustic mode identification for higher order modes near the cut-off region based on the calculated particle displacement profiles.

- Development, construction and commissioning of a reactive d.c. sputtering system for the deposition of aluminium and aluminium nitride thin films. Preliminary characterisation of the aluminium nitride films indicate a preferential c-axis orientation, with the piezoelectric properties determined by the unique application of an Atomic Force Microscope (AFM). A complete description of this technique has been accepted by an international journal for publication in late 2007.

In addition to the aforementioned achievements, the author has published four papers in international conference journals, of which the results are incorporated into this thesis. The author's list of publications are as follows:

- G. I. Matthews, S. J. Ippolito, W. Wlodarski, and K. Kalantar-zadeh, "Electrical parameter extraction of a Flexural Plate Wave device using the Finite Element

Method," *Proc. IEEE Ultrason. Symp.*, pp. 1136–1139, 2006.

- G. I. Matthews, S. J. Ippolito, K. Kalantar-zadeh, W. Wlodarski, and A. S. Holland, "Finite Element Modelling of Flexural Plate devices," *Conference on Optoelectronic and Microelectronic Materials and Devices, (COMMAD)*, pp. 145–148, 2004.

- A. S. Holland, G. K. Reeves, G. I. Matthews, and P. W. Leech, "Finite Element Modeling of misalignment in interconnect vias," *Conference on Optoelectronic and Microelectronic Materials and Devices, (COMMAD)*, pp. 307–310, 2004.

- S. J. Ippolito, K. Kalantar-zadeh, W. Wlodarski, and G. I. Matthews, "The study of ZnO/XY $LiNbO_3$ layered SAW devices for sensing applications," *IEEE Sensors*, vol. 1, pp. 539–542, Oct. 2003.

- S. Sriram, M. Bhaskaran, K. T. Short, G. I. Matthews, and A. S. Holland, "Piezoelectric response characterization using atomic force microscopy with standard contact-mode imaging," *Micron*, In Press.

The author was also fortunate enough to attend the 2006 IEEE Ultrasonics Symposium, October 3-6, 2006, Vancouver, Canada to present his novel work on the analysis of FPW structures.

During the period of this PhD program, the author has also actively been involved in the development of test instruments for gas sensing. The most notable success was the development of a non-specific vehicle cabin air quality monitor for the Australian motor vehicle fleet [22]. The results have been presented to the Federal Department of Health and Ageing where a legislative mandate is under consideration.

A microprocessor controlled ozone generator, capable of concentrations below $200$ parts-per-billion has also been developed by the author, which has resulted in numerous publications by colleagues. The automated test and measurement system compliments the group's advanced multi-channel gas calibration system to allow for the accurate evaluation of novel acoustic wave sensor designs.

## 1.4 Thesis Organisation

The objective of this thesis is to provide a conclusive and thorough evaluation of FPW structures sensing applications in both gas and liquid media. This thesis is segregated into six further chapters, each with a comprehensive discussion of a particular aspect of FPW device design and simulation. The main chapters, and their contribution to the overall evaluation of FPW device designs, are as follows:

- Chapter 2 provides a critical review of current literature relating to the use of acoustic wave devices for sensing applications in both gas and liquid media. Four acoustic wave devices are discussed and their applicability to sensing discussed. A brief introduction to modelling techniques will also be given, where it will be shown that various limitations in current methods exist, thereby warranting the author's novel approach to the analysis of FPW structures.

- Chapter 3 introduces the commonly used Transmission Matrix method and its application to solving the piezoelectric wave propagation problem in multilayered FPW structures. A brief introduction to the concepts of stress and strain, piezoelectric constitutive equations and the underlying assumptions of the technique will be given. The basic operating parameters of FPW structures, such as dispersion characteristics, electromechanical coupling coefficient and boundary conditions are discussed. The inherent numerical instability of the transmission matrix method is discussed in detail, with an example given to illustrate the inability of the technique to evaluate FPW structures with large thickness-frequency products and complex material properties.

- Chapter 4 presents a recently developed technique known as the Stiffness Matrix method as a potential replacement for the transmission matrix method to solve the piezoelectric wave propagation problem in multilayered FPW structures. This technique is known to be unconditionally stable for large frequency-thickness products as well as for complex material properties. Using this approach, the particle displacement profiles and mass sensitivity of multilayered FPW devices is presented and a comparison performed with simpler, single layer, isotropic models. The frequency domain characteristics of FPW devices, in terms

of input and output admittance, is also presented in this chapter based on a spectral domain Green's function, which was originally developed for SAW devices. The necessary modifications of the spectral domain Green's function undertaken by the author for the analysis of FPW structures is presented. Various parameters of the spectral domain Green's function are investigated to evaluate their respective influence on solution convergence. The analysis performed in this chapter, relating to both the stiffness matrix method and the spectral domain Green's function will serve as a benchmark to the authors novel approach to FPW device analysis.

- Chapter 5 introduces the author's novel approach to the analysis of FPW structures based on the convergence of the FEM with modified SAW techniques and related procedures. A brief introduction into the foundering principals of the FEM will be given, illustrating the numerous benefits of utilising this technique. A discussion will be held on the application of coupled-field analysis techniques and the necessary parameters required to efficiently and effectively simulate a FPW structure. A three dimensional FPW device will be investigated, where the electrostatic charge density and displacement profiles will be studied. This simulation will also assist in the development of various optimisations, thereby reducing the solution computation time. From these results, a two dimensional FPW device simulation will be considered, with the effect of the surrounding silicon support structure evaluated, which is typically neglected using other modelling techniques. The frequency domain characteristics of the 2D FEM FPW structure will be determined by considering the induced charge on the electrodes, which will allow the admittance characteristics to be calculated. A comparison will be performed between the results obtained by the author and another recently suggested technique [21] used for the analysis of SAW structures. This chapter will also provide, to the best of the authors knowledge, the first published detailed discussion of the FEM simulation parameters and how these affect solution convergence when applied to the analysis of FPW structures. In particular, the influence of the simulated structure length, simulation time, solution time step and finite element node density will be discussed. Chapter 5 concludes with a com-

parison between the novel approach developed by the author and the widely accepted spectral domain Green's function.

- Chapter 6 illustrates the use of FPW devices for sensing applications in liquid media. Using the modelling techniques of Chapters 4 and 5 the influence of liquid media on the frequency domain characteristics of FPW devices is considered. It will be shown that the author's approach based on the FEM is more appropriate than other conventional techniques in evaluating critical performance parameters of these devices. A discussion is also held on the performance of the FEM and the influence of several of the modelling parameters on the insertion loss characteristics. From this discussion generic guidelines will be established concerning the use of the FEM when considering liquid loaded acoustic wave structures. Although a FPW device is employed within this study, the techniques developed by the author can potentially be applied to other acoustic wave devices, thereby illustrating the versatility and applicability of the approach. A study will also be undertaken on the ability of a FPW device to detect changes in liquid density, viscosity and applied mass. The author concludes the theoretical analysis of FPW devices for sensing applications in liquid media with a brief introduction into the physical realisation of the FPW structures discussed herein. Particular emphasis is placed on the development and commissioning of a d.c. sputtering system design by the author.

- Chapter 7 concludes this thesis and presents suggestions for future work in terms of the development of the author's novel approach to FPW device analysis using the FEM.

[ This page has intentionally been left blank. ]

# Chapter 2

# Literature Review

## 2.1 Introduction

This chapter provides a critical review of current literature related to sensing applications in both gas and liquid media using acoustic wave devices. The knowledge gained from this review will form the basis for the author's novel approach to modelling Flexural Plate Wave devices for sensing applications.

Section 2.2 is devoted to the study of acoustic wave devices that can be utilised in both gas and liquid environments. In particular, Flexural Plate Wave, Quartz Crystal Microbalance, Shear-Horizontal Surface Acoustic and Thin Film Bulk Acoustic Wave Resonator devices will be discussed. For each device studied, potential applications and basic operating principals will be presented. It will be illustrated that FPW devices are well suited to sensing applications in liquid media, where it is necessary to quantify changes in physical properties such as applied mass, liquid density and viscosity. The application of these structures in liquid media is also presented and where possible the effect of the applied liquid quantified, in terms of change in resonant frequency or attenuation. Sample values of mass sensitivity are also given to allow the reader to appreciate the highly sensitive nature of acoustic wave devices.

Section 2.3 focuses on the myriad of techniques to model FPW structures. The analysis is split into two sections, with the first focusing on techniques to determine basic operating parameters, such as phase velocity and resonant frequency, primarily determined by the physical nature of the device. The review will initially focus on sin-

gle isotropic layer structures, which allows the basic concepts to be understood. The more advanced Transmission Matrix method is introduced and the basic premise of this technique presented. A brief explanation of the limitations of this approach will be given, with a more in-depth analysis presented in Chapter 3. The more recently developed Stiffness Matrix method will then be considered and its relationship to the generalised spatial Green's function highlighted.

The second group of modelling techniques briefly reviewed focus on the frequency response of FPW devices. The simplest technique known as the Delta-Function method will be discussed. From there, an introduction into the Coupling of Modes approach will be given, which can be applied to resonator style FPW structures. The commonly applied spectral domain Green's function will also be presented, which serves as a basis for comparison to the author's novel approach to FPW analysis. A discussion will be undertaken on the electrostatic approximation for the analysis of interdigital transducers and the relationship between the spatial and spectral domain Green's functions established. Finally, the Finite Element Method, and its use for evaluation of FPW structures will be discussed. A concise history on the technique will be given and its applicability to various different problems discussed.

## 2.2 Acoustic Wave Sensors

This section discusses the use of acoustic wave devices for sensing applications. Depending on the particular device employed and the materials utilised, these structures can be applied to detect a wide range of measurands such as mechanical properties of thin films, electric fields, as well as chemical and biological quantities in both gas and liquid media [8]. To act as sensors, the output of these structures must change as a result of the perturbation of the propagating electro-acoustic wave. For the same structure, the excited acoustic modes can offer different sensitivities to mass, density, viscosity or conductivity.

Acoustic wave sensors have been developed using Rayleigh, Lamb, Love, acoustic plate and surface transverse modes [5]. Each of these particular modes have advantages, however there are limitations on the type of media that these structures can be operated in. For example, in a liquid environment Rayleigh mode devices are typically

not utilised as much of the acoustic energy is dissipated into the surrounding medium due to their inherently high phase velocity and elliptical surface particle displacement. Throughout this thesis, the use of FPW devices for sensing applications in gas and liquid media will be discussed. It will be demonstrated that, provided certain design criteria are met, FPW structures are particularly well suited to measuring changes in density, viscosity and applied mass in liquid media.

The remainder of Section 2.2 considers four alternative acoustic wave devices and their applicability to sensing applications are discussed. A brief outline of their mode of operation is presented and where available examples of their sensitivity towards applied mass, density or viscosity given.

### 2.2.1 Flexural Plate Wave Devices

The first detailed description of acoustic modes propagating in a thin isotropic plate was given by Sir Horace Lamb in 1917 [23]. In this classic paper, Lamb investigated the propagation of elastic vibrations in a layer bounded by two parallel infinite plates. Since then many researchers have investigated the propagation of acoustic waves within thin plates, particularly for non-destructive evaluation of composite materials and as a method of detecting biological agents in liquid media. Although the acoustic modes are typically referred to as Lamb waves, the term Flexural Plate Wave (FPW) is used to describe the physical device due to the primary antisymmetric mode 'flexing' surface particle motion.

Viktorov [24], in his early discussion on Rayleigh and Lamb waves, describes Lamb waves as elastic perturbations in a solid plate for which displacements occur in both the direction of propagation and perpendicular to the surface. He showed that in an acoustically thin isotropic material, two primary modes propagate of which the solutions can be grouped according to their antisymmetric or symmetric displacements about the mid-plane of the structure. The primary modes, denoted $A_0$ and $S_0$, for antisymmetric and symmetric displacements respectively, exist for any plate thickness. When the thickness of the structure is small compared to the acoustic wavelength, these waves can be identified by their distinct velocities. However, as the thickness of the structure is increased, the two modes converge to the bulk, or Rayleigh, velocity of

the substrate. The antisymmetric mode is identified in the small thickness-wavelength region, $(h/\lambda << 1)$, by its low velocity, whereas in the same region the symmetric mode typically has a phase velocity greater than the Rayleigh velocity. It will be demonstrated in Chapter 3 that as the thickness of the structure is further reduced, so is the phase velocity of the antisymmetric mode.

Wenzel et al. [25] derived a simple analytical solution for the phase velocity, in m/s, of the two primary acoustic modes propagating in an isotropic plate, given by:

$$v_p^{A_0} = \sqrt{\omega h}\left(\frac{E^{'}}{12\rho}\right)^{\frac{1}{4}} \tag{2.1a}$$

$$v_p^{S_0} = \sqrt{\frac{E^{'}}{\rho}}, \tag{2.1b}$$

where $v_p^{A_0}$ and $v_p^{S_0}$ represent the phase velocity of the antisymmetric and symmetric modes respectively, $E^{'} = E/\left(1-v^2\right)$, $E$ is the Young's modulus, $v$ is Poisson's ratio, $\rho_p$ is the plate density and $d$ is the plate thickness. Equation 2.1b indicates that the phase velocity of the symmetric mode is constant, however this is not the case for the antisymmetric mode which is highly dispersive. This theory was later extended to include the effects of in-plane tension which is primarily a fabrication issue [14]. It should be noted that the phase velocity of the symmetric mode can only be assumed to be constant for small device thickness-wavelength ratios.

The relatively low phase velocity of the primary $A_0$ mode, coupled with the surface particle displacement profiles, makes FPW structures attractive for sensing applications in liquid media [5]. From equation 2.1a, the velocity of the $A_0$ mode is dependent on the structure thickness. Typical FPW liquid media sensors are fabricated with a total thickness of less than $3$µm [14], which corresponds to a $A_0$ phase velocity of approximately $474$m/s. Via Huygens' principal [26], if the velocity of the mode is below the compressional velocity of the surrounding liquid, energy will not radiate from the plate into the liquid, thereby minimising attenuation. However, a frequency shift will occur caused by the effective mass loading of the structure, therefore providing an easily measurable method of evaluating the properties of the applied liquid.

When a FPW device is placed in contact with liquid media the propagation characteristics of the primary $A_0$ mode change significantly. A tightly coupled, non-lossy surface wave is generated within the structure and liquid that propagates with a phase

velocity very close to the longitudinal wave velocity within the liquid. This interface wave, termed a Scholte mode [27], is typically responsible to many of the sensing results presented in literature. The characteristics of this mode will be discussed in Chapter 6.

FPW structures are typically fabricated on a silicon substrate, thereby allowing the signal processing electronics to be integrated on the same die. As the resonant frequency of these structures is quite low, typically less than 10MHz for $A_0$ and 100MHz for $S_0$, signal processing electronics are quite simple and inexpensive. Shown in Figure 2.1 is the typical construction of a FPW device [28]. In most devices, a low stress silicon nitride ($Si_xN_y$) film is deposited on one side of the Si wafer to define the active area of the sensor. A low pressure plasma enhanced chemical vapour deposition (LPPECVD) technique is favoured to create a silicon rich non-stoichiometric low stress film [8].

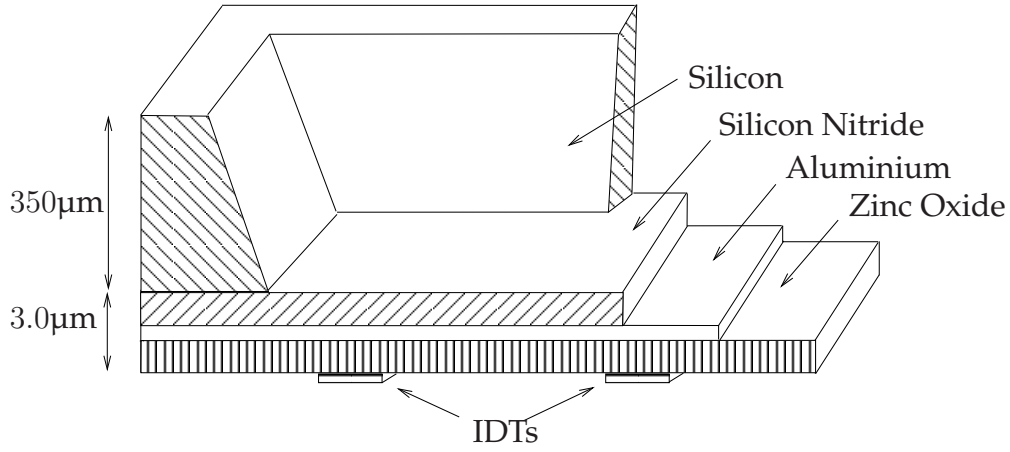


Figure 2.1: Typical FPW Device Cross-Section

Via bulk micromachining techniques, a cavity is anisotropically etched in the Si substrate to form the thin plate, or membrane which defines the active area of the device. After etching, an aluminium or gold metallic layer is then deposited on the $Si_xN_y$ to form a ground plane as well as to minimise the intrinsic stress when the piezoelectric layer is deposited [29]. A piezoelectric layer, such as zinc oxide or aluminium nitride, is then deposited to convert the applied electrical energy to a mechanical deformation and vice-versa. In this particular implementation, a metallic layer is deposited to form interdigital transducers which are used in conjunction with the piezoelectric layer to

excite and detect the propagating acoustic waves. A IDT electrode period of $\approxeq 100$µm is typically used, which provides a thickness-wavelength ratio of $0.03$.

A wide variety of acoustic wave excitation methods exist for FPW structures. For sensing applications, IDTs are typically used due to the ease of manufacture and low cost. Magnetic excitation in a resonator structure has been recently investigated by Martin [30] which simplifies the fabrication process by excluding the piezoelectric layer. Here a meandering line transducer and a static magnetic field is used to excite and detect Lamb waves. The reduced thickness of the membrane also increases the mass sensitivity. Other acoustic wave generation techniques include electrostatic excitation and capacitative detection as suggested by Giesler et al. [31]. Similar to the device described by Martin, this excitation method does not employ a piezoelectric layer. In this approach, a glass substrate was bonded to the FPW device and an electric field applied between the metallic layer and the glass to attract the membrane. Other excitation methods will be discussed in Chapter 4.

Lamb waves have also been applied to the non-destructive evaluation (NDE) and monitoring of materials for several years. Alleyne [32] has shown that both the $A_0$ and $S_0$ modes can be applied to determine defects within metallic plates. Here, the sensitivity of various Lamb modes to notches of different depths and widths was investigated, where it was found that the reflection and transmission of the modes is dependent on the frequency-thickness product, mode type, mode order and the geometry of the defect. It was concluded that Lamb waves can be used to find notches when the wavelength to notch ratio is on the order of $40$. As Lamb waves induce stresses throughout the plate, this technique can be used to probe the surface for defects as well as the complete thickness of the structure. For NDE tasks, a wedge bonded transducer is typically used to excite the acoustic modes rather than IDTs as with sensing applications. Coupling is achieved by either grease, or immersion in water. For non-contact evaluation, laser excitation can be used which is beneficial for process monitoring in harsh environments [33]. Lamb waves have also been applied to evaluate surface roughness. It was found by Leduc et al. [34] that the phase velocity of the $A_0$ and $S_0$ modes is largely unaffected by the surface condition, however the wave attenuation can significantly vary. For small surface roughnesses, a linear dependance of attenuation was found.

At an average surface roughness of $67$µm, a $25\%$ amplitude reduction was detected for $A_0$, whereas for $S_0$ a $20\%$ shift was observed.

Although in the context of this study, FPW devices are investigated for their ability to detect changes in density, viscosity and mass in liquid media, they have also been successfully applied to many other applications. FPW structures were applied as micro-actuators in liquid media by Moroney [9] where displacements of $6.5$nm at a pumping speed of $100$µl/s were obtained for a FPW device operating at $4.7$MHz. The elastic properties of thin films and composite structures have also been rigorously investigated by Nayfeh and Chimenti [35] and Moreau [36]. In work conducted by Nayfeh et al., a fibre-reinforced graphite-epoxy composite plate was immersed in a liquid to couple the acoustic energy into the structure. The reflected acoustic wave was measured from where the dispersion characteristics of the composite structure could be obtained.

An interesting feature of FPW devices is the symmetry of the surface particle displacement profiles. For isotropic layer devices, similar acoustic energy is present at the upper and lower surfaces, therefore either side of the structure can be applied for sensing applications. With reference to Figure 2.1, the etched side is preferred as this shields the sensitive IDTs from potentially corrosive environments. Also, in terms of liquid media applications, the cavity formed during the fabrication process creates a well for the analyte. In other acoustic wave devices, a flow cell typically must be added to the device, thereby increasing the cost and also affecting the wave propagation due to substrate loading.

In terms of micromachined sensors, which is the focus of this study, FPW devices have successfully been applied to sense pressure [10], humidity [11], protein concentration [12], liquid density and viscosity [13]. The ability of a FPW structure to be adapted to a wide variety of sensing applications makes the platform very appealing for study. The basic layout of the structure is the same, however for each different application, the sensitivity towards a particular measurand is typically achieved by an additionally deposited sensitive layer. For gas-phase experiments, metal oxide sensitive layers such as indium oxide or zinc oxide can be applied [37–39].

The mass sensitivity of a single isotropic layer FPW structure operating in the gas-

phase, expressed in cm$^2$/g, has been determined by Wenzel [14] and Wang [40] as:

$$S^f_{A0m} = -\frac{1}{2\rho d} \tag{2.2a}$$

$$S^f_{S0m} = -\frac{1}{\rho d}, \tag{2.2b}$$

where $d$ represents the half thickness of the single layer FPW structure. At first glance, a discrepancy exists in the mass sensitives between [14] and [40], which can be explained by the variables used to describe the thickness of the single layer structure. Note that $S^f_{A0m}$ and $S^f_{S0m}$ represents the mass sensitivity for the antisymmetric and symmetric modes respectively. The negative sign indicates that with the addition of an unknown mass the phase velocity, and hence frequency, of the acoustic modes are reduced. From equation 2.2 it can be seen that the mass sensitivity of the structure can be increased by reducing the thickness of the device. It will be shown through the course of this thesis that equation 2.2 can not be applied to multilayered structures, thereby requiring the mass sensitivity to be evaluated by numerical methods.

Experimental mass sensitives of $-1014$cm$^2$/g have been reported by Wenzel et al. [41] for a FPW structure consisting of a ZnO on $Si_3N_4$ delay line operating at $2.6$MHz, immersed in a fluid. Wenzel et al. have also conducted various experiments to determine the response of FPW devices when loaded with a liquid on one side. Antisymmetric phase velocities of $473$, $303.5$ and $322$m/s were obtained when the device was exposed to air, deionised water and methanol respectively, further indicating the versatility of FPW structures.

Ballantine et al. [42] have shown that a FPW structure is more sensitive to mass perturbations than an SAW device operating at the same frequency. White [26] has also shown that when an additional $10$Å of material is placed upon a FPW, the fractional frequency shift of the $A_0$ mode is $7$ times that obtained for a SAW structure with an identical wavelength. A larger shift of $14$ times was obtained for the $S_0$ mode when compared against the same SAW device.

In terms of biosensing applications, a sensing layer is usually spin-coated onto the surface of the device. The additional layer, which is typically a polymer, causes attenuation of the acoustic modes due to viscous losses. The application of a FPW device to detect changes in density and viscosity will be fully explored in Chapter 6, however

this ability can be exploited to examine the binding of various biological agents to the sensitive layer. Costello et al. [28] have shown that a FPW device can be configured to detect bovine serum albumim (BSA) at a concentration of $3$mg/ml in a phosphate buffer. A frequency shift of $2$kHz was detected for their structure, corresponding to $2.8$µg/cm$^2$ of protein being adsorbed onto the device. More recently, FPW biosensors have been constructed by Pyun et al. [43] to detect E.coli bacteria where a lower detection limit of $6.2 \times 10^7$ cells/ml was obtained.

### 2.2.2 Quartz Crystal Microbalance

The Quartz Crystal Microbalance, originally applied to sensing applications by Sauerbrey in 1959 [44], is the simplest of acoustic wave devices that can be used in both gas and liquid media. These devices typically consist of a thin circular AT-cut quartz crystal with gold or platinum electrodes, Figure 2.2. For the fundamental resonance the shear particle displacement at the device surface is at a maximum, which makes these structures ideal for mass sensing applications. It has also been found that excitation by surface electrodes cause only the odd harmonics to be generated [8], which do not excite longitudinal modes. As the particle displacement is parallel to the surface, these devices are well suited to sensing applications in liquid media, due to the acoustic energy being theoretically confined to the device rather than being radiated into the surrounding environment.

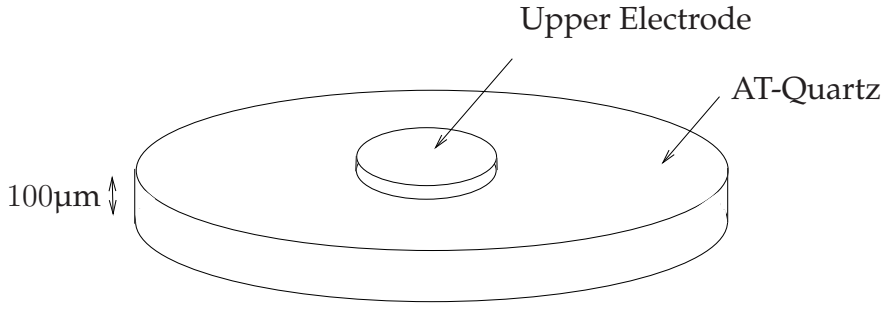


Figure 2.2: Typical QCM Structure

A significant benefit of QCMs, particularly when operated in a gas phase, is the relatively inexpensive signal processing electronics when compared to other acoustic wave devices. QCM's are typically configured as a feedback element in an oscillator,

where the resonant frequency, originally derived by Sauerbrey [45], is given by:

$$f_0 = \frac{N}{2h}\sqrt{\frac{\mu}{\rho}}, \tag{2.3}$$

where $f_0$ is the unperturbed resonant frequency, $N$ represents the $N_{th}$ harmonic excited, $h$ is the structure thickness, $\mu$ and $\rho$ represent the elastic shear modulus and density of the crystal respectively.

Several examples exist in literature of the processing electronics to excite the shear mode in QCM structures [46, 47]. In systems studied by the author, a series of inexpensive high-speed TTL inverters are used. The QCM resonant frequency can then determined with a standard counter through a buffer to prevent loading of the circuit. More advanced systems used a Phase-Lock Loop (PLL) system. In liquid media, the processing electronics, depending on the attenuation caused by viscous losses, are substantially more complex therefore often requiring an automatic gain stage.

QCMs were originally employed as a mass sensors in vacuum and gas phase experiments [48]. In a vacuum environment, QCMs are routinely applied to measure the thickness of a thin film during the deposition process. Similar to FPW structures, the additional mass placed on the surface causes the resonant frequency of the structure to decrease. To determine the mass sensitivity of these structures, the Rayleigh hypothesis can be applied, where it is assumed that the added mass layer does not affect the peak kinetic and potential energies [8]. For small accumulated mass, in a gas or vacuum environment, a linear relationship exists for the change in resonant frequency [49]:

$$\frac{\Delta f}{f_0} = -\frac{\Delta m}{m}, \tag{2.4}$$

where $\Delta f$ is the change in resonant frequency, $m$ and $\Delta m$ represents the mass per unit area of the unloaded resonator and the additional mass respectively. Equation 2.4 has been shown to be valid for an additional mass of $1 - 2\%$ of the original resonator mass [49].

For a QCM operating in a gas phase, the mass sensitivity is inversely proportional to the device thickness. Thus, analogous to a single layer FPW device, a higher mass sensitivity can be achieved when the QCM thickness is reduced. However, as the QCM is thinned, the device becomes quite fragile, therefore limiting the application of these

structures. Reported mass sensitivities of $-14\text{cm}^2/\text{g}$ have been achieved for QCM structures operating at $6$MHz [14] in a gas phase.

When loaded with a liquid, the characteristics of a QCM vary significantly. The change in resonant frequency induced by the additional liquid layer, under the no-slip condition, has been described by Kanazawa and Gordon [50] as:

$$\Delta f = -f_0^{\frac{3}{2}} \sqrt{\eta_l \rho_l / \pi \mu \rho}, \tag{2.5}$$

where $\eta_l$ and $\rho_l$ are the shear viscosity and density of the added liquid layer. Although the resonant frequency of the QCM is varied by the addition of a liquid layer, the mass sensitivity remains mainly unchanged if the added layer is assumed to be rigidly coupled. Similar to FPW devices, either side of the structure can be used for liquid media sensing applications, provided the electrodes are electrically isolated. This is typically achieved using a flow-cell structure where the QCM is clamped in a specially designed holder and supported by a series of gaskets [51]. Furthermore, both sides of the structure can be simultaneously loaded with alternative liquids for differential sensing applications.

When used as a mass sensor in a liquid environment, Tessier et al. [51] have shown that if the quality factor and resonant frequency are measured simultaneously a discrimination can be made between the viscous effects of the liquid and the additional mass. In this configuration, a standing shear wave was also established which caused attenuation of the resonant mode, thereby necessitating the aforementioned further gain stage in the signal processing electronics.

Much work has taken place on enhancing the sensitivity of QCMs when used for sensing applications in liquid media. As the devices are relatively simple to construct, they are often preferred over other acoustic wave structures. Martin et al. [52] have shown that the surface roughness of a QCM has an effect on the sensitivity of the structure. It was found that for surface features that are much less than the acoustic decay length, the frequency response of the structure depends only on the density-viscosity product. Beyond this point, the acoustic impedance of liquid load increases, caused by the effective trapping of the liquid via surface features and the device exhibits characteristics similar to a mass being deposited on the surface.

More recently, multichannel QCM structures have been developed which allows for

two simultaneous measurements [53]. There are significant benefits to this approach, including cost and size reductions, however the overall structure must be carefully designed to minimise interference between the two devices. These types of structures can also be used in a differential configuration to minimise environmental effects such as temperature, humidity and other mitigating factors.

### 2.2.3 Surface Acoustic Wave Devices

The use of Surface Acoustic Wave devices for sensing applications is a highly studied area. Although originally developed by White and Voltmer in 1965 [54] for signal processing applications, since the 1970's these structures have been widely used as chemical sensing platforms. Depending on the device materials and layout, several different acoustic modes can be generated. Unlike bulk mode devices, such as QCMs, a SAW structure is capable of generating acoustic waves with displacement components primarily in two planes. For example a Rayleigh mode, which is closely coupled to the device surface, consists of displacement components in the propagation and surface normal directions, making this type of device well suited to gas phase experiments. Conversely, a Love mode device contains displacement components in the shear and longitudinal directions, thereby making them compatible with liquid media sensing applications.

A wide variety of substrates exist for SAW device fabrication, with recent sensors fabricated in quartz, lithium niobate ($LiNbO_3$), lithium tantalate ($LiTaO_3$) and langasite ($La_3Ga_5SiO_{14}$) piezoelectric substrates. Due to the anisotropic nature of these substrates, different orientations provide the designer with the ability to tailor the device for a given wave type. Due its well understood properties, silicon was initially used as a substrate material for SAW structures with a further piezoelectric layer deposited to excite the acoustic wave. However, devices fabricated in silicon are prone to electromagnetic feedthrough [55], which is a capacitive coupling between input and output transducers that can significantly mask the device response. The use of the aforementioned non-conductive substrates minimise the effect of electromagnetic feedthrough, thereby simplifying the device layout. The other benefit of these substrates is their high electromechanical coupling coefficients, which allow a SAW structure to be fabricated

without the need for further piezoelectric layers. In filter applications, this is typically the case, whereas in acoustic wave sensors a further layer is deposited to increase the sensitivity of the structure. Figure 2.3 depicts a typical layered delay line SAW device configured for sensing applications. Depending on the application, the IDTs can either be placed on the upper exposed surface or between the sensitive layer and the piezoelectric substrate.

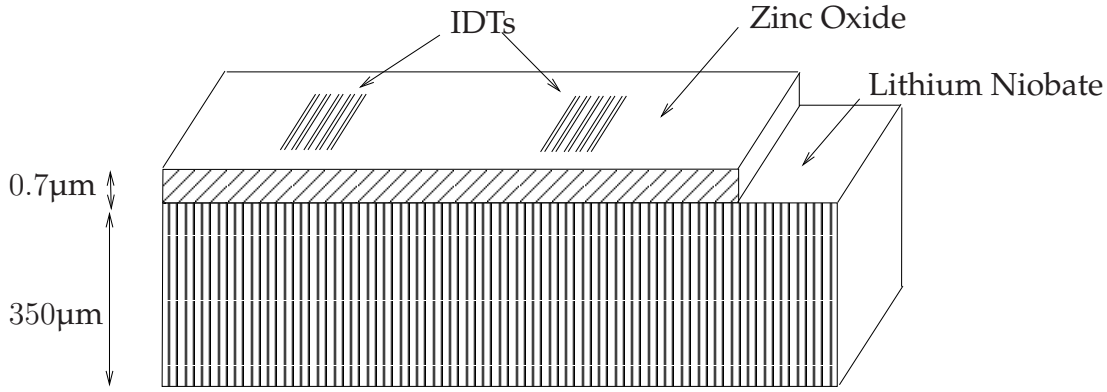


Figure 2.3: Typical Layered SAW Device Cross-Section

As was mentioned in Chapter 1, two surface metallisation configurations exist to excite and detect acoustic waves for SAW structures. For oscillator applications a resonator structure is typically used, which relies on in-phase reflections of the acoustic wave caused by metallic gratings deposited on the device surface. Similar to QCMs, these types of structures exhibit a high quality factor which improves the signal to noise ratio. The second type of surface metallisation is known as a delay line structure, which is typically used in filter and sensing applications. Modification of the delay path manifests as a change in phase velocity and hence resonant frequency.
The resonant, or synchronous, frequency of a SAW device is given by:

$$f_0 = \frac{v_p}{\lambda} \tag{2.6}$$

Unlike FPW devices, for a bare substrate, the phase velocity of a SAW device is independent of the thickness of the substrate. For modelling these devices, as will be discussed in Section 2.3, the substrate is assumed to be semi-infinite due to the limited interaction of the propagating wave with the lower surface. For sensing applications, devices have been fabricated with electrode periods in the order of $24$µm on

$LiNbO_3$, corresponding to free surface frequency and phase velocities of $145.13$MHz and $3483.2$m/s respectively [7]. SAW filters for wireless applications are routinely fabricated with centre frequencies of up to $2.5$GHz [1].

A SAW device can potentially be more sensitive than its QCM counterpart to perturbation in boundary conditions due to the confinement of acoustic energy at the device surface, coupled with the increase in resonant frequency. In gas phase sensing, which is typically based on Rayleigh mode structures, a majority of the wave energy is within one to two wavelengths of the device surface. This implies that the propagating electro-acoustic wave will be affected by changes in both electrical and mechanical boundary conditions. Based on this principal, SAW structures have been successfully employed to measure temperature, force, displacement, flow [42], pressure [29], electric field [56], humidity [57], gas concentrations [7] and biological quantities [58].

In terms of electrical measurements, SAW devices can be configured to evaluate conductivity changes of an additional sensitive layer. As the SAW propagates along the piezoelectric structure, a layer of bound charge accompanies the mechanical wave. When the device is exposed to particular gases the electrical characteristics of the additional layer are modified, thereby causing a measurable change in the acoustic wave phase velocity via the acousto-electric effect [2]. Using a perturbation theory approach, where the thickness and electrical properties of the sensitive layer were ignored, Ricco and Martin [59] have shown the fractional shift in phase velocity and normalised attenuation due to changes in surface conductivity is given by:

$$\frac{\Delta v}{v_p} = -\frac{K^2}{2}\frac{\sigma_{sh}^2}{\sigma_{sh}^2 + v_p^2\varepsilon_p^2} \tag{2.7a}$$

$$\frac{\alpha}{k_x} = \frac{K^2}{2}\frac{v_p\varepsilon_p\sigma_{sh}}{\sigma_{sh}^2 + v_p^2\varepsilon_p^2}, \tag{2.7b}$$

where $K^2$ is the electromechanical coupling coefficient of the SAW mode at the device surface, $\sigma_{sh}$ is the sheet conductivity of the layer, $\varepsilon_p$ represents the permittivity of the structure and $\alpha$ is the imaginary component of the propagating mode wavenumber $k_x$. As mentioned in [21], care must be taken when evaluating $K^2$ for determining the properties of the SAW structure. For modelling purposes, $K^2$ is typically calculated at the IDT location, whereas for calculation of the conductometric sensitivity, it should be evaluate at the surface exposed to the gas species.

Recent work by Ippolito [7] has shown that conductometric sensitivity of a SAW device can be improved by the addition of an intermediate zinc oxide and indium oxide sensitive layers. By examining equation 2.7, it can be seen that the conductometric sensitivity is a function of the sheet resistance and is a maximum when $\sigma_{sh} = v_p \varepsilon_p$. Therefore, by modifying the velocity-permittivity product of the intermediate layers, the sensitivity of the structure can be improved. One technique is to modify the thickness of the piezoelectric ZnO layer. In [7] it was found that for a $LiNbO_3$ structure, an optimum ZnO thickness of $1.2$µm results in a shift of $514.7$kHz at a centre frequency of $165.3$MHz when exposed to $1\%$ hydrogen in synthetic air. It was also shown that using a similar structure, with the addition of a further sensitive layer, frequency shifts as large as $750$kHz, corresponding to a fractional frequency shift of $0.45\%$, can be obtained towards the same gas species [60].

The mass response of a SAW device is highly dependent on the substrate orientation and the acoustic mode utilised. Similar to FPW structures, the mass sensitivity for SAW devices can be determined by perturbation theory [61], which assumes that the deposited mass is rigidly coupled, can be approximated as isotropic and is of infinitesimal thickness. The added mass on the surface causes the mechanical wave to be perturbed, thus providing a measurable shift in both phase velocity and attenuation. Depending on the mass to be measured, and the method of delivery, several different acoustic modes can be used. In liquid media, a shear mode is typically used due to the high attenuation of the Rayleigh mode caused by viscous losses [62]. For the Rayleigh mode, the transverse and longitudinal displacements are within the same order of magnitude and hence the transverse component is highly damped in the presence of the liquid. In the gas phase, where a Rayleigh mode is typically employed, a chemically active sensitive film is coated onto the device to adsorb specific molecules [5] thereby increasing the effective mass on the device surface. The addition of the sensitive layer also presents an interesting problem in terms of mathematical models as this causes a further loss mechanism. Via perturbation theory, for a simple SAW structure, the mass sensitivity is given by [40]:

$$S_m^v = \frac{-V_R}{4|P|}\left(|v_x|^2 + \left(1 - \frac{E_3^{'}/\rho^{'}}{V_R^2}\right)|v_z|^2\right)_{z=0}, \tag{2.8}$$

where $V_R$ is the Rayleigh wave velocity, $v_x$, and $v_z$ represent the surface particle veloc-

ities of the longitudinal and transverse components of the unperturbed device and $|P|$ represents the power flow per unit width. The subscripted terms, $E_3^{'}$ and $\rho^{'}$ are the additional sensitive layers' Young's modulus and density respectively.

With the addition of sensitive layers, shear modes may exist and hence for multilayered structures equation 2.8 must be modified. Due to further assumptions in construction equation 2.8, discrepancies can exist between theoretical and measured values. For an ST-cut SAW delay line structure operating in the gas phase at $112$MHz, theoretical sensitivities of $-151$cm$^2$/g were calculated, whereas experimental values of $-91$cm$^2$/g were obtained [14].

Another widely studied area is the use of SAW Love modes for sensing applications in liquid media. This particular acoustic mode has primary displacement components in the shear direction, thereby limiting energy loss into the surrounding liquid medium. Unlike Rayleigh modes specific conditions, mainly pertaining to the velocities of additional guiding layers, are necessary to excite, and contain, Love waves. To realise a Love mode device, a SAW structure is initially fabricated on a piezoelectric substrate such as $90^\circ$ rotated ST-cut Quartz which supports a shear-horizontal acoustic wave. If an additional layer is deposited on the surface, such as silicon dioxide ($SiO_2$) or zinc oxide [58] which has a lower shear velocity than that of the substrate, then a highly trapped Love mode is generated within the upper layer. Mass sensitivities of $380$cm$^2$/g have been achieved for these structures operating at $110$MHz in water [63]. Before the wave guiding layer was deposited, a sensitivity of $14$cm$^2$/g was obtained.

Similar to the conductometric case, the sensitivity of a Love mode device is tailored by the thickness of the additional guiding layer. For the aforementioned device, an optimum $SiO_2$ thickness of $5.5$µm was experimentally determined [58]. Wang et al. [40] have shown that the maximum mass sensitivity for a Love wave device is achieved when the optimal thickness of the guiding later is proportional to the ratio of the shear velocities and densities of the materials via:

$$S_m^f = \frac{-4v_{s1}}{v_{s2}\rho_2\lambda_1}, \tag{2.9}$$

where $v_{s1}$ and $v_{s2}$ represent the shear velocity in the substrate and guiding layer respectively, $\lambda_1$ is the acoustic wavelength and $\rho_2$ is the density of the guiding layer.
From equation 2.9, it can be seen that maximum mass sensitivity is achieved when

the shear velocity and density of the guiding layer is low. As the thickness of the waveguiding layer is increased beyond the optimal thickness, the sensitivity decreases rapidly. The sensitivity of a Love mode device can be further increased by depositing a chemically sensitive viscoelastic layer on top of, or instead of, the solid $SiO_2$ or ZnO layers. These layers naturally damp the acoustic mode due to viscous losses, however allow the structure to be theoretically sensitive to a particular biological agent [64–66].

One difficulty of using Love mode devices for liquid media sensing applications is the dielectric influence of the target liquid. Du et al. [63] have shown that attenuation in a Love mode device is a function of both viscous losses and dielectric coupling. For a device operating in air, the insertion loss was experimentally determined to be $13$dB, whereas the addition of deionised water increased the insertion loss to approximately $39$dB. As has been discussed, due to the IDTs being on the opposite side of the FPW structure, as well as the metallic ground plane, these devices should not be greatly affected by the dielectric properties of the liquid.

### 2.2.4 Thin Film Bulk Acoustic Wave Resonators

More recently, Thin Film Bulk Acoustic Wave Resonator (TFBAR) structures have gained popularity for sensing applications. These devices share design principals from both FPW and QCM structures. A typical TFBAR device consists of a thin piezoelectric layer, typically less than a few micrometres thick with electrodes deposited either side of the film [67]. The layer can either be supported by the substrate, or suspended identical to that of a FPW device. Depending on the mode utilised, the surface particle motion of a TFBAR device can be either in shear or longitudinal direction. For a device presented by Wingqvist et al. [68], consisting of a $2$µm AlN piezoelectric thin film, the shear mode is generated at $1.25$GHz, whereas the longitudinal mode is substantially higher at $2.15$GHz. As has been previously discussed, for sensing applications in liquid media, shear surface particle motion is preferred to minimise losses caused by damping of the acoustic mode.

Initially TFBARs were applied to signal processing applications. By using a thin film, rather than a bulk quartz crystal, resonant frequencies can be obtained beyond $1$GHz for film thicknesses ranging from $1.2$µm to $5$µm. For economic reasons, it is

impractical to physically machine quartz plates to these dimensions, let alone the reduction in electromechanical coupling coefficient as the thickness of the substrate is reduced. Note that the calculation of $K^2$ is different to that for delay line structures as it depends on the series and parallel resonant frequencies. The suggested definition of effective electromechanical coupling can be found in [67]. Similar to most acoustic wave devices, ZnO or AlN is employed as the piezoelectric layer in TFBAR structures.

Several different approaches can be used to fabricate a TFBAR device, each with varying levels of difficulty. The most common approach is very similar to the fabrication of FPW structures [69]. A Si membrane is formed using the same fabrication processes as for FPW structures. Whereas in a FPW, IDTs are fabricated on the piezoelectric surface, two unpatterned metallic electrodes are deposited on opposite sides of the membrane, Figure 2.4. A second style of structure, known as a solidly mounted resonator, shares design principals from SAW resonator structures. Here, a series of acoustic reflectors, each a quarter wavelength thick can be sequentially deposited on a solid substrate. The number of layers depends on the reflection coefficient required. The structure should also be fabricated with alternating mechanical impedances to minimise residual stress. An example given in [67] shows that alternating layers of $SiO_2$ and AlN with the electrodes and subsequent piezoelectric layers can be used to realise this style of device. The third most common approach is the use of a sacrificial layer on a Si substrate [67]. A thin layer of $SiO_2$ is deposited on select areas of a Si substrate with the resonator structure formed on the top. The last step in the process is the etching of the sacrificial layer to form a suspended composite piezoelectric and metal resonator. This is typically the most difficult type of structure to fabricate as the $SiO_2$ layer must be carefully etched to fully release the device.

For signal processing applications, the longitudinal mode of a TFBAR is typically used, which becomes highly damped when placed in contact with liquid media. To resolve this issue the deposited ZnO or AlN piezoelectric layer must be c-axis orientated to generate a shear mode identical to that of a QCM. Care must also be taken to match the temperature coefficients of frequency between the different materials used to form the resonator. In comparison to quartz, thin film ZnO and AlN have a rather high negative dependence on temperature, which can be minimised by the deposition of

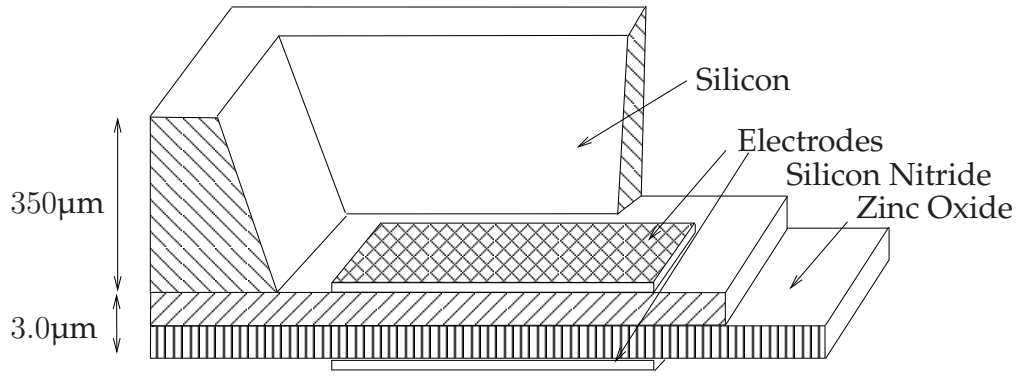


Figure 2.4: Typical TFBAR Cross-Section

other materials, such a $SiO_2$, with a positive temperature dependence [70]. However, the addition of other materials will increase the device thickness, therefore reducing the resonant frequency and hence the sensitivity of the structure. A recent discussion by Bjurström et al. [70] has shown that the second harmonic shear mode is better suited than the fundamental to liquid media sensing applications due to its higher quality factor and higher frequency thereby providing better resolution. It has also been found that temperature compensation for the second shear mode can be more readily achieved, with variances of $\pm 2$ppm/°C obtained over a range of $25$ to $95$°C in air.

The resonant frequency of a TFBAR is calculated in an identical manner to the QCM, equation 2.3, with the mass sensitivity given by equation 2.4 for small changes in applied mass. Although based on the same principals as QCM structures, due to the thin nature of the platform, the device is highly sensitive to mass changes. Benetti et al. [71] have shown that the theoretical mass sensitivity of a TFBAR device constructed with a $1$µm c-axis AlN membrane is approximately $34.8$kHZcm$^2$/ng, whereas for QCMs, the sensitivity is several orders of magnitude lower. The high sensitivity is attributed to the shear velocity of the AlN film, whereas an equivalent thickness device constructed with c-axis ZnO yields a theoretical sensitivity of $11.2$kHZcm$^2$/ng. Although these device exhibit a higher mass sensitivity than their QCM counterparts, attenuation increases with the square of frequency and hence a tradeoff exists between device instability and resolution [68].

TFBAR structures have successfully been applied to biosensing applications by Weber et al. [72], where it was found that the minimum detectable limit of $2.3$ng/cm$^2$ was

obtained towards bovine serum albumin (BSA). The particular structure was based on the solidly mounted resonator design, where alternating layers of zinc oxide and platinum were used to form an acoustic Bragg mirror, providing a centre frequency of $790$MHz. TFBAR devices have also been applied to viscosity sensing applications by Wingqvist et al. [68]. Here different concentrations of glycerol were added to water and the effect on the resonant frequency determined. For a viscosity-density product of $23.04$kgPam$^{-3}$s$^{-1}$ a frequency shift of $6,000$ppm was observed, corresponding to an actual deviation of $7.5$MHz. Although seemingly a relatively large shift, the long term stability of the oscillator must be considered. By applying the IEEE procedure for measuring noise in oscillators [73], Wingqvist et al. determined the mass sensitivity of their particular TFBAR structure was approximately $7.5$cm$^2$/ng. Campanella et al. [49] have also demonstrated an AlN composite device operating at $2$GHz where a minimum detectable mass of $0.158$ng/cm$^2$ was found.

## 2.3 Modelling Techniques

Over the years, a wide array of techniques have been applied to solve the piezoelectric wave propagation problem in acoustic wave devices. Many of these techniques and related procedures have directly focused on SAW technology, as this group of devices are commonly used for signal processing applications. With some modification, these techniques can be adapted for finite thickness FPW structures. This section provides a brief introduction to a select group of modelling techniques and highlights many of the assumptions made during their development.

Current acoustic wave device modelling techniques can be divided into two distinct groups. The first series of techniques focuses on the solution to the wave propagation problem. Using these methods, parameters such as phase velocity, electromechanical coupling coefficient, attenuation and power flow angle of various acoustic modes can be obtained. The second group evaluates the influence of the excitation source, which for this study is a series of interwoven electrodes, or IDTs. From these techniques, the frequency response characteristics of an acoustic wave device can be obtained via admittance parameters.

### 2.3.1 Potential Method Analysis

An excellent discussion of Lamb wave propagation in single isotropic layer structures appears in Viktorov [24], however the essential details are repeated here to demonstrate the applicability of this technique to the analysis of FPW structures.

Potential Method Analysis, or Potential Theory, is a commonly used technique to describe wave propagation in isotropic media in terms of a scalar and vector potential. The derivation of the potential method can be found in [61], which is based on the Christoffel equation. Potential method analysis is well suited to NDE applications, where single layer structures, such as steel or aluminium plates, are analysed. Due to the complex nature of multilayered structures, an analytical solution is often difficult to obtain, making the technique difficult to apply to acoustic wave sensors. The propagation of an acoustic wave along a single isotropic layer device can be written in terms of a scalar potential, $\phi$, and a vector, $\boldsymbol{\psi}$ of the displacements, which are related to the particle displacement, $\mathbf{u}$, by [74]:

$$\mathbf{u} = \boldsymbol{\nabla}\phi + \boldsymbol{\nabla} \times \boldsymbol{\psi} \tag{2.10a}$$

$$u_x = \frac{\partial \phi}{\partial x} + \frac{\partial \psi}{\partial z} \tag{2.10b}$$

$$u_z = \frac{\partial \phi}{\partial z} - \frac{\partial \psi}{\partial x} \tag{2.10c}$$

Under stress free boundary conditions at the upper and lower surfaces, omitting the factor $e^{j(\omega - k_x x)}$, trial solutions for the scalar potential and displacements are written in terms of simple trigonometric functions:

$$\phi = B \cos\left(k_{tl} z + \alpha\right) \tag{2.11a}$$

$$\psi = A \sin\left(k_{ts} z + \alpha\right), \tag{2.11b}$$

where $\alpha$ can take on successive values of $0$ or $\pi/2$, corresponding to symmetric or antisymmetric solutions respectively, $A$ and $B$ are constants and $k_{tl}$ and $k_{ts}$ are the wave vectors in the transverse and shear direction defined by:

$$k_{tl}^2 = \left(\frac{\omega}{V_L}\right)^2 - k_x^2 \tag{2.12a}$$

$$k_{ts}^2 = \left(\frac{\omega}{V_S}\right)^2 - k_x^2, \tag{2.12b}$$

where $V_L$ and $V_S$ are the material longitudinal and shear velocities and $\omega$ is the angular frequency. Substituting equations 2.11 and 2.12 into equation 2.10 results in the isotropic Rayleigh-Lamb characteristic equation, which describes acoustic wave propagation in a single layer isotropic plate structure of thickness $h$:

$$\frac{\omega^4}{V_S^4} - 4k_x^2 k_{tl}^2 k_{ts}^2 \left(1 - \frac{k_{tl}}{k_{ts}} \frac{\tan\left(k_{tl}h/2 + \alpha\right)}{\tan\left(k_{ts}h/2 + \alpha\right)}\right) = 0 \tag{2.13}$$

The solution to equation 2.13 can be obtained by a simple numerical search routine. To evaluate the propagating wavenumber the frequency, device thickness, longitudinal and shear velocities are held constant whilst the value of $k_x$ is scanned. Some very important concepts can be obtained by considering equation 2.13. Although only strictly valid for isotropic materials, the behaviour of the propagating modes is similar in the low frequency-thickness range for multilayered configurations. In the limit as $h \to 0$, the primary antisymmetric and symmetric mode velocities tends to a finite value, given by:

$$V_{A0} = \frac{V_{S0} k_x h}{2\sqrt{3}} \tag{2.14a}$$

$$V_{S0} = 2V_S \left(1 - \frac{V_S^2}{V_L^2}\right) \tag{2.14b}$$

Limits are also placed on the velocity of the symmetric mode, given by $V_S\sqrt{2} < V_{S0} < V_L$, which in turn also restricts $A_0$. However as $k_x \to 0$ for the $A_0$ mode, the velocity also tends towards zero. In the high frequency regime, as will be discussed more in detail in Chapter 4, the primary modes tend towards the Rayleigh mode velocity of the structure.

The behaviour of other Lamb modes can also be directly determined from the characteristic equation. Higher-order modes exhibit a cutoff frequency, which implies that they can only be excited above a certain frequency-thickness product. Below the cutoff frequency, these modes have an imaginary wavenumber $k_x$, however above this frequency, the wavenumber becomes complex and hence a propagating mode is created. This is typically plotted on a three dimensional figure as in [61].

### 2.3.2 Transmission Matrix Method

An alternative, and widely used, approach to solve the piezoelectric wave propagation problem in multilayered structures is known as the Transmission Matrix method, de-

veloped by Fahmy and Adler [75] in 1972. In this method, the piezoelectric wave propagation problem is solved by relating essential field variables at the upper and lower surfaces of a FPW structure via a transmission matrix. The essential field variables for piezoelectric media consist of normal stress, mechanical and dielectric displacements as well as scalar potential, from which all other components can be calculated. The technique has been successfully applied to bulk and Rayleigh [20, 76, 77] mode devices and to a lesser extent FPW structures [78]. One benefit of this approach is that it is based on the individual layer properties, including thickness, rather than the overall device geometry.

Similar to the potential method described previously, the transmission matrix method assumes that the wave propagation problem can be described in terms of longitudinal and transverse components. The effect of the shear components can be included, however for FPW and Rayleigh mode SAW structures, its influence has been found to be negligible in the context of this study. Throughout the development of the transmission matrix method, several improvements have been made. In the first paper published on the topic [75], unpublished work by Tonning and Ingebrigsten [79] was formalised into what is now commonly referred to as the transmission matrix method. The construction of the transmission matrix method is similar to that used for the analysis of tectonic plates within the Earth's crust [80]. Several analogies were drawn between the composition of the Earth's crust and the construction of acoustic wave devices. Similar to the layout of the Earth's crust, an acoustic wave device consists of multiple layers, each typically with unique material properties. In earthquake analysis, the acoustic wavelength may be on the order of several kilometres, whereas in the case of FPW structures, the wavelength is typically less than $100\mu$m.

In the original paper by Fahmy et al. [75], the technique is extended to support piezoelectric media, however in this formulation, the state vector $\boldsymbol{\tau}$, which consists of the essential field variables, contained ten components rather than the more recently presented version which consists of eight [76]. In structures comprised of purely isotropic materials this can be further reduced to six. The piezoelectric wave propagation problem, which describes the $z$-dependence of the eight partial modes, is ex-

pressed in terms of a first-order matrix differential equation, given by:

$$\frac{d\boldsymbol{\tau}}{dz} = j\omega \mathrm{A}\boldsymbol{\tau} \tag{2.15}$$

The solution to equation 2.15 is the well known matrix exponential [81]:

$$\boldsymbol{\tau}(z+h) = e^{j\omega \mathrm{A}h}\boldsymbol{\tau}(\mathbf{z}) = \phi(h,\omega,v_p)\boldsymbol{\tau}(z), \tag{2.16}$$

where $h$ represents the thickness of the layer under consideration, $\mathrm{A}$ is a $8 \times 8$ matrix that consists of material properties, angular frequency and phase velocity. The term $\phi$ is called the global transmission matrix.

In multilayered structures, the transmission matrices of the individual layers are calculated and then cascaded to form a global transmission matrix, which automatically satisfies all interfacial boundary conditions. The solution to the transmission matrix is then obtained by considering the upper and lower surface boundary conditions. For a FPW structure, with two free surfaces, the normal component of stress is zero. The electrical boundary conditions depend on the assumed surface metallisation. If a metalised surface is assumed, the tangential electric field is zero, whilst the surface charge remains unknown. Conversely, for a non-metalised surface, the tangential electric field is unknown, whilst the surface charge is zero. This results in the requirement that the determinant of a section of the transmission matrix is zero, which is well suited to a numerical search procedure. In solving equation 2.16, either the angular frequency, or the via the phase velocity term, the wavelength can be fixed, whilst the other parameter scanned to find all local minima. Assuming that both terminal surfaces are open-circuit, a propagating mode is determined by the condition:

$$\det|\phi_{\mathrm{ur}}| = 0, \tag{2.17}$$

where $\phi_{\mathrm{ur}}$ represents the upper right $4 \times 4$ block of the global transmission matrix $\phi$.

Although mathematically powerful, the technique becomes unstable for large frequency-thickness products as well as when working with lossy materials. The instability is evidenced for structures consisting of both anisotropic and isotropic materials. The cause of the numerical instability will be fully investigated in Section 3.4.1 and potential methods to alleviate this problem will be discussed. The instability induced at large frequency-thickness products is caused by the decoupling of the components that

relate the upper and lower surface of the structure, thereby causing the transmission matrix to become ill-conditioned. Many researchers have considered methods to rectify the instability [82, 83], of which the Stiffness Matrix method, discussed in Section 2.3.3, appears to be the most popular.

### 2.3.3 Stiffness Matrix Method

Although an elegant solution to the wave propagation problem for multilayered piezoelectric media, the transmission matrix method becomes ill-conditioned when working with large frequency-thickness products as well as complex material parameters. Much work has been undertaken in an attempt to reformulate the transmission matrix method to improve its stability. One of the more recent attempts developed by Wang and Rokhlin [84] is known as the Stiffness Matrix method. Whereas the transmission matrix method describes the relationship between the essential field variables at the upper and lower surfaces, the stiffness matrix method relates the displacement on both sides of a layer to the normal stress. The stiffness matrix method is known to be unconditionally stable for large frequency-thickness products, where the solution converges to the Rayleigh case, as well as for lossy materials.

Similar to the transmission matrix, the stiffness matrix method utilises a recursive algorithm that can be used to construct a global matrix to evaluate multilayered structures. Although slightly more complicated to implement, this operation retains the same computational efficiency as the transmission matrix chain multiplication [85]. The improved stability of the method is partial attributed to a modification of the coordinate system when considering the propagating modes. In this method, modes are split into either 'upwards' or 'downwards' modes based on the direction of power flow. Whereas the transmission matrix method is based on a first-order linear differential equation, the stiffness matrix method satisfies a nonlinear Riccati equation [85] which is known to be well suited to problems with unevenly growing terms [86].
The stiffness matrix for multilayered media is given by:

$$\begin{bmatrix} \mathbf{T}(z+h) \\ \mathbf{T}(z) \end{bmatrix} = \mathrm{K} \begin{bmatrix} \mathbf{U}(z+h) \\ \mathbf{U}(z) \end{bmatrix}, \tag{2.18}$$

where $\mathbf{T}$ is the normal components of stress, $\mathbf{U}$ is the generalised displacement vector

and $\mathrm{K}$ is the stiffness matrix for the given structure. Many of the numerical procedures used to evaluate the determinant of the transmission matrix can be applied to determine the solution to the wave propagation problem via the stiffness matrix method. If similar stress free boundary conditions are used, then the solution depends on evaluating the determinant of the stiffness matrix, $\mathrm{K}$, equation 2.18, at a given frequency or wavelength.

However, the benefit of the stiffness matrix method comes from its relationship to the generalised Green's function [87]. The spatial Green's function is a well documented solution technique used for the analysis of various branches of physical science, including electromagnetism, thermodynamics and acoustics. The spatial Green's function fully describes the electro-acoustic problem in terms of the mechanical displacement, normal stress, voltage and charge. Using this approach the electromechanical coupling coefficient, mass sensitivity and effective permittivity can be obtained at any position within the multilayered structure. This allows for the analysis of buried electrodes within the FPW device, which has been recently been discussed by Powell [21] for SAW resonator structures. The effective permittivity function is especially useful as it contains the complete information about all piezoelectrically coupled modes of the structure, whereas in some cases if the determinant of the stiffness matrix is taken, pure mechanical modes can be identified which are not of interest for this study.

### 2.3.4 Delta-Function Model

The Delta-Function model, introduced by Tancrell and Holland [88], is the simplest method of evaluating the frequency domain characteristics of acoustic wave devices. Although relatively straightforward to implement, it provides relative insertion loss values, which can only be used as a reference during the design phase [1]. The model is unable to provide details about IDT admittance, circuit loading, bulk wave interference and diffraction. Electrode influences, such as mass loading and perturbation of the acoustic wave as it travels under a metalised region are also ignored. Even though an IDT is a bidirectional device, only the acoustic wave propagating towards the receiving electrodes is considered, thereby neglecting triple-transit effects.

The technique is typically used to determine approximate frequency domain char-

acteristics of Rayleigh mode devices where the input and output IDTs are identical. In the initial discussions by Tancrell et al. [88], it has been shown that if an alternative form of the electrode weighting factor is used, which relates to the overlap of the finger pairs, then apodised IDTs can be analysed. Campbell [1] provides a explanation of the technique using uniform IDTs and makes further simplifying assumptions which again reduces the complexity of the problem.

In this technique, the electric field distribution is approximated as a series of delta functions at the electrode edges. The electric field is assumed to be uniform across the entire electrode. For the transmitting IDT, it is assumed that at any point in time neighbouring electrodes have equal, but opposite voltages. The summation of the delta functions corresponding to the applied voltage can be used to determine the frequency response of the structure. In a two transducer device, the transfer function is given by:

$$|H(f)| = |H_T(f)| \cdot |H_R(f)|, \tag{2.19}$$

where $|H_T(f)|$ and $|H_R(f)|$ represent the individual transfer functions of transmitter and receiver IDTs respectively.

To calculate the individual transfer functions, the contribution by each electrode must be considered. Typically, the centre of an IDT is used as a reference plane, which further simplifies the problem. Using this system, the IDT transfer function can be described in terms of the spatial coordinates of the electrode fingers as [1]:

$$H_T(f) = \sum_{n=-(N-1)/2}^{(N-1)/2} (-1)^n A_n e^{-jk_x x_n}, \tag{2.20}$$

where $N$ is the electrode number, $x_n$ is the electrode location and $A_n$ is a factor that relates to the overlap of the IDT fingers. For uniform IDTs, $A_n$ is equal to $1$.

When a large number of electrode exist, equation 2.19 can be further simplified. Close to the centre frequency of the device, the transfer function can be approximated as a sinc function by:

$$|H(f)| \propto \left| \frac{\sin\left[N_p \pi (f - f_0)/f_o\right]}{N_p \pi (f - f_0)/f_0} \right|, \tag{2.21}$$

where $N_p$ is the number of electrode pairs, $f_0$ and $f$ represent the centre frequency and analysis frequency for the structure. The centre frequency is obtained by assuming that the electrodes are $\lambda/4$ wide and evenly spaced. The analysis for the receiver is

the same as the transmitter with the exception of a phase shift caused by the centre to centre spacing of the two structures.

The delta-function model is suited to acoustic wave devices where only one main mode is of interest. In a FPW structure, as has already been discussed, an infinite number of modes can exist, thereby making this approach invalid. Using this technique the contributions due to the individual acoustic modes can not be appropriately weighted, thus the calculated frequency response would be incorrect. Furthermore, this technique does not take into account the dispersive nature of plate modes, which makes it unsuitable for the analysis of FPW structures.

### 2.3.5 Coupling of Modes

The Coupling of Modes (COM) approach was developed by Pierce in 1954. In his original paper [89], the technique was applied to evaluation of coupling between two lossless modes of propagation in a linear system. It was extended by Suzuki [90] and Haus [91] to describe wave propagation in periodic SAW structures in 1976. For the Rayleigh mode of operation, analogies can be taken from the case of laser wave propagation in optics. Recently, the COM model has been further developed to include shear horizontal and leaky surface acoustic waves on commonly used $LiTaO_3$ and $LiNbO_3$ substrates [92].

The COM approach is designed to be used in systems were reflections are dominant, therefore the approach is well suited to the analysis of acoustic wave resonators. Unlike the delta-function model, the COM technique considers wave propagation in both directions from an IDT. As the model is based on periodic structures, electrode end effects are ignored which can degrade the results for devices with a small number of electrodes and delay line structures. In the formulation of the COM model, the propagating eigenmodes are described as an infinite number of Floquet harmonics. As it is not possible to solve the wave propagation problem by considering an infinite number of solutions, either the weakly interacting higher order harmonics are ignored, or a differential approach can be used with a truncated set of equations [92]. Using the

differential approach, the COM equations can be represented by a $3 \times 3$ matrix as [1]:

$$\frac{d}{dx}\begin{bmatrix} R \\ S \\ I \end{bmatrix} = \begin{bmatrix} -j\delta & jk_{12} & j\zeta \\ -jk_{12}^{*} & j\delta & -j\zeta^{*} \\ -j2\zeta^{*} & j2\zeta & j\omega C_s \end{bmatrix}\begin{bmatrix} R \\ S \\ V \end{bmatrix}, \tag{2.22}$$

where $R$ and $S$ are slowly varying acoustic wave amplitudes, $I$ and $V$ represent the electrode current and voltage respectively, $k_{12}$ is a reflectivity coupling factor, which close to the centre frequency can be assumed to be constant, $C_s$ is the capacitance per unit length, $\zeta$ is the transduction coefficient and $\delta$ represents a detuning factor which accounts for changes in parameters off the centre frequency. Note that all fields in equation 2.22 are normalised to the total power flow of the structure.

From equation 2.22 it can be seen that the COM approach models the acoustic wave device as two acoustic ports and one electrical port. For a uniform IDT, the COM parameters, which relate to the substrate type, orientation, metallisation ratio and period, remain constant. Once the COM parameters have been extracted from the model, they are converted to a P-matrix description [21]. This allows different sections, such as reflectors and IDTs, to be cascaded to calculate the complete frequency response.

Although well suited to applications where a fast, efficient calculation is required, the COM model is limited in several areas. Primarily the accuracy of the COM model depends on the material properties. Determination of many COM parameters depends on experimental analysis, which by its own nature, incorporates uncertainty, thereby a design can not be optimised until some form of experimental data is collated. Other parameters can be obtained from alternative numerical techniques such as Boundary Element and Finite Element Methods, which also make numerous assumptions about the solution to the wave propagation problem.

As previously mentioned, the COM model assumes that IDTs are infinitely periodic. Physical IDTs are of finite length and due to manufacturing defects may not be periodic in some regions, thereby causing potential errors in the subsequent analysis. The spectral domain Green's function applied by the author in Section 4.4.1 can account for these effects and is thus preferred for the analysis of FPW structures. Furthermore, as the COM approach is only valid over a narrow frequency range, the technique is potentially unsuitable for sensing applications, where changes in frequency

response can occur at some distance from the primary modes.

### 2.3.6 Spectral Domain Green's Function

Whilst it has been illustrated that the stiffness matrix method can be related to a generalised Green's function to evaluate the phase velocity of multilayered piezoelectric structures, a second Green's function can be applied to determine the spectral characteristics. The spectral domain Green's function considers the response spectra due excitation by a series of IDTs. Unlike the COM approach, this technique can be applied to both periodic and aperiodic structures [92] and fully includes electrode end-effects. The spectral domain Green's function is used to convert the system differential equations into more manageable coupled integral equations which are typically easier to solve [16].

The spectral domain Green's function analysis is a Boundary Element method (BEM) as it only considers the variables on the external interfaces of the structure [19]. Similar to the Finite Element method (FEM) to be discussed shortly, the problem is discretised into smaller, more manageable sections. For the analysis of IDTs, each finger is split into a series of strips, allowing the applied voltage to be approximated as a Dirac, or point source, and its influence on the remaining fingers calculated. In calculating the spectral response of a FPW device, two different Green's functions must be considered. The first relates to the electrostatic charge, which is a first-order approximation of the piezoelectric case [2]. In this approximation, it is assumed that the structure is non-piezoelectric and the electrical and magnetic fields do not interact [93]. For piezoelectric structures bounded by a metallic plane, Baghai-Wadji [19] et al. derived a closed-form formulae for the electrostatic component of the spectral domain Green's function. This means that the often difficult task of integrating singularities is avoided. For simplicity, it is also assumed that all field variables, including charge, are constant in the $y$-direction. It will be shown in Chapter 5, that this is not precisely the case, however this approximation is suitable for this analysis.

The second component of the spectral domain Green's function considers the effect of the propagating surface wave. Unlike the SAW case, the frequency response of a FPW device must consider the influence of both the $A_0$ and $S_0$ modes. The problem

can be further extended to encompass higher order modes, however for sensing applications this is typically unnecessary. Milsom et al. [94] illustrate that the spectral domain Green's function is related to the effective permittivity, which is then used to determine the charge on the electrodes for a given applied voltage via the application of:

$$\Phi\left(x\right) = \int_{-\infty}^{+\infty} G\left(x - x^{'}\right) \sigma\left(x^{'}\right)\, dx^{'}, \tag{2.23}$$

where $G$ is a spectral domain Green's function which depends on the specific problem geometry, $x$ is the spatial location of the electrode strip under consideration, $\sigma$ is the charge per unit length and $\Phi$ is the applied voltage. Equation 2.23 can be identified as a convolution integral, and as such a simple Fourier transform can be applied to simplify the calculation process as:

$$\Phi\left(x\right) = \frac{1}{2\pi} \int_{-\infty}^{+\infty} \overline{G}\left(k_x\right) \overline{\rho}\left(k_x\right)\, dk_x, \tag{2.24}$$

where the bar represents the Fourier transform of a particular term. For $k_x \rightarrow 0$, the integral in equation 2.24 is regular therefore the issue of combining a numerical integration with analytical solutions is avoided. If appropriate weighting functions are selected, the integral in equation 2.23 can be rewritten as a sum, thereby simplifying the calculation process:

$$\varphi_k = \sum_{l=1}^{N} q_l A_{kl} \;\; k = 1, 2, ..N, \tag{2.25}$$

where the term $A_{kl}$ contains both electrostatic and surface wave coefficients, $N$ is the number of individual electrode strips, $q_l$ represents the charge per unit area and $\varphi_k$ is the applied strip voltage. The same approach can be used to determine the influence of guard and floating electrodes.

Whilst many analogies can be drawn from the analysis of SAW devices as done by Milson et al. [94], there are some significant differences which must be taken into account when considering FPW structures. In particular, the definition of the piezoelectric coupling factor for SAW structures can not be applied to FPW structures. The influence of these parameters, and the authors approach to this issue will be discussed in Section 4.4.

Via the spectral Green's function, the transducer capacitance and admittance can be calculated. This data is then converted to the more commonly used scattering matrix

parameters, where absolute insertion loss parameters can be obtained.

### 2.3.7 Finite Element Method

Historically, the FEM was used for the mechanical analysis of structures such as beams, trusses and frames. In the early stages of development, the FEM, or its early inception, was used throughout the aerospace industry. It was not until 1960, four years after the first credited paper [95] was published that the term 'finite element' was used.

Finite Element modelling became significantly more popular with the advent of fast computers. Since its development in 1956, the speed and storage capabilities of computers has increased significantly which has lead to the use of the FEM in a wide variety of industries ranging from Process Control to Medical Instrumentation [96]. Although initially designed for structural analysis, the FEM has lent itself to many different fields such as electromagnetism, fluidics and thermodynamics. Many analogies can be drawn between different scientific fields such as heat transfer, one dimensional fluid flow and axial loading. The general applicability of the FEM makes it a valuable tool in many different facets of science.

Whilst the FEM has been applied to determine the surface displacements of FPW structures when operating as micropumps, to the best of the author's knowledge, it has not been applied to evaluate the frequency domain characteristics of these devices when excited via planar IDTs. Recent work by Ippolito [17] used the power spectral density function to evaluate the frequency response of SAW devices, where good agreement was obtained. The implementation of this approach is discussed in Chapter 5, however it has been found that this technique does not provide accurate results for FPW structures. It is believed that the technique suggested by Ippolito should be modified to consider the electrode charge density rather than the open-circuit output voltage as is done with other accepted techniques.

In early FEM models of FPW structures reported by Friedrich et al. [97], simulations were conducted to determine the eigenfrequencies of a single layer piezoelectric plate. Once the eigenfrequencies of the structure were determined, they were applied in a continuous manner to determine the mechanical displacement. The transducers were modelled as individual input and output gates across the thickness of the plate.

Acoustic absorbers were also incorporated into this model, which minimised standing waves generated by the acoustic wave being reflected at the model boundaries. Although a viable method of investigating the mechanical behaviour of FPW structures, this technique provides an ideal representation of the frequency spectra, rather than the approximated impulse response applied by the author.

The FEM has also been employed in conjunction with analytical techniques to describe the scattering behaviour of the primary symmetric Lamb mode around a wedge shaped crack for NDE applications [98]. The same technique can be applied for Rayleigh mode scattering by increasing the thickness of the plate structure. A combined FEM / BEM approach was also used by Finger et al. [99] to determine the frequency response of SAW filters. The FEM was used to model the electrode interactions and the BEM, which comprised of a generalised Green's function, was used to describe the substrate. The benefit of this approach was that a small number of finite elements were used, as the bulk of the structure was described the BEM, which by nature only requires the external surface to be considered.

The FEM presents many advantages over the previously discussed techniques within this chapter. Whereas other methods can be segregated into two categories that focus on either determining the basic properties of an acoustic wave structure, such as phase velocity, or frequency characteristics, the FEM based technique demonstrated by the author solves both problems simultaneously. Moreover, the FEM can operate with both two and three-dimensional models, which incorporate many second order effects [100], such as diffraction, electrode reflections and triple-transit, which can not be simultaneously solved with any of the aforementioned techniques. The FEM is independent of geometry and as will be shown in Chapter 6, can even be applied to calculate the frequency characteristics of FPW structures when subjected to liquid media.

### 2.3.8 Summary of Modelling Techniques

From the presented discussion of commonly employed modelling techniques applied to acoustic wave devices, it is obvious that a unified approach does not exist to evaluate both the basic properties, such as phase velocity, and the more advanced frequency domain characteristics of multilayered FPW structures. Throughout the course of this

thesis, the author aims to rectify this shortfall by combining the FEM with techniques and related procedures routinely applied to SAW structures to obtain key electrical and mechanical properties of FPW devices. To the best of the author's knowledge, this approach has not yet been reported in the literature. The underlying principals and assumptions used to determine properties of SAW devices will be examined in detail and modified to suit FPW structures. To aid in the development of a unified approach to the analysis of FPW structures, Table 2.1 lists the information that can be obtained from each of the previously discussed techniques. A 'Y' indicates that the listed property can be obtained directly from the applied method, whereas a 'N' indicates that the item is not supported. Furthermore, a '-' indicates that the technique is not applicable to obtain a particular property and an 'I' indicates that the term can be calculated indirectly via the results obtained from the technique.

Table 2.1: Summary of Modelling Techniques

| | Modelling Technique | | | | | | |
|---|---|---|---|---|---|---|---|
| Property | Potential Method | Transmission Matrix | Stiffness Matrix | Delta Function | COM | Spectral Green's | FEM |
| Anisotropic Layers | N | Y | Y | N | N | Y | Y |
| Multilayered Structures | N | Y | Y | N | N | Y | Y |
| Finite Thickness | Y | Y | Y | Y | Y | Y | Y |
| Infinite Substrate | Y | Y | Y | Y | Y | Y | Y |
| Geometry Independent | N | N | N | N | N | N | Y |
| Buried IDTs | - | - | - | N | N | Y | Y |
| Viscous Liquid | - | N | Y | N | Y | N | Y |
| Phase Velocity | Y | Y | Y | - | - | - | I |
| Electromechanical Coupling | - | Y | Y | - | - | - | I |
| Delay Line Structures | - | - | - | Y | N | Y | Y |
| Charge Density | - | - | - | N | Y | Y | Y |
| Second-Order Effects | - | - | - | N | N | Y | Y |

From Table 2.1 it can be seen that the FEM provides the most comprehensive information pertaining to wave propagation in piezoelectric multilayered media. Although the FEM was primarily designed for the analysis of mechanical structures, it is evident

that it can be applied to FPW structures. In areas where the FEM can not directly calculate the required properties, the author intends to further post-process the mechanical and basic electrical data drawing analogies from other techniques.

To further verify the results of the FEM, the author intends to use a combination of the spectral domain Green's function and the stiffness matrix methods. Although not directly used to verify the FEM results, the transmission matrix method discussed in the next chapter will serve as a simple method to describe the basic properties of a FPW structure.

## 2.4 Conclusion

This chapter has provided a critical review of current literature in the field of acoustic wave devices for sensing applications. A brief introduction into the operation of four commonly used acoustic wave devices has been given, and where possible, mass sensitivities quoted. It is quite apparent from this analysis that FPW structures offer the unique ability to be used in both gas and liquid media, whilst maintaining high mass sensitivity and relatively low operating frequencies, thereby reducing the need for expensive and elaborate signal processing electronics.

A discussion has also been given on conventional modelling techniques for the analysis of acoustic wave structures. From this review, it has been shown that each modelling technique has its own unique abilities, whilst also highlighting potential areas that need to be refined to create a more complete understanding of acoustic wave propagation in multilayered piezoelectric media. It is also clearly evident from this review that there exists a need for a unified approach to modelling acoustic wave devices that can be applied to both two and three dimensional models with relatively little difference in implementation.

The author's novel approach to this problem with be discussed in Chapter 5, utilising the FEM. The basic operating parameters of a FPW structure is given in Chapter 3 based on the transmission matrix method. The inherent instability in this method will be examined, thus further illustrating the benefit of utilising the author's novel approach. A reformulation of the transmission matrix method, known as the stiffness matrix method is given in Chapter 4 which forms the basis to verify the results ob-

tained from the author's approach based on the FEM. Device characteristics, such as particle displacement profiles and mass sensitivity are obtained via the stiffness matrix method. A discussion will also be held on the frequency domain characteristics of FPW structures, where it is shown that in a gas phase a spectral domain Green's function can be applied.

The application of FPW devices in liquid media is presented in Chapter 6, where it will be shown that the author's novel approach is more correct than other accepted techniques in determining the frequency domain characteristics of liquid loaded structures when compared to experimental results presented in literature.

# Chapter 3

# Transmission Matrix Analysis of FPW Devices

## 3.1 Introduction

The first numerical modelling technique discussed is commonly known as the Transmission Matrix method. It is a well established technique originally devised for the analysis of tectonic plates within the Earth's crust in the early 1950's. Since then it has been extended to evaluate the propagation of acoustic waves in multilayered media. The transmission matrix method is quite universal, as it can be applied for various types of acoustic wave devices, ranging from bulk devices such as QCMs to two dimensional propagation in FPW structures. The method can be further extended to three dimensional propagation, however it this is not strictly necessary for the analysis of FPW devices.

Although a relatively simplistic method to implement, it will be shown that inaccuracies exist which are addressed in Chapter 4. In particular, the transmission matrix becomes unstable when applied to structures with large frequency-thickness products as well as complex material parameters, which are characteristic of liquid loaded devices. The analysis presented in this chapter serves as an introduction into the basic electrical and mechanical behaviour of FPW devices in the gas phase. The theory presented within will be further extended to allow a comparison between conventional modelling techniques and the author's novel approach based on the FEM in Chapters

4 and 5 respectively.

Section 3.2 provides a brief introduction to the mathematical development of the transmission matrix method. It will be shown that the piezoelectric wave propagation problem can be solved by considering eight essential field variables which depend only on the spatial $z$-location within the FPW structure. Quantities such as stress, strain and the piezoelectric constitutive equations are reviewed and form the basis of the solution. Section 3.3 discusses the use of the transmission matrix for multilayered media. It will be shown that interfacial boundary conditions are automatically satisfied by the chain multiplication of the individual layer matrices. The solution to the piezoelectric wave propagation problem is then determined by considering the boundary conditions on the two remaining free surfaces. For a FPW structure, four possible combinations of electrical boundary conditions exist and their effect on the phase velocity of the propagating modes is presented. Via this analysis, the electromechanical coupling coefficient, $K^2$, is evaluated.

Finally, Section 3.4.1 explores the numerical instability associated with the transmission matrix method. The two main causes, large frequency-thickness products and lossy material properties are discussed. A preliminary discussion is presented on possible solutions for the inherent numerical instability.

## 3.2 Transmission Matrix Method Development

The transmission matrix method dates back to the early 1950's where it was developed for the analysis of stratified media in the Earth's crust [80]. The method has since been extended to include piezoelectric materials, which by nature are anisotropic [20]. Further modifications have allowed the technique to be used with multilayered structures and a freely available computer program based on these methods has been written to solve the piezoelectric wave propagation problem [101]. However, several drawbacks exist in the method, which are detailed in Section 3.4.1. A brief discussion of the method is presented to prepare the reader for the more advanced stiffness matrix method, spectral domain Green's function and FEM analysis in Chapters 4 and 5 respectively.

The basis of the transmission matrix method is a mapping of essential field vari-

ables across two surfaces. The essential field variables are quantities that can be used to calculate all other fields within a structure. Irrespective of the number of layers within a structure, the field variables are described by their relationship between the upper and lower surfaces. For a single isotropic layer, the transmission matrix can be found analytically. The concept can be further extended to composite structures, where a transmission matrix is constructed for each individual layer and then cascaded to form a single global matrix. A solution is then obtained by considering the free surface boundary conditions.

In its most general form, the transmission matrix method describes the $z$-plane dependence of the essential field variables. For a piezoelectric SAW or FPW structure eight essential variables are necessary. In an isotropic material, the problem can be further reduced to six. In this study, the essential field variables describe the dependence of mechanical and electrical displacement, normal stresses and electric potential with respect to the $z$-coordinate. The first derivative of mechanical displacement, velocity, can also be used. For simplicity, it is convenient to also take the time derivative of the electric potential, which is the approached presented here. Throughout the following analysis it is assumed that all fields vary as $e^{j\omega t}$, thus this term is omitted.

Figure 3.1 illustrates the coordinate system used throughout this thesis unless explicitly stated otherwise. The FPW device membrane is assumed to extend to infinity in the $x$ and $y$ directions, with the acoustic wave propagating along $x$. The thickness of the plate structure is given by $h$, with the upper surface located at $z = h$ and the lower at $z = 0$.

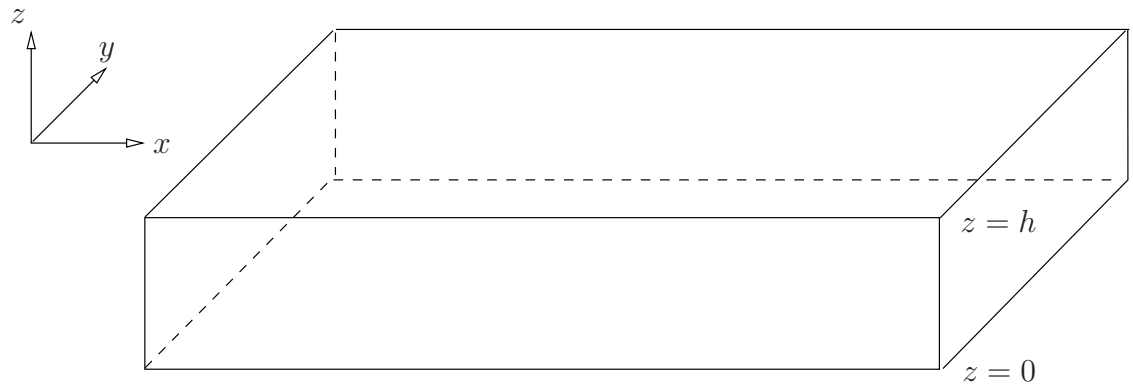


Figure 3.1: Adopted Coordinate System

### 3.2.1 Review of Stress / Strain Relationship

Before the implementation of the transmission matrix method can be discussed, a basic review of the stress and strain relationship is presented. In conjunction with the quasistatic piezoelectric constitutive equations, the solution to the wave equation can be explored.

In the context of this study, strain, a measurement of deformation for a point, is given by equation 3.1 [74].

$$S_{ij} = \frac{1}{2}\left(\frac{\partial u_i}{\partial x_j} + \frac{\partial u_j}{\partial x_i} + \frac{\partial u_k}{\partial x_i}.\frac{\partial u_k}{\partial x_j}\right) \quad i,j,k = 1,2,3, \tag{3.1}$$

where $u_i$ represents the particle displacement in direction $x_i$.

For acoustic wave devices, where displacements are quite small $(\partial u_i/\partial x_j \leqslant 1)$, the quadratic term can be ignored resulting in the linearised strain relationship, equation 3.2.

$$S_{ij} = \frac{1}{2}\left(\frac{\partial u_i}{\partial x_j} + \frac{\partial u_j}{\partial x_i}\right) \tag{3.2}$$

The strain tensor is a $3 \times 3$ matrix, however exhibits properties of symmetry and is can be reduced to a $6$ element vector. The diagonal terms, $(i = j)$, represent in-plane strain whilst the other values $(i \neq j)$ are shear components. An abbreviated subscript notation can be adopted, allowing the elements of the strain matrix to be written as in equation 3.3. A factor of $1/2$ is introduced to allow a simple relationship to be established between strain and particle displacement [102].

$$\mathbf{S_{ij}} = \begin{bmatrix} S_{xx} & S_{xy} & S_{xz} \\ S_{xy} & S_{yy} & S_{yz} \\ S_{xz} & S_{yz} & S_{zz} \end{bmatrix} = \begin{bmatrix} S_1 & \frac{1}{2}S_6 & \frac{1}{2}S_5 \\ \frac{1}{2}S_6 & S_2 & \frac{1}{2}S_4 \\ \frac{1}{2}S_5 & \frac{1}{2}S_4 & S_3 \end{bmatrix} \tag{3.3}$$

Strain can also be identified as the symmetric part of the displacement gradient [102], equation 3.4a. The symmetrical gradient operator, $\nabla_s$ is converted to a more conve-

nient notation, as in equation 3.4b.

$$\begin{bmatrix} S_1 \\ S_2 \\ S_3 \\ S_4 \\ S_5 \\ S_6 \end{bmatrix} = \begin{bmatrix} \frac{\partial}{\partial x} & 0 & 0 \\ 0 & \frac{\partial}{\partial y} & 0 \\ 0 & 0 & \frac{\partial}{\partial z} \\ 0 & \frac{\partial}{\partial z} & \frac{\partial}{\partial y} \\ \frac{\partial}{\partial z} & 0 & \frac{\partial}{\partial x} \\ \frac{\partial}{\partial y} & \frac{\partial}{\partial x} & 0 \end{bmatrix} \begin{bmatrix} u_x \\ u_y \\ u_z \end{bmatrix} \tag{3.4a}$$

$$\mathbf{S} = \nabla_s \mathbf{u} \tag{3.4b}$$

Similarly to the strain tensor, stress can be described as a second rank tensor which represents the applied force per unit area on an infinitesimally small volume [74]. It also exhibits properties of symmetry and thus the complete tensor is described by a $3 \times 3$ matrix, equation 3.5. Using the convention in equation 3.5, the term $T_{ij}$ is the stress component in the $i$-th direction, acting on a surface normal to the $j$-th direction.

$$T_{ij} = \begin{bmatrix} T_{xx} & T_{xy} & T_{xz} \\ T_{xy} & T_{yy} & T_{yz} \\ T_{xz} & T_{yz} & T_{zz} \end{bmatrix} = \begin{bmatrix} T_1 & T_6 & T_5 \\ T_6 & T_2 & T_4 \\ T_5 & T_4 & T_3 \end{bmatrix} \tag{3.5}$$

To further condense the development of the transmission matrix method, the strain and stress matrices are represented by transposed column vectors, equations 3.6 and 3.7 respectively. The superscript $T$ indicates the transpose operator.

$$\mathbf{S} = \begin{bmatrix} S_1 & S_2 & S_3 & S_4 & S_5 & S_6 \end{bmatrix}^T \tag{3.6}$$

$$\mathbf{T} = \begin{bmatrix} T_1 & T_2 & T_3 & T_4 & T_5 & T_6 \end{bmatrix}^T \tag{3.7}$$

From Hooke's law, stress and strain are linearly related by the material stiffness tensor $c_{ijkl}$, equation 3.8 [1]. Using the Einstein notation convention summation is implied over the repeated subscripts $k$ and $l$. Up to $81$ constants are required to fully describe the relationship between stress and strain, however a high degree of symmetry is present such that $c_{ijkl} = c_{jikl} = c_{ijlk} = c_{jilk} = c_{klij}$ reducing the number of independent constants to $21$. Depending on the crystallinity of the material, the number of constants can be further reduced. For the piezoelectric material used in the attempted realisation

of a FPW device, Chapter 6.5, five independent constants are sufficient whereas an isotropic material only requires two.

$$T_{ij} = c_{ijkl} S_{kl}, \quad i, j, k, l = 1, 2, 3 \tag{3.8}$$

In developing the transmission matrix method a set of essential field variables must be selected. The decision as to which field variables to select primarily depends on the assumed solution and the coordinate system adopted. It is also assumed that the width of the FPW structure is large when compared to the acoustic wavelength, allowing effects such as diffraction to be ignored. From potential mode theory [61], the field variables are assumed to be either constant or zero in the $y$-direction, which allows the following simplification to be made:

$$\frac{\partial}{\partial y} = 0 \tag{3.9}$$

Neglecting variation in the $y$ direction, the assumed solution for a wave propagating along $x$ with variation in $z$, is given by:

$$f(x, z, t) = f(z) e^{j\omega(t - \frac{x}{v_p})}, \tag{3.10}$$

where $v_p$ is the phase velocity of the propagating mode.
The time and spatial derivatives of the assumed can therefore be written as equations 3.11a and 3.11b respectively.

$$\frac{\partial f}{\partial t} = j\omega f \tag{3.11a}$$

$$\frac{\partial f}{\partial x} = \frac{-j\omega f}{v_p} \tag{3.11b}$$

In three dimensions, and with no applied force, the vector form of Newton's equation of motion is written as equation 3.12a [102]. Considering only the $x$ and $z$ dependance, the condensed vector form is given by equation 3.12b

$$\nabla_s \cdot \mathbf{T} = \rho \frac{\partial^2 \mathbf{u}}{\partial^2 t} \tag{3.12a}$$

$$\frac{\partial \mathbf{T^x}}{\partial x} + \frac{\partial \mathbf{T^z}}{\partial z} = j\omega\rho\mathbf{v} \tag{3.12b}$$

where the substitutions,

$$\mathbf{T^x} = \begin{bmatrix} T_1 & T_6 & T_5 \end{bmatrix}^T \tag{3.13a}$$

$$\mathbf{T^z} = \begin{bmatrix} T_5 & T_4 & T_3 \end{bmatrix}^T \tag{3.13b}$$

$$\frac{\partial^2 \mathbf{u}}{\partial^2 t} = j\omega \mathbf{v}, \tag{3.13c}$$

have been made. Note that in equation 3.13c, the term $\mathbf{v}$ is the time derivative of the particle displacement vector $\mathbf{u}$, or simply the particle velocity vector.

### 3.2.2 Piezoelectric Constitutive Equations

The piezoelectric constitutive equations describe the electromechanical properties of a material. They provide a linear relationship between the mechanical stress and strain components and the electric displacement, $D$ and electric field, $E$, via equation 3.14 [103].

$$T_{ij} = c^E_{ijkl} S_{kl} - e_{ijk} E_k \tag{3.14a}$$

$$D_i = \varepsilon^S_{ij} E_j + e_{ijk} S_{jk} \tag{3.14b}$$

As illustrated previously, stress is related to the strain by the material stiffness tensor, $c_{ijkl}$. The dielectric tensor, $\varepsilon_{ij}$, is a $3 \times 3$ matrix that relates the applied electric field to the electric displacement vector. The material stiffness and dielectric tensors are evaluated at constant electric field and constant strain respectively. Finally, the piezoelectric coefficient matrix, $e_{ijk}$ is $3 \times 6$.

In a source free medium, the divergence of the electric displacement can be written as in equation 3.15 [102] :

$$\nabla \cdot \mathbf{D} = 0, \tag{3.15}$$

where $\nabla\cdot$ represents the divergence of the vector field.
In a piezoelectric material, the acoustic velocities are typically five orders of magnitude less than the speed of light. Under these conditions, the electric field component is described as the gradient of a scalar potential, $\varphi$, [20]:

$$E = -\nabla\varphi \tag{3.16}$$

Considering only the $x$ and $z$ dependence, the dielectric displacement vector is written as:

$$\nabla \cdot \mathbf{D} = \frac{\partial D_x}{\partial x} + \frac{\partial D_z}{\partial z} = 0 \tag{3.17}$$

Equations 3.12b and 3.17 are converted to matrix form, and the substitution of equation 3.11b yields:

$$\frac{-j\omega}{v_p} \begin{bmatrix} \mathbf{T^x} \\ D_x \end{bmatrix} + \frac{d}{dz} \begin{bmatrix} \mathbf{T^z} \\ D_z \end{bmatrix} = j\omega\rho \begin{bmatrix} \mathbf{v} \\ 0 \end{bmatrix} \tag{3.18}$$

The piezoelectric constitutive equations in their current form, equation 3.14, contain more terms than the required eight essential field variables. Substitution of equations 3.4b and 3.16 into 3.14, and introducing the velocity vector rather than displacement yields:

$$j\omega \begin{bmatrix} \mathbf{T^x} \\ D_x \end{bmatrix} = \Gamma^{11} \frac{\partial}{\partial x} \begin{bmatrix} \mathbf{v} \\ j\omega\varphi \end{bmatrix} + \Gamma^{13} \frac{\partial}{\partial z} \begin{bmatrix} \mathbf{v} \\ j\omega\varphi \end{bmatrix} \tag{3.19a}$$

$$j\omega \begin{bmatrix} \mathbf{T^z} \\ D_z \end{bmatrix} = \Gamma^{31} \frac{\partial}{\partial x} \begin{bmatrix} \mathbf{v} \\ j\omega\varphi \end{bmatrix} + \Gamma^{33} \frac{\partial}{\partial z} \begin{bmatrix} \mathbf{v} \\ j\omega\varphi \end{bmatrix} \tag{3.19b}$$

The $\Gamma^{ik}$ matrices contain components of the material stiffness, piezoelectric and permittivity tensors. For the coordinate system used here, the matrix $\Gamma^{ik}$ is described as [104]:

$$\Gamma^{\mathrm{ik}} = \begin{bmatrix} c_{1i1k} & c_{1i2k} & c_{1j3k} & c_{k1i} \\ c_{2i1k} & c_{2i2k} & c_{2i3k} & c_{k2i} \\ c_{3i1k} & c_{3i2k} & c_{3i3k} & c_{k3i} \\ e_{i1k} & e_{i2k} & e_{i3k} & -\varepsilon_{ik} \end{bmatrix} \tag{3.20}$$

For non-piezoelectric materials the piezoelectric constants $e$ are set to zero and the method still remains valid. For structures consisting of purely isotropic materials, the $\Gamma^{\mathrm{ik}}$ matrices can be further reduced, containing only the material stiffness constants and permittivity tensors.

For simplicity, the piezoelectric constitutive equations 3.19a and 3.19b have been separated into individual $x$ and $z$ components. Equation 3.19a contains only the $x$ normal components of $\mathbf{T}$ and $\mathbf{D}$, whilst 3.19b has only the $z$ components of the stress and electric field vectors. As the $x$ dependence has been assumed, equations 3.19a

and 3.19b can be converted from partial differential equations to ordinary differential equations via the substitution:

$$\frac{\partial}{\partial x} = \frac{-j\omega}{v_p} \tag{3.21}$$

Therefore, with the $x$-dependence removed, the time derivative of the piezoelectric constitutive equations becomes:

$$j\omega \begin{bmatrix} \mathbf{T^x} \\ D_x \end{bmatrix} = \frac{-j\omega}{v_p}\Gamma^{11} \begin{bmatrix} \mathbf{v} \\ j\omega\varphi \end{bmatrix} + \Gamma^{13}\frac{d}{dz} \begin{bmatrix} \mathbf{v} \\ j\omega\varphi \end{bmatrix} \tag{3.22a}$$

$$j\omega \begin{bmatrix} \mathbf{T^z} \\ D_z \end{bmatrix} = \frac{-j\omega}{v_p}\Gamma^{31} \begin{bmatrix} \mathbf{v} \\ j\omega\varphi \end{bmatrix} + \Gamma^{33}\frac{d}{dz} \begin{bmatrix} \mathbf{v} \\ j\omega\varphi \end{bmatrix} \tag{3.22b}$$

Equations 3.18, 3.22a and 3.22b are used to remove all other terms except the essential field variables. The result is an eigenvalue problem, equation 3.23, which describes the $z$-dependence of the eight partial modes supported by the structure.

$$\frac{d\boldsymbol{\tau}}{dz} = j\omega \mathrm{A}\boldsymbol{\tau}, \tag{3.23}$$

with

$$A = \begin{bmatrix} \Gamma^{13}\frac{Z}{v_p} & \mathrm{G} - \frac{(\Gamma^{11} - \Gamma^{13}Z\,\Gamma^{31})}{v_p^2} \\ Z & \Gamma^{31}\frac{Z}{v_p} \end{bmatrix} \tag{3.24a}$$

$$\boldsymbol{\tau} = \begin{bmatrix} T_{xz} & T_{yz} & T_{zz} & D_z & v_x & v_y & v_z & j\omega\varphi \end{bmatrix}^T \tag{3.24b}$$

$$= \begin{bmatrix} \mathbf{T^z} & D_z & \mathbf{v} & j\omega\varphi \end{bmatrix}, \tag{3.24c}$$

where $Z = (\Gamma^{33})^{-1}$. The matrix G is $4 \times 4$ given by:

$$G = \begin{bmatrix} \rho & 0 & 0 & 0 \\ 0 & \rho & 0 & 0 \\ 0 & 0 & \rho & 0 \\ 0 & 0 & 0 & 0 \end{bmatrix} \tag{3.25}$$

The $8 \times 8$ system propagator matrix, A, equation 3.24a, consists of components of the material stiffness, piezoelectric, permittivity matrices as well as density and phase velocity. When considering anisotropic layers the material properties must be rotated to the correct plane before calculating the propagator matrix. The vector $\boldsymbol{\tau}$, equation 3.24b, consists of the eight selected essential field variables: $z$ plane normal stress,

velocity, $z$ plane normal dielectric displacement and the time derivative of the scalar potential.

According to linear system theory [81], the solution to the first order differential eigenvalue problem, equation 3.23, is the well known matrix exponential:

$$\boldsymbol{\tau}(z+h) = e^{j\omega \mathrm{A} h}\boldsymbol{\tau}(\mathbf{z}) = \phi(h, \omega, v_p)\boldsymbol{\tau}(z) \tag{3.26}$$

If the solution is known at a plane perpendicular to the z-axis, then via the application of equation 3.26, the corresponding solution can be determined at a distance $h$ from the initial point. The transmission matrix, $\phi$, is seen to depend on spatial location, angular frequency and phase velocity. For the presented analysis, at least one of these variables is held constant whilst the remaining are varied. It will also be shown that various substitutions can be made, which reduce the transmission matrix dependence to two variables.

Several approaches can be used to calculate the solution of a matrix exponential. The numerical computing language used by the author contained an in-built function to solve the problem, however the following appeared to be more numerically stable [105]:

$$e^{j\omega \mathrm{A} h} = \mathbf{M} e^{j\omega \Lambda h} \mathbf{M^{-1}}, \tag{3.27}$$

where $\mathbf{M}$ and $\mathbf{M^{-1}}$ are the eigenvector and its respective inverse matrices of the system propagator matrix $\mathrm{A}$. The eigenvalue matrix of $\mathrm{A}$, which corresponds to the partial mode wavenumbers, is denoted $\Lambda$.

Consider the material constants and their approximate magnitudes listed in Table 3.1. In solving the matrix exponential problem, many of these quantities are added or multiplied together, thus the smaller terms can be lost due to rounding errors of the larger numbers. One potential solution is to scale the dielectric and mechanical displacement variables [105]. Substitution of the normalised field variables into the piezoelectric constitutive equations shows that the same process can be achieved by scaling the material constants [21]. For improved numerical accuracy, it is desirable to bring the variables in Table 3.1 close to unity. Therefore the stiffness and density parameters are divided by $10^{11}$ whilst the permittivity matrix is multiplied by the same value. The piezoelectric constants are unaltered, however phase velocity is divided by $\sqrt{10^{11}}$.

Table 3.1: Material Constants - SI Unit Comparison

| Parameter | Magnitude | SI Unit |
|---|---|---|
| $c$ | $10^{11}$ | $\mathrm{N/m^2}$ |
| $e$ | $1$ | $\mathrm{C/m^{-2}}$ |
| $\varepsilon$ | $10^{-11}$ | $\mathrm{F/m}$ |

The same technique can be used to determine the propagation characteristics of a SAW device, where the eigenvalue problem is split into two solutions depending on the direction of energy decay. A physically meaningful partial mode is determined by evaluating the Poynting vector, of which a decision is made as to which modes decay with depth. This technique will be further discussed when considering liquid loaded FPW devices, Chapter 6, where the additional liquid layer is approximated as being semi-infinite.

## 3.3 Transmission Matrix Analysis of Multilayered Structures

A distinct advantage of the transmission matrix method is its ability to cater for an arbitrary number of layers. The algorithm does not depend on the total number of layers, rather the individual transmission matrices and respective layer thicknesses. However, the algorithm suffers from numerical instability when working with large frequency-thickness products which will be discussed in Section 3.4.1.

Consider the multilayered structure consisting of $n$ layers in Figure 3.2. The overall transmission matrix for the layered structure is given by the chain multiplication of the individual layer, $m$, matrices from the upper layer, $n$, to the lower layer, $1$. It is imperative that the chain multiplication is in the correct order to ensure continuity of boundary conditions at the layer interfaces. In deriving the transmission matrix, it is assumed that all essential field variables, the components of $\boldsymbol{\tau}$, are continuous across both sides of the interface. In Figure 3.2, this is indicated by the terms $\boldsymbol{\tau}_+$ and $\boldsymbol{\tau}_-$.

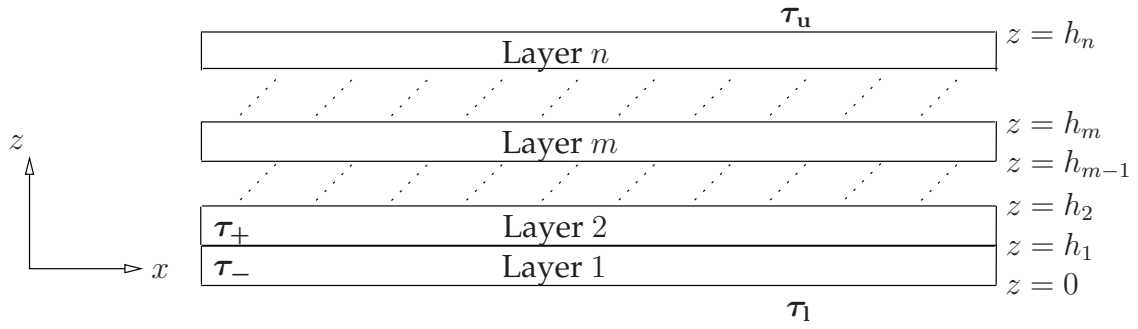


Figure 3.2: Multilayered Structure Coordinate System

The overall transmission matrix for a multilayered structure is given by:

$$\phi = \phi_{\mathrm{m}}(h_n)\phi_{\mathrm{m-1}}(h_{n-1})\phi_{\mathrm{m-2}}(h_{n-2}), ...., \phi_1(h_1), \tag{3.28}$$

with the thickness of the individual layers determined by:

$$h_n = h_m - h_{m-1} \tag{3.29}$$

From equation 3.28 an important relationship, equation 3.30, can be established that relates the essential field variables at the upper surface of the structure (subscript u), through an arbitrary number of layers to the corresponding fields at the lower surface (subscript $l$). The upper and lower free surfaces of the structure are commonly termed the terminal surfaces. For a multilayered structure, the terminal surface essential field variables are calculated by deriving the individual layer transmission matrices, $\phi_{\mathrm{m}}$, then multiplying the corresponding solutions in the appropriate order to obtain the global transmission matrix, $\phi$. This allows for relatively simple mode identification by considering the terminal surface essential field variables rather than generating the complete particle displacement profiles throughout the structure. A simple selection criteria can be used to identify whether a mode is antisymmetric or symmetric, which is covered in Section 4.3.1.

$$\boldsymbol{\tau}_{\mathbf{u}} = \phi\boldsymbol{\tau}_{\mathbf{l}} \tag{3.30}$$

From equation 3.30 the solution to the multilayered piezoelectric wave propagation problem can be determined by substituting the appropriate interfacial boundary conditions.

### 3.3.1 Boundary Conditions

For a FPW structure up to four different electrical boundary conditions exist. The upper, lower, both or neither surfaces can be metalised, which will alter the phase velocity of the propagating electro-acoustic modes. A metal ground plane can also be inserted within the structure which requires further modification of the boundary conditions between layers. One electrical and three mechanical boundary conditions are required at each interface to solve the piezoelectric wave propagation problem. Between the layers, as previously mentioned, the boundary conditions are automatically satisfied by the chain multiplication of the individual transmission matrices. The solution to the wave propagation problem can then be determined by considering the essential field variables at the terminal surfaces of the structure. In a mechanically free structure, the surface normal stresses, $\mathbf{T^z}$, tend to zero at the upper and lower surfaces. In formulating appropriate boundary conditions, it is assumed that the no slip condition is enforced between individual layers and the displacement is identical on both sides of an interface.

Two alternative boundary conditions exist for the electrical parameters $D_z$ and $j\omega\varphi$. If the surface is electrically short, then the scalar potential is zero, however an unknown charge exists on the surface. Conversely, under open circuit conditions the dielectric displacement must satisfy Laplace's equation [106] and the scalar potential remains unknown. The dielectric displacement must be continuous at the solid-air interface, therefore a simple substitution can be made which constrains the dielectric displacement according to [76]:

$$D_z^{'} = D_z - D_z(\text{free space}) = 0 \tag{3.31}$$

Table 3.2 lists the boundary conditions and constrained variables for all four possible electrical surface combinations. Applying the appropriate boundary conditions reduces the number of terms within the transmission matrix, which can also be reordered to minimise the computational effort to solve the problem. Consider the case where both sides of the FPW device are mechanically and electrically free. For a propagating wave under a open-open circuit boundary condition, the dielectric displacement and the normal mechanical stresses are set to zero, therefore leaving the scalar potential and particle velocity components unknown. The full solution procedure ap-

Table 3.2: FPW Device Mechanical and Electrical boundary conditions

| Upper Condition | Lower Condition | Constrained Mechanical | Constrained Electrical |
|---|---|---|---|
| Open | Open | $\mathbf{T_u^z} = 0$, $\mathbf{T_l^z} = 0$ | $D'_{zu} = 0$, $D'_{zl} = 0$ |
| Open | Short | $\mathbf{T_u^z} = 0$, $\mathbf{T_l^z} = 0$ | $D'_{zu} = 0$, $j\omega\varphi_l = 0$ |
| Short | Open | $\mathbf{T_u^z} = 0$, $\mathbf{T_l^z} = 0$ | $j\omega\varphi_u = 0$, $D'_{zl} = 0$ |
| Short | Short | $\mathbf{T_u^z} = 0$, $\mathbf{T_l^z} = 0$ | $j\omega\varphi_u = 0$, $j\omega\varphi_l = 0$ |

pears in Appendix A, however an abbreviated set of results is reiterated here. To meet the conditions implied by equation A.3 the coefficients of the first four equations must be zero. Mathematically, this can be described as:

$$\det \begin{vmatrix} \phi_{15} & \phi_{16} & \phi_{17} & \phi_{18} \\ \phi_{25} & \phi_{26} & \phi_{27} & \phi_{28} \\ \phi_{35} & \phi_{36} & \phi_{37} & \phi_{38} \\ \phi_{45} & \phi_{46} & \phi_{47} & \phi_{48} \end{vmatrix} = 0, \tag{3.32}$$

Similarly, the boundary conditions for the other three cases, open-short, short-open and short-short, are given by:

$$\det \begin{vmatrix} \phi_{15} & \phi_{16} & \phi_{17} & \phi_{14} \\ \phi_{25} & \phi_{26} & \phi_{27} & \phi_{24} \\ \phi_{35} & \phi_{36} & \phi_{37} & \phi_{34} \\ \phi_{45} & \phi_{46} & \phi_{47} & \phi_{44} \end{vmatrix} = 0, \det \begin{vmatrix} \phi_{15} & \phi_{16} & \phi_{17} & \phi_{18} \\ \phi_{25} & \phi_{26} & \phi_{27} & \phi_{28} \\ \phi_{35} & \phi_{36} & \phi_{37} & \phi_{38} \\ \phi_{85} & \phi_{86} & \phi_{87} & \phi_{88} \end{vmatrix} = 0, \det \begin{vmatrix} \phi_{15} & \phi_{16} & \phi_{17} & \phi_{14} \\ \phi_{25} & \phi_{26} & \phi_{27} & \phi_{24} \\ \phi_{35} & \phi_{36} & \phi_{37} & \phi_{34} \\ \phi_{85} & \phi_{86} & \phi_{87} & \phi_{84} \end{vmatrix} = 0 \tag{3.33}$$

The determinants in equations 3.32 and 3.33 are commonly referred to as $\mathbf{\Phi_{ur}}$ as they are mainly composed of elements from the upper right quadrant of the transmission matrix. The task of finding the determinant of equations 3.32 and 3.33 is well suited to a numerical search procedure. Due to numerical considerations the magnitude of the determinant may not go exactly to zero, and as such an iterative search procedure is required to identify a local minimum. Analysis of equation 3.26 indicates that the solution is dependant on frequency as well as phase velocity. A simple substitution can also be made to solve the wave propagation problem in terms of wavelength, rather

than frequency or phase velocity.

### 3.3.2 Phase Velocity

Figure 3.3 presents a determinant scan for a FPW device with an open-open circuit boundary condition. The structure is similar to that reported in literature [8, 14] however the underlying membrane material has been replaced with Si. The structure consists of a $2.0$µm silicon, $0.4$µm aluminium and $0.6$µm zinc oxide layers. The wavelength was fixed at $100$µm and the phase velocity scanned from $100$ to $7,000$m/s. Analysis of Figure 3.3 indicates that three modes are present in the prescribed velocity range.

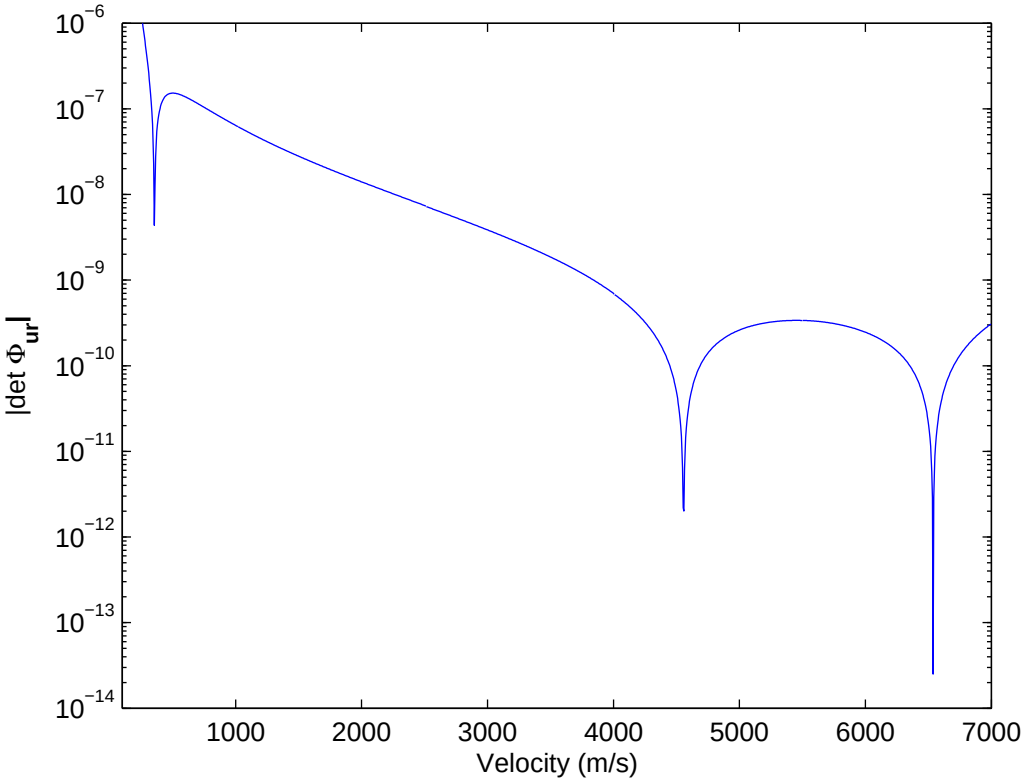


Figure 3.3: Determinant Scan - Open Circuit Boundary Conditions

The scan in Figure 3.3 is quite coarse thus making it quite difficult to determine the exact points where the determinant approaches zero. To obtain a better indication of operating points, the approximate phase velocity is calculated and an iterative 'golden section' search is performed about that point [107]. The search algorithm resolves modes at $356$, $4558$ and $6540$m/s, corresponding to resonant frequencies of $3.56$, $45.58$

and $65.40$MHz respectively.

Although three modes have been calculated, the second mode at $4558$m/s is a shear mode which cannot be excited piezoelectrically [78]. The transmission matrix method can be easily modified to remove the terms relating to field variables in the $y$-direction, neglecting such modes from future determinant scans. When this process is undertaken, the method resolves only pure Lamb modes.

Figure 3.4 illustrates the dispersion characteristics of the first five piezoelectric modes generated in the aforementioned FPW structure as a function of normalised Si thickness. Of potential interest for sensing applications are the first two low velocity modes, denoted $A_0$ and $S_0$. Modes are named according to the particle displacement about the mid-plane of the structure. In an isotropic plate, the first antisymmetric, or $A_0$, mode has an antisymmetric displacement about the centre of the structure, where the symmetric mode, $S_0$, is clearly symmetrical about the median. This will be further examined in Section 4.3.1, however Figure 3.5 provides a simple model of the particle displacements, with the arrows indicating the direction of the primary displacements for the first $A_0$ and $S_0$ modes.

Interestingly, the $A_0$ and $S_0$ modes are present regardless of the plate thickness. These fundamental modes are identified from the dispersion relationship by their finite phase velocities as the plate thickness decreases. The higher order modes become asymptotic and as such exhibit a cutoff characteristic [74]. For the higher order modes their nature, whether symmetric or antisymmetric, can be obtained from the displacement profile, or via a comparison with other theoretical models. In an isotropic material, the family of modes, whether symmetric or antisymmetric, do not cross each other, however the two mode types may.

The first antisymmetric mode is clearly identified by its reducing velocity as the plate thicknesses approaches zero. It can also be seen from Figure 3.4 that all modes appear to be approaching a finite phase velocity as the plate thickness increases, indicated by the dotted line. Recall for a SAW device, the Rayleigh mode acoustic displacement is confined to within one to two wavelengths from the upper surface. As the thicknesses of the plate increases beyond the acoustic wavelength, the structure becomes sufficiently large that it can be thought of as an very thick plate with two

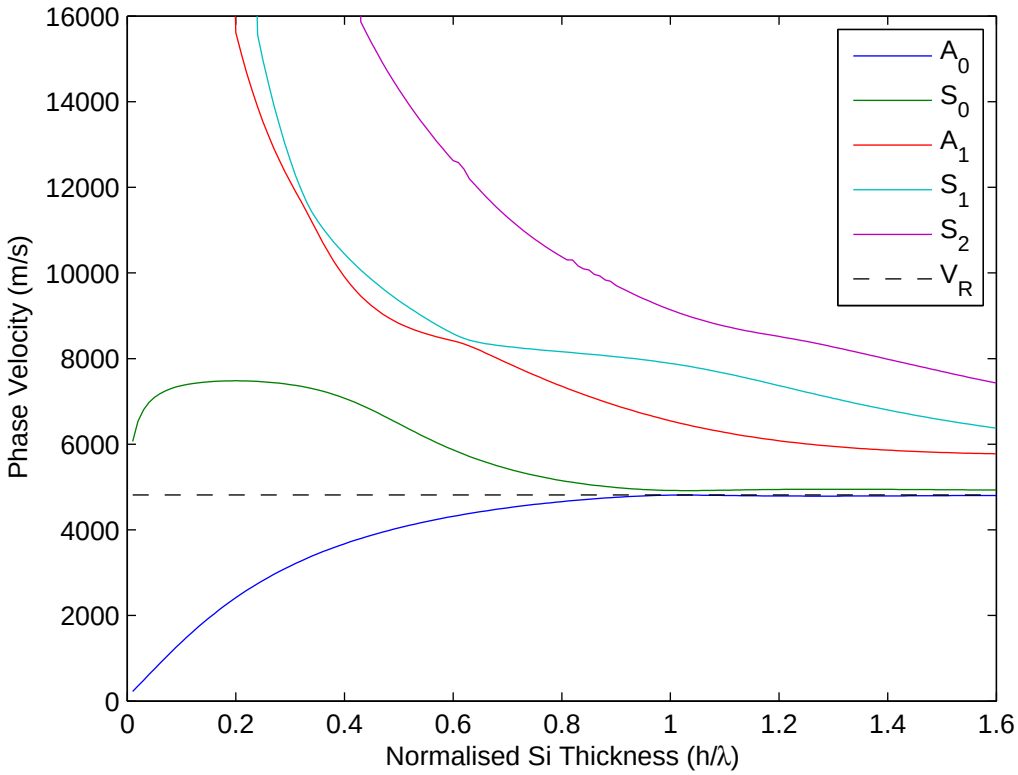


Figure 3.4: Phase Velocity - Normalised Layer Thickness

independent non-interfering Rayleigh modes propagating along both surfaces with a velocity $V_R$. In the presented device, the Rayleigh mode velocity is $4815$m/s.

In terms of density and mass sensing, the $A_0$ mode is a prime candidate for operation in liquid media [8]. In a liquid environment, the acoustic wave phase velocity must be lower than the compressional velocity of the fluid to confine energy to the structure rather than it dissipating into the surrounding medium. For water, this velocity is $1435$m/s. Using the characteristics presented in Figure 3.4, the maximum permissible thickness of the structure to confine the $A_0$ mode is approximately $17.4$µm, which can easily be obtained using current microfabrication techniques. It will also be seen from the displacement profiles, Section 4.3.1, that the $A_0$ mode has desirable characteristics for sensing applications in liquid media. Another benefit of the low velocity $A_0$ mode is that it allows for relatively inexpensive signal processing equipment to be used due to the low resonant frequency. Furthermore, the necessary support electronics can be integrated onto the substrate paving the way for 'lab-on-chip' applications.

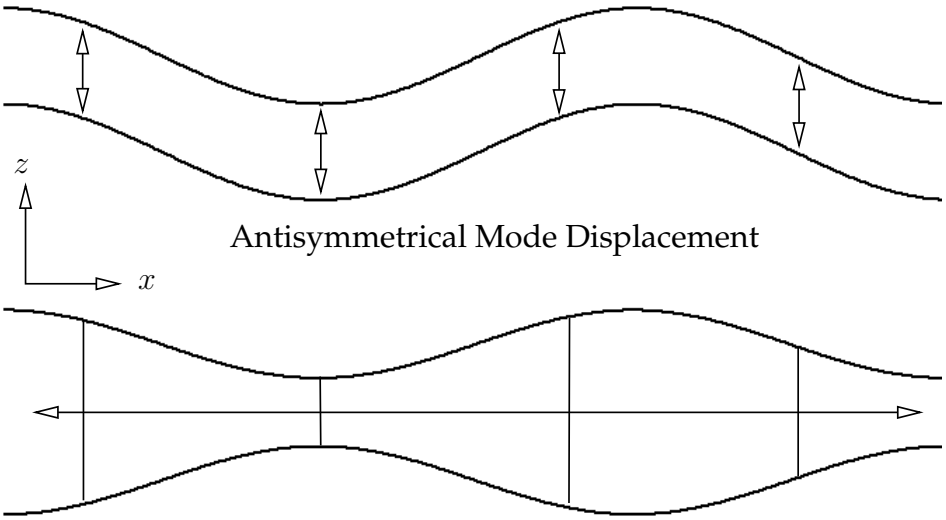


Figure 3.5: Primary Mode Displacement

The symmetric mode displacement is primarily longitudinal, and not of interest for liquid density sensing applications.

### 3.3.3 Electromechanical Coupling Coefficient

The electromechanical coupling coefficient, $K^2$, is often used as a measure of the coupling between the electrical and mechanical fields. It can be calculated from dispersion characteristics of a structure by evaluating the fractional difference in phase velocity caused by a metalised boundary condition:

$$K^2 = 2\frac{v_o - v_m}{v_o}, \tag{3.34}$$

where $v_o$ and $v_m$ represent the open-circuit and metalised surface phase velocities respectively.

As previously mentioned a plate structure has two free surfaces, of which either, both, or neither can be metalised. Depending on the boundary conditions, the velocities will be slightly different. In the multilayered device presented, the coupling coefficient is calculated at the free space interface, which is also the location of the IDTs. If a further sensitive layer was deposited it would be necessary to determine the value at the sensitive/piezoelectric layer interface. In calculating $K^2$, it is assumed that an infinitely thin and conducting metal film is deposited over the device surface that does not affect the mechanical boundary conditions.

Figures 3.6 and 3.7 depict the coupling coefficient as a function of normalised plate thickness for the $A_0$ and $S_0$ modes respectively. The three metalised boundary conditions are presented to illustrate the slight differences in calculations. The ZnO and Al layers were kept consistent at $0.6$µm and $0.4$µm respectively whilst the thickness of the Si membrane was altered.

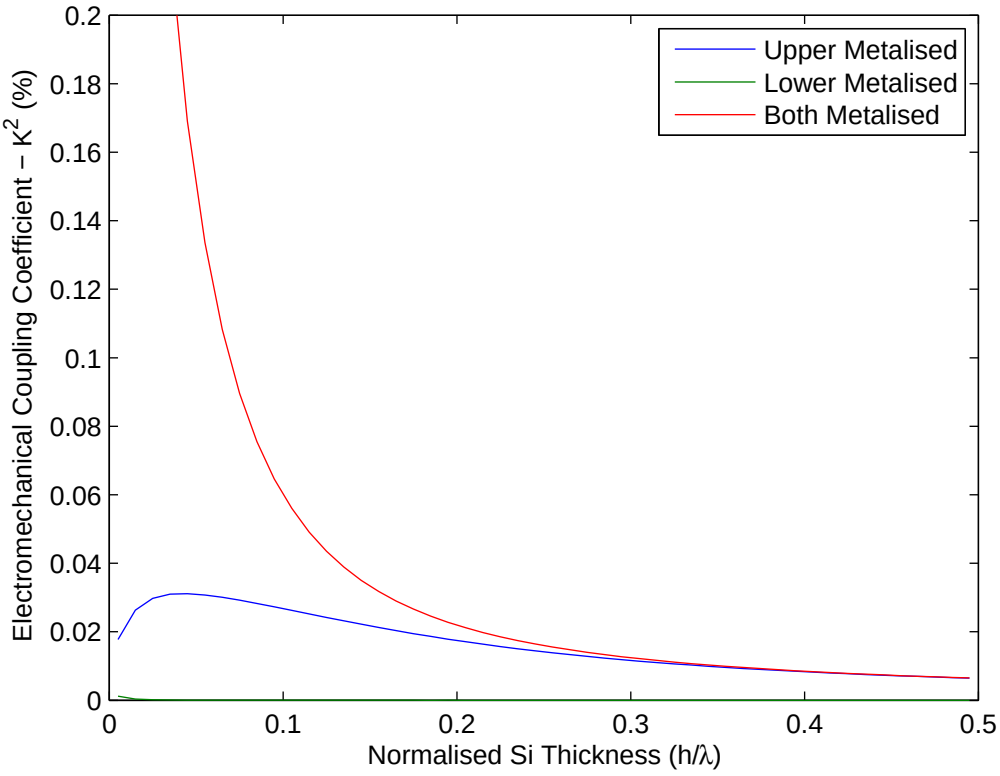


Figure 3.6: Primary Antisymmetric Mode Coupling Coefficient

From Figures 3.6 and 3.7, the coupling coefficient varies significantly depending on which surface is metalised. From this point, the upper metalised approach will be used to evaluate electromechanical coupling. For both $A_0$ and $S_0$ modes, the coupling coefficient is not a maximum at the smallest dimension, rather at a normalised silicon thickness of approximately $0.045$, $(4.5$µm$)$, for $A_0$ and $0.065$ for $S_0$, corresponding to phase velocities of $683$ and $7212$m/s respectively. For conductometric sensing applications, the coupling coefficient should be as large as possible to achieve maximum sensitivity [108], but in terms of non-conductive mass sensing applications the surface particle displacement profiles and the overall thickness of the structure are far more

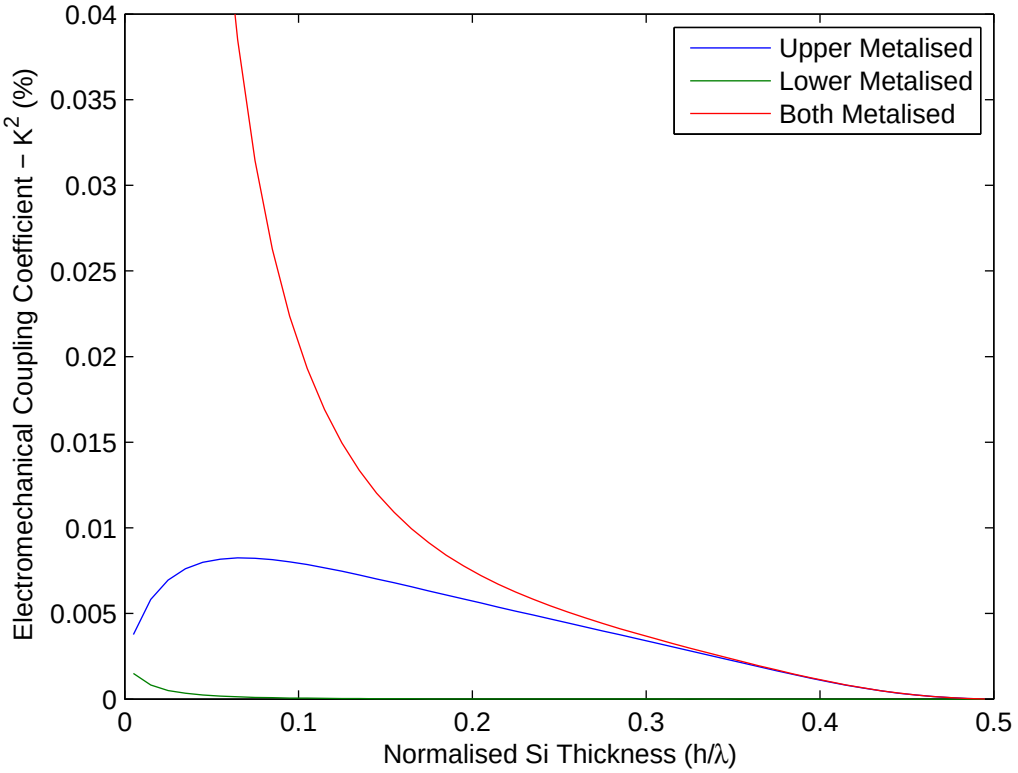


Figure 3.7: Primary Symmetric Mode Coupling Coefficient

important [14, 109]. A FPW device can be used to detect analytes in both liquid and gaseous media, but in the case of the sensing applications in liquid media the phase velocity of the $A_0$ mode should be below that of the target liquid, which for the presented structure, at maximum coupling, is the case. Therefore, the corresponding FPW structure could be realised to have a relatively high value of $K^2$ as well as low velocity. The implications of using an FPW in a liquid environment is further discussed in Chapter 6.

The low value of $K^2$ when compared to other acoustic wave structures can make it difficult to determine the acoustic response of the device. With such a low coupling coefficient, it may be necessary to have a significant number of electrode finger pairs to ensure that sufficient electrical energy is converted to mechanical and vice-versa.

## 3.4 Assumptions and Limitations

In the presented discussion on the transmission matrix method, several key simplifying assumptions have been made. The first, and the most important, is the assumption of negligible variation of fields along the $y$-direction. This is not a shortfall of the method, as it can be simply adapted for all three dimensions [104], rather a process to simplify the calculation of the transmission matrix. As will be shown in Chapter 4, the displacement component along $y$ is non-zero, however significantly less than that of the $x$ and $z$ directions. In terms of substrate dimensions, the method also assumes that the plate extends to infinity in $x$ and $y$, thus reflections from model boundaries are omitted. For devices with a narrow aperture width it may become necessary to include these effects. Techniques such as the FEM, discussed in Chapter 5, can be used to determine the change in response due to decreased substrate dimensions with relative ease.

In a physical device, the resonant frequency is determined by the combination of electrode period, the thickness of the structure and the materials employed. It is assumed that these quantities are constant across the device. Due to variations in the fabrication process, the electrode metallisation ratio may vary, thus affecting the transducer period of the device as well as the phase velocity and electromechanical coupling coefficient. For the FPW devices studied here, it is assumed that a metallisation ratio of $0.5$ is used. Secondly, the acoustic wave velocity is perturbed as it travels along the metalised region of the electrodes [2] which is not accounted for using this method. Alternative techniques, such as the FEM are ideal for this type of analysis as the problem is discretised where localised structural and electrical variations can be considered more appropriately.

Material damping has not been included in the construction of the transmission matrix method. Several authors have attempted to extend the method to include damping which appears as either a complex wavenumber or frequency [15]. A determinant scan can still be used to determine the operating parameters of the device, however the zeros of the determinant occur for complex values of frequency or wavenumber. Damping is a critical parameter, particularly when dealing with liquid loaded structures. In the authors implementation, Chapter 6, damping is introduced via a complex

angular frequency term.

The simulations presented in this chapter do not take into account the electrical properties of the metallic ground plane within the layer stack. It would be a relatively simple process to include the electrical effects, however analysis using the FEM in Chapter 5 has shown that there is insignificant influence on the properties of the propagating modes. However, as was seen in Figure 3.4, it is imperative that all layers are included as they have a significant influence on phase velocity.

### 3.4.1 Numerical Instability of Transmission Matrix Method

Although the transmission matrix method has accurately predicted the operating characteristics of a multilayered FPW device [8], the method can suffer from numerical instability. The most prevalent problem is when evaluating structures with large frequency-thickness products or complex material parameters [15, 80, 82, 110]. Although the transmission matrix technique developed has been applied to micron size structures, it can be equally applied to millimetre or larger configurations, provided that the thickness to wavelength ratio is small.

Several techniques exist to improve the computational stability of the transmission matrix method. The instability will be shown to be brought about by poor conditioning of the transmission matrices, resulting in uneven growth of the partial mode wavenumbers. Modifications can be made, which appear in Chapter 4, to improve the numerical stability of the technique, whilst retaining its simplicity. This section will highlight the computational issues with the transmission matrix method to illustrate the necessary changes for increased stability.

#### 3.4.1.1 Large Frequency-Thickness Products

Consider a plate structure consisting of a $350$µm Si substrate, $0.4$µm Al and a $0.6$µm ZnO piezoelectric layers. The wavelength has been intentionally set at $10$µm to exaggerate the instability of the method. A determinant scan was conducted, Figure 3.8, between $4,500$ and $7,500$m/s corresponding to a frequency-thickness product of $1.58 \times 10^5$ to $2.63 \times 10^5$Hzµm respectively. The numerical error can clearly be seen by the oscillation in the determinant scan. The upper limit, before the method becomes

ill-conditioned appears to be $1.84 \times 10^5$Hzµm.

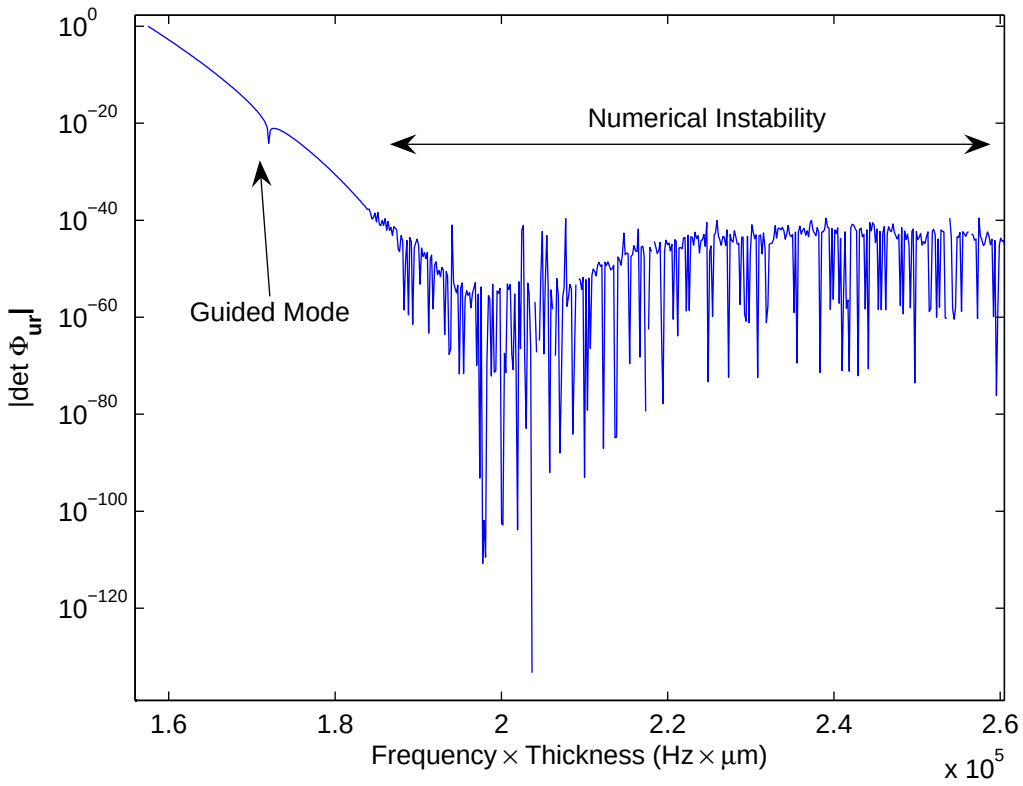


Figure 3.8: Determinant Scan - Large Frequency-Thickness Product

As the frequency-thickness product begins to increase, the upper and lower surfaces become uncoupled and the solution can be thought of as two independent Rayleigh modes propagating along the upper and lower surfaces of the structure. The transmission matrix, which relates the essential field variables at the two surfaces becomes unstable, as the relationship is no longer valid. Recall from equation 3.27 that the transmission matrix solution is an eigenvalue problem, with the eigenvalues representing the eight partial mode wavenumbers present in the structure. The extent of the problem can be illustrated by considering the wavenumber components, $\Lambda$, in the $z$-direction.

Two different wavelengths were considered, $100$µm and $10$µm, which through equation 2.6 are seen to modify the resulting frequency of the device. Table 3.3 depicts the eigenvalue matrix for both cases at a fixed phase velocity of $7,000$m/s. The fixed velocity term corresponds to a frequency thickness product of $2.45 \times 10^4$Hzµm and

$2.45 \times 10^5$Hzμm for the $100$ and $10$μm wavelengths respectively.

Table 3.3: Partial Mode Wavenumbers - Large Frequency-Thickness Products

| P.M Wavenumber ($m^{-1}$),$\lambda = 10$μm | P.M. Wavenumber ($m^{-1}$),$\lambda = 100$μm |
|---|---|
| $7.2170 \times 10^{-1} + 6.9221 \times 10^{-1}i$ | $-4.9974 \times 10^{11} - 5.3425 \times 10^{-9}i$ |
| $7.2170 \times 10^{-1} - 6.9221 \times 10^{-1}i$ | $-1.7508 \times 10^{6} - 1.8716 \times 10^{8}i$ |
| $2.2989 \times 10^{-32} - 9.0675 \times 10^{-46}i$ | $-4.9974 \times 10^{-11} + 5.3425 \times 10^{-9}i$ |
| $4.3499 \times 10^{31} - 1.7158 \times 10^{18}i$ | $-1.7508 \times 10^{6} + 1.8716 \times 10^{8}i$ |
| $7.4085 \times 10^{-1} + 6.7167 \times 10^{-1}i$ | $2.8234 \times 10^{-10} + 1.6829 \times 10^{-25}i$ |
| $7.4085 \times 10^{-1} - 6.7167 \times 10^{-1}i$ | $3.5419 \times 10^{+9} + 2.1112 \times 10^{-6}i$ |
| $3.1164 \times 10^{-96}$ | $2.8143 \times 10^{-10}$ |
| $3.2088 \times 10^{95}$ | $3.5533 \times 10^{9}$ |

Particular attention is drawn to the last two values in Table 3.3. In the case of the high frequency-thickness product simulation, $\lambda = 10$μm, the terms have become increasing large, which is the root of the numerical instability. In terms of numerical values, the partial mode wavenumbers exhibit solutions across $191$ and $19$ orders of magnitude for the high and low frequency-thickness products respectively. For the $\lambda = 100$μm simulations, it can be seen that within the bounds of numerical error, the eigenvalues occur in conjugate pairs, whereas with a large frequency-thickness product this is no longer the case. It should also be noted that a slight numerical error is present in the $100$μm case as the last two terms are purely real, where if the solution was exact, they would contain a corresponding imaginary term.

Consider the transmission matrix components for a structure with a large frequency-thickness product. From equation A.1, the first row of the transmission matrix relates the stress component $T_{xz}$ at the upper surface to essential field variables at the lower surface. If the two surfaces are sufficiently uncoupled, the components of $\phi$ should be small. However, as $\phi$ is also frequency dependent, these terms grow, adding to the instability of the solution [82]. In the example given previously, terms within the first row of the transmission matrix exhibit values excess of $1 \times 10^{79}$. Due to the addition of the exponentially increasing and decreasing terms significant digits can be lost in

the mathematical processes performed on these values, thereby further increasing the numerical error.

#### 3.4.1.2 Complex Material Parameters

As previously mentioned, FPW devices are well suited to liquid sensing applications due to the low phase velocity of the $A_0$ mode. In a liquid environment it is important that attenuation and loading effects are considered, as these will have a marked impact on the response of the device. The complete solution to the fluid loading problem is discussed in Chapter 6, however it is necessary to illustrate the inability of the transmission matrix method in its current form, to work with liquid loaded structures.

For sensing applications, it is typically necessary to deposit a sensitive layer on the FPW device to promote sensitivity toward a given analyte. Sensitive layers can range from polymer-based functional materials [64], to thin film metal oxides used for gas sensing applications. The addition of viscoelastic polymer layers can cause significant attenuation of the acoustic wave, which must be accounted for by the analysis technique applied. Although solid thin film materials cause attenuation of the acoustic wave, these effects are relatively small and most analysis techniques, including the one discussed in this chapter, ignore these effects.

Liquid loading can influence the phase velocity, attenuation and mechanical boundary conditions of the structure, requiring modification of the transmission matrix to accurately predict the device response. The simplest approach is to modify the material properties to introduce damping. Isotropic material properties are adopted for a non-conductive liquid, thereby allowing the influence of damping to be introduced without the need to completely reformulate the solution path. With reference to Chapter 6, the material stiffness matrix properties are modified to allow for the frequency dependent nature of visco-elastic damping via the relationship:

$$c_{11} = K + \frac{4}{3} j\omega\eta \tag{3.35a}$$

$$c_{44} = j\omega\eta, \tag{3.35b}$$

where $\eta$ is the first coefficient of viscosity.

With the inclusion of lossy materials, the system propagator matrix also contains complex terms. For a liquid layer, the corresponding eigenvalues are several orders of mag-

nitude larger than that of a solid material. As was shown for large frequency-thickness products, the partial mode wavenumbers become increasingly large and hence unstable. Therefore, if the partial modes wavenumbers are already excessively large, multiplication by the frequency-thickness terms increases their size and adds to the instability of the solution.

One traditional approach to modelling liquid loaded acoustic wave devices is to assume that the additional liquid layer is semi-infinite. Another suggested method prescribes that the liquid interaction is limited to the acoustic delay length, thereby the layer should be at least this thickness. For the presented structure, this corresponds to approximately $5$µm [111]. A determinant scan of the structure at the prescribed thickness fails to provide an adequate solution. It was necessary to reduce the fluid thickness to $2.6$µm before a phase velocity solution for the $A_0$ and $S_0$ modes could be found. Examination of the overall transmission matrix, whilst keeping the solid layer material properties constant, indicates that a change in fluid thickness from $1$µm to $5$µm, corresponding to a change of $27$ orders of magnitude for upper left term, $\phi_{11}$. Clearly, if the solid parameters are identical, the difference can be attributed to the liquid layer, which has become dominant in the solution.

In its present form, irrespective of the inherent numerical inaccuracies, the transmission matrix method must be modified before it can be successfully used for the evaluation of damped modes. Currently it operates in the velocity domain, where the wavelength is fixed and the phase velocity scanned to determine the minimum of the determinant. To include the effects of attenuation, it is more convenient to operate in the wavenumber domain. A simple substitution can be made for phase velocity as:

$$v_p = \frac{\omega}{k_x} \tag{3.36}$$

The wavenumber can be now fixed according to the wavelength of the device and the angular frequency scanned to obtain a solution. To include the damping effects of a lossy material, either the frequency or wavenumber could be complex. Both solutions are equally valid.

## 3.5 Conclusion

This chapter has introduced the Transmission Matrix method and its application in the evaluation of multilayered Flexural Plate Wave structures. The method has been shown to be well suited to the analysis of multilayered structures with low frequency-thickness products typically used for sensing applications. The transmission matrix method assumes that fields in the $y$-direction are either constant or zero and the solution is determined by considering the essential field variables normal to a plane perpendicular to the $z$-axis. The electrical boundary conditions have been fully described and as a consequence the electromechanical coupling coefficient, $K^2$ calculated. It has been demonstrated that a FPW device supports many modes, of which the primary antisymmetric and symmetric are of interest. For liquid sensing applications, the first antisymmetric is of prime importance. The phase velocity of the antisymmetric mode has been shown to exhibit a strong dependence on the overall structure thickness. Using this knowledge, the structure can be configured such that the velocity of the $A_0$ mode is below the compressional velocity of the liquid medium and hence the acoustic energy is confined to the structure rather than radiated into the surrounding medium.

Limitations of the method have been highlighted, particularly when analysing materials with lossy material parameters and structures with large frequency-thickness products. The cause of the numerical error has been determined to be caused by exponentially growing partial mode wavenumber terms when evaluating the transmission matrices of the individual layers. Due to the numerical error alternative methods are required to solve the piezoelectric wave propagation problem in such structures. The suggested method, known as the Stiffness Matrix method, extends on the transmission matrix whilst retaining much of its computational efficiency and simplicity. This technique will be discussed in Chapter 4.

[ This page has intentionally been left blank. ]

# Chapter 4

# Stiffness Matrix Analysis of FPW Devices

## 4.1 Introduction

This chapter presents an improved numerical technique for the analysis of multilayered FPW structures known as the Stiffness Matrix method. Whereas the transmission matrix method presented in Chapter 3 was formulated as a first order differential equation, the stiffness matrix method is based on a nonlinear Riccati equation which has been shown to be well suited to problems with unevenly growing terms. The stiffness matrix method will be shown to be numerically stable even when working with large frequency-thickness products, whilst retaining much of the simplicity of the transmission matrix method.

Similar to the transmission matrix method, this technique can be applied to piezoelectric structures consisting of an arbitrary number of layers. The increased stability of the stiffness matrix method is attributed to the choice of local coordinate system as well as the field variables used to map the components across the layer interfaces. The stiffness matrix method relates displacement on both sides of a layer to the normal stress, rather than mapping the essential field variables across the terminal surfaces as was done in the transmission matrix method. For large frequency-thickness produces, the external surfaces of the structure become decoupled, thus the transmission matrix becomes ill-conditioned. It will be shown that the stiffness matrix method, when applied to acoustically thick structures, converges to the Rayleigh case. The use of the stiffness matrix method for acoustically lossy materials will be discussed in Chapter

6. The techniques developed within this chapter will serve as a benchmark for the author's novel approach to the analysis of FPW devices based on the FEM.

Section 4.2 presents an overview of the necessary modifications to the transmission matrix to convert to the improved stiffness matrix method and examples given to illustrate its increased stability. It will be shown that the overall stiffness matrix for a multilayered structure can be generated by applying a computationally efficient recursive algorithm.

Section 4.2.3 relates the stiffness matrix method to a generalised Green's function which fully describes the electrical and mechanical interactions of the FPW device. The appropriate boundary conditions will be discussed for a FPW device, which varies significantly from the SAW case. The effective permittivity function will be employed as an alternative method to calculate the operating parameters of a FPW device. The effective permittivity will be used in subsequent sections to evaluate the insertion loss characteristics of a FPW device using interdigital transducers as an excitation source.

Section 4.3 examines the displacement profiles and mass sensitivity of a multilayered FPW device operating in the gas phase. A comparison will be given between single isotropic layer devices, where in many cases simplistic analytical expressions exist to describe operational parameters, and more complex multilayered structures. Due to the nature of multilayered structures analytical solutions are typically not possible, and hence utilising the author's implementation of the stiffness matrix method, parameters such as mass sensitivity and particle displacement are evaluated numerically. A general rule will be developed to identify the numerous possible acoustic modes in a FPW structure, with an emphasis on the difference between purely isotropic single layer and composite piezoelectric multilayered devices. Mass sensitivity will be analysed for two primary modes operating in a gaseous environment using perturbation theory. It will be shown that the multilayered design has significantly higher sensitivity than a single isotropic layer structure.

Finally, Section 4.4 develops the necessary processes to analyse the electrical performance of a FPW device based on a spectral domain Green's function. The particular approach taken will focus on the frequency domain response of a FPW device with a ground plane between the Si membrane and the piezoelectric layer. It will be shown

that many of the assumptions used for SAW devices can no longer be applied when evaluating the characteristics of a FPW transducer and in such cases potential modifications will be discussed and implemented.

## 4.2 Stiffness Matrix Method Development

Section 3.4.1 demonstrated the inability of the transmission matrix method to accurately solve the piezoelectric wave propagation problem in lossy as well as acoustically thick materials. It was shown that the cause of the transmission matrix's numerical instability is due to exponentially growing eigenvalue terms. This section will present a recently developed approach known as the Stiffness Matrix method which is unconditionally stable and retains much of the computational efficiency and simplicity of the transmission matrix method [85].

In this approach the transmission matrix is reformulated to prevent the exponentially increasing eigenvalue terms from affecting the stability of the solution. Part of the reformulation is based on the selection of an alternative coordinate system when considering the propagating modes. In the previous method, the solution did not depend on the direction of power flow of the eight partial modes, whereas the stiffness matrix method requires the partition of these modes into either 'upwards' or 'downward' modes. With reference to Figure 4.1, for modes propagating 'downwards', $z^-$, the local origin is defined as the top of layer $m$, denoted $z = h_m$. Conversely, for modes propagating 'upwards', $z^+$, the origin is located at the bottom of layer $m$, $z = h_{m-1}$.

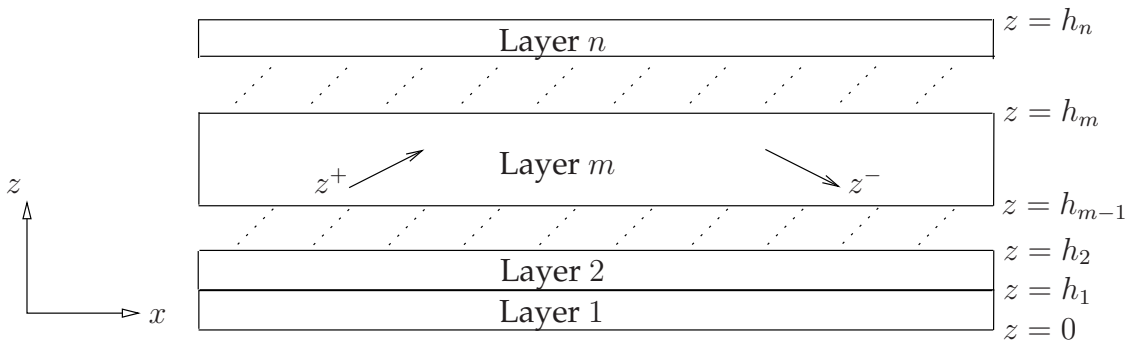


Figure 4.1: Stiffness Matrix Method Multilayered Coordinate System

The transmission matrix discussed in Chapter 3 was formulated as a first order lin-

ear ordinary differential equation, with the solution describing the $z$-dependence of the essential field variables. Although describing a slightly different set of essential field variables, the stiffness matrix method is quite different in that it satisfies a nonlinear Riccati equation. This method is quite well suited to systems with unevenly growing terms, such as those found in the partial mode eigenvalues of nonhomogeneous waves [86]. The technique is routinely applied to 'decision and control systems' where it has been shown that the Riccati equation can be decoupled into pure-fast and pure-slow terms which allows the problem to be solved by considering a single differential equation [112]. Much of the derivation of the stiffness matrix method is similar to that seen in Chapter 3, however the field variables are redefined to clearly indicate the changes in the solution path.

### 4.2.1 Reformulation of the Transmission Matrix Method

Reformulation of the transmission matrix involves relating stress to displacement on both sides of a layer. Therefore, apart from the increased stability of the stiffness method, there is a slight difference in field variables, which are defined as:

$$\mathbf{U} = \begin{bmatrix} u_x & u_y & u_z & \varphi \end{bmatrix}^T \tag{4.1a}$$

$$\mathbf{T} = \begin{bmatrix} T_{xz} & T_{yz} & T_{zz} & D_z \end{bmatrix}^T \tag{4.1b}$$

As the stiffness matrix method operates on displacement rather than velocity, it is not necessary to take the time derivative of the scalar potential in equation 4.1a.

The same assumed solution, equation 3.10, is used, with a substitution made to operate in the wavenumber domain rather than velocity. By assuming the same solution, the system propagator matrix, $\mathrm{A}$, can be used, but is reordered to accommodate for the change in field variables. The state vector, $\boldsymbol{\zeta}$ which is conceptually identical to $\boldsymbol{\tau}$ is given by:

$$\boldsymbol{\zeta} = \begin{bmatrix} \mathbf{U} \\ \mathbf{T} \end{bmatrix}, \tag{4.2}$$

with the modified system propagator matrix given by:

$$\mathrm{A_s} = \begin{bmatrix} k_x \mathrm{X}\Gamma^{31} & -j\mathrm{X} \\ -j\left(\Gamma^{11} - \Gamma^{13}\mathrm{X}\Gamma^{31}\right)k_x^2 + j\rho\omega^2\mathrm{I} & k_x\Gamma^{13}\mathrm{X} \end{bmatrix}, \tag{4.3}$$

which allows the ordinary differential equation and the subsequent solution to be written as:

$$\frac{d\boldsymbol{\zeta}}{dz} = j\mathrm{A_s}\boldsymbol{\zeta} \tag{4.4a}$$

$$\boldsymbol{\zeta}\left(z+h\right) = e^{j\mathrm{A_s}h}\boldsymbol{\zeta} \tag{4.4b}$$

The terms in equation 4.3 are the same as in equation 3.24a, with the exception of $k_x$ being introduced as the propagation direction wavenumber. The term $e^{j\mathrm{A_s}h}$, is equivalent to $\phi$ in the transmission matrix method. As before, the eigenvalues of equation 4.4a are the partial mode wavenumbers with the eigenvectors corresponding to the individual components of the state vector $\boldsymbol{\zeta}$. As was with the transmission matrix, the parameters in equation 4.4b are assumed to vary as $e^{j\omega t - k_x x - k_z z}$ and are hence omitted. The material scaling factors introduced in Table 3.1 are also consistent between the transmission and stiffness matrix methods. With reference to equation 4.4a, the solution of the differential equation is still the matrix exponential. The initial part of the procedure is the same as before, with the eigenvalues of the propagator matrix calculated.

To evaluate the power flow direction of the propagating modes the quasi-static approximation of the complex Poynting vector is calculated. The eight propagating modes are sorted into two groups, upwards and downwards modes by considering the imaginary component of the eigenvalue matrix. Solutions with purely negative imaginary eigenvalues are deemed to be a downwards propagating modes and conversely a positive purely imaginary wavenumber corresponds to an upwards mode. These two mode directions can be determined simply by inspection which improves the computational efficiency. This procedure is valid only for propagation of partial modes, whereas evanescent modes requires the complete Poynting vector to be evaluated. On the other hand, if a real or complex eigenvalue is found, then it is necessary to calculate the quasistatic Poynting vector, which is defined as [102]:

$$P = \mathrm{Re}\left(\frac{-\mathbf{v}^* \cdot \mathbf{T}}{2} + \frac{j\omega D_z \varphi^*}{2}\right), \tag{4.5}$$

where the superscript $*$ represents the complex conjugate.

If the result of equation 4.5 is positive, then an upwards mode is identified, or if negative a downward mode has been found. The quasi-static Poynting vector is also

checked for zero, which represents the critical velocity of a bulk wave in the material. A FPW device does not support bulk waves if a zero value was found the solution process was halted.

The cause of the numerical instability of the transmission matrix was found to be due to large uneven partial mode eigenvalues. The root of the problem is much more evident if the system propagator matrix is rewritten in a diagonalised form [87]:

$$\mathrm{A_s} = \mathbf{M}\beta_\mathrm{z}\mathbf{M^{-1}} \tag{4.6a}$$

$$= \begin{bmatrix} \mathrm{P^-} & \mathrm{P^+} \\ \mathrm{D^-} & \mathrm{D^+} \end{bmatrix} \begin{bmatrix} \beta_\mathrm{z}^- & 0 \\ 0 & \beta_\mathrm{z}^+ \end{bmatrix} \begin{bmatrix} \mathrm{P^-} & \mathrm{P^+} \\ \mathrm{D^-} & \mathrm{D^+} \end{bmatrix}^{-1} \tag{4.6b}$$

The eigenvector matrix $\mathbf{M}$ is split into general components of displacement, $P$ and stress, $D$. The subscripts $+$ and $-$ indicate the mode direction as determined from the power flow direction. Therefore, analogous from equations 3.26 and 4.6, the solution to the eigenvalue problem is given by:

$$\begin{bmatrix} \mathbf{U}\left(z+h\right) \\ \mathbf{T}\left(z+h\right) \end{bmatrix} = \begin{bmatrix} \mathrm{P^-} & \mathrm{P^+H^+} \\ \mathrm{D^-} & \mathrm{D^+H^+} \end{bmatrix} \begin{bmatrix} \mathrm{P^-H^-} & \mathrm{P^+} \\ \mathrm{D^-H^-} & \mathrm{D^+} \end{bmatrix}^{-1} \begin{bmatrix} \mathbf{U}\left(z\right) \\ \mathbf{T}\left(z\right) \end{bmatrix} \tag{4.7}$$

The $\mathrm{H}$ matrices are the exponential of the partial mode wavenumbers, given by:

$$\mathrm{H^+} = \mathrm{I}\begin{bmatrix} e^{j\beta_z^{+1}h} & e^{j\beta_z^{+2}h} & e^{j\beta_z^{+3}h} & e^{j\beta_z^{+4}h} \end{bmatrix}^T \tag{4.8a}$$

$$\mathrm{H^-} = \mathrm{I}\begin{bmatrix} e^{-j\beta_z^{-1}h} & e^{-j\beta_z^{-2}h} & e^{-j\beta_z^{-3}h} & e^{-j\beta_z^{-4}h} \end{bmatrix}^T, \tag{4.8b}$$

where $\mathrm{I}$ represents the $4 \times 4$ identity matrix. Note that the superscripts in equation 4.8a and 4.8b relate to the partial mode wavenumbers and are not mathematical operators. Inclusion of the partial mode wavenumbers into the general displacement and stress vectors prevents the numerical instability demonstrated in Section 3.4.1 from arising [84]. For example, if a partial mode becomes nonhomogeneous or evanescent, the wavenumber in the $z$-direction will become complex. As the magnitude of the imaginary component increases, the exponential term becomes increasingly smaller. When the inverse is taken, this naturally becomes quite large, thus promoting instability. By including these terms with the general displacement and stress vectors, the instability is avoided. If equation 4.7 is reordered, then the stiffness matrix, which relates normal

stress to displacement is written as:

$$\begin{bmatrix} \mathbf{T}(z+h) \\ \mathbf{T}(z) \end{bmatrix} = \mathrm{K} \begin{bmatrix} \mathbf{U}(z+h) \\ \mathbf{U}(z) \end{bmatrix} \tag{4.9a}$$

$$\mathrm{K} = \begin{bmatrix} \mathrm{D}^{-} & \mathrm{D}^{+}\mathrm{H}^{+} \\ \mathrm{D}^{-}\mathrm{H}^{-} & \mathrm{D}^{+} \end{bmatrix} \begin{bmatrix} \mathrm{P}^{-} & \mathrm{P}^{+}\mathrm{H}^{+} \\ \mathrm{P}^{-}\mathrm{H}^{-} & \mathrm{P}^{+} \end{bmatrix}^{-1} \tag{4.9b}$$

### 4.2.2 Stiffness Matrix Analysis of Multilayered Structures

Similar to the transmission matrix, the stiffness matrix can be formulated to solve the piezoelectric wave propagation problem for multilayered structures. For a multilayered FPW structure, a global stiffness matrix, $\mathrm{K}^{\mathrm{T}}$, to relate stress and displacement between the two exposed terminal surfaces must be calculated. With the bottom of the structure, $z = 0$, defined as the reference plane, the recursive calculation is applied in an upwards manner. Care should be taken in this regard, as the transmission matrix multiplied the successive layer matrices from the upper to the lower surfaces. The global stiffness matrix for a multilayered structure is given by the repeated application of:

$$\mathrm{K}^{\mathrm{T}} = \begin{bmatrix} \mathrm{K}_{11}^{\mathrm{m}} + \mathrm{K}_{12}^{\mathrm{m}} \left(\mathrm{K}_{11}^{\mathrm{M}} - \mathrm{K}_{22}^{\mathrm{m}}\right)^{-1} \mathrm{K}_{21}^{\mathrm{m}} & -\mathrm{K}_{12}^{\mathrm{m}} \left(\mathrm{K}_{11}^{\mathrm{M}} - \mathrm{K}_{22}^{\mathrm{m}}\right)^{-1} \mathrm{K}_{12}^{\mathrm{M}} \\ \mathrm{K}_{21}^{\mathrm{M}} \left(\mathrm{K}_{11}^{\mathrm{M}} - \mathrm{K}_{22}^{\mathrm{m}}\right)^{-1} \mathrm{K}_{21}^{\mathrm{m}} & \mathrm{K}_{22}^{\mathrm{M}} - \mathrm{K}_{21}^{\mathrm{M}} \left(\mathrm{K}_{11}^{\mathrm{M}} - \mathrm{K}_{22}^{\mathrm{m}}\right)^{-1} \mathrm{K}_{12}^{\mathrm{M}} \end{bmatrix}, \tag{4.10}$$

where $\mathrm{K}^{\mathrm{m}}$ is the layer under consideration, and $\mathrm{K}^{\mathrm{M}}$ is the stiffness components of the bottom M layers. The subscripted terms relate to the individual $4 \times 4$ matrices derived from the overall $8 \times 8$ global matrix. For example, $\mathrm{K}_{11}$ represents the upper left hand components and $\mathrm{K}_{12}$ is the upper right section. In the case of the first layer, $\mathrm{K}^{\mathrm{M}}$ is simply the stiffness matrix for the bottom layer. Similar to the transmission matrix method, the stiffness matrix method can be applied to an arbitrary number of layers as the algorithm is dependent on the individual layer characteristics rather than the dimensions of the overall structure.

To highlight the computational stability of the stiffness matrix method consider Figure 4.2 which presents an open-circuit boundary determinant scan using the same parameters as those in Section 3.4.1.1. Recall for the transmission matrix the solution could not be sufficiently resolved. A small frequency attenuation term is also included to promote solution convergence [113]. The frequency-thickness scanning range has

been slightly enlarged to illustrate the solution approaching the Rayleigh wave velocity of $4815$m/s corresponding to a frequency-thickness product of $1.67 \times 10^5$Hzμm.

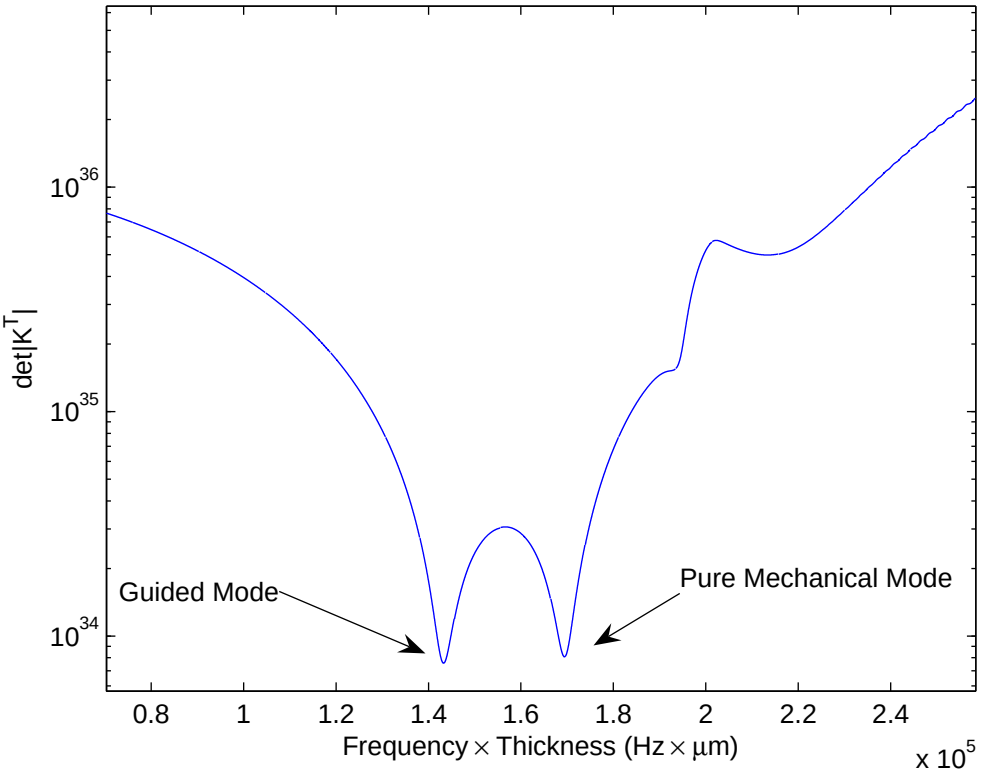


Figure 4.2: Determinant Scan - Large Frequency-Thickness Product

From Figure 4.2, two modes have been resolved, however only the first at a frequency-thickness product of $1.44 \times 10^5$Hzμm, or $4151$m/s, is piezoelectric as determined by the electromechanical coupling coefficient. If the effective permittivity was used instead to determine the operating frequencies of the structure, discussed in Section 4.2.4, only the piezoelectric mode would be found. As the thickness of the structure is increased the solution is found to converge to the Rayleigh wave velocity, thus even in its current form the stiffness matrix could potentially be used to model a multilayered semi-infinite structure. However to further improve the stability, the method is modified to consider only modes that propagate with depth, which will be discussed in Chapter 6.

A reported benefit of computing the wave propagation solution using the stiffness matrix method is the ability to incorporate imperfect interfaces. In such a scenario, the normal stress is consistent on both sides of the imperfect interface, however a dis-

continuity in displacement exists [113]. Mathematically, an imperfect interface can be included in the global stiffness matrix recursive calculation by incorporating a modified layer stiffness matrix. This type of calculation would be beneficial when working with films with different crystal structures or microstructural defects.

### 4.2.3 Stiffness Matrix Method and the Generalised Green's Function

To solve for finite thickness structures the stiffness matrix approach can be used to derive a generalised Green's function via the application of equation 4.11a. The Green's function describes the mechanical displacement and electric potential generated by the mechanical stresses, $\boldsymbol{\sigma}$ and electrical charge, $\gamma$ [87]. The subscripts $l$ and $u$ relate to the lower and upper surfaces of the structure respectively.

$$\begin{bmatrix} \mathbf{u_u} \\ \varphi_u \\ \mathbf{u_l} \\ \varphi_l \end{bmatrix} = \mathbf{G} \begin{bmatrix} \boldsymbol{\sigma}_\mathbf{u} \\ \gamma_u \\ \boldsymbol{\sigma}_\mathbf{l} \\ \gamma_l \end{bmatrix} \tag{4.11a}$$

$$\mathbf{G} = \begin{bmatrix} \mathrm{K}_{11}^{\mathrm{f}} & \mathrm{K}_{11}^{\mathrm{fe}} & \mathrm{K}_{12}^{\mathrm{f}} & \mathrm{K}_{12}^{\mathrm{fe}} \\ -\mathrm{K}_{11}^{\mathrm{ef}} & \theta + K_{11}^{e} & -\mathrm{K}_{12}^{\mathrm{ef}} & -K_{12}^{e} \\ \mathrm{K}_{21}^{\mathrm{f}} & \mathrm{K}_{21}^{\mathrm{fe}} & \mathrm{K}_{22}^{\mathrm{f}} & \mathrm{K}_{22}^{\mathrm{fe}} \\ \mathrm{K}_{21}^{\mathrm{ef}} & K_{21}^{e} & \mathrm{K}_{22}^{\mathrm{ef}} & K_{22}^{e} - \theta \end{bmatrix}^{-1} \tag{4.11b}$$

$$\theta = \varepsilon_0 |k_x| \times 10^{11} \tag{4.11c}$$

As the material properties are scaled, similar to that for the transmission matrix method, it is also necessary to scale $\theta$ which accounts for the free space above and below the structure.

The terms in equation 4.11a relate to the electrical and mechanical properties of the multilayered plate structure, and as such fully describe the acousto-electric problem. Table 4.1 lists the parameters of equation 4.11a and provides a brief description of their significance.

If $i = j$, then the components of the stiffness matrix relate to self action terms, otherwise they are mapped across the multilayered structure. By using the stiffness matrix to derive a Green's function, device parameters, such as electromechanical coupling and

Table 4.1: Stiffness Matrix Method to Green's Function Conversion

| Parameter | Size $(n \times m)$ | Terms |
|---|---|---|
| $\mathrm{K}_{ij}^{f}$ | $3 \times 3$ | Pure Mechanical Terms |
| $\mathrm{K}_{ij}^{fe}$ | $3 \times 1$ | Mechanical to Electrical Coupling |
| $\mathrm{K}_{ij}^{ef}$ | $1 \times 3$ | Electrical to Mechanical Coupling |
| $\mathrm{K}_{ij}^{e}$ | $1 \times 1$ | Pure Electrical Terms |

conductometric sensitivity, can be calculated at any interface within the layer stack. This is particularly useful when considering a structure containing buried electrodes. It should be noted that this approach does not take into account the mass of the electrodes, however this has recently been reported in [21]. The Green's function technique is well established in literature and has been shown to be a robust method to solve the piezoelectric wave propagation problem.

### 4.2.4 Boundary Conditions and Effective Permittivity

The boundary conditions for the stiffness matrix method can be obtained either from considering the Green's function presented in Section 4.2.3, or from the global stiffness matrix $\mathrm{K}^{\mathrm{T}}$. For a simple single isotropic layer FPW device, where no sources are present, the normal stress and the discontinuity in the dielectric displacement, must vanish at the surface. These conditions can be expressed by satisfying the following equation:

$$\det\left(\mathrm{K}^{\mathrm{T}}\right) = 0 \tag{4.12}$$

The same boundary determinant scan procedure developed for the transmission matrix can be used to determine the solution to equation 4.12.

In a structure where an excitation source exists the solution is slightly more complex. As previously intimated, by applying the generalised Green's function, the terminal boundary conditions can be described in terms of charge, electric potential, displacement and normal stress. Alternatively, the effective permittivity, discussed later in this section could be used, but requires a modified determinant search procedure. For mechanically free surfaces the normal stress components are zero. Under an open-

circuit condition, the surface charge density is zero, whilst the potential remains unknown. For the metalised condition, the charge density is unknown and the electric potential is set to zero. Equation 4.11a is reordered to suit the particular boundary condition of interest. Thus, for the top short-bottom open configuration, the following conditions must be met:

$$\begin{bmatrix} \mathbf{u_u} \\ 0 \\ \mathbf{u_l} \\ \varphi_l \end{bmatrix} = \begin{bmatrix} \mathrm{K}_{11}^{\mathrm{f}} & \mathrm{K}_{11}^{\mathrm{fe}} & \mathrm{K}_{12}^{\mathrm{f}} & \mathrm{K}_{12}^{\mathrm{fe}} \\ -\mathrm{K}_{11}^{\mathrm{ef}} & \theta + K_{11}^{e} & -\mathrm{K}_{12}^{\mathrm{ef}} & -K_{12}^{e} \\ \mathrm{K}_{21}^{\mathrm{f}} & \mathrm{K}_{21}^{\mathrm{fe}} & \mathrm{K}_{22}^{\mathrm{f}} & \mathrm{K}_{22}^{\mathrm{fe}} \\ \mathrm{K}_{21}^{\mathrm{ef}} & K_{21}^{e} & \mathrm{K}_{22}^{\mathrm{ef}} & K_{22}^{e} - \theta \end{bmatrix}^{-1} \begin{bmatrix} \mathbf{0} \\ \gamma_u \\ \mathbf{0} \\ 0 \end{bmatrix} \tag{4.13a}$$

$$\boldsymbol{\sigma}_{\mathbf{u}}, \boldsymbol{\sigma}_{\mathbf{l}}, \varphi_n, \gamma_0 = 0 \tag{4.13b}$$

Equation 4.13a is then rearranged to describe the displacement in terms of the unknown charge and electric potential. As was found with the transmission matrix method, the only way in which the reordered equation can be satisfied is if the coefficients of the remaining terms are zero. Therefore, the same computational procedure used with the transmission matrix can be used. Due to complexity of the boundary condition equations, they are included in Appendix B rather than being discussed here.

A more convenient method of determine the operating wavenumbers of multilayered piezoelectric structures is via the poles and zeros of the effective permittivity function. This technique also improves the reliability of the stiffness matrix method as only piezoelectrically excited modes are found. Another benefit of this approach is the ability to determine the solution for both metalised and open-circuit boundary conditions during one calculation process.

Evaluation of the effective permittivity for a FPW device is not a simple as that for a semi-infinite substrate. In semi-infinite structures, where it is assumed that negligible electrical or mechanical contributions exist due to the lower surface of the substrate, the generalised Green's function is reduced to a $4 \times 4$ matrix. The effective permittivity can then simply be written in terms of a single component of the Green's function. However, in a FPW device, as was discussed in Chapter 3, there are four possible electrical boundary conditions, of which two can be described by a single effective permittivity function. That is, for a FPW structure, the effective permittivity of the upper piezoelectric surface can be described by considering two different electrical

boundary conditions on the bottom layer. The concept of effective permittivity was introduced in [114], and is defined as:

$$\varepsilon_{eff}\left(k_x,\omega\right)=\frac{\gamma\left(k_x,\omega\right)}{|k_x|\varphi\left(k_x,\omega\right)} \tag{4.14}$$

From equation 4.14 it can be seen that the effective permittivity is dependent on both angular frequency and wavenumber. The value of the effective permittivity, evaluated at infinite $k_x$, is also used in the calculations for the transducer frequency response covered in Section 4.4.3. In formulating the effective permittivity, it is assumed that all mechanical stresses are zero at the top and bottom surfaces. Therefore, considering only pure electrical terms, a relationship between charge, $\gamma$, and voltage, $\varphi$, can be established via the Green's function:

$$\begin{bmatrix}\varphi_u\\ \varphi_l\end{bmatrix}=\begin{bmatrix}G^e_{11} & G^e_{12}\\ G^e_{21} & G^e_{22}\end{bmatrix}\begin{bmatrix}\gamma_u\\ \gamma_l\end{bmatrix}, \tag{4.15}$$

where the terms $G^e_{11}$, $G^e_{12}$, $G^e_{21}$, $G^e_{22}$ can be obtained from the inversion of the modified stiffness matrix presented in equation 4.11b, which are the terms $G_{(4,4)}$, $G_{(4,8)}$, $G_{(8,4)}$, $G_{(8,8)}$ respectively. Of interest in this study is the effective permittivity evaluated at the uppermost surface. Typically this is where the piezoelectric layer is deposited and the interdigital transducers are placed. Where electrodes are buried within the structure, it is necessary to calculate the effective permittivity at that particular interface. Equation 4.15 can be rearranged to describe the potential and charge on the upper surface for the electrical conditions on the bottom interface. The two effective permittivity functions for the upper surface are written as:

$$\varepsilon^{OC}_{eff}\left(k_x,\omega\right)=\varepsilon_0-\frac{1}{|k_x|\left(G^e_{11}-G^e_{12}\left(\frac{1}{\eta}+G^e_{22}\right)^{-1}G^e_{21}\right)} \tag{4.16a}$$

$$\varepsilon^{SC}_{eff}\left(k_x,\omega\right)=\varepsilon_0-\frac{1}{|k_x|\left(G^e_{11}-G^e_{12}\left(G^e_{22}\right)^{-1}G^e_{21}\right)}, \tag{4.16b}$$

where equation 4.16a represents the open circuit bottom condition, $\gamma_l=0$, and equation 4.16b is the short circuit bottom condition, $\varphi_l=0$.

Figure 4.3 presents the effective permittivity for the structure discussed in Section 3.3.2. The poles correspond to the top surface short-circuit surface condition and the zeros represent an electrically open upper surface. In comparison with Figure 3.3, only

the first two piezoelectrically coupled antisymmetric and symmetric modes have been resolved.

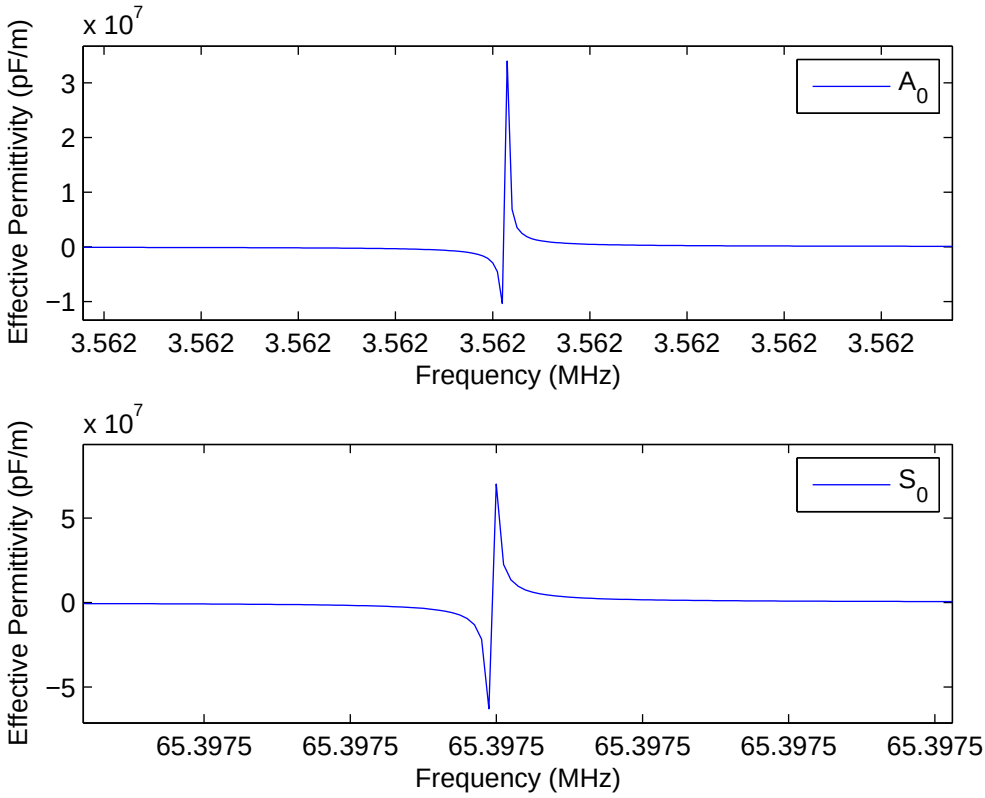


Figure 4.3: Upper Surface Effective Permittivity - Bottom Surface Open Circuit

## 4.3 Device Analysis

In this section the displacement profiles and mass sensitivity for an ideal FPW device will be presented. The simulated structure studied is identical to that discussed in Chapter 3 which will be shown to be well suited to sensing applications in liquid media. Where appropriate the differences between FPW and SAW device calculations will be highlighted. A general rule will be developed to identify the piezoelectrically coupled acoustic modes within a FPW structure by considering the particle displacement profiles in conjunction with the dispersion characteristics. In developing the transmission matrix method of Chapter 3, and also forming the basis of this chapter, it was assumed that the $y$-component of the essential field variables is either zero or constant.

By examining the displacement profiles this hypothesis can be further examined.

Perturbation theory will used to evaluate the mass sensitivity of a FPW device operating in a gas phase. It will also be shown that a FPW structure is well suited to liquid media sensing applications provided that the phase velocity of the primary $A_0$ mode is below that of the compressional velocity of the liquid environment. A more in-depth discussion on the use of a FPW device in a liquid environment will be presented in Chapter 6. Potential methods to increase the mass sensitivity of a FPW device will also be discussed.

### 4.3.1 Displacement Profiles and Mode Identification

It was found in Chapter 3 that a FPW structure can theoretically support an infinite number of piezoelectrically coupled Lamb modes. Although the $A_0$ and $S_0$ modes can be determined by their finite phase velocity as the thickness of the structure decreases, Figure 3.4, it becomes increasingly difficult to identify other modes by solely considering the dispersion characteristic. For FPW structures comprised of a single isotropic layer the task is relatively straightforward, but with the inclusion of alternative materials within the layer stack the task becomes significantly more difficult. This section investigates the particle displacement profiles of a FPW device, highlighting the difference between structures comprised of isotropic and anisotropic materials. A general rule will be developed to allow simple mode identification in conjunction with the dispersion characteristics when considering the displacement about the cutoff point of the higher order modes. By identifying the modes about this point, an iterative algorithm can be used to track a particular mode to a given operating point. With the aid of the surface displacement profiles recommendations will be given on appropriate modes for mass sensing applications. However, this does not mean that a FPW structure is strictly limited to sensing applications. Due to the surface particle motions, these types of structures have been successfully applied as micropumps and fluid mixers in biomedical applications [115].

Recall that for a FPW structure eight partial modes are present. As previously discussed, under free electrical and mechanical surface conditions, the normal stress and charge components are zero. Therefore, to obtain the displacement at the upper and

lower surfaces of the structure, the Green's function is rewritten as:

$$\begin{bmatrix} \boldsymbol{\sigma}_{\mathbf{u}} \\ \gamma_u \\ \boldsymbol{\sigma}_{\mathbf{l}} \\ \gamma_l \end{bmatrix} = \begin{bmatrix} \mathrm{K}_{11}^{\mathrm{f}} & \mathrm{K}_{11}^{\mathrm{fe}} & \mathrm{K}_{12}^{\mathrm{f}} & \mathrm{K}_{12}^{\mathrm{fe}} \\ -\mathrm{K}_{11}^{\mathrm{ef}} & \theta + K_{11}^{e} & -\mathrm{K}_{12}^{\mathrm{ef}} & -K_{12}^{e} \\ \mathrm{K}_{21}^{\mathrm{f}} & \mathrm{K}_{21}^{\mathrm{fe}} & \mathrm{K}_{22}^{\mathrm{f}} & \mathrm{K}_{22}^{\mathrm{fe}} \\ \mathrm{K}_{21}^{\mathrm{ef}} & K_{21}^{e} & \mathrm{K}_{22}^{\mathrm{ef}} & K_{22}^{e} - \theta \end{bmatrix} \begin{bmatrix} \mathbf{u}_{\mathbf{u}} \\ \varphi_u \\ \mathbf{u}_{\mathbf{l}} \\ \varphi_l \end{bmatrix} \tag{4.17}$$

At the device surface the components on the left side of equation 4.17 are set to zero and the mode of interest identified via a boundary determinant scan. The resulting eigenvector matrix describes the stress and displacement components of the eight partial modes which is of interest for evaluating the particle displacement profiles. The components of seven partial modes are normalised to the eighth which allows the relative stress and displacement at the upper and lower surfaces to be evaluated.

Once the displacement at the surfaces of the structure has been calculated, their respective values within the structure can be evaluated by considering the state vector $\boldsymbol{\zeta}$, equation 4.4b, which describes the individual fields by their respective values at the interface $(z + h)$. To determine the complete internal particle displacements, it is necessary to divide the physical layers into $n$ virtual layers. There is no apparent limit on the layer divisions, however a too fine segregation will greatly affect the computation time. For the multilayered FPW structure presented, the lower $2.0$µm Si layer can be split into a further $20$ individual layers, all consisting of the same material properties. From the application of the recursive stiffness matrix equation, equation 4.10, the global stiffness matrix is identical, however now the fields can be described in terms of the interfaces of the newly created $n$ layers via the application of:

$$\mathbf{U_{m-1}} = \left(K_{11}^{m} - K_{22}^{M}\right)^{-1} K_{21}^{M} \mathbf{U_u} - \left(K_{11}^{m} - K_{22}^{M}\right)^{-1} K_{12} \mathbf{U_m} \tag{4.18a}$$

$$\mathbf{T_{m-1}} = K_{22}^{M} \mathbf{U_m} + K_{21}^{M} \mathbf{U_u} \tag{4.18b}$$

Note that the terms in equations 4.18a and 4.18b are in a different order to those in [87] to allow the profiles to be generated from the lower to upper surface.

Dividing a physical layer into $n$ individual virtual layers requires the stiffness matrix to be recalculated for the remaining components of the layer. As an example for the Si layer, when considering the $10$th virtual layer, it would be necessary to calculate the stiffness matrix for the below $10$ layers as well as the $10$ above. Once this has been per-

formed, the global stiffness matrix is calculated by applying the recursive algorithm, equation 4.10, for all other physical layers.

To determine the internal particle displacement profiles, the propagating wavenumber is set and a boundary determinant scan performed to determine the operating frequency of a particular mode. Once the operating frequency has been obtained, the relative displacement at the interfacial surfaces is calculated followed by the displacement and normal stress throughout the structure by the continual application of equation 4.18a and 4.18b. Figure 4.4 presents the displacement profile for the first antisymmetric mode. The displacement profiles have been normalised to the maximum displacement in the propagation direction, $x$. The mid-plane of the structure and the upper surface is located at a normalised structure thickness of $0.5$ and $1$ respectively. Due to the limited interaction of the fields in the $y$-direction, where the normalised maximum displacement is approximately $13$ orders of magnitude less than that of the $x$, or longitudinal, component, the particle displacement for the primary $A_0$ can be thought of as only in the longitudinal and transverse directions. Individual layer boundaries have also been included on all displacement profiles to illustrate the derivative discontinuities caused by changes in material properties.

Analysis of Figure 4.4, although defined as an antisymmetric mode, shows that the transverse displacement profile is not symmetrical about the centre of the structure. This discrepancy is caused by the inclusion of different materials within the layer stack. If a structure comprised of a single isotropic material is considered, such as silicon, then the profile is indeed symmetrical. However, under such conditions to successfully excite an acoustic wave, it would be necessary to use an externally coupled transducer which is typically the case in NDE rather than sensing applications. The antisymmetric mode can be seen to consist of both transverse and longitudinal components, however the transverse component is dominant. For small thickness-wavelength ratios, the longitudinal component can be seen to be a factor of $2/k_x h$ smaller than that of the transverse component [24]. The longitudinal component undergoes a change in direction between the free surfaces of the structure and is a maximum at the external faces. Particle displacement also approaches zero at the median of the structure. Again, as the device under consideration is a multilayered structure, the displacement is not exactly

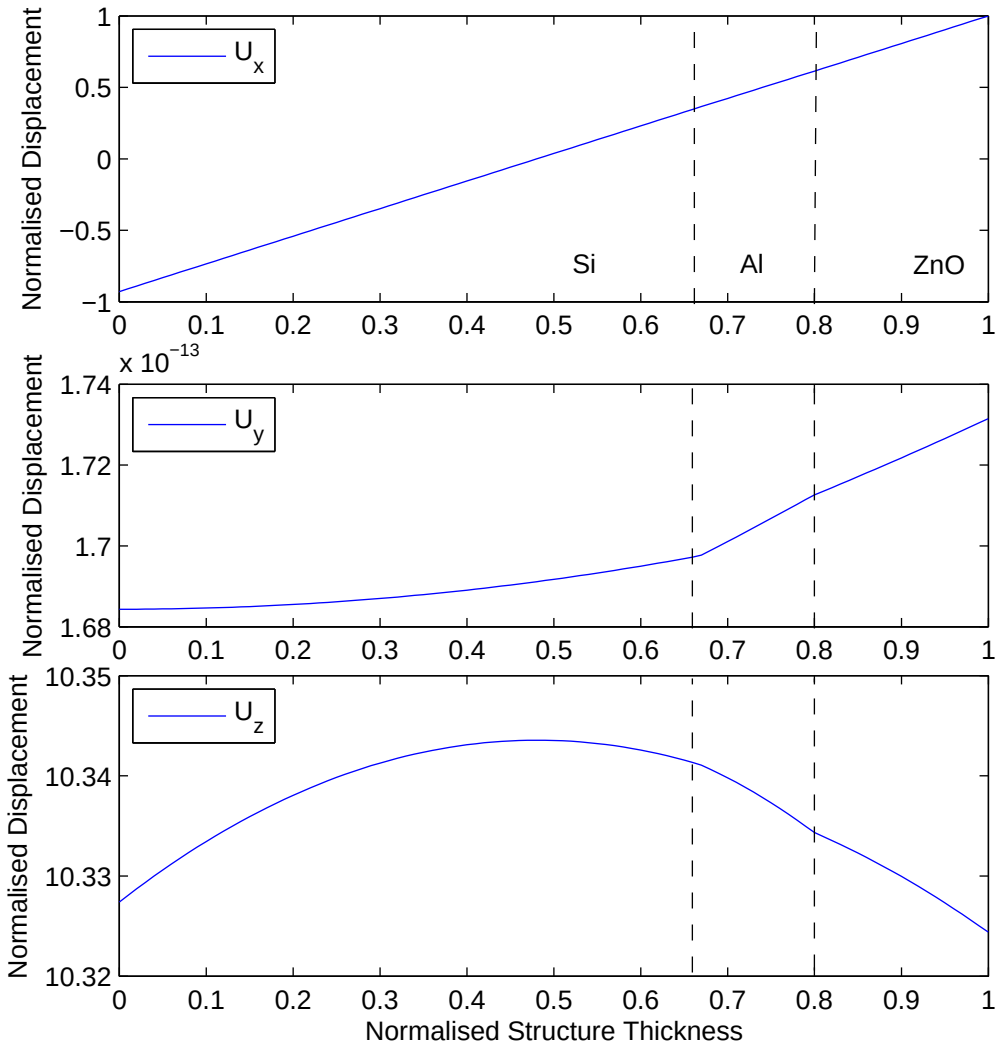


Figure 4.4: Primary Antisymmetric Mode Displacement Profile

zero at the mid-plane.

For a device consisting of a single isotropic layer the transverse component should be constant throughout the device. In the presented multilayered structure this is not the case, however the variation is insignificant. Derivative discontinuities can be seen at the various layer interfaces indicating a change in normal stress at these locations. For the structure presented, the interfaces correspond to a normalised thickness of $0.66$ and $0.80$ for the Si-Al and Al-ZnO layers respectively. It can also be seen that in the multilayered structure the maximum transverse displacement is at the mid-plane of the device. Due to its dominant transverse component, the primary $A_0$ mode is well suited to mass sensing applications in both gas and liquid mediums. A further restric-

tion is placed upon the use of a FPW structure in a liquid environment as the phase velocity of $A_0$ should be below the compressional velocity of the liquid to minimise the loss of acoustic energy into the surrounding environment. For the FPW structure presented, the transverse displacement is virtually identical at either external interface and thus one, or both sides of the structure, could be used for mass sensing applications. However, in potentially corrosive environments it is beneficial to protect the IDTs and piezoelectric layer from the target analyte. This is typically achieved by depositing a passivation layer such as $SiO_2$.

Once the displacement profiles have been established, equation 4.18b can be used to determine the normal stress profile within the structure, Figure 4.5. As stress is related to the change in longitudinal and transverse displacement with respect to a given point, a large variation in displacement will cause a corresponding large change in stress. Considering the mid-plane of the structure, the stress component $T_{xz}$ is a maximum as the phase of the displacement profile changes and is generally parabolic in nature. The derivative discontinuities in the upper half of the structure are caused by the layer change from Si to Al and then finally to ZnO. The normalised transverse stress component, $T_{zz}$, is quite small as the displacement profile is relatively consistent throughout the layers.

Conversely, Figure 4.6 presents the displacement profile for the first symmetric mode. Similar to the antisymmetric mode, the $y$-component is $15$ orders of magnitude smaller than the longitudinal component and hence can be disregarded. For the symmetric mode the longitudinal motion dominates and is relatively constant throughout the structure. The maximum longitudinal displacement for both primary modes are approximately equal. In comparison to the antisymmetric mode, the symmetric longitudinal displacement does not undergo a change in particle direction between the upper and lower surfaces. In a FPW device comprised of a single isotropic layer, the longitudinal displacement should be the same at all points within the structure, however as discussed for the antisymmetric mode, the inclusion of alternative materials slightly alters the particle profile. The displacement in the transverse direction is also seen to be significantly smaller than that of the longitudinal direction. According to [24] this is caused by the Poisson effect which reduces the displacement by a factor

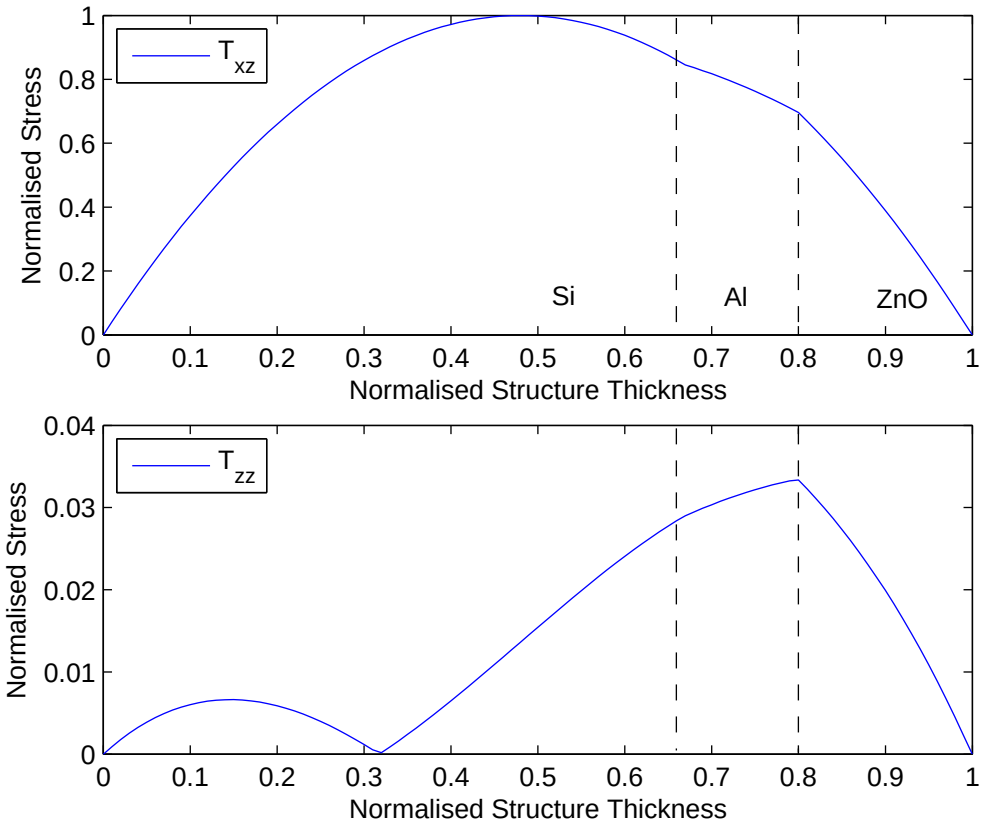


Figure 4.5: Primary Antisymmetric Mode Normal Stress Profile

of $2/k_{tl}h$. Unlike the transverse component of the antisymmetric mode, the symmetric mode component undergoes a change of direction between the upper and lower surfaces of the structure and is approximately zero at the mid-plane of the device. The normal stress profiles for primary symmetric mode appear in Figure 4.7. A maximum in the normalised longitudinal stress component appears at the Si-Al interface, whereas for the transverse component it can be found between the Al and ZnO layers.

As the displacement profiles have been evaluated for the primary $A_0$ and $S_0$ modes a simple selection process can be established to identify the modes when performing a boundary determinant scan rather than relying solely on the phase velocity characteristic. If a change in particle direction is present in the longitudinal component and a minimum occurs at some point within the structure, then an antisymmetric mode has been identified. Alternatively, if the sign of the longitudinal component is the same at the FPW external interfaces, then a symmetrical mode has been found.

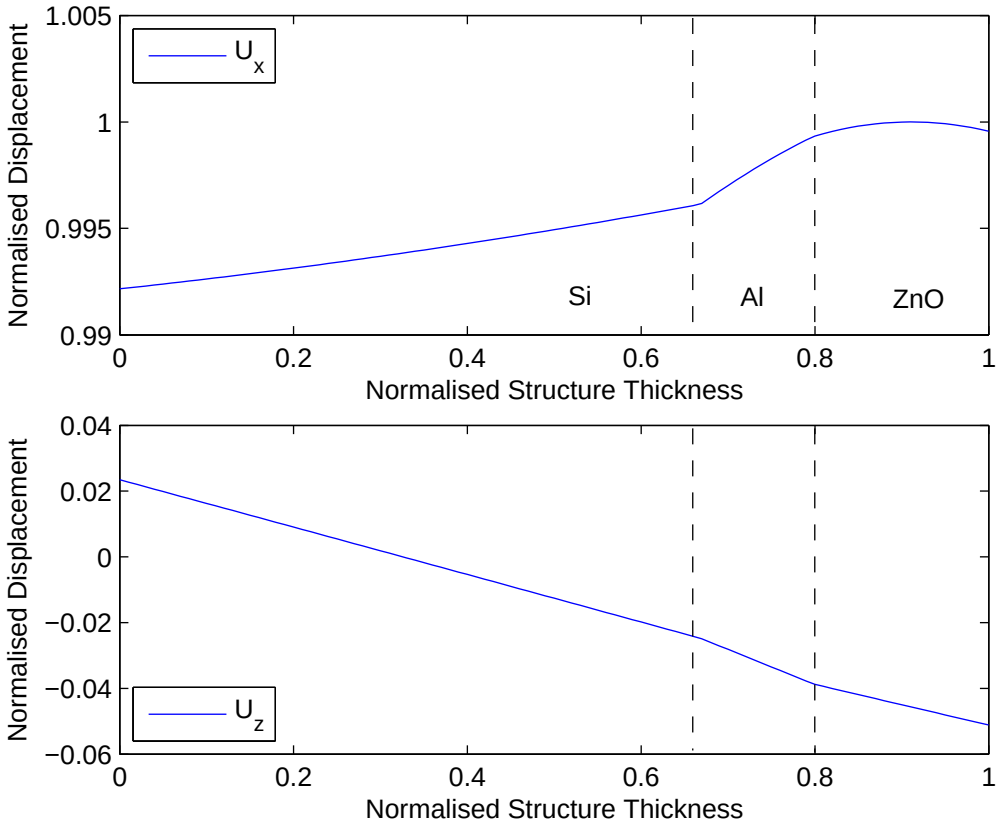


Figure 4.6: Primary Symmetric Mode Displacement Profile

As the thickness of the FPW structure increases it becomes increasingly difficult to correctly identify the higher order modes due to the complex nature of the particle displacements. One viable solution is to identify the normalised cutoff thickness and velocity for a particular mode from the dispersion characteristics, Figure 3.4, and then use this information in conjunction with the displacement profiles to confirm the family of a given mode. Once a mode has been identified as either antisymmetric or symmetric, it can then be tracked to any other value of normalised thickness of interest. A simulation was performed to evaluate the displacement profiles of the next two antisymmetric and symmetric modes to confirm whether these selected higher order modes conform to the selection criteria for the $A_0$ and $S_0$ modes. The FPW Si thickness was set at 22µm, 25µm, 46µm and 50µm to resolve $A_1$, $S_1$, $A_2$ and $S_2$ respectively, Figure 4.8.

The particle displacement profiles have been normalised to their respective maximum values of displacement in the longitudinal direction. With the Si thickness set to the

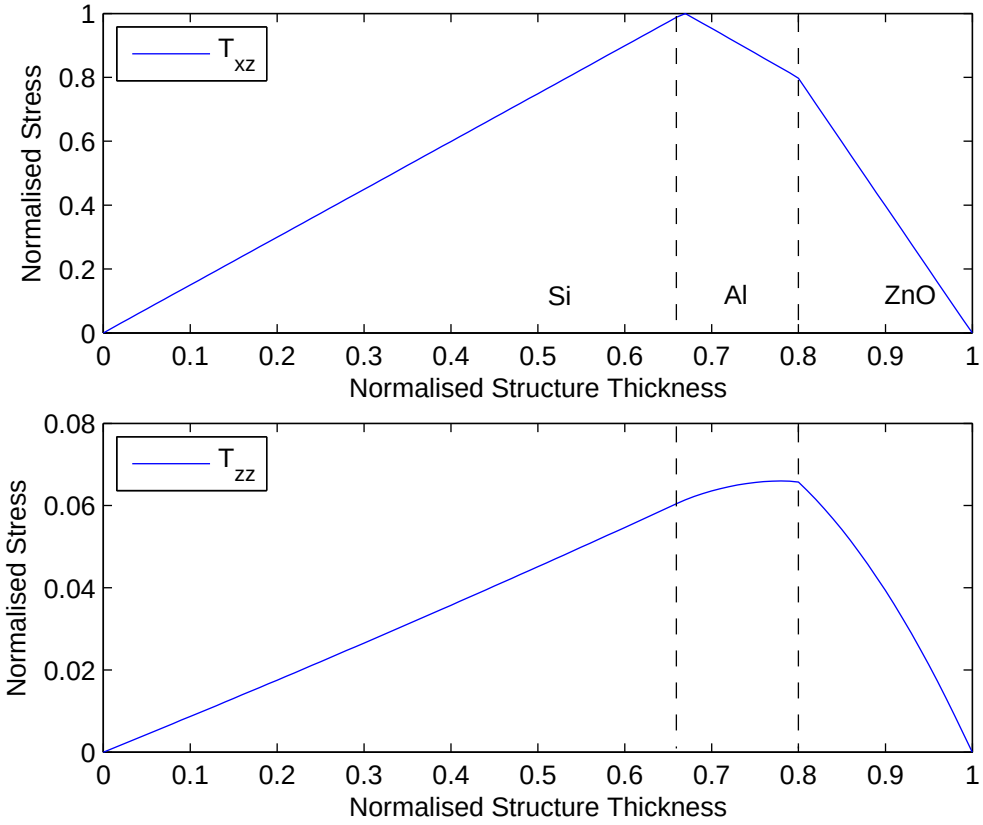


Figure 4.7: Primary Symmetric Mode Normal Stress Profile

modes respective cutoff values, it appears that the antisymmetric modes adhere to same selection criteria used for $A_0$. That is, a change in particle direction is present between the upper and lower surfaces in the longitudinal component, whilst the transverse component motion is in the same direction at the external interfaces. As expected, as the order of the mode increases, an increase in the number of oscillations within the structure can be seen. This also implies that for identification purposes of the higher order modes particle displacements at the surfaces should be used, rather than searching for a local maximum at the mid-plane of the structure.

For the symmetric modes, it also appears that the basic selection criteria can also still be used. When considering $S_0$, the transverse displacement is significantly less than the longitudinal component, however this is shown not to be the case for the higher order symmetric modes. Again, examining the particle displacement at the external interfaces appear to be the most appropriate method of identification. Therefore, if the direction of the particle motion of the longitudinal component is consistent at the

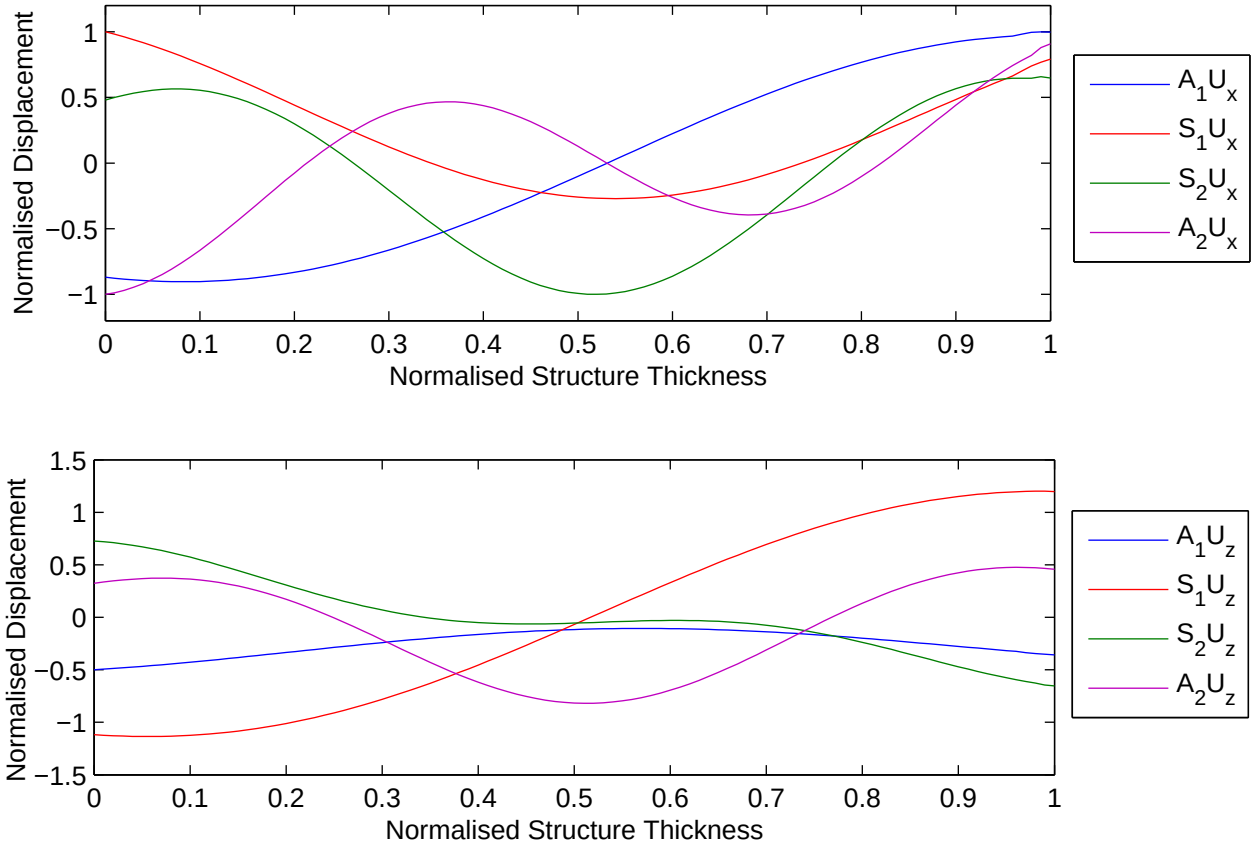


Figure 4.8: Higher Order Mode Displacement Profiles

interfaces and a change found for the transverse component, then a symmetric mode is determined.

In terms of mass sensing applications, to be discussed further in Section 4.3.2, displacement at the external interfaces is of interest. Table 4.2 lists the normalised displacements for the first six modes in the transverse and longitudinal directions. To allow the displacement of the various modes to be compared, the calculated values are normalised to the power flow per unit width of the lowest order family modes. The components have also been normalised to the longitudinal displacement of $A_0$ or $S_0$ at the lower surface and group in their respective mode families. As usual, the upper surface is the top piezoelectric layer and the lower the Si layer. A negative sign indicates a change in direction between the upper and lower surfaces. Although it has been shown that alternative materials within the FPW layer stack cause the modes to

be no longer purely antisymmetric or symmetrical, the variation for at least the first two primary modes is insignificant.

Table 4.2: Normalised Surface Particle Displacement Profiles

| Mode | $U_{xu}$ | $U_{xl}$ | $U_{zu}$ | $U_{zl}$ |
|---|---|---|---|---|
| $A_0$ | $1$ | $-1.08 \times 10^{0}$ | $1.03 \times 10^{1}$ | $1.03 \times 10^{1}$ |
| $A_1$ | $1.63 \times 10^{-3}$ | $-1.78 \times 10^{-3}$ | $-7.84 \times 10^{-4}$ | $-6.14 \times 10^{-4}$ |
| $A_2$ | $1.06 \times 10^{-3}$ | $-9.62 \times 10^{-4}$ | $3.44 \times 10^{-4}$ | $4.84 \times 10^{-4}$ |
| $S_0$ | $1$ | $1.01 \times 10^{0}$ | $-2.37 \times 10^{-2}$ | $5.19 \times 10^{-2}$ |
| $S_1$ | $5.19 \times 10^{-3}$ | $4.11 \times 10^{-3}$ | $5.80 \times 10^{-3}$ | $-6.22 \times 10^{-3}$ |
| $S_2$ | $1.27 \times 10^{-3}$ | $1.71 \times 10^{-3}$ | $1.92 \times 10^{-3}$ | $-1.73 \times 10^{-3}$ |

Examining Table 4.2, the $A_0$ transverse displacement is virtually identical at the upper and lower surfaces. Therefore, either side of the structure could be potentially used for mass sensing applications. As the order of the antisymmetric mode increases, the maximum displacement shifts between the upper and lower surfaces. If a symmetric mode was of interest, then from the surface displacements, it would be advisable to use lower order modes as the displacement is significantly larger.

When the thickness-wavelength ratio is greater than unity, the primary $A_0$ and $S_0$ modes approach the Rayleigh velocity and as previously discussed behave as two decoupled acoustic waves propagating on both surfaces of the structure. To investigate this phenomenon the Si thickness of the presented FPW device was increased to approximately $400$µm, whilst keeping all other layers constant. Under these conditions, the $A_0$ and $S_0$ phase velocities have not fully converged to the Rayleigh velocity and two different solutions, albeit very close, have been resolved. The displacement profiles for this condition appear in Figure 4.9. The particle displacement for the transverse component appears to penetrate to a normalised thickness of $0.4$, corresponding to a physical depth of $160$µm. This is consistent with SAW theory in that the acoustic energy is confined to between one and two wavelengths from the surface [2]. The longitudinal component indicates that the particle displacements are in opposite directions on the surfaces of the structure.

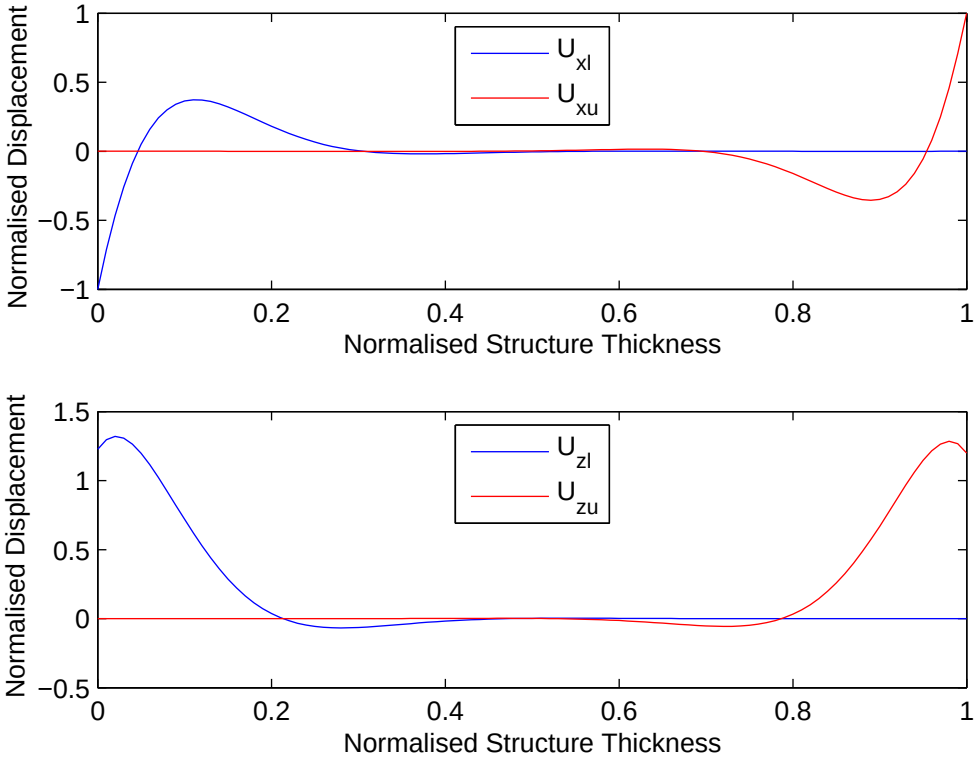


Figure 4.9: FPW Device Mode Decoupling

### 4.3.2 Mass Sensitivity

This section examines the use of a FPW device for mass sensing applications in the gas phase. The performance of a multilayered FPW structure is compared against a commercially available SAW device and an equivalent thickness FPW device comprised of a single isotropic layer. A brief review of the sensing mechanism and assumptions for modelling an added mass on the surface of the device is also discussed. The evaluation of a FPW for liquid sensing applications is reserved for Chapter 6.

As previously mentioned, a FPW structure can support an infinite number of propagating Lamb modes. This is advantageous in a sensing environment as any given mode can be selected and tuned for a particular application. For sensing applications in liquid media, the primary $A_0$ mode is of interest, however in the gas phase, either $A_0$ or $S_0$, or indeed any of the higher order modes, could be used. Depending on the measurement configuration, either or both primary modes could be used simultaneously.

To configure the FPW device as a sensor, a chemically active film is added to the

surface of the structure, Figure 4.10. The active film is designed to attract and capture specific molecules on the surface of the device thereby increasing the mass on the sensitive area of the structure. The effects of the chemically active film can also be modelled as an additional layer within the overall stack, provided that it can be described in terms of stiffness, density, permittivity and piezoelectric properties. However, many of the currently applied thin films are polymer based and as such the damping effect on the propagating wave must also be determined.

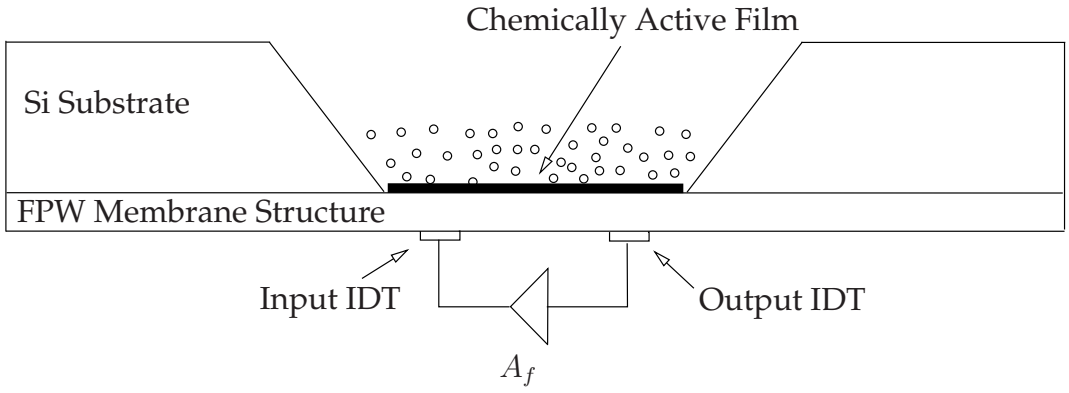


Figure 4.10: Mass Sensor Configuration

The system pictured in Figure 4.10 is configured for resonant frequency measurements, where an amplifier, $A_f$, is employed to ensure that the closed loop gain is greater than unity. If the primary $A_0$ mode was of interest, a low pass filter could be included to ensure that on startup that this was the only mode excited. Note that the frequency at which the device would oscillate is dependent on the period of the IDTs which is discussed in Section 4.4. Utilising this configuration, once exposed to a target analyte, the frequency of oscillation will vary based on the concentration and hence applied mass. Via a frequency counter this deviation can be evaluated and a measurement of target gas concentration can be determined. For the relatively low frequencies of a FPW structure, this method is typically used as the required electronics are quite inexpensive. An alternative technique, based on the direct measurement of the phase difference between the applied and received acoustic wave can also be used. Here a fixed frequency is applied to the input IDT and the corresponding output detected with a vector voltmeter. Although a simplistic technique this approach requires significantly more support equipment and hence is typically not used in sensing ap-

plications [116]. Depending on the approach taken, the sensitivity of the FPW will be different. In this study, the resonant frequency measurement technique of Figure 4.10 will be used.

The mass sensitivity of a FPW device is based upon the Rayleigh hypothesis [117], where it is assumed that the added mass layer is infinitesimally thin and the effect of its elasticity is negligible. Furthermore, it is assumed that the perturbing mass layer does not significantly alter the distribution of the acoustic wave within the structure. This can be confirmed by examining the displacement profiles described in Section 4.3.1. For a FPW device, which by nature is quite thin, this may not strictly be the case.

When configured in a feedback element in an oscillator system, mass sensitivity is defined as [118]:

$$S_m^f = \frac{1}{f_0} \lim_{\Delta m_s \to 0} \frac{\Delta f}{\Delta m_s} \quad \left(cm^2/g\right), \tag{4.19}$$

where $m_s$ is the applied mass per unit area and $f_0$ is the unperturbed resonant frequency. The term $\Delta f$ is the change in frequency due to the change in applied mass, $\Delta m_s$. The subscripts $f$ indicates that the FPW structure is configured for frequency measurements.

A simple conversion can be applied to determine the mass sensitivity of a FPW structure when configured for phase velocity measurements:

$$S_m^v = \frac{v_p}{v_g} S_m^f \tag{4.20a}$$

$$v_g = \frac{d\omega}{dk} \tag{4.20b}$$

The term $v_g$ in equation 4.20a is known as the group velocity. It is defined as the change in angular frequency due to the change in wavenumber and can be numerically evaluated by considering the gradient of the dispersion characteristic at the device wavelength. The group and phase velocities must clearly be recalculated for every mode of interest. The subscript $v$ indicates that FPW structure is configured for phase velocity measurements.

For a FPW device consisting of a single isotropic layer, the mass sensitivity can be determined by analytical means. If the primary $A_0$ mode is considered and the FPW structure acoustically thin, then only the transverse displacement component is

present. Under this assumption, the mass sensitivity can be written as [14]:

$$S^f_{A0m} = \frac{-1}{2\rho d}, \tag{4.21}$$

where $d$ represents the half thickness of the FPW structure. The negative sign indicates that the added mass causes a reduction in resonant frequency. In the case of the $S_0$ mode, the mass sensitivity is twice that of equation 4.21 due to the symmetry of the structure [40].

However, from Table 4.2 it can be seen that for the presented FPW structure, displacement components exist in the transverse and longitudinal direction making the assumptions for formulating equation 4.21 invalid. To determine the mass sensitivity of a multilayered FPW structure all surface displacement components must be considered. An alternative method to evaluate the mass sensitivity of an FPW structure is to model the effect of an additional acoustically thin isotropic layer. The added mass layer must be sufficiently small as that it does not greatly affect the acoustic displacement profile. A recent study [21], found this approach to be suitable for evaluating the mass sensitivity of a SAW structure. In this study, a fictional mass layer with a thickness of $1 \times 10^{-12}$m was added to the structure and the corresponding shift in resonant frequency determined. In terms of computational efficiency, this method is advantageous as the simulated mass layer can simply be added to the overall layer stack and the sensitivity easily determined. However, this technique can not be used to determine the mass sensitivity using the FEM described in Chapter 5. This is primarily due to the small dimension of the mass layer causing elemental mesh inconsistencies in the FEM software. Therefore, the perturbation method approach, where it is assumed that the added mass is infinitesimally small, will be adopted to determine the mass sensitivity of a FPW device.

Using perturbation theory, the mass sensitivity for a FPW device operating in resonant frequency mode can be described by [117]:

$$S^f_m = \frac{-1}{4U_a}\left[\left(1 - \frac{c^p_{44}/\rho_p}{v^2_p}\right)|v_x|^2 + |v_y|^2 + \left(1 - \frac{c^p_{44}\left(3c^p_{11} - 4c^p_{44}\right)}{\rho_p\left(c^p_{11} - c^p_{44}\right)v^2_p}\right)|v_z|^2\right] \tag{4.22a}$$

$$U_a = \int_0^{h_1} U^1_{av}\, dz + \int_{h_1}^{h_2} U^2_{av}\, dz + \int_{h_2}^{h_3} U^3_{av}\, dz \tag{4.22b}$$

$$U^i_{av} = \frac{\rho_i}{2}\sum_j |\mathbf{v}_j(z)|^2, \tag{4.22c}$$

where $U_a$ is the area density of the average stored energy in the structure, $\rho_p$ is the density of the added perturbing layer, $c^p$ represents the material stiffness coefficients of the added mass layer and the subscript $i$ indicates the layer under consideration. Note in equation 4.22b, the area density of the average stored energy is calculated for each individual layer as indicated by the integration limits, which specify the start and end $z$-coordinate of the layer under consideration.

If the added layer is soft, that is the phase of the added perturbing layer is significantly lower than that of the device, then equation 4.22a can be simplified to:

$$S_m^f = \frac{(|v_x|^2 + |v_y|^2 + |v_z|^2)}{4U_a} \tag{4.23}$$

The mass sensitivity can be seen to be highly dependent on the surface velocity of the structure. Therefore, for maximum mass sensitivity, a mode should be selected with the largest surface velocity profile for a fixed total power flow.

Due to the physical construction of a FPW device, the added mass can be applied to either the upper or lower surface. In harsh environments it is advantageous to isolate the delicate IDTs to prevent damage to the device. For the $A_0$ mode, there is insignificant variation in the mass sensitivity when shifting the mass layer between the upper and lower. Conversely, a deviation of $-10$ cm$^2$/g was found for the $S_0$ mode.

Figure 4.11 depicts the mass sensitivity of primary $A_0$ and $S_0$ modes of the presented FPW structure as a function of Si thickness. The Al and ZnO layers were kept consistent at $0.4$µm and $0.6$µm respectively. For comparative purposes the theoretical sensitivity for a single layer Si structure of identical thickness is also included.

From Figure 4.11, it can be clearly seen that the mass sensitivity is inversely proportional to the overall structure thickness. Maximum mass sensitivity is achieved when the composite membrane thickness is at a minimum, however this will greatly depend on the fabrication constraints. If the FPW device is too thin and thus fragile, it may not be suitable for environments where abrupt pressure or flow changes occur, causing the device to fracture. In terms of individual modes, the higher velocity $S_0$ mode appears to have a higher sensitivity than $A_0$ until the thickness of the structure reaches approximately $16$µm corresponding to a $S_0$ phase velocity of $7467$m/s.

An investigation was also performed on the next four higher order modes. The dispersion characteristic, Figure 3.4, indicates that the cutoff frequencies for these modes

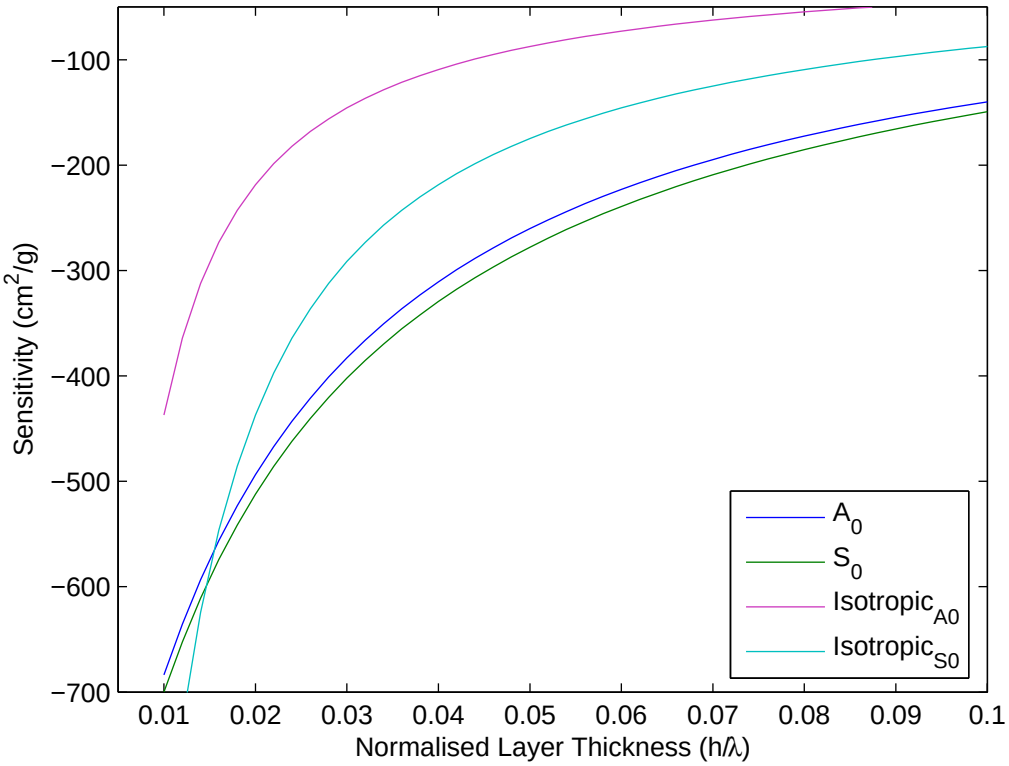


Figure 4.11: Mass Sensitivity

are quite high, which in a fabricated device would require more expensive signal processing electronics. The initial thickness of the structure was set at $40$µm and then systematically increased to $60$µm. Over this range, the third symmetrical mode, $S_2$, had the highest sensitivity at approximately $-68\text{cm}^2/\text{g}$ , whereas at the same thickness the sensitivity of the $A_0$ and $S_0$ modes is $-38$ and $-23\text{cm}^2/\text{g}$ respectively. Although having a potentially higher sensitivity, the increased velocity, which then leads to increased frequency, means that the device could not be used in liquid media sensing applications as the energy of the mode would radiate into the surrounding environment.

In comparison with SAW devices, the mass sensitivity of FPW devices is significantly larger, which in turn decreases the minimal detectable concentration. In [119] a FPW device with a centre frequency of $5.5$MHz was compared against a $250$MHz SAW used in a gas chromatograph system. With a sensitive layer, the minimum detectable methanol concentration using FPW device was $75$ppm, whilst that of the SAW structure was $535$ppm, corresponding to a $613\%$ increase. The FPW device was also

subjected to nitrous oxide and helium where in both cases the minimum detectable limit was below that of the SAW sensor.

A comparison was also performed against a device fabricated by the authors colleagues. Here a SAW device was fabricated on a lithium tantalate substrate with a ZnO intermediate layer. The mass sensitivity was determined as a function of guiding layer thickness. A maximum sensitivity of $-120$ cm$^2$/g was found at a thickness-wavelength ratio of $0.16$ corresponding to a ZnO thickness of approximately $3.2$µm. For the presented FPW device, the same sensitivity can be achieved in a structure with an overall Si thickness of $11.8$µm.

To increase the mass sensitivity of a SAW device, the operational frequency must be increased [8], whereas for a FPW structure, the thickness of the overall structure should be reduced. Although potentially making the device more difficult to handle, a reduction in device thickness also brings about a decrease in centre frequency and the requirements for the signal processing electronics. Another method to increase the mass sensitivity of a FPW device, by examining equation 4.23, is to increase the surface velocities. This can be achieved by using a higher velocity piezoelectric layer, which in turn increases the operational frequency of the device.

Recently, aluminium nitride has gained popularity as a suitable guiding layer for acoustic wave devices. It can be d.c. reactively sputtered from a pure aluminium target, or deposited in a r.f. sputtering system using an AlN target. Figure 4.12 represents the mass sensitivity for the FPW device presented as a function of Si thickness, with the exception of the ZnO layer being replaced with $0.6$µm of AlN. For comparative purposes, the sensitivity for the ZnO layer is included. Further discussion on the use of AlN as a piezoelectric layer will be discussed in Chapter 6.5.

From Figure 4.12 it can be seen that the AlN piezoelectric layer improves the sensitivity of the device, particularly in the low thickness limit. For the two primary modes, an increase in sensitivity of $97$ and $110$cm$^2$/g is shown for $A_0$ and $S_0$ respectively. Using identical layer thicknesses as the ZnO based device, the centre frequencies for $A_0$ and $S_0$ have increased to $4.7$ and $80.9$MHz respectively. In deriving the mass sensitivity, it is assumed that the added mass and sorptive layers are homogenous, which may not be the case for biosensing applications.

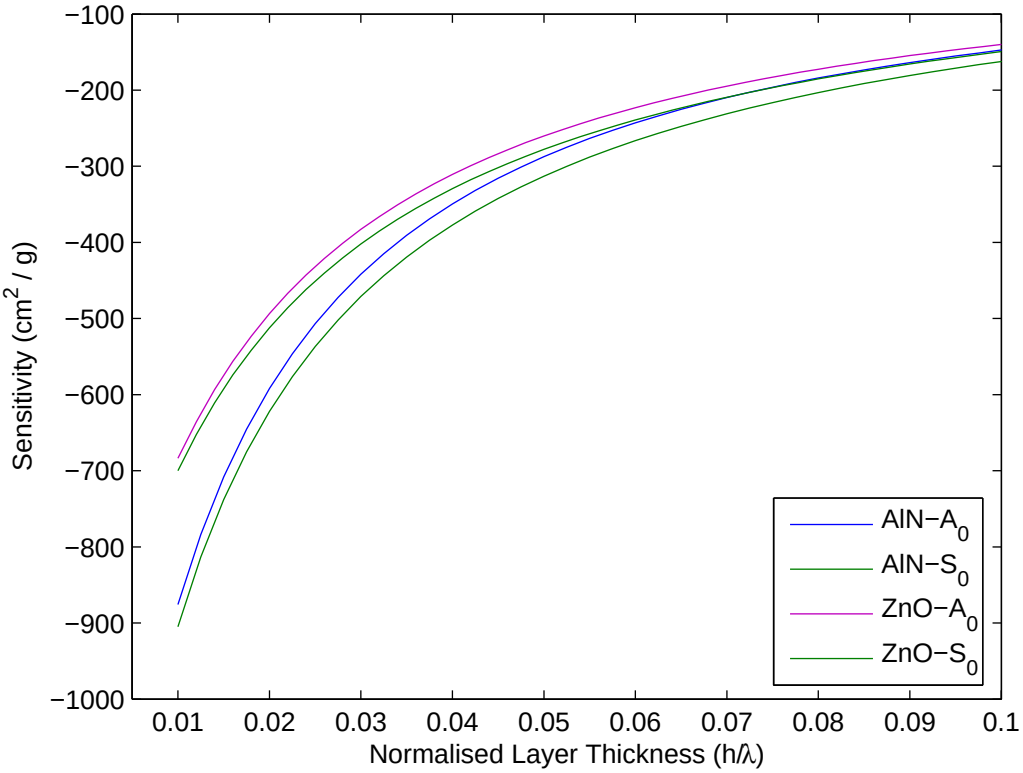


Figure 4.12: Mass Sensitivity - AlN and ZnO

## 4.4 Analysis of Interdigital Transducers

The analysis so far presented for a FPW device has not taken into consideration the generation and detection of acoustic waves. A multitude of techniques exist for exciting an acoustic wave, ranging from wedge bonded transducers used for NDE applications [24], non-contact laser excitation [33], magnetic excitation [30] and an array of differentially driven electrodes commonly referred to as interdigital transducers (IDTs) [120]. Each technique has its own advantages, however the application of any given process has been shown to affect the response spectra of the device. In a sensing environment, a cost effective, simple and low power approach is required. To that end, an analysis will be presented on the use of IDTs as an excitation source with a discussion on the frequency response spectra. The IDT electrodes are fabricated by the deposition a metallic layer and a selective pattern produced via a photolithographic process.

The technique reviewed here is developed for a finite number of electrodes allowing end effects to be closely examined, which can not be achieved with a periodic, or

infinite array, model [121]. Although the computation time is increased using the discussed method, for structures with a small number of electrodes, second order effects of which the Green's function approach takes into full account, may be significant. Although not discussed here, the technique employed can also be used to evaluate charge accumulation caused by grounded guard electrodes and acoustic end reflections[19]. Numerous techniques exist to determine the spectral characteristics of SAW devices [93, 94, 122], however not so for FPW devices. Many analogies can be drawn between the FPW and SAW device cases, with the main difference of a metalised ground plane inserted between the Si and piezoelectric ZnO layers.

To analyse the influence of the IDTs, a spectral domain Green's function is applied which considers the response due to a Dirac, or line source, excitation. The inclusion of the metallic plane also allows the problem dimension to be reduced. The metallic plane is electrically grounded, which implies that the effective permittivity of the structure can be calculated by considering only the upper piezoelectric layer and ground plane. In developing the spectral characteristics for the FPW structure, it is assumed that the IDTs are infinitely thin and conductive, neglecting the effects of electrode mechanical loading. In a FPW device where the IDT metallisation layer is comparable to the thickness of the composite layers, these effects can simply not be ignored. A recent discussion in [21] illustrates an approach to include electrode effects utilising a periodic model.

The following analysis is split into two sections. The first deals with the electrostatic problem, whilst the second considers the effect of the propagating wave on the response spectra. FPW device performance is evaluated in terms of admittance characteristics and then converted to the more commonly used insertion loss characteristics.

### 4.4.1 Spectral Domain Green's Function

A comprehensive discussion of the electrostatic spectral Green's functions appears in [19], however the essential details are reiterated here to highlight the differences in solution paths between this method and the novel technique developed by the author using the FEM in Chapter 5. Under the quasi-static approximation electrode interactions are ignored and it is assumed that no bulk modes are excited [93]. Similarly it is

assumed that the magnetic and electrical fields do not interact.

From analysis described previously in this chapter, the electrical components of the Green's function can be formulated to relate charge and voltage on both sides of a layered structure. When considering the properties of an IDT, the same concept can be used. If only the electrical conditions are considered, then the potential on the surface of a piezoelectric layer can be written as:

$$\Phi\left(x\right) = \int_{-\infty}^{+\infty} G\left(x - x^{'}\right) \sigma\left(x^{'}\right)\, dx^{'}, \tag{4.24}$$

where $G\left(x\right)$ represents the Green's function describing the problem and $\sigma$ is the charge. If the Green's function is split into two components, representing the electrostatic and surface wave solutions respectively, then it can be stated:

$$G\left(x\right) = G^{e}\left(x\right) + G^{FPW}\left(x\right) \tag{4.25a}$$

$$\Phi\left(x\right) = \Phi^{(1)}\left(x\right) + \Phi^{(2)}\left(x\right) \tag{4.25b}$$

$$\Phi^{(1)}\left(x\right) = \int_{-\infty}^{+\infty} G^{e}\left(x - x^{'}\right) \sigma\left(x^{'}\right)\, dx^{'} \tag{4.25c}$$

$$\Phi^{(2)}\left(x\right) = \int_{-\infty}^{+\infty} G^{FPW}\left(x - x^{'}\right) \sigma\left(x^{'}\right)\, dx^{'} \tag{4.25d}$$

The superscript in equation 4.25b indicates the equation component, rather than a mathematical operation. By inspection, equation 4.25c can be identified as convolution in the spatial domain. Recall that convolution in the spatial domain is identical to multiplication in the spectral domain [123]. For simplicity, equation 4.25c is therefore converted to the spectral domain, and written as:

$$\Phi^{(1)}\left(x\right) = \frac{1}{2\pi} \int_{-\infty}^{+\infty} \overline{G^{e}}\left(k_x\right) \overline{\sigma}\left(k_x\right) e^{-jk_x x}\, dk_x, \tag{4.26}$$

where the bar over the operators indicates the Fourier transform of the respective components. In most cases, the inverse Fourier transform of equation 4.26 can not be determined by analytical means, and hence must be evaluated numerically. To determine the solution to equation 4.26, a change of integrand is performed, which allows the Fourier transform of the metalised approximation electrostatic Green's function to be written in closed form as [19]:

$$\overline{G^{e}}\left(k_x\right) = \frac{1}{\varepsilon_0 |k_x|} \frac{1}{1 + \varepsilon_P \coth\left(\frac{\varepsilon_P}{\varepsilon_{33}} D |k_x|\right)}, \tag{4.27}$$

where

$$\varepsilon_P = \sqrt{\varepsilon_{11}\varepsilon_{33} - \varepsilon_{13}^2}, \tag{4.28}$$

and $D$ represents the thickness of the piezoelectric layer. If further layers were introduced it would be necessary to include their contribution in a similar method described in [124]. The change of integrand in equation 4.26 implies that the integration is performed across the unknown charge density rather than the electrostatic Green's function, equation 4.27.

Consider the section of a single electrode depicted in Figure 4.13. The electrode is split into $N$ strips of varying widths. About the electrode edges, more strips can be included to account for the logarithmic singularity at the electrode edge [125–127]. By subdividing the problem in a similar procedure to the FEM, the effect of each individual strip can be determined by the superposition theorem [128]. That is, a single electrode strip is considered to be a pulse source of charge in isolation, and the resulting potential determined on all other electrode strips within the array.

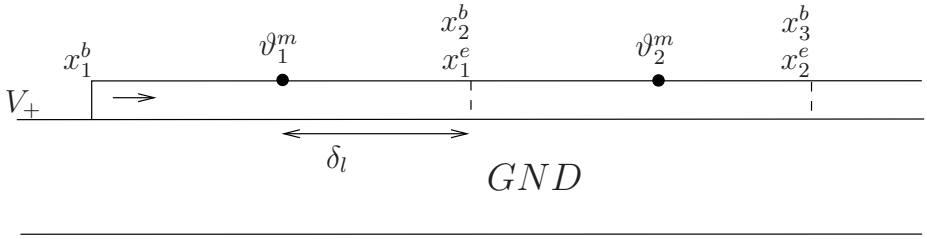


Figure 4.13: Electrode Subdivision

A known voltage is placed on the electrode strips, ensuring that all strips within one electrode have the same applied potential. For simplicity, typically $\pm 0.5$V is applied on alternating input electrode fingers, therefore defining the total potential difference $V_T$ as 1V. Floating electrodes can also be incorporated with their voltage determined by forcing the overall structure to be charge neutral [16]. The output electrodes are set at 0V to allow the short-circuit output current to be determined.

With reference to Figure 4.13, two important parameters are used, $\vartheta_l^m$ and $\delta_l$ which denote the mid-point and half the width of strip $l$ respectively. The start and end points of the electrode strip are given by $x_l^b$ and $x_l^e$ respectively. For a given electrode the end point of one strip, $x_l^e$ is identical to the start of the following, $x_{l+1}^b$. Employing pulse basis functions [19], the individual strip charges can be written as equation 4.29b, with

the spatial charge density given by equation 4.29c.

$$\sigma(x) = \sum_{l=1}^{N} \sigma_l P_l(x) \tag{4.29a}$$

$$q_l = \sigma_l \left(x_l^e - x_l^b\right) \tag{4.29b}$$

$$\sigma(x) = \sum_{l=1}^{N} q_l \frac{1}{\left(x_l^e - x_l^b\right)} P_l(x), \tag{4.29c}$$

where $P_l$ is a function of the electrode polarities. For the input electrodes, if a positive voltage is applied then $P_l$ has a value of $1$. Conversely, if a negative voltage is applied then $P_l$ assumes a value of $-1$. For the output electrodes, as the voltage is forced to zero, the polarity function depends on connection to the upper or lower bus-bar, corresponding to $1$ and $-1$ respectively. The term $q_l$ is the strip charge density integral.

The Fourier transform of equation 4.29c is taken and then substituted in equation 4.26, resulting in the spectral domain solution for the electrostatic charge density:

$$\Phi^{(1)}(x) = \sum_{l=1}^{N} q_l \frac{1}{\left(x_l^e - x_l^b\right)} \times \frac{1}{2\pi} \int_{-\infty}^{+\infty} \overline{G^e}(k_x) \frac{e^{jk_x\left(x_l^e - x\right)} - e^{jk_x\left(x_l^b - x\right)}}{jk_x} \tag{4.30}$$

The solution to equation 4.30 can be evaluated in terms of the unknown electrode strip charge densities $q_l$. Therefore, considering only the electrostatic component of the spectral domain Green's function, the solution in terms of the known voltage applied to the individual strips, is written as:

$$\varphi_k^{(1)} = \sum_{(l=1)}^{N} q_l I_{kl}^{(1)} \quad k = 1, 2, ..N, \tag{4.31}$$

where

$$I_{kl}^{(1)} = \frac{1}{\pi} \int_0^{+\infty} \overline{G^e}(k_x) \operatorname{sinc}(\delta_k k_x) \operatorname{sinc}(\delta_l k_x) \cos\left(k_x |\vartheta_k^m - \vartheta_l^m|\right) dk_x \tag{4.32}$$

$I_{kl}^{(1)}$ is symmetrical about $k_x = 0$ and therefore the integration limit has been changed. From a computational perspective it is not possible to integrate to infinity and hence an upper limit must be defined. In the results presented here, a linear integration space is taken consisting of $25,000$ points, between $k_x = 0.01$ and $k_x = 1 \times 10^7$.

An alternative device structure was used to determine the electrostatic characteristics of a FPW transducer to coincide with an attempted physical device fabricated by

the author. The simulated device consists of a $24$µm Si, $0.2$µm Au and $3.0$µm piezoelectric ZnO layers. The acoustic wavelength was fixed at $96$µm corresponding to theoretical centre frequencies for $A_0$ and $S_0$ of $28.5$ and $70.5$MHz respectively. For calculation of the admittance, an aperture of $200$µm was used. The simulated device consists of eight electrode pairs, with $8$ strips of equal width per electrode.

With reference to equation 4.32, the integral depends on the width of the source and observing strip and the distance between their centres, therefore for a regular array of electrodes a slight optimisation can be made. A routine was constructed that identified the unique combinations of $\delta_l$ and $\vartheta_l$ and only calculated the quasi-static spectral Green's function for these components. For the presented structure, equation 4.32 must be calculated $9,269$ times, whereas without the optimisations a total of $65,536$ points would need to be evaluated.

Figure 4.14 depicts the electrostatic charge density per unit area, for the aforementioned device designed by the author. The input electrode is located between $x = 0$ and $x = 7.455 \times 10^{-4}$ and the output between $x = 1.141 \times 10^{-3}$ and $x = 1.888 \times 10^{-3}$.

From Figure 4.14 it is quite difficult to identify the electrode end effects. This is primarily caused by the relatively small thickness of the ZnO piezoelectric layer. The method employed has assumed that the charge density is constant in the $y$-direction, which will be shown not to be precisely the case in Chapter 5. In many cases where the electrode width is several multiples of the acoustic wavelength, the variation in $y$ can be safely ignored [129]. A small charge exists on the output electrodes due to the voltage applied across the input electrodes. This is commonly referred to as electromagnetic feedthrough and can be considered to be a capacitive coupling between the input and output electrodes. It is a quite important parameter as its influence can significantly degrade the frequency response characteristics of the FPW device. It will discussed in further detail in Section 5.3.2.

The transducer static capacitance, which forms part of the overall admittance characteristic, is determined by equation 4.33. Using the lumped and ground capacitance model [130], this value can be used to quantify the electromagnetic feedthrough between the input and output IDTs. The technique is not applied here but will be evaluated using the FEM in Chapter 5. Note that as a pulse basis function was used, it is

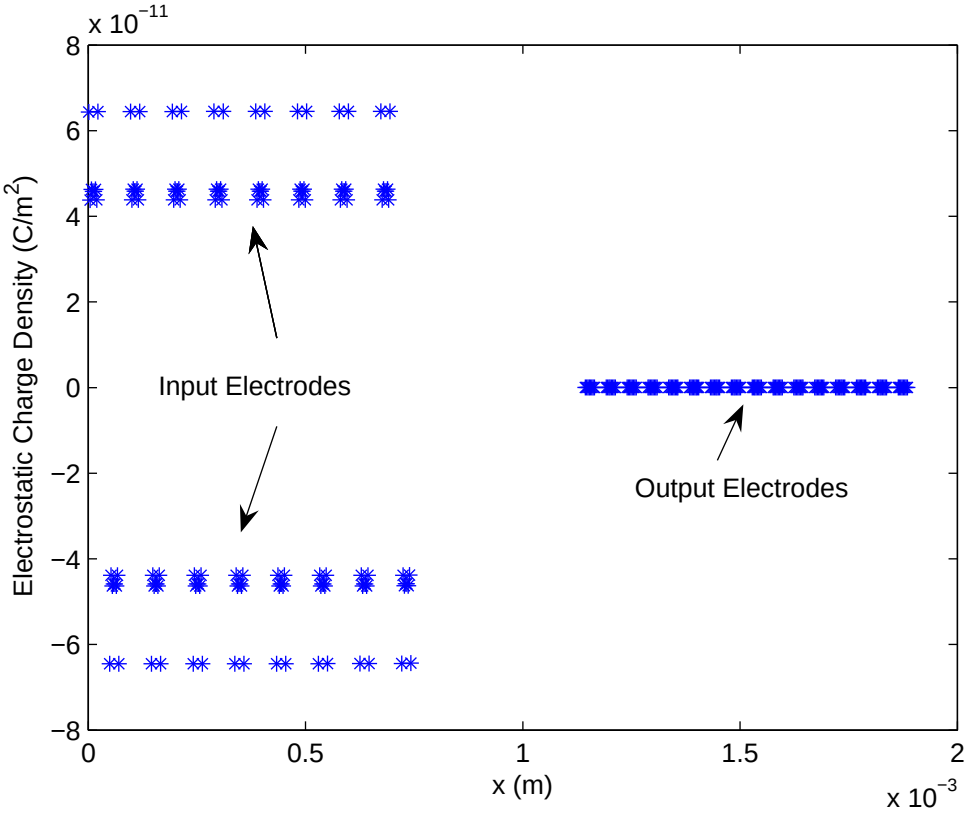


Figure 4.14: Electrostatic Charge Density

necessary to divide the obtained charge density integral by the individual strip widths to obtain the effective charge density, $\sigma_l$.

$$C_T = \frac{1}{2} W \int_{-\infty}^{+\infty} P_l(x)\, \sigma_l^e(x)\; dx, \tag{4.33}$$

where $\sigma_l^e$ indicates the electrostatic component of the charge density and $W$ is the transducer aperture.

The contribution of the electrostatic Green's function only needs to be calculated once for a given transducer arrangement. In the following section, the surface wave component is evaluated therefore allowing the complete solution to equation 4.25b to be evaluated.

### 4.4.2 Green's Function Analysis of FPW Surface Wave Component

Conversely to SAW structures, the overall thickness of a FPW device should ideally be less than the acoustic wavelength. In calculating the electrostatic component of

the spectral domain Green's function the finite thickness of the piezoelectric layer has been accounted for. For a SAW device, the substrate is assumed to be semi-infinite and hence the surface wave component of the Green's function can is written as [131]:

$$G^{SAW}(x) = -jG_s e^{-jk_x|x|}, \tag{4.34}$$

The term $G_s$, in the case of a dominant Rayleigh wave, can be seen to be essentially $K^2/2$ multiplied by the inverse of the effective permittivity at zero velocity:

$$G_s \approx \frac{1}{\varepsilon_0 + \varepsilon_P} \frac{v_0 - v_m}{v_0} \tag{4.35}$$

The approximation in 4.35 assumes that there are no piezoelectrically coupled bulk modes, no leaky modes exist and a Rayleigh wave is the primary acoustic mode [93]. For a FPW device the approximation is invalid and thus term $G_s$ should be calculated from the surface-wave power flow [2]. The term $G_s$ is a measure of coupling of electrical sources to the piezoelectric eigenmode and can be determined from the residue of the pole of the spatial Green's function corresponding to the guided mode. In the case of a FPW structure this term must be calculated separately for the $A_0$ and $S_0$ modes. An alternative definition of $G_s$ is written as equation 4.36.

$$G_s^{FPW} = \frac{-1}{k_x} \left( \frac{\varepsilon_{eff}(k_+) - \varepsilon_{eff}(k_-)}{k_+ - k_-} \right), \tag{4.36}$$

where $k_+$ and $k_-$ represent slight positive and negative shifts in the operating wavenumber $k_x$. A comparison of calculated insertion loss characteristics between the SAW and FPW definitions of $G_s$ is presented later in this chapter.

A further assumption was made in determining the effective permittivity of the multilayered FPW structure. As the piezoelectric layer is bounded by an ideal metallic ground plane, no electric field, and hence no contribution to the effective permittivity, is given by the underlying Si layer. This allows the effective permittivity to be evaluated by considering only the upper piezoelectric and metallic layer. However, if only the upper layer is considered, the wavenumber term will be incorrect, as a change in structure thickness also causes a deviation in operating wavenumber. If the effective permittivity were to be evaluated at the overall structure wavenumber then a constant value would be obtained, rather than evaluation about the pole-zero pair expected. Therefore, the SAW modelling assumption was used, where the effective permittivity

was calculated by considering the piezoelectric layer to be a semi-infinite substrate. Excellent agreement in insertion loss characteristics has been obtained when making this assumption when comparing against the FE Method presented in Chapter 5.

Another key difference between the FPW and SAW device case is the number of solutions. For a Rayleigh mode SAW, only one solution is typically of interest, corresponding to a singular wavenumber term which varies with frequency. In a FPW device a minimum of two modes propagate along the structure, therefore by applying the superposition principle [128], the Green's function surface wave term is written as:

$$G_s^{FPW}(x) = -j\left(G_{s(A_0)}^{FPW} e^{-jk_{A_0}|x|} + G_{s(S_0)}^{FPW} e^{-jk_{S_0}|x|}\right), \tag{4.37}$$

Recall from equation 4.25b, the potential on the surface of the piezoelectric is the contribution to both electrostatic and surface wave components. Following the same process as the electrostatic component, the surface wave potential can be written as:

$$\varphi_k^{(2)} = \sum_{l=1}^{N} q_l I_{kl}^{(2)} \quad k = 1, 2, ..N, \tag{4.38}$$

where

$$I_{kl}^{(2)} = \begin{cases} -jG_s^{FPW} e^{-jk_0|\zeta_k^m - \zeta_l^m|} \text{sinc}\left(\delta_k k_0\right) \text{sinc}\left(\delta_l k_0\right) & \text{if } k \neq l, \\ \frac{G_s^{FPW}}{\delta_l k_0}\left[-1 + e^{-jk_0\delta_l} \text{sinc}\left(\delta_l k_0\right)\right] & \text{if } k = l, \end{cases} \tag{4.39a}$$

In formulating equation 4.38, only the forward propagating acoustic wave has been considered. Although in a physical device the output IDT will generate another acoustic wave travelling back towards the input electrodes via regeneration, the effects are relatively small and can be ignored [93].

Once the electrostatic and surface wave components have been calculated, the total charge density is determined via the solution of:

$$\varphi_k = \sum_{l=1}^{N} q_l \left(I_{kl}^{(1)} + I_{kl}^{(2)}\right) \quad k = 1, 2, ..N \tag{4.40}$$

The total transducer current can be obtained by summing the charge across the electrode surface and multiplying by the transducer aperture, equation 4.41 [94]. For consistency with SAW device techniques, the charge is evaluated across the even input electrodes. In most cases, the input electrodes are identical, and thus the overall current can be determined by doubling the calculated current. The same process can also

be applied on the output electrodes, which will provide the short-circuit current used as a basis for the frequency response characteristics.

$$I_{TX} = j\omega W \sum_{-\infty}^{+\infty} \sigma_{TX} \tag{4.41a}$$

$$I_{RX} = j\omega W \sum_{-\infty}^{+\infty} \sigma_{RX}, \tag{4.41b}$$

where $TX$ and $RX$ represent the transmitting and receiving IDTs respectively. If the input and output IDTs are physically identical, then the admittance characteristics of the FPW device can be described as:

$$Y_{11} = Y_{22} = \frac{I_{TX}}{V_T} \tag{4.42a}$$

$$Y_{12} = Y_{21} = \frac{I_{RX}}{V_T}, \tag{4.42b}$$

with the individual components of the admittance characteristic defined as:

$$Y_{xy}(\omega) = G_a(\omega) + jB_a(\omega) + j\omega C_T, \tag{4.43}$$

where $G_a$ represents the radiation conductance and $B_a$ the susceptance. The susceptance component, $B_a(\omega)$ can be evaluated as the imaginary component of the admittance as the capacitive term can be subtracted by the application of equation 4.33. These terms can be used to create a matching network for maximum power transfer.

### 4.4.3 Frequency Response of FPW Devices

The device admittance characteristics are usually converted to the more commonly used four-port scattering parameters [1, 128]. Of particular interest is $S_{21}$, which is termed the forward transmission coefficient. If the magnitude of $S_{21}$ is taken, then the insertion loss characteristics can be obtained. Figure 4.15 illustrates the insertion loss characteristics for the presented device under an assumed load termination of $50\Omega$. A comparison between the SAW approximation for $G_s$ and the direct calculation from the effective permittivity has also been included.

From Figure 4.15, it can be seen that the two primary $A_0$ and $S_0$ have been resolved at the correct frequencies. The most noticeable difference between the two implementations of $G_s$ is the deviation in insertion loss characteristics at the primary mode centre frequencies. Using the FPW formulation, the insertion loss is $-51.1$ and $-44.21$dB

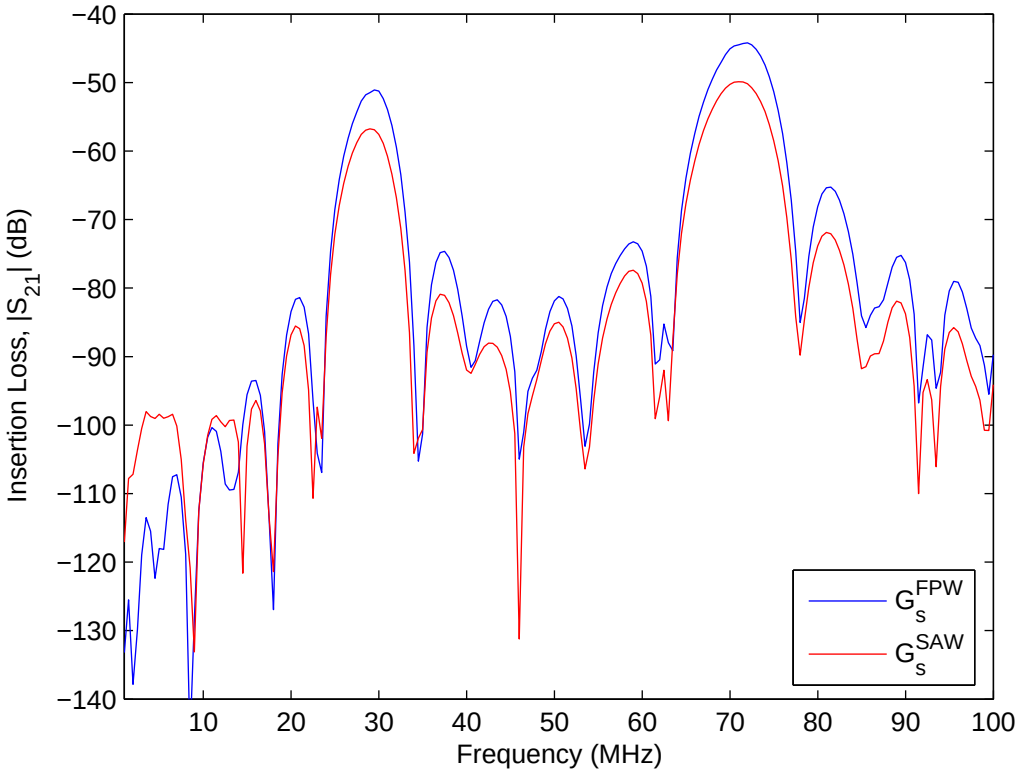


Figure 4.15: Insertion Loss Characteristics

for $A_0$ and $S_0$ respectively, whereas under the SAW assumption values of $-56.8$ and $-49.9$dB are obtained. The insertion loss characteristics presented here are quite low and in many cases are unsuitable for sensing applications. The inclusion of more finger pairs, as in most physical devices, will decrease the insertion loss at the centre frequencies as well as reducing the bandwidth of the primary modes. For example, using the same structure, but with $16$ finger pairs, the insertion loss decreased by $11.3$dB for both primary modes. A typical FPW device contains approximately $25$ finger pairs, thus much lower insertion loss values can be expected for a physical device. It should be noted that the insertion loss characteristics presented have assumed than an ideal metallic ground plane exists below the piezoelectric layer and as such the electrical effects of the Si have been neglected.

A significant deviation can be seen between the two insertion loss curves in the low frequency limit of Figure 4.15. In this region, where with a small fixed frequency a large wavelength is assumed, the primary modes behave as ideal antisymmetric and

symmetric modes. Under these conditions, the approximation for $G_s$ is known to be inaccurate [92]. Even for SAW structures with a high value of $K^2$, errors as high as $7 - 12\%$ have been reported [132]. As the frequency term is increased the primary modes begin to behave similar to Rayleigh modes, and hence the SAW approximation for $G_s$ becomes more accurate but not sufficiently so to use for the analysis of a FPW transducers. However, before assuming that the FPW formulation was correct, the insertion loss characteristics were compared against the authors novel approach using the FEM, where excellent agreement was obtained. A full discussion of the implementation of the FEM to analyse multilayered FPW devices appears in Chapter 5.

Care must also be taken in ensuring that the Green's function solution has converged. Many numerical assumptions, ranging from the integration of the electrostatic component of the Green's function to the number of strips used to simulate the electrodes, will have an impact on solution convergence. Of particular interest is the number of individual strips used to represent the charge on an electrode. An analysis was performed on the change in insertion loss characteristics due to a reduction in the number of individual electrode strips, Figure 4.16.

From Figure 4.16, the insertion loss characteristics do not significantly deviate until $2$ strips are used to represent the physical electrodes. Here, the electrostatic component of the charge density is grossly approximated and end effects are totally disregarded. Therefore, for a large number of electrode pairs, it appears appropriate to use a minimum of $4$ individual divisions to represent the electrodes, with a fixed period of $96$µm. Between all simulations, the centre frequencies of the primary $A_0$ and $S_0$ modes do not change.

## 4.5 Conclusion

In this chapter key operating parameters of a multilayered FPW device have been evaluated. A recent development in the analysis of the piezoelectric wave propagation known as the stiffness matrix method has been presented. The technique, based on a nonlinear Riccati equation, has been shown to be unconditionally stable for large-frequency thickness products and complex material parameters. The stiffness matrix method retains much of the simplicity of the transmission matrix and similarly

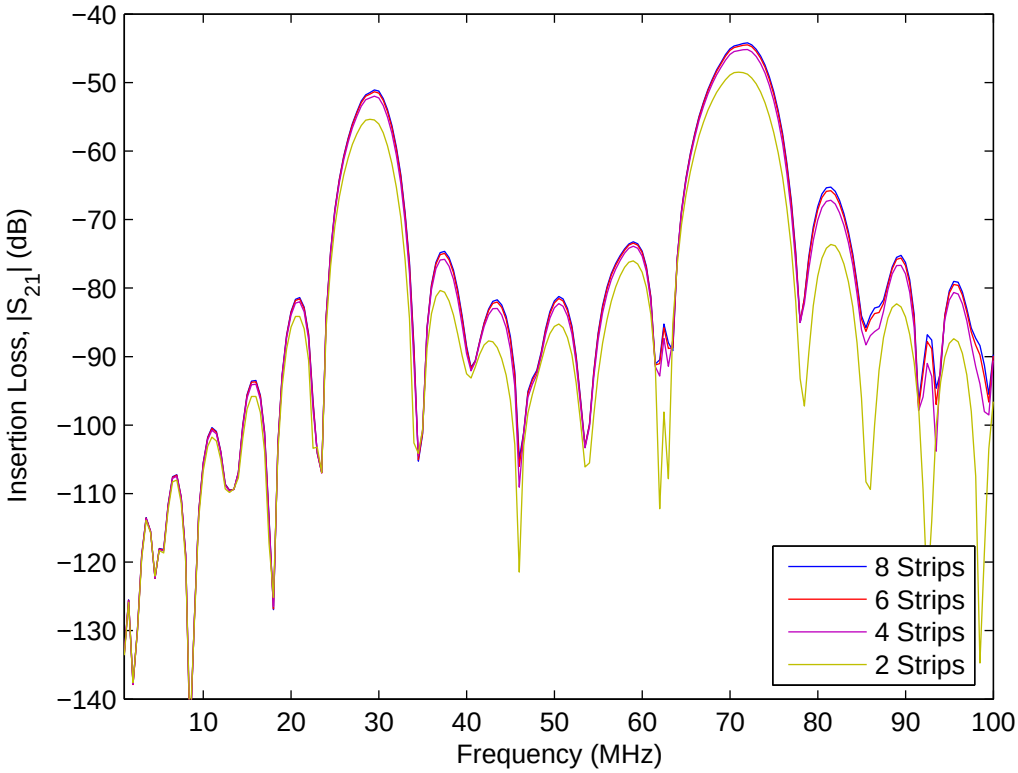


Figure 4.16: Insertion Loss Characteristics - Alternative Strip Sizes

is capable of determining the propagation characteristics of multilayered structures via a recursive calculation. A relationship was established between the stiffness matrix method and the generalised Green's function which fully describes the acousto-electrical properties of the structure. As a consequence the effective permittivity has been defined and the appropriate electrical boundary conditions discussed for satisfying the piezoelectric wave problem.

Particle displacement profiles for a multilayered FPW device have been considered in the low thickness limit which has allowed a procedure to be developed for the identification of the various modes generated. In conjunction with the particle displacement profiles, mass sensitivity for a multilayered FPW device has been calculated and compared against a single layer structure. It was found that the multilayered device provided significantly higher mass sensitivity for a given structure thickness.

It was also shown that the mass sensitivity of the first two primary modes in a multilayered FPW device is dependent on the overall device thickness, where a thin-

ner structure results in higher sensitivity. A thinner structure reduces the operating frequency of the device, whereas for SAW devices sensitivity is typically improved by increasing the operational frequency. Alternative methods of increasing the mass sensitivity have been presented, where it was found that the optimal solution was to replace the piezoelectric ZnO layer with a higher velocity AlN thin film. Although marginally increasing the frequency of the primary modes, an increase in mass sensitivity of $19.8\%$ and $21.5\%$ was found for the $A_0$ and $S_0$ modes respectively.

Using a spectral Green's function, the theoretical insertion loss characteristics of a FPW device have been developed. It was found that many of the assumptions used in SAW theory can not be applied for a FPW structure and as such an explanation presented. Between the SAW and FPW device assumptions, an average deviation in insertion loss characteristics at centre frequency of $11.9\%$ was found. The applicability of the modified FPW theory will be fully compared against the universal FEM discussed in Chapter 5.

# Chapter 5

# FEM Analysis of FPW Devices

## 5.1 Introduction

This chapter presents a novel two and three dimensional Finite Element Method (FEM) analysis of multilayered Flexural Plate Wave devices. The author has successfully evaluated key electrical and mechanical parameters that until recently were evaluated via more traditional numerical methods, such as those discussed in Chapters 3 and 4. In this chapter, the author combines the FEM with modified SAW analysis techniques and related procedures to determine essential performance parameters of FPW structures. The result is a unified analysis technique, that to the best of the author's knowledge, can be applied to FPW structures as well as other acoustic wave devices, thereby illustrating the unique and powerful modelling procedures developed. Although the computation time for the proposed simulations are potentially longer, the development time of a suitable FEM simulation may take only a fraction of that required for alternative numerical techniques. The techniques presented in Chapters 3 and 4 are problem specific, thus small changes in geometry or boundary conditions require an alternative mathematical description. In contrast, the FEM method is non-specific allowing it to be applied across a wide range of problems.

In particular, the author has been able to successfully calculate device admittance, input capacitance, particle displacement profiles and electromechanical coupling coefficient with excellent agreement to the stiffness matrix methods and spectral domain Green's function previously employed. To the best of the author's knowledge, this is

the first time that the aforementioned parameters of a FPW structure have been obtained via a FEM based approach. From the techniques and simulations presented, the author has also successfully developed a series of guidelines relating to the use of the FEM for the analysis of acoustic wave structures. Furthermore, it is shown that the FEM techniques developed improve on previous classical simulation procedures by allowing the simultaneous calculation of various second-order effects, such as electromagnetic feedthrough and diffraction.

Section 5.2 describes the development of the FEM with an emphasis placed on structural analysis. The discretisation process is introduced and a simple example illustrating the underlying concepts of the FEM is presented. Application specific implications of using the FEM to model piezoelectric media are discussed. Section 5.3 presents the three dimensional (3D) FPW device simulated and demonstrates how future FEM simulations can be refined for more efficient processing. Section 5.4 introduces the two dimensional (2D) FPW structure studied and provides further insight into potential modelling optimisations. The reader will be introduced to the mathematical methods behind the electrical and structural parameter extraction and how they differ from previous implementations. Section 5.5 illustrates the change in simulated device characteristics caused by modification of the FEM simulation package parameters. The effect of timestep, simulation time and substeps on insertion loss, or frequency response, characteristics is presented. Attention is drawn to the difficulties in simulating a high aspect ratio structures such as a FPW devices and how careful design of the FEM simulation can greatly reduce errors in the subsequent analysis. Section 5.6 provides a comparison of the two dimensional FEM FPW device insertion loss characteristics against those obtained via the more computationally efficient spectral Green's function presented in Chapter 4, where excellent agreement has been obtained. Finally, Section 5.7 presents the potential disadvantages of the FEM and how future advances in analysis software will lead to a simplification of simulation development and analysis. Liquid loading of a FPW device, in terms of the novel approach undertaken by the author, will be discussed in Chapter 6.

All results presented in this chapter were developed with the commercially available ANSYS 8.0 FEM package, produced by ANSYS Inc. The author decided to utilise

a commercially available package to enable other research groups to directly employ the methods developed within this thesis.

## 5.2 FEM Theoretical Background and Assumptions

In this section, a brief introduction to the theoretical background and underlying assumptions of the FEM is presented. An example of the basic FEM solution procedure is presented with an analysis undertaken on the displacement of a simple beam structure. This example serves to illustrate the powerful analysis capabilities and the general applicability of the FEM to a wide range of problems. It will be seen that the FEM is independent of problem geometry, thereby making the technique attractive for the analysis of acoustic wave devices.

As previously mentioned in Chapter 2, the FEM was historically applied for the analysis of structures such as beams, trusses and frames. More recently, the technique has been extended and refined to determine the influence of piezoelectric materials, perform complex electromagnetic analyses and even model the behaviour of liquids [96]. Many analogies can be drawn between different scientific fields such as heat transfer, one dimensional fluid flow and axial loading. The general applicability of the FEM makes it a valuable tool in the many different facets of science.

Several commercial packages, such as ANSYS, ABACUS and NASTRAN/MSC, are used in industry to solve these often complex problems. The FEM used throughout this chapter was ANSYS 8.0, provided by ANSYS Inc. This software was initially developed for the nuclear industry [133], however in recent years has been expanded to perform static, transient, modal and harmonic analyses of various structures.

The FEM revolves around the discretisation of a large problem into smaller, more manageable sections. Depending on the required solution accuracy, a tradeoff exists between the computation time and the number of finite elements, or simply elements, used. As expected, employing more elements results in an increase in computation time, however may increase the solution accuracy. As will be shown in this chapter, when working with piezoelectric structures, the number of elements and hence nodes has a marked impact on solution convergence.

To solve a FEM problem, appropriate boundary conditions must be applied to the

simulated structure. These are areas in which the solution is at least partially known which provides the FEM tool with a starting point for the solution. The FEM can be applied to any problem where a 'field' and the associated 'potential' is to be calculated. In most cases these two quantities are related by a differential equation. Considering a simple structural analysis, the mechanical stress is the 'field' and the displacement is the 'potential'. In this thesis, the structural analysis is extended to include a piezoelectric material, hence the author's work with the FEM is termed a coupled-field analysis, the implementation of which will be discussed later in this section.

The FEM solves a problem by attempting to minimise the equations of equilibrium [134]. The conservation of energy law states that the total energy in a system must be equal to zero. In terms of a structural analysis, the equilibrium equation can be written as:

$$\mathrm{K}\mathbf{u} = \mathbf{F}, \tag{5.1}$$

where $\mathrm{K}$ represents the structural stiffness matrix, $\mathbf{u}$ is a vector of displacements and $\mathbf{F}$ is the total applied force. Depending on the type of solution required, the meaning of the symbols in equation 5.1 will change.

To illustrate the use of the FEM, consider the simple structural problem of a beam fixed at one end, under a constant load as shown in Figure 5.1. The two beam sections are comprised of the same material, however have different cross-sectional areas.

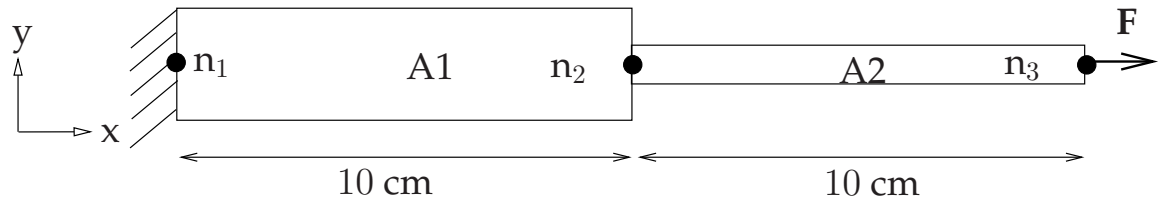


Figure 5.1: FEM Structural Analysis

A distinct advantage of the FEM is the structured approach of the solution computation. Irrespective of the physics under consideration, the same six steps can be followed. However in most FEM packages five of the following steps are handled by the application. For the given example, the solution path is as follows:

- **Discretisation**. The structure is converted from a single large complex problem into smaller, more manageable 'finite elements'. In the above example, the prob-

lem has been split into two elements (A1 and A2), with a total of three nodes and one degree of freedom. The term $u_i$, is defined as the nodal displacement where the subscript $i$ indicates the node under consideration.

- **Define Interpolation Model**. The interpolation model, or element shape function, defines the quantity sought in a given element. For this model, a linear shape function is assumed of the form in equation 5.2 [135]. The superscript $(e)$ indicates that this quantity is per element. Care must be taken to select the correct interpolation model as this will dictate the accuracy of the solution. For example, if a problem contains a field that varies significantly within the element interior then a linear approximation may be insufficient. Here, an element with a quadratic, or higher order shape function would be selected. Such elements typically have nodes in the centre of the element as well at the vertices.

$$u^{(e)} = u_1^{(e)} + x\left(\frac{(u_2^{(e)} - u_1^{(e)})}{l}\right) \tag{5.2}$$

- **Construction of the local stiffness matrices and loads**. From equation 5.1, the stiffness matrices are constructed. When the structure is deformed, the work done by the applied external force is stored as strain energy. The strain energy, $\Lambda$ for each element is given by:

$$\Lambda^{(e)} = \int_x \frac{\sigma\nu}{2}\,dx = \int_x \frac{E\nu^2}{2}\,dx, \tag{5.3}$$

where $\sigma$ and $\nu$ and element stress and strains respectively.

The total system potential energy, equation 5.4, is given by the addition of the strain forces minus the work done by any applied forces. As previously stated, the aim of the FEM is to minimise this function as shown in equation 5.5.

$$\prod = \sum_{e=1}^{e} \Lambda^{(e)} - \sum_{i=1}^{n} F_i u_i \tag{5.4}$$

$$\frac{\partial \prod}{\partial u_i} = \frac{\partial}{\partial u_i}\left(\sum_{e=1}^{e} \Lambda^{(e)} - \sum_{i=1}^{n} F_i u_i\right) = 0 \tag{5.5}$$

Substitution of equation 5.2 into equation 5.3 yields the strain energy per element:

$$\Lambda^{(e)} = \frac{AE}{2l}\left(u_2^{(e)2} + u_1^{(e)2} - 2u_2^{(e)}u_1^{(e)}\right), \tag{5.6}$$

where A represents the cross-sectional area of the element and $l$ is the element length.

The strain energy must now be minimised. Substituting equation 5.6 into 5.5 and converting into matrix form gives the derivative of the total strain energy for a given element.

$$\begin{bmatrix} \frac{\partial \Lambda^{(e)}}{u_1} \\ \frac{\partial \Lambda^{(e)}}{u_2} \end{bmatrix} = \frac{A^{(e)}E^{(e)}}{l} \begin{bmatrix} 1 & -1 \\ -1 & 1 \end{bmatrix} \begin{bmatrix} u_1 \\ u_2 \end{bmatrix} \tag{5.7}$$

- **Evaluation of the overall equilibrium equation**. Once the element strain functions have been constructed, the overall equilibrium equation can be determined. By inspection, and with reference to equations 5.1 and 5.7, the element stiffness matrix, $\mathrm{K}^{(e)}$,is defined as:

$$\mathrm{K^{(e)}} = \frac{A^{(e)}E^{(e)}}{l} \begin{bmatrix} 1 & -1 \\ -1 & 1 \end{bmatrix} \tag{5.8}$$

Thus, the total equilibrium equation is the addition of all elemental stiffness matrices and the corresponding load vectors.

$$\frac{\partial \prod}{\partial u_i} = \sum_{e=1}^{e} \left( \mathrm{K^{(e)}}\mathbf{u^{(e)}} - \mathbf{F^{(e)}} \right) = 0 \tag{5.9}$$

- **Solve for unknown nodal displacements**. To solve for the nodal displacements, the appropriate boundary conditions are substituted into equation 5.8. For the problem given, the Young's modulus for both elements is identical at $23.2 \times 10^9$ N/cm$^2$, the cross sectional area of A1 is 5cm$^2$ and A2 is 2.5cm$^2$. Both elements have a length of 10cm and the applied force, $\mathbf{F}$, is 1N. The displacement of node $\mathrm{n}_1$ is zero, and hence the associated column and row in the FEM stiffness matrix can be removed. Firstly, consider the FEM stiffness matrix:

$$\mathrm{K}^1 = \frac{5 \times 23.2 \times 10^9}{10} \begin{bmatrix} 1 & -1 \\ -1 & 1 \end{bmatrix} \tag{5.10a}$$

$$\mathrm{K}^2 = \frac{2.5 \times 23.2 \times 10^9}{10} \begin{bmatrix} 1 & -1 \\ -1 & 1 \end{bmatrix} \tag{5.10b}$$

The equilibrium equation, equation 5.1 becomes equation 5.11

$$5.8 \times 10^9 \begin{bmatrix} 2 & -2 & 0 \\ -2 & 3 & -1 \\ 0 & -1 & 1 \end{bmatrix} \begin{bmatrix} u_1 \\ u_2 \\ u_3 \end{bmatrix} = \begin{bmatrix} F_1 \\ F_2 \\ F_3 \end{bmatrix} \tag{5.11}$$

The initial problem shows that the displacement of $u_1$ is set to zero. Thus the associated column and row in the equilibrium equation can be removed. The applied load, $F_3$ is set to 1. This results in the final equilibrium equation, equation 5.12 which can be solved easily,

$$5.8 \times 10^9 \begin{bmatrix} 3 & -1 \\ -1 & 1 \end{bmatrix} \begin{bmatrix} u_2 \\ u_3 \end{bmatrix} = \begin{bmatrix} 0 \\ 1 \end{bmatrix}, \tag{5.12}$$

resulting in displacements $u_2 = 8.62 \times 10^{-11}$cm and $u_3 = 2.59 \times 10^{-10}$cm

- **Calculation of element stress and strains**. The final step in the example FEM problem given is to calculate the element stress ($\sigma$) and strains ($\nu$). For element 1,

$$\nu^{(1)} = \frac{\partial u}{\partial x} = \frac{u_2 - u_1}{l} = 8.62 \times 10^{-12} \tag{5.13a}$$

$$\sigma^{(1)} = E^{(1)}\nu^{(1)} = 23.2 \times 10^9 \times 8.62 \times 10^{-12} \approx 2.0 \times 10^{-1}\text{N/cm}^2 \tag{5.13b}$$

And for element 2,

$$\nu^{(2)} = \frac{\partial u}{\partial x} = \frac{u_3 - u_2}{l} = 1.73 \times 10^{-10} \tag{5.14a}$$

$$\sigma^{(2)} = E^{(2)}\nu^{(2)} = 23.2 \times 10^9 \times 1.73 \times 10^{-10} \approx 4.01\ \text{N/cm}^2 \tag{5.14b}$$

The FEM, although a very useful tool, is an approximation to the exact solution. When performing a transient analysis, it will be shown that solution convergence can be increased with more timesteps, elements and finer iterations. In most cases the solution obtained via the FEM is sufficiently accurate for most problems. Although extra simulations are required to confirm solution convergence, the benefits of the FEM are numerous and outway the potentially longer computation time. The FEM can be applied to complex geometries which are often very difficult to describe via alternative numerical techniques.

To achieve a relatively accurate solution, the FEM makes various assumptions about the problem. In the example presented in Figure 5.1, the shape functions were assumed to be linear. In a piezoelectric problem, relatively high stresses and electric fields may be present in a localised region and hence a linear approximation may not be sufficient. Higher order elements, known as p-elements, typically have mid-point nodes and as such may be more suitable for this type of analysis. One drawback of using a higher order element is the total number of nodes required for a particular simulation. Whilst a high number of nodes translates into a more accurate solution, the computation time will increase considerably. This may be rectified by using a simpler h-element structure, with a smaller aspect ratio.

For the work presented here, the frequency response, or insertion loss characteristics, of a FPW device are studied. Other electrical and mechanical solutions are discussed, however the insertion loss characteristics are typically the metric to evaluate device performance. In constructing the FEM simulations, several key assumptions have been made. These range from assuming a perfectly flat homogenous layered structure to the type of function used to excite the device. It will also be shown that several other assumptions have been made to convert the structure from a 3D to a much more manageable 2D simulation.

To fully simulate a FPW device, several different fields of engineering are required. A simple structural analysis, as illustrated previously, is insufficient as there needs to be a method to determine the contribution due to piezoelectric materials. Thus, the structural analysis must be coupled to the piezoelectric constitutive equations which were discussed in Chapter 3. Dedicated elements, known as coupled-field elements are used to couple different degrees of freedom together. Depending on the type of problem, the coupling is calculated by the inclusion of a coupling matrix, or converting the particular field to another load. In the case of a thermal-electric problem, coupling between the two fields is determined by converting the electrical parameters to a thermal load. In a piezoelectric-structural analysis a coupling matrix is used. The advantage of using coupled-field elements is that the software package automatically handles the necessary matrices. The same results could be achieved by performing a multiphysics analysis, however this process is significantly more computationally intensive and re-

quires an intimate knowledge of the FEM and how load vectors are translated between different engineering fields.

The ANSYS coordinate system varies from the industry adopted IEEE standard therefore requiring the elements of the stiffness and piezoelectric matrices to be entered as shown in Tables 5.1 and 5.2 respectively. The table headings relate to the ANSYS coordinate system, whilst the values indicate the IEEE standard form of the respective constants. In the case of piezoelectric materials, the IEEE coordinates must first be rotated to the correct material orientation, and then reordered to suit the ANSYS implementation. The $\varepsilon_{33}$ and $\varepsilon_{22}$ components of the dielectric matrix, $\varepsilon$, must also be interchanged. Care must also be taken to ensure that the simulated FPW device is aligned along the correct working plane. The alignment of the particular structures will be discussed in their respective sections, however it should be noted that it is necessary to reorder the $y$ and $z$ components as the ANSYS $XY$ workplane was used instead of the $XZ$. The second reordering is not shown in Tables 5.1 and 5.2.

Table 5.1: IEEE and ANSYS Stiffness Matrix Conversion

$D_{IJ} =$

| | **x (1)** | **y (2)** | **z (3)** | **xy (4)** | **yz (5)** | **xz (6)** |
|---|---|---|---|---|---|---|
| **x (1)** | $c_{11}$ | - | - | - | - | - |
| **y (2)** | $c_{21}$ | $c_{22}$ | - | - | - | - |
| **z (3)** | $c_{31}$ | $c_{32}$ | $c_{33}$ | - | - | - |
| **xy (4)** | $c_{61}$ | $c_{62}$ | $c_{63}$ | $c_{66}$ | - | - |
| **yz (5)** | $c_{41}$ | $c_{42}$ | $c_{43}$ | $c_{46}$ | $c_{44}$ | - |
| **xz (6)** | $c_{51}$ | $c_{52}$ | $c_{53}$ | $c_{56}$ | $c_{54}$ | $c_{55}$ |

### 5.2.1 Coupled-Field Solution

The full solution for an undamped structure can be found in [136], equation 2.58. In this study, many simplifications can be made to reduce the complexity of the problem. For the analysis undertaken here all mechanical surface resistances, pressure and thermal effects are set to zero and with the inclusion of damping, results in the modified

Table 5.2: IEEE and ANSYS Piezoelectric Matrix Conversion

$e_{IJ} =$

| | **x (1)** | **y (2)** | **z (3)** |
|---|---|---|---|
| **x (1)** | $e_{11}$ | $e_{21}$ | $e_{31}$ |
| **y (2)** | $e_{12}$ | $e_{22}$ | $e_{32}$ |
| **z (3)** | $e_{13}$ | $e_{23}$ | $e_{33}$ |
| **xy (4)** | $e_{16}$ | $e_{26}$ | $e_{36}$ |
| **yz (5)** | $e_{14}$ | $e_{24}$ | $e_{34}$ |
| **xz (6)** | $e_{15}$ | $e_{25}$ | $e_{35}$ |

structural solution equation:

$$\mathrm{M}\ddot{\mathbf{u}} + \mathrm{C}\dot{\mathbf{u}} + \mathrm{K}\mathbf{u} = \mathbf{F(t)}, \tag{5.15}$$

where $\mathrm{M}$ is the mass matrix, $\mathrm{C}$ is the damping matrix, $\mathrm{K}$ is the FEM stiffness matrix, $\mathbf{F(t)}$ is the time varying load vector. The single and double dotted displacement refer to the velocity vector and nodal acceleration respectively.

Coupling between the piezoelectric and structural solution is achieved via a strong coupling matrix. For an arbitrary problem with two degrees of freedom, coupling is obtained by the off diagonal matrices $\mathrm{K}_{12}$ and $\mathrm{K}_{21}$ as shown in equation 5.16, with $\mathbf{X_n}$ the degree of freedom under consideration and $\mathbf{F_n}$ the applied load vector. In terms of a piezoelectric transducer, the nodal voltage and displacements are coupled via the piezoelectric constitutive equations.

$$\begin{bmatrix} \mathrm{K}_{11} & \mathrm{K}_{12} \\ \mathrm{K}_{21} & \mathrm{K}_{22} \end{bmatrix} \begin{bmatrix} \mathbf{X_1} \\ \mathbf{X_2} \end{bmatrix} = \begin{bmatrix} \mathbf{F_1} \\ \mathbf{F_2} \end{bmatrix} \tag{5.16}$$

The size of the coupling matrices is dependant on the simulation degrees of freedom. In a 3D FPW simulation there are four degrees of freedom, thus the coupling matrices are $4 \times 4$. Conversely, the 2D simulations contain a coupling matrix of size $3 \times 3$.

For the simulations performed in this thesis, the complete solution is obtained via the solution of equation 5.17 with the parameters given in Table 5.3.

$$\begin{bmatrix} \mathrm{M} & 0 \\ 0 & 0 \end{bmatrix} \begin{bmatrix} \ddot{\mathbf{u}} \\ \ddot{\mathbf{v}} \end{bmatrix} + \begin{bmatrix} \mathrm{C} & 0 \\ 0 & 0 \end{bmatrix} \begin{bmatrix} \dot{\mathbf{u}} \\ \dot{\mathbf{v}} \end{bmatrix} + \begin{bmatrix} \mathrm{K} & \mathrm{K_z} \\ \mathrm{K_z}^T & \mathrm{K_d} \end{bmatrix} \begin{bmatrix} \mathbf{u} \\ \mathbf{v} \end{bmatrix} = \begin{bmatrix} \mathbf{F} \\ \mathbf{L} \end{bmatrix} \tag{5.17}$$

Table 5.3: Equation 5.17 Parameters

| Parameter | Description |
|---|---|
| $\mathrm{K} = \int_{vol} \mathrm{B}^T \mathrm{DB}\, d_{vol}$ | Structural Stiffness |
| $\mathrm{K^z} = \int_{vol} \mathrm{B}^T \mathrm{eB_v}\, d_{vol}$ | Piezoelectric Coupling Matrix |
| $\mathrm{K^d} = -\int_{vol} \mathrm{B_v}^T \varepsilon \mathrm{B_v}\, d_{vol}$ | Dielectric Conductivity |
| $\mathrm{M} = \rho \int_{vol} \mathrm{N}^T \mathrm{N}\, d_{vol}$ | Element Mass Matrix |
| $\mathrm{N^v}$ | Finite Element Electrical Shape Function |
| $\mathrm{N}$ | Finite Element Structural Shape Function |
| $\mathbf{v}$ | Nodal Electric Potential Vector |
| $\mathbf{F}$ | Applied Structural Loads |
| $\mathbf{L}$ | Applied Electrical Loads |

From the strain relationship equation 3.4b, it can be seen that the matrices $\mathrm{B}$ and $\mathrm{B_v}$ can be identified as the structural and electrical divergence operators.

A dynamic transient analysis, where the load varies with time, was used to determine the impulse, or frequency response of the simulated structure. If the FPW device did not have an excitation source, then the natural frequencies could be determined by performing a simpler modal analysis. This has typically been the approach used by other researchers. The solution path varies depending on the type of elements used in the simulated structure. First order systems, such as thermal, magnetic and electrical are solved using the general trapezoidal rule. Second order systems, including acoustic and structural problems, are solved either using the Newmark method or the forward difference method. The ANSYS Sparse Solver is used to solve the piezoelectric transducer problem. As its name suggests, this solver takes advantage of the sparseness of the finite element matrices as a majority of the terms are located on, or around, the main diagonal. The equations are reordered to minimise the total computation time of the problem. Although potentially a more efficient solver than other iterative methods, the sparse solver is computationally intensive in terms of hardware requirements. Due to reordering of the matrices, several temporary files are created so it is not possible to

gauge the total simulation temporary storage requirements.

ANSYS uses the implicit Newmark time integration to solve equation 5.17, where each timestep is considered a discrete static problem. The integration parameters $\alpha$, $\beta$ are set to $0.25$ and $0.5$ respectively to ensure numerical stability [137]. The damping matrix is computed from $\alpha$ and $\beta$ as well as the mass and stiffness matrices via equation 5.18.

$$\mathrm{C} = \alpha\mathrm{M} + \beta\mathrm{K} \tag{5.18}$$

## 5.3 3D Simulation of a Multilayered FPW Device

Initially, a 3D simulation of a multilayered FPW device was considered by the author to evaluate potential sensor designs. A 3D simulation contains significantly more information about the device behaviour and in particular can graphically illustrate various second-order effects such as beam-steering, diffraction and triple transit. Such a design would require up to $1,000,000$ nodes which was, at the time of writing, beyond the research licence purchased by the author's university. Therefore a simplified 3D structure has been constructed to illustrate the use of the FEM in such an environment. Although the natural progression is from 2D to 3D simulations, due to limitations imposed, a distinct set of criteria were developed to determine whether a 2D simulation would be sufficient to accurately analyse a FPW device. Several geometrical optimisation plans have been developed for the simplified structure whilst still retaining a high degree of accuracy.

Two different analyses of the 3D FPW structure were conducted. The first, an electrostatic analysis, was used to determine the electrode charge density. The second, a dynamic transient analysis, was used to evaluate the acoustic displacement profiles. To ensure consistency between both simulated devices, a higher order element was used for both simulations.

The 3D structure simulated appears in Figure 5.2 and consists of a $2.0$µm Si layer, a $0.2$µm Au ground plane and a $3.0$µm ZnO piezoelectric layer. The material properties appear in Appendix C. Initially a static analysis was performed, allowing the overall structure length to be reduced to $1500$µm. Nodes were evenly distributed through device to the licence limit of $128,000$.

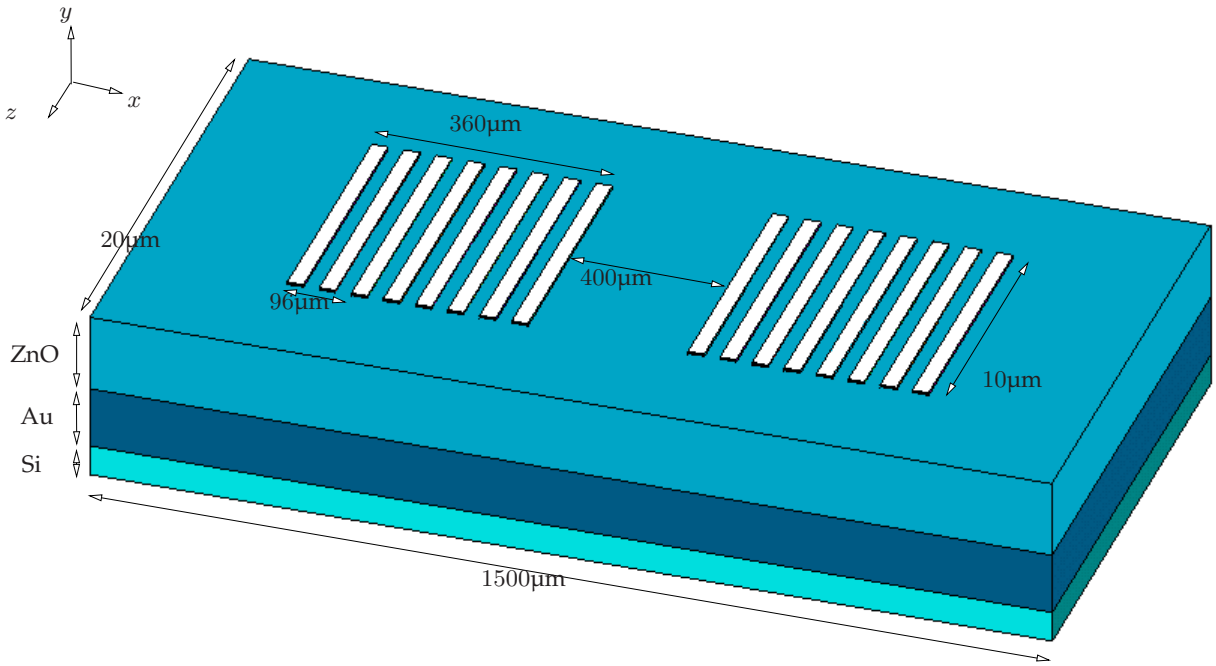


Figure 5.2: Simulated 3D FEM FPW Device

The ANSYS element *Solid98* was used throughout the structure. This is a 10 node tetrahedral element that supports up to six degrees of freedom per node. Although another element, *Solid5*, with less nodes could be equally used, Solid98 is more suited for large displacements which may be the case when considering a transient analysis. Solid98 can be used for a wide variety of analyses, including magnetic, electric, structural and piezoelectric. Although having six degrees of freedom, several can be disabled in the preprocessing stage to reduce the number of variables, increasing the speed of calculation and reducing the computing resource requirements. For this analysis, three displacement ($U_x$, $U_y$, $U_z$) and one electrical (V) degrees of freedom are used. The term degree of freedom is used within the ANSYS package to define the known nodal solution at a given point. The 'free space' around the device perimeter was not modelled for simplicity.

Interdigital transducers were simulated by coupling the voltage degree of freedom on the ZnO surface. This approximation depicts the electrodes as an infinitely thin and conductive layer, thus neglecting mass loading effects. The simulations could quite simply be extended to include mass loading effects, however the impact of these changes is beyond the scope of this thesis. Coupling of the voltage degree of freedom

involves selecting a group of nodes in a given $xyz$-plane and issuing the 'CP' command. The IDTs consisted of four input and output electrode pairs with a period of $96$µm. Four different coupling groups were assigned for the input and output IDTs. A fifth group was also used to simulate the electrical ground plane between the ZnO and Si layers. The total thickness of the Au was coupled instead of just the interfacial nodes between the ZnO and the ground plane. All electrodes had the same acoustic aperture of $10$µm.

### 5.3.1 Initial Conditions

In terms of a piezoelectric analysis, and provided that no displacement load has been set, ANSYS assumes that initial displacements are equal to zero. This in turn assumes that velocity and acceleration are also zero. In the simulations presented the only initial condition set was the voltage on the electrodes and unless explicitly stated, all output electrodes were set to zero volts. Alternating input electrodes were either set at $\pm 0.5$V depending on their location and the type of analysis performed. With the output electrodes set to $0$V, the output short circuit current can be measured by integrating the charge across the electrodes. Figure 5.3 depicts the voltage degree of freedom initial conditions. A $'+'$ sign indicates $+0.5$V where a $'-'$ sign indicates $-0.5$V.

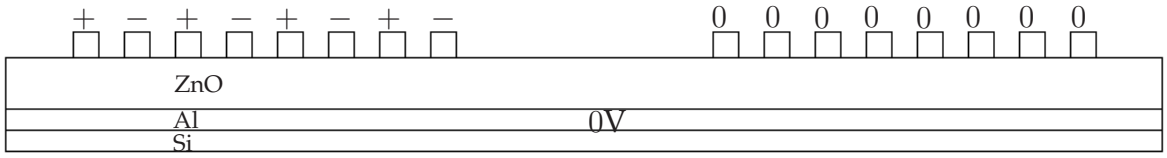


Figure 5.3: FEM Simulation Initial Conditions

Depending on the type of analysis undertaken, whether electrostatic or transient, a slightly different electrical load was placed on the input electrodes. In the case of the electrostatic analysis the input was set at a constant $\pm 0.5$V, whereas in the subsequent transient analyses, an input step function was defined, equation 5.19. It should be noted that the step function is an approximation to an impulse function typically used to define the transient response of a system. The approximation is known to have a marginal effect on the frequency response, however this discrepancy will be minimised

in the postprocessing stage of the analysis.

$$V_s = \begin{cases} \pm 0.5\text{V} & \text{if } 0 < t < t_s \\ 0 & \text{if } t > t_s, \end{cases} \tag{5.19}$$

where $t_s$ is the discrete sampling time, $V_s$ is the voltage applied to the input electrodes and $t$ is the current simulation time.

### 5.3.2 3D FPW Device Electrostatic Charge Density

A 3D electrostatic analysis was performed to evaluate the electrode charge density. In this type of first order analysis, inertia and damping effects are ignored. An electrostatic analysis solves the Maxwell equations and assumes that the electric field is proportional to voltage [126]. The piezoelectric constants are ignored and the device is modelled as a dielectric thin film. The electrode flux density in $x$, $y$ and $z$ directions was extracted into an element table. Of interest is the flux density in the $y$ direction, termed *FLUXDY*. A plot of this data for the input and output electrodes appears in Figures 5.4 and 5.5 respectively.

Firstly consider the input electrode flux density, Figure 5.4. As expected, in locations where a positive voltage was placed on the electrode, a positive region of charge exists and vice-versa. It can also be clearly seen that the tangential electrode flux density exists only on the electrode positions, consistent with the approach developed in [94]. Square root singularities exist on the electrode edges caused by the imposed boundary conditions [138].

An interesting second-order effect is noticeable in Figure 5.5, the output electrode flux density. It can be seen that charge exists on the electrode fingers with no acoustic wave present. This is commonly known as electromagnetic feedthrough, which essentially is capacitative coupling between input and output electrodes. This effect is often disregarded by many modelling techniques for simplicity. Electromagnetic feedthrough is an important parameter particularly when working with highly dielectric thin films such as zinc oxide or aluminium nitride. If the coupling between the input and output electrodes is relatively high then the output signal of the transducer can be degraded. Several manufacturing techniques, such as the inclusion of a carefully designed metal package, can be applied to minimise this effect [1]. In this manner,

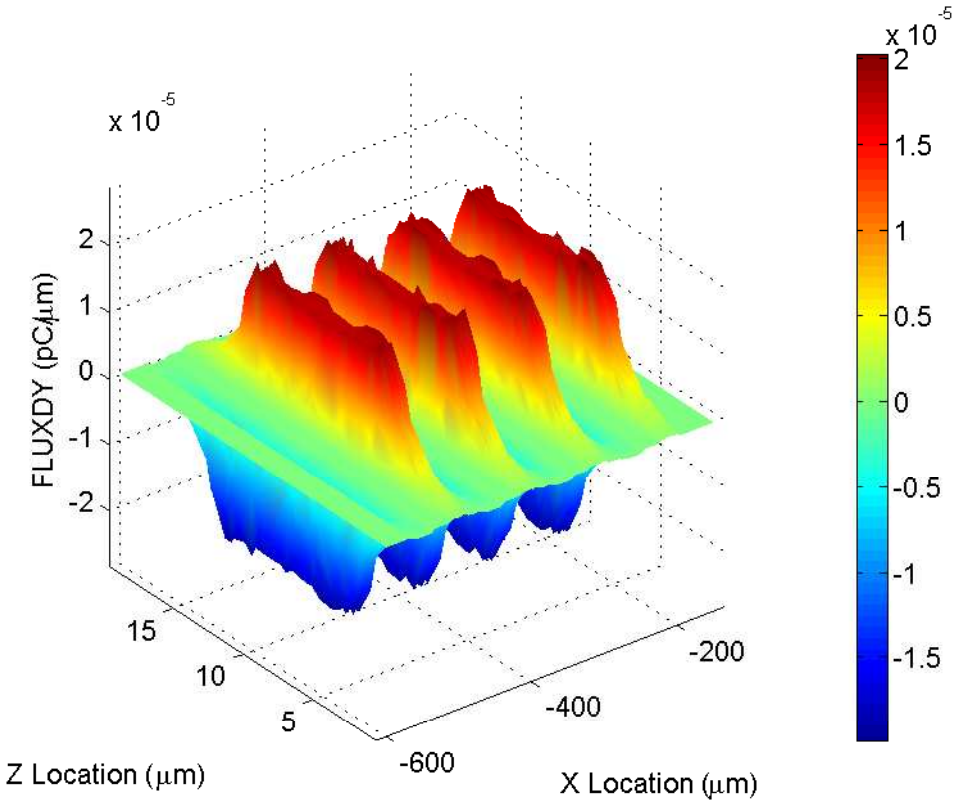


Figure 5.4: 3D FEM FPW Device - Input Electrode Electrostatic Charge Flux Density

a metal construct is placed between the input and output electrodes to minimise the feedthrough effect. Such packaging effects could easily be applied to the presented analysis, which is not as easily achieved with other numerical techniques as the problem basis equations must be redefined for each specific geometry. In a research environment, the influence of electromagnetic feedthrough can be minimised by analysing the device using a Vector Network Analysis with a time domain gating function.

Using the FEM for an electrostatic analysis allows complex geometric structures to be evaluated. The more computationally efficient Green's function analysis, introduced in Chapter 4, requires an expression to be derived for each different structure [19] thus requiring intimate knowledge of its construction and associated techniques. Here, it has been shown that readily available software tools can be used to solve the electrostatic problem with ease.

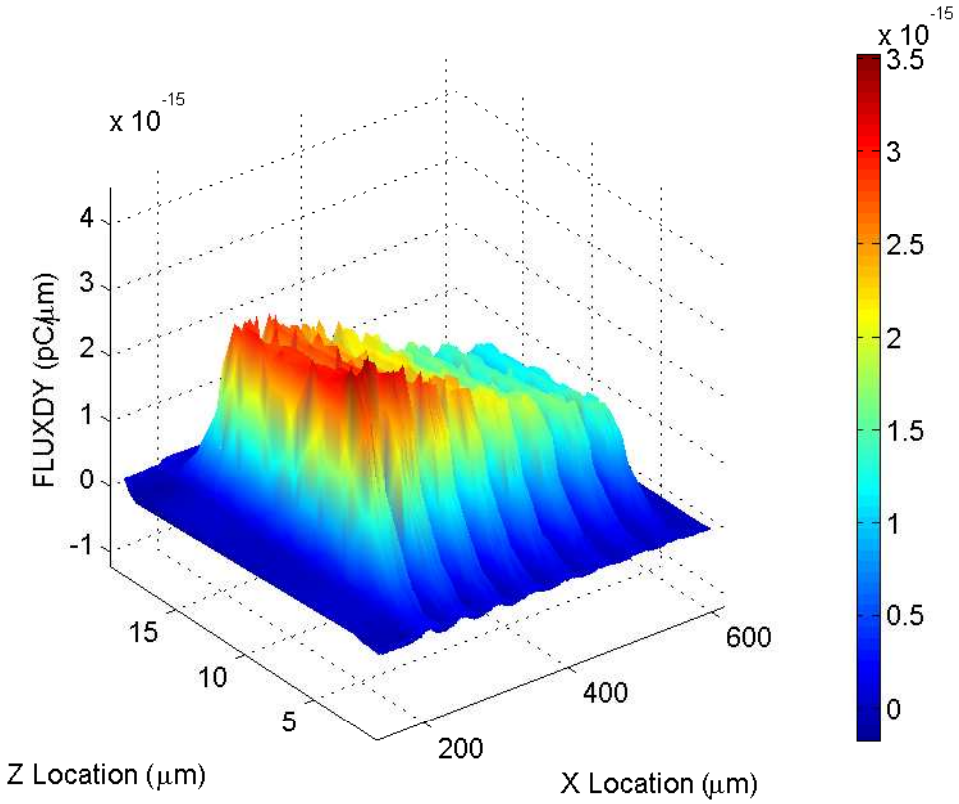


Figure 5.5: 3D FEM FPW Device - Output Electrode Electrostatic Charge Flux Density

### 5.3.3 3D FPW Device Displacement Profiles

To determine the displacement profiles of the 3D FPW device a dynamic transient analysis was performed. A step function, equation 5.19, was applied to the input electrodes. The simulation was conducted for a total of $250$ns with a timestep of $1$ns. Using the method described in Chapter 3, the first antisymmetric and symmetric modes propagate at approximately $509$ and $5247$m/s respectively. The FPW structure was extended to a total length of $2000$µm in the $x$-direction to minimise the impact of the reflected symmetric mode at the simulated structure boundaries.

In a physical device, the reflection of the acoustic wave at the device boundaries is commonly termed triple-transit. In practise, the reflected acoustic wave is substantially attenuated and the reflection appears as ripple on the transducer frequency response. However, at the time of writing, the ANSYS package did not contain an infinite acoustic element that could be used when performing a piezoelectric analysis, thus the reflected wave was of significant amplitude. Further details of this limitation and po-

tential methods to reduce its effect are discussed in Section 5.5.1.1.

The displacement profiles were constructed by considering a node at centre of the top surface of the structure. Displacement in all three primary directions was extracted for the total simulation time and appears in Figure 5.6. For comparative purposes the displacement profiles have been normalised to the peak displacement in the $x$-direction. Immediately noticeable is that the displacement profiles are not sinusoidal in nature. This is due to the many different acoustic modes interfering with each other as they propagate along the structure.

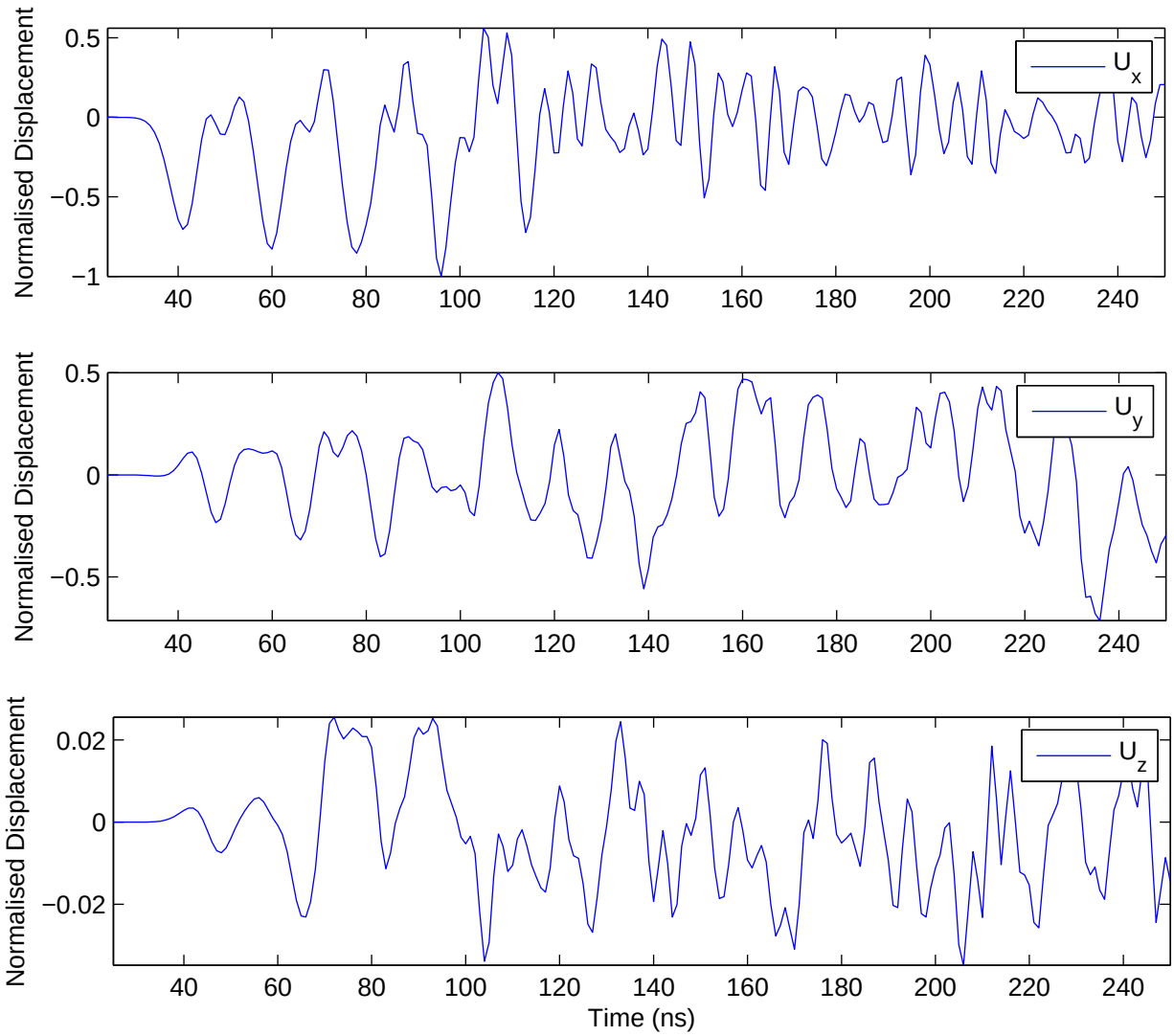


Figure 5.6: 3D FEM FPW Device - Displacement Profile

To confirm that both primary modes were successfully excited, an Fast Fourier Transform (FFT) of the displacement profiles was performed [7]. This analysis is not as rigourous as the method introduced for the 2D FPW device simulations in the following sections and as such should only be used as a guide. The FEM resolves the primary modes at approximately $4.0$MHz and $52.0$MHz for $A_0$ and $S_0$ respectively, whereas the theoretical frequencies, obtained using the techniques of Chapter 4, generated from a 2D approximation are $5.3$MHz and $54.6$MHz. Although there is an apparent deviation from the theoretical frequency, the FEM has shown that it can successfully model a FPW device. Techniques for improving the frequency domain resolution will be discussed later in Section 5.5.

Due to the limitations of the ANSYS licence, it was not possible to simulate a device sufficiently wide to examine other second order effects such as beam-steering. Several authors have confirmed that these phenomena can be successfully modelled with the ANSYS package [7].

### 5.3.4 2D FPW Device Simulation Criteria

Whilst is has been shown that the FEM is capable of successfully modelling a 3D FPW device, the significant computation time makes the technique unsuitable to evaluate preliminary sensor designs in a commercial environment. In terms of computation time, the 3D transient analysis presented took over $120$ hours to complete. Therefore, at least for the initial development process, where possible, further assumptions and geometrical approximations should be undertaken, however the simulations must still be capable of providing sufficiently accurate results. To that end, a 2D FPW device simulation was investigated.

Two separate criteria were used to determine if a 2D approximation would be sufficient to accurately simulate a FPW device. The first related to the charge density on the electrodes. The assumption made in Chapter 4 is that charge is uniform in the ANSYS $z$-plane and hence the total charge density can be calculated by integrating across the electrode surface and then multiplying by the electrode aperture. If the FEM simulations proved this hypothesis, within the bounds of numerical error, then a 2D simulation would be considered sufficient. The second criterion involves the displace-

ment of the individual $x$, $y$ and $z$-components. Potential theory [61] shows that FPW devices mainly support longitudinal and normal displacements. If the displacement in the $z$ plane, Figure 5.2, was at least one order of magnitude less than that of in the $x$ and $y$-plane, then this particular criterion would be met.

With reference to Figure 5.4, the 3D electrostatic simulations have shown that the charge density is approximately uniform along the $z$ axis and hence one criterion is filled for the further development of a 2D FPW device simulation. In devices with a narrow substrate, in comparison to the acoustic wavelength, the $z$-direction electrode end-effects must also be considered [16]. The $z$-direction end effects will manifest as a diffraction pattern at the receiving IDT. In the following 2D analysis it is assumed that the electrode is many multiples of the acoustic wavelength and hence these effects can be safely ignored.

From Figure 5.6 the normalised displacement in the $z$-plane is approximately $0.03$ times that of the peak $x$ displacement. Thus, the two criteria for the use of a 2D simulation have been successfully satisfied. A more in-depth analysis of FPW device displacement profiles will be presented in Section 5.4.5.

Further simplifications are made with respect to the simulated 2D FPW device, however will be discussed in Section 5.4.1.

## 5.4 2D Simulation of a Multilayered FPW Device

The analysis performed in the preceding section has demonstrated that FEM, and in particular ANSYS, is capable of simulating a FPW device. The two criteria specified for a 2D FPW device simulation, constant charge density across the electrode depth and displacement in the $z$-plane is less than one order of magnitude less than that of in other directions, has been successfully met. The computation time for a 2D simulation is also significantly less as size of the matrices to be solved are greatly reduced. The reduction in computation time, combined with more available elements has allowed the author to investigate the impact of node density, simulation run and step time on solution convergence. As a benchmark, the frequency response obtained via the FEM is compared against the spectral Green's function in Chapter 4.

Another advantage of a 2D FPW device simulation is the ability to simultaneously

study various second-order effects that cannot be determined via other techniques. In particular, simulations can be developed to examine triple-transit interference caused by structural boundaries and the bidirectional nature of IDTs.

Two different approaches have been used to determine the device frequency response. The first evaluates the open circuit voltage on the output electrodes due to equation 5.19 [17]. The second measures the short circuit current in the output electrodes by integrating the electric flux density across the electrode surface. To the best of the authors knowledge, this is the first time that this approach has been used to calculate the frequency response of a FPW device using the FEM package ANSYS. During the course of this PhD programme the author has been in contact with various other researchers to discuss this approach and ultimately suggest that this method is the most accurate when compared against other proven methods.

All 2D simulations were constructed with the four node ANSYS *Plane13* coupled-field element. Similar to the *Solid98* used in the 3D simulations, Plane13 is used in magnetic, thermal, electric, piezoelectric or structural analyses [136]. Three degrees of freedom, two displacement and one voltage were used for all 2D simulations. The IDTs and ground plane were constructed using the same technique as the 3D simulations. When meshing the structure, care must be taken to ensure that the element does not become degenerate as the voltage degree of freedom will be automatically deleted.

### 5.4.1 2D FPW Device Design and Development

Although is has been shown that the 2D FPW device approximation is valid, there are still several optimisations that can be made to the structure. This section examines how the simulated structure can be modified to improve computation time and reduce storage requirements. In most simulation techniques a FPW device is considered to consist solely of an acoustically thin plate, thus ignoring the surrounding silicon structure. At the point where the silicon substrate thicknesses increases due to the fabrication process a disruption of the propagating wave will occur. Using the FEM, the changes in the wavefront, in terms of insertion loss characteristics, can be analysed.

The full 2D structure under consideration can be found in Figure 5.7. It consists of a $350\mu$m silicon wafer which has been preferentially etched at $54.6^{\circ}$ to the surface

normal. The etched section consists of a $24$µm Si layer, a $0.2$µm Au ground plane and a $3.0$µm ZnO piezoelectric layer. The overall simulated device measures $5500$µm in the $x$ direction, with the etched cavity measuring $1888$µm. The layer thicknesses were chosen so that the FEM simulations could be compared against a device fabrication attempt by the author. The simulated structure consisted of eight electrode pairs, with an IDT edge to edge spacing of $400$µm and a wavelength of $96$µm. The first input electrode was placed at $-944$µm in $x$.

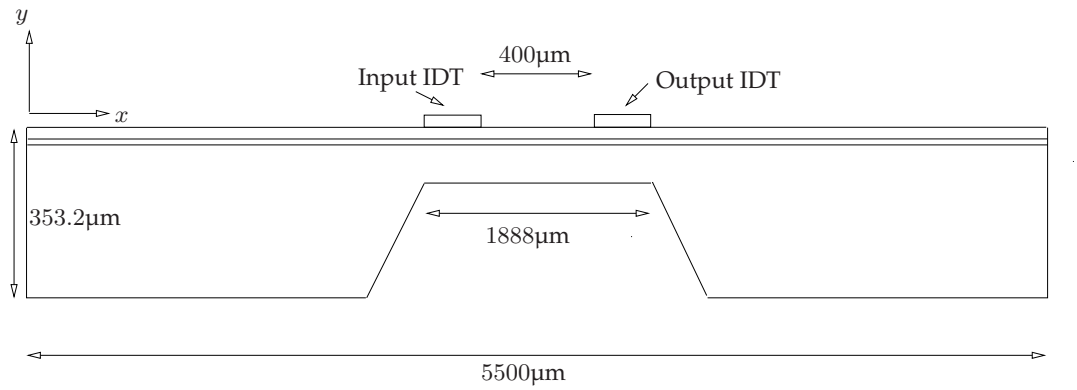


Figure 5.7: Simulated 2D FEM FPW Device

Various node densities were used throughout the full 2D simulated structure. The etched cavity consisted of one node per $2.0$µm in $x$, with one node per $0.5$µm, one node per $0.1$µm and one node per $1.0$µm in the thickness direction of the ZnO, Au and Si layers respectively. Outside the etched cavity, in the bulk of the silicon, a reduced nodal density was used. For the simulated device, the velocities of the first antisymmetric and symmetric modes using the techniques developed in Chapter 4 are $2790$ and $6836$/ms respectively. Although these velocities are typically higher than devices used liquid media, the spacing between the two primary modes in the frequency domain is quite close allowing the subsequent analysis to be simplified.

### 5.4.2 Electrical Output Parameters

Two different techniques were used to evaluate the frequency response of the simulated FPW device. In the subsequent analysis, an impulse was applied as per equation 5.19, however the boundary conditions on the output electrodes were altered. In the first case, the output electrodes were electrically coupled, however left 'floating' to

measure the induced output voltage. The second series of simulations set the output electrodes to $0$V to measure the output short circuit current.

To determine the insertion loss characteristics of the simulated device, a full dynamic transient analysis was performed. The simulations were ran for a total time of $758$ns, with a timestep of $1$ns. The results file options were modified to output all flux densities as this option is disabled by default. It is not possible to specify a group of nodes to be written to the results file, thus the output contain the solution for the complete structure. This produces a extremely large results file, which is generally split into numerous $1$GB files for easy postprocessing.

#### 5.4.2.1 Open Circuit Voltage Model

The first technique is similar to that described in [139], where the induced output voltage is used to determine the frequency response. This approach has been successfully applied to SAW devices and since been used by several other researchers. In the original simulations, termed 'Single Electrode Model', a positive voltage was placed on the even numbered input electrodes whilst the output electrodes were coupled, but left floating. The amplitude of the applied voltage was inversely proportional to the timestep. Thus, in many cases, a d.c. impulse of $100$V was applied. A further series of simulations, where a $\pm 0.5$V step function is placed on alternating electrodes, to maintain consistency with Chapter 4, have also been completed to provide a comparison with the charge based model. This simulation is referred to as 'Differential Electrode Model'.

The response of the FPW device is determined by taking a Fourier Transform of the induced voltage on the even electrodes. As the output electrodes are electrically coupled, the same voltage appears on all nodes in the finger. The result implies that the response for a large number of output electrodes can be determined by multiplying the output voltage on one electrode by the total number of electrode pairs. This approach is typically used in a periodic model where the response for one electrode pair is determined and simply cascaded for all other electrodes in the IDT. The response of the device was originally determined using the power spectral density function (PSD), which is a measure of the relative power of each frequency, Figure 5.8. The response has been

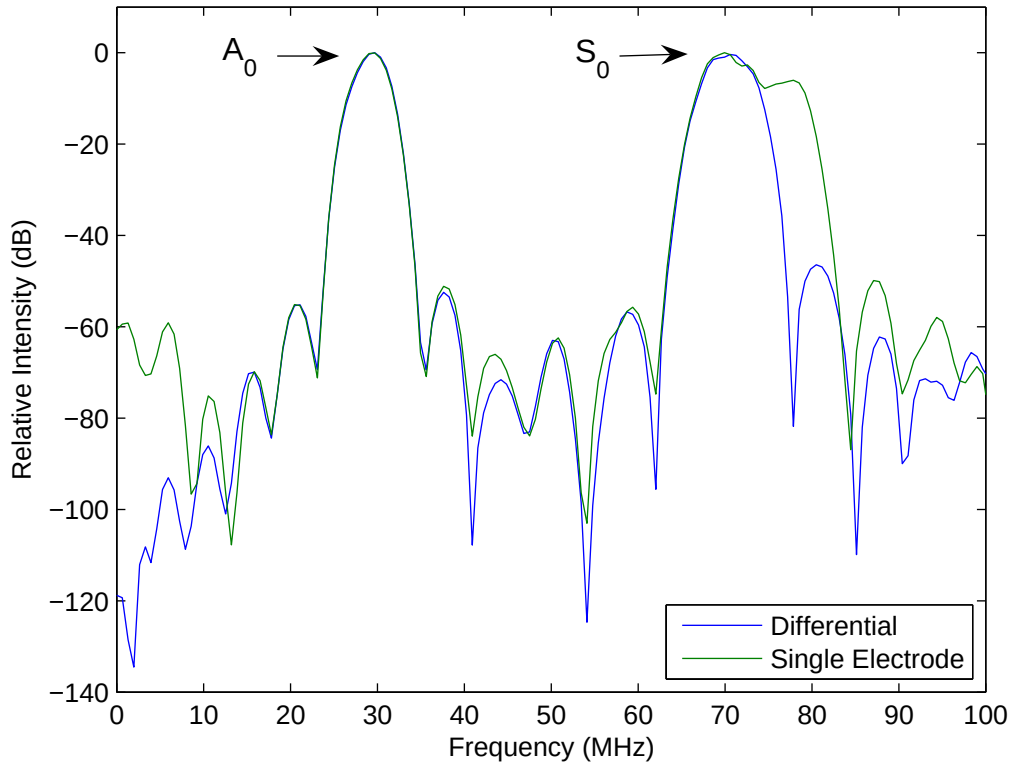


Figure 5.8: 2D FEM FPW Device - Voltage Model Output Spectral Power Density

normalised to the peak intensity of the first antisymmetric mode. Two different results are presented, where the 'differential' curve represents the structure that had $\pm 0.5$V placed on alternating input electrodes. For both structures it can be clearly seen that the first antisymmetric and symmetric modes have been excited at $30.15$ and $71.02$MHz respectively. It is believed that the deviation from the theoretical centre frequencies of $29.06$ and $71.21$MHz is caused by the inclusion of the silicon support structure. For the single electrode model, there appears to be an inconsistency in the sidelobe values at the extreme ranges of frequency. This is caused by the impulse being placed only on the even input electrodes. The same type of phenomenon can be achieved using the techniques in Chapter 4 if the odd input electrodes are grounded. For the antisymmetric mode, the sidelobes are approximately $-55$dB from the main response. Using the modelling techniques of Chapter 4, they are less than $-29$dB. Therefore the PSD method has not been able to accurately resolve the sidelobes, thus another technique is required.

Although the voltage model is not suitable to determine the insertion loss of a FPW device, it can still be successfully used to determine centre frequencies, displacement profiles and other time domain characteristics. Other groups have applied this technique to determine the mass sensitivity of a SAW device by measuring changes in the induced voltage on the output electrodes due to modification of a sensitive layer in the time domain [18].

#### 5.4.2.2 Short Circuit Charge Density Model

The second technique used evaluates the frequency response of the simulated device by measuring the output short circuit current. This method is basically identical to that used in the spectral domain Green's function analysis discussed in Section 4.4. The electric flux density is extracted by selecting the nodes at the IDT electrode locations and tabulating the results using the element table command. Electric flux density in both $x$ and $y$-planes is stored as well as the node spatial locations. Figure 5.9 depicts the $y$-component of the electrode flux density on the output electrodes at $100$ns. As expected, the electrode flux density is present only at the simulated electrode locations. At this particular point in time, the acoustic wave has not fully propagated along the total length of the IDT.

Integration of the electric flux density presented in Figure 5.9, via the trapezoidal rule, results in the total charge on the IDT for a given point in time. The integration process was performed across all timesteps using a script written in Microsoft QuickBasic 4.5. Due to the limited number of surface nodes, $13$ in this case, and the timestep used, the calculated charge density has relatively poor resolution. To improve the time domain response of the charge density, several signal processing techniques were considered. The most beneficial was a simple interpolation technique, where the average value between two successive calculated samples was added. Figure 5.10 depicts the total charge for the first output electrode after interpolation. Whilst the raw nodal charge data exported from ANSYS could have been interpolated, the solution would be slightly inaccurate due to the limited floating point calculation ability of the QuickBasic application. Therefore, the integrated charge density was interpolated via MATLAB. An issue with Figure 5.10, the interpolated total charge density, is the inability to

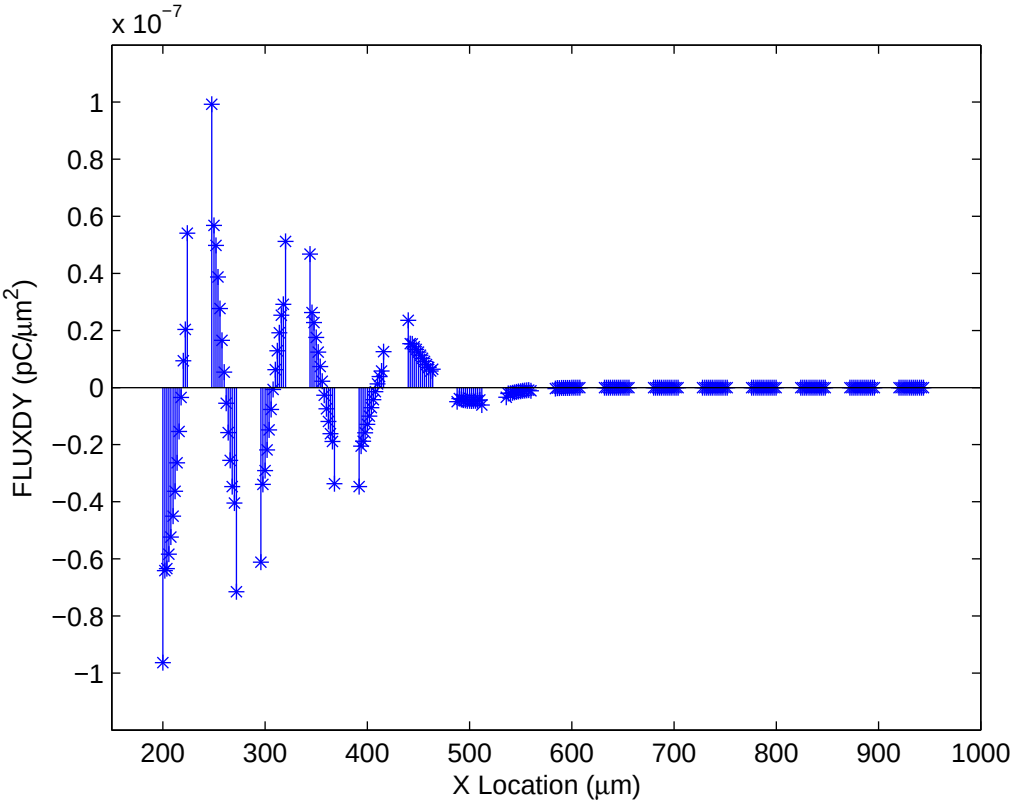


Figure 5.9: 2D FEM Current Model - Output Electrode Flux Density, t=100ns

gain useful information with regards to the spectral characteristics of the device. Thus, further processing is required to convert the data to a more usable form.

To determine the short circuit current of the device, equation 5.20 is used. As was shown in Section 5.3, the electrode flux density is assumed to be constant in the $z$-plane and hence the charge integral is multiplied by a constant aperture, $W$, of 200µm. For consistency between the voltage and current models, the total electrode charge, $q_l$, is calculated by summing the even numbered input and output electrode components. The frequency term, $f$, in equation 5.20 is obtained from a FFT of the charge data.

$$I_{sc} = j2\pi f W q_l \tag{5.20}$$

Once the short circuit current of both IDTs has been determined, the device admittance, $Y$ can be calculated, equation 5.21. This is an important parameter as describes the interaction of the transducer with external circuity. The admittance is converted to an equivalent scattering parameter representation where the insertion loss, $S_{21}$, can be

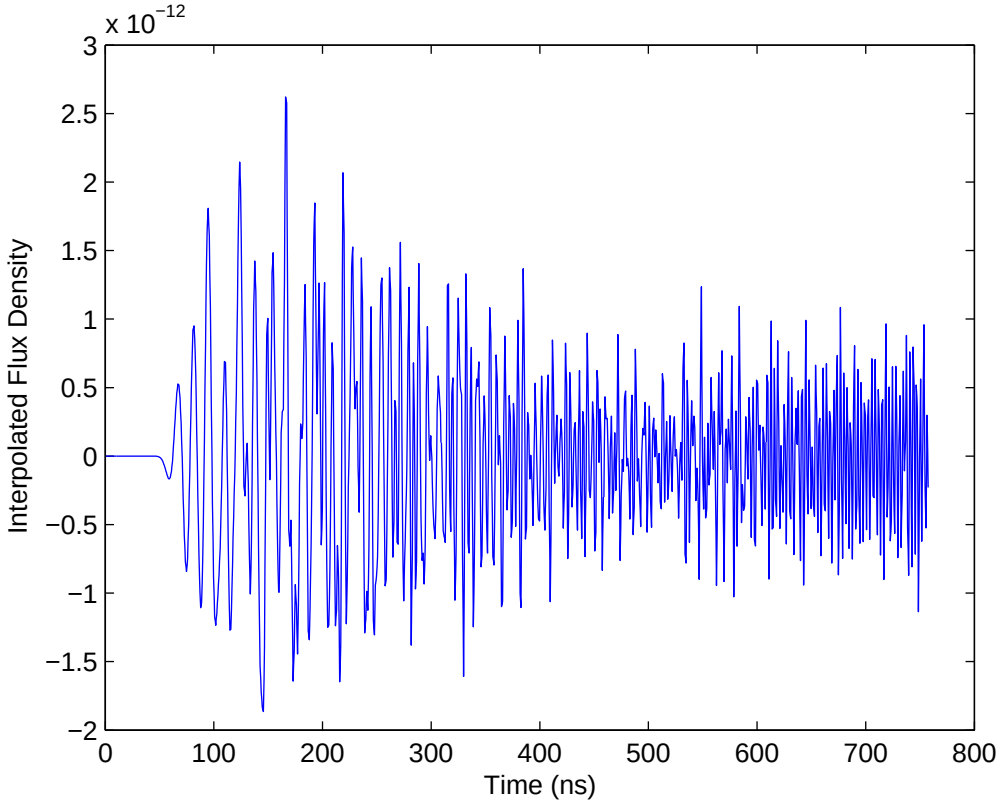


Figure 5.10: 2D FEM Current Model - Interpolated Total Charge

determined. Note the presented insertion loss characteristics assume a $50\Omega$ load termination. The voltage term in equation 5.21 is the total differential voltage applied to the input transducer, which for convenience has been set to $1V$.

$$Y = \frac{I_{sc}}{V_T} \tag{5.21}$$

Ideally the ANSYS transient simulation should continue until equilibrium is reached or the acoustic wave sufficiently decayed. For any finite length time domain analysis the frequency domain representation will contain spectral leakage or unwanted ripple caused by the effective truncation of the data [123]. The truncation of the data can be considered the same as applying a rectangular windowing function. Spectral leakage can be minimised by applying a windowing function whose Fourier transform has low sidelobes compared to the main response. For this analysis a Hann window, which has sidelobes at $-32$dB compared to $-13$dB for the rectangular window, is applied to the spectral data. Although other windowing functions exist with even lower lobes, they can suppress low amplitude signals making it difficult to correctly resolve the side-

lobes of the original function. An issue with applying a Hann window to the data is that the bandwidth of the main lobe is slightly larger than the effectively applied rectangular window, thus a slight shift in frequency of minor features may be observed [123]. Figure 5.11 illustrates the insertion loss characteristics for the simulated 2D FPW device between 1 and 100MHz. The blue trace represents the rectangular windowed spectral data, whilst the green trace is the Hann windowed spectral data.

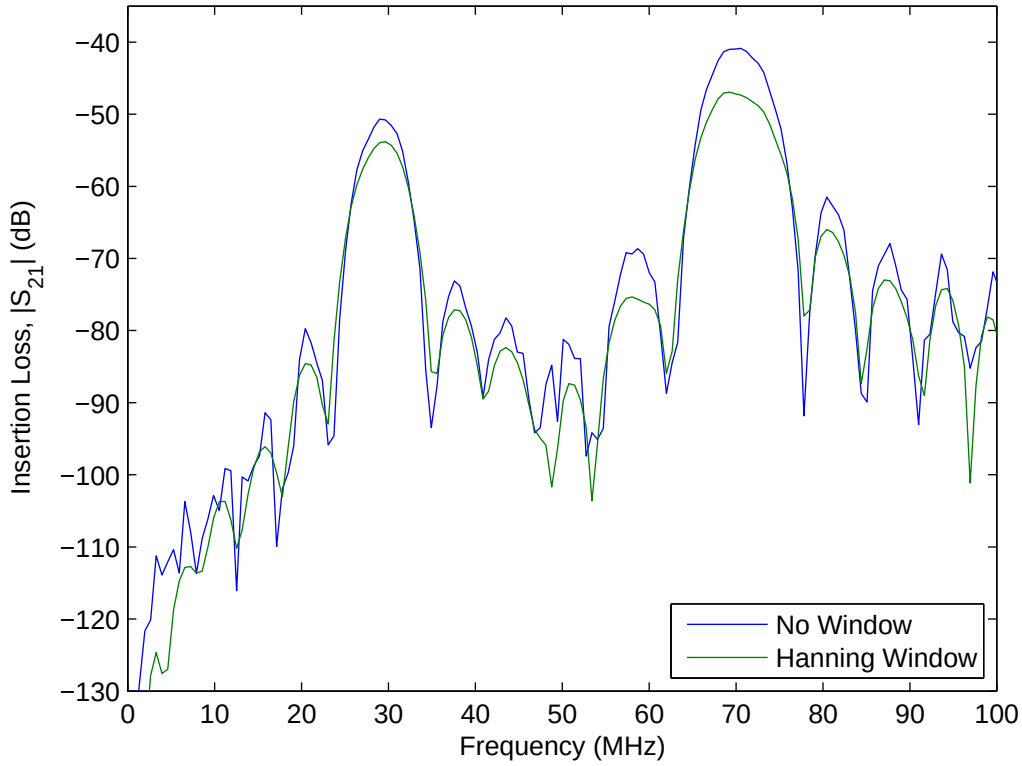


Figure 5.11: 2D FEM Current Model - Insertion Loss Window Comparison

It can be seen from Figure 5.11 that the application of a windowing function greatly improves the 'resolution' of the insertion loss characteristics. The perceived increase in resolution is not due the addition of extra time domain values, but rather from the reduction in spectral leakage. Both antisymmetric and symmetric modes appear to have been resolved correctly at approximately 30.15 and 70.97MHz respectively. The shift in amplitude is caused by the leakage factor of the windowing functions [140]. For a rectangular window, the ratio between the amplitudes of the mainlobe and the sidelobes is approximately 9.14% whilst for the Hann window, the ratio is 0.05%. Thus it

is anticipated that before a comparison is made with a physical device, the amplitudes should be scaled accordingly.

In comparison to the voltage model presented in Section 5.4.2.1 a slight discrepancy exists between the centre frequency of the two primary modes. This is caused by the integration technique used, which assumes that the charge density across the electrode surface is well behaved. From Figure 5.10, the charge can become singular at the electrode edge possibly introducing error particularly when using the trapezoidal rule. A higher order integration technique, such as Simpson's rule, could be used to improve the accuracy of the integration, however within the bounds of this study the slight discrepancy is considered negligible.

Another key difference between the voltage and charge-based models is the sidelobe characteristics. For the first antisymmetric mode, the lobes correspond to $-55.2$ and $-30.7$dB from the centre frequency peak, for the differential voltage and Hann windowed charge model respectively. A full comparison between the charge model and the Green's function described in Section 4.4 will be discussed later, however preliminary results indicate that the simulation has correctly resolved frequency response of the device including the sidelobes. From the results presented here, it is clearly evident that the PSD is not an appropriate tool to evaluate the insertion loss characteristics of a FPW device. Thus, from this point the charge-based approach will be used to evaluate the use of the FEM to accurately determine the characteristics of a FPW device.

### 5.4.3 2D FPW Device FEM Structural Simplification

Most analytical techniques, such as those discussed in Chapters 3 and 4, model the FPW device as a thin plate or membrane without the silicon supporting structure. This section investigates the effect on the FPW device frequency response by making these assumptions. One advantage of neglecting the support structure is the significant reduction in computation time. For the 2D simulation developed previously, a total of $120,309$ elements were used, comprising of $122,095$ nodes. A membrane structure, with the same major dimensions, contains a total of $55,000$ elements and $57,771$ nodes. This results in greatly reduced computation and storage requirements making the FEM

a more viable analysis tool.

Two alternative investigations were undertaken to evaluate the change in device frequency response brought about by neglecting the supporting structure. The first examines the displacement profiles of the full FPW device in the silicon bulk and the second evaluates the change in the insertion loss.

An advantage of ANSYS platform is the ability to plot a particular solution over time, thus providing immediate visual feedback to the designer. In terms of the bulk silicon, the displacement degree of freedom was animated over time to confirm that there was indeed motion in the depth of the device warranting further investigation. A plane within the bulk silicon, approximately $1446$µm from the last input electrode, was selected to determine the displacement versus depth profiles. Figure 5.12 illustrate the displacement at $410$ns for the specified plane. The lack of resolution, particularly towards the bottom of structure, $-350$µm, is brought about by the relatively small amount of nodes in the bulk of the device. It is evident that a displacement occurs throughout the bulk of the material which requires further investigation.

As silicon is a non-piezoelectric material and no electrodes exist on the bottom of the device, it is not possible to use the previously described insertion loss technique to determine the oscillation frequency throughout the bulk of the material. However, an FFT can be applied on the nodal displacement to gain an approximate oscillation frequency. The analysis was repeated for three alternative points within the structure corresponding to the upper and lower surfaces as well as point at the middle of the silicon structure. If a mode conversion occurred, where the antisymmetric or symmetric modes converted to a Rayleigh wave, a peak at $46.56$MHz would be seen in FFT of the displacement data. A Rayleigh mode could also be identified by the confinement of the acoustic energy to one to two wavelengths from the surface, corresponding to approximately $192$µm in depth. The frequency domain representation of the $y$-plane displacement data is shown in Figure 5.13. It can be seen that the frequency domain resolution is far less than that used for the insertion loss characteristics but is suitable for a basic determination of frequency. The plots correspond to the upper surface, middle and lower surface of the structure respectively.

The main acoustic peaks appear to be present throughout the complete depth of the

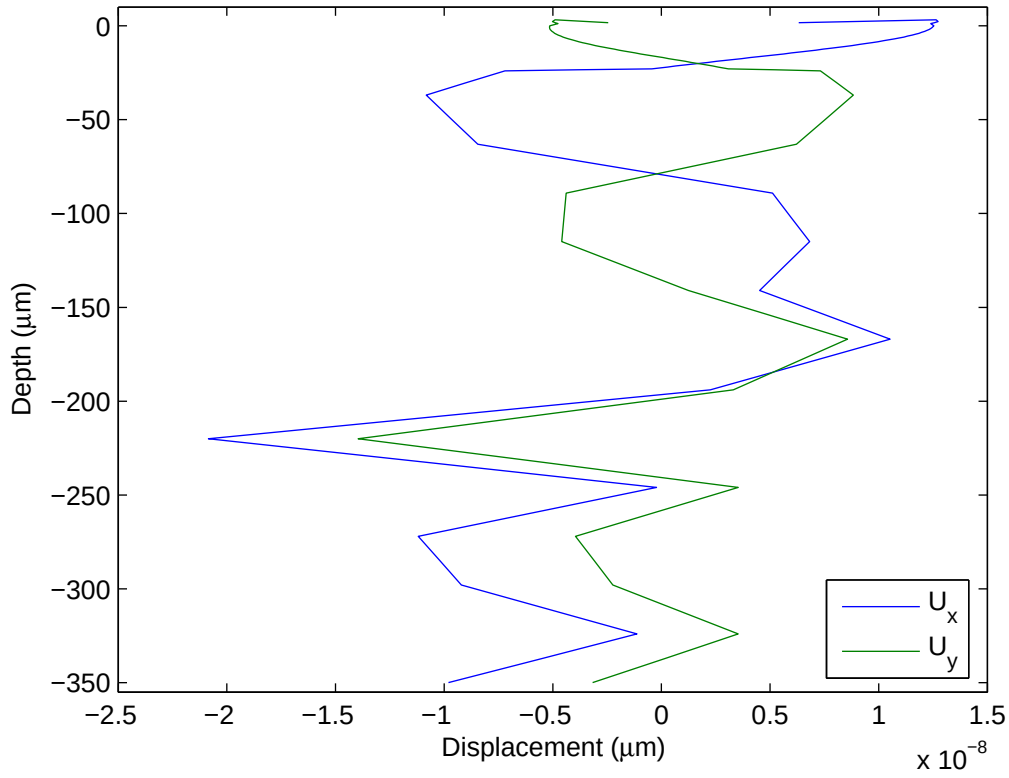


Figure 5.12: 2D FEM FPW Device - Substrate Displacement Analysis, $t = 410$ns

structure however appear slightly shifted and broader towards the bottom of the device. It is therefore assumed that mode conversion does not occur and that the main two modes exist at the depth of the structure for the simulated wavelength of $96$µm. A further series of simulations would be required to investigate the impact of a smaller wavelength, however it is believed that the two primary modes would converge to the Rayleigh mode phase velocity [24].

A second simulation was developed to evaluate the change in insertion loss characteristics due to the removal of the membrane support structure. The simulated device appears in Figure 5.14. This particular structure is typical of that used by other simulation techniques where the FPW device is assumed to be a thin plate or membrane. For consistency, the overall length of the two structures is identical. The insertion loss characteristics for the pure plate structure appears in Figure 5.15. For comparative purposes the frequency response characteristics for the complete structure are also included.

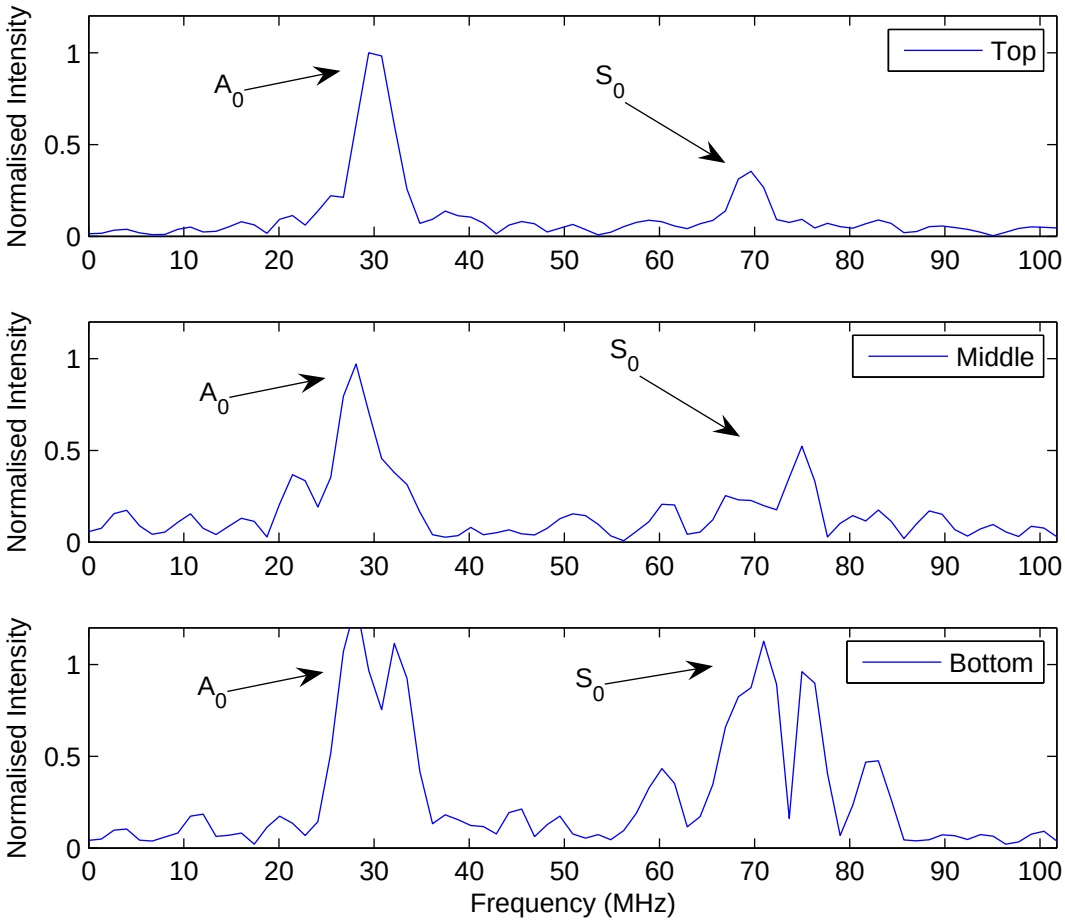


Figure 5.13: 2D FEM FPW Device - Spectral Content of Substrate Displacement ($y$)

Immediately noticeable is a change in the centre frequencies of the pure plate structure simulation. The centre frequency for antisymmetric mode has decreased to $29.46$MHz, corresponding to a shift of $0.67$MHz. The symmetric mode appears to be unaffected by the change in geometry, with a centre frequency of $70.97$MHz. With respect to the spectral domain Green's function model, the centre frequencies are $29.06$ and $71.21$MHz. The deviation from the theoretical simulation can be attributed to the frequency domain resolution of the ANSYS model. It will be shown in Section 5.5.1, that the timestep and total simulation length are related to the frequency domain resolution, thus techniques will be developed to improve the accuracy of results. As expected, there is also a slight change in the amplitude of the insertion loss characteristics between the two simulated structures, with improved insertion loss at the centre frequencies for the pure

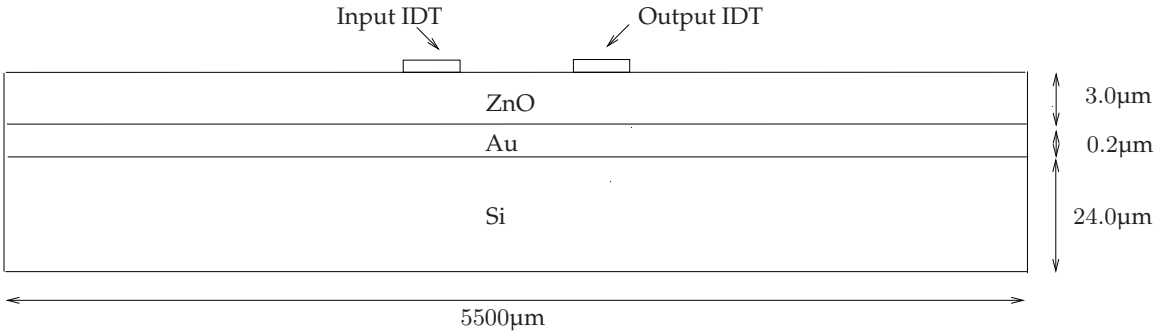


Figure 5.14: Simulated 2D FEM FPW Simplified Device

plate structure. With respect to the full FPW structure, Figure 5.7, small acoustic reflections occur at the point where the silicon thickness begins to increase thus interfering with the electrode flux density. Currently it is not possible to image this with ANSYS, however it is these reflections that bring rise to destructive interference, increasing the insertion loss characteristic of the device.

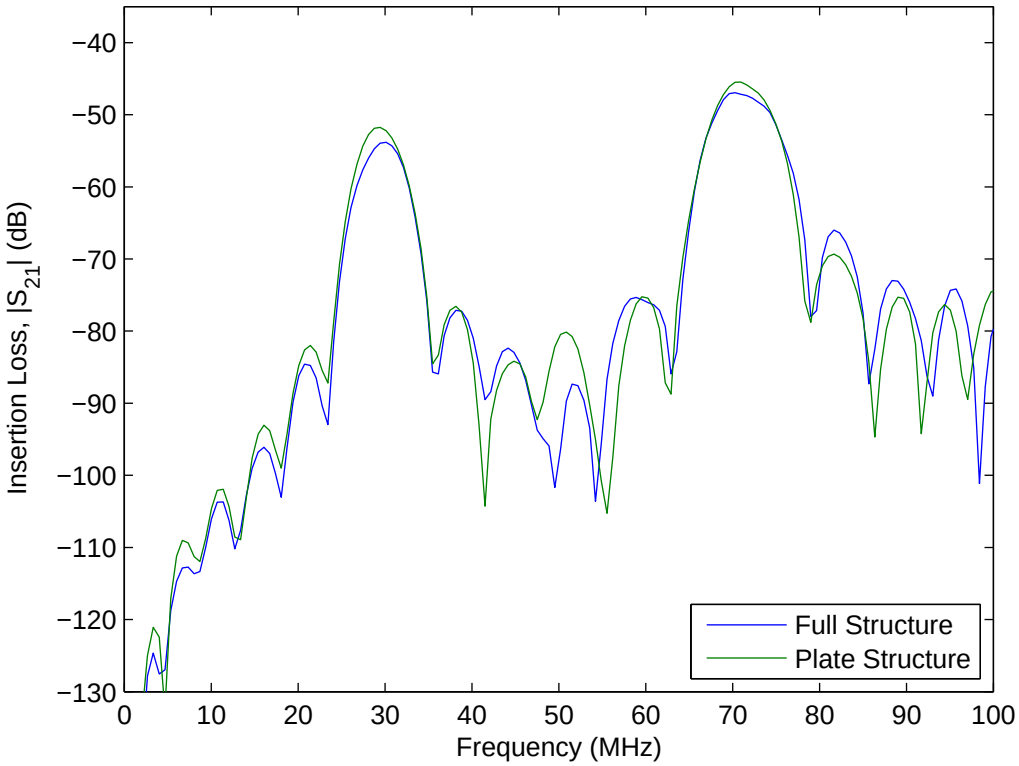


Figure 5.15: 2D FEM FPW Device - Insertion Loss Characteristics

From the results presented in this section, it is plausible to simulate a FPW device as

a thin plate without the supporting silicon structure. However, the centre frequencies of a fabricated device may deviate slightly from the FEM simulation results due to the geometrical assumptions applied. The deviation is response may be insignificant as process parameters, such as layer thickness, metallisation ratio and crystallography could induce a larger shift than those brought about by these assumptions. For the rest of the simulations presented in this chapter, the thin plate structure will be used.

### 5.4.4 2D FPW Device Electrostatic Charge Density and Capacitance

Whilst the insertion loss characteristics for a 2D FPW device have already been presented, Figure 5.15, it is instructive to examine the 2D electrostatic charge density. In particular, the electrode node density and its relationship to solution convergence is investigated. To undertake this analysis, it is necessary to increase the number of nodes on the surface, thus to avoid licensing limitations an alternative structure is used. Surface densities in $x$ are varied between $5000$ and $1400$ nodes and the input transducer charge density determined. The particular design considered is similar to devices studied in literature used for sensing applications in liquid media [8], however this structure consists of a reduced number of IDT electrodes. The simulated device consists of $2$ electrode pairs, with a $2.0$µm $Si_3N_4$, $0.4$µm Al and a $0.6$µm ZnO layers and a wavelength of $96$µm. As the output IDT was not modelled, electromagnetic feedthrough is ignored. The simulated device measures $2800$µm in the $x$-direction. Similarly to all other charged-based simulations, the aluminium ground layer is forced to $0$V and a d.c. voltage of $\pm 0.5$V is applied on alternative transmitter electrodes.

Electrostatic analysis of an IDT indicates that the charge density approaches infinity at the electrode edge. The FEM however assumes that the field variables vary smoothly, thus some error will be associated with the charge at these edges. However, provided that the nodal density is relatively high over the electrode width, this error should be insignificant. The spectral domain Green's function analysis of interdigital transducers already discussed will serve as a benchmark as which to compare the FEM simulations. Care must be taken when comparing the alternative modelling techniques as the spectral domain Green's function results must be scaled by the effective nodal spacing to convert to the correct units.

Figure 5.16 depicts the FEM derived surface charge density with a nodal density of 1 node / 2.0µm. It can be seen that along the electrode edges, the charge begins to increase, however does not approach infinity. The FEM simulation demonstrates that the charge density changes polarity at the electrode edge. It is believed that this discrepancy is caused by the linear interpolation used in the analysis. If the node density is increased about the electrode edge, this effect is reduced, however not totally negated. As there is no conducting medium between the IDT fingers, the charge in this region should be zero.

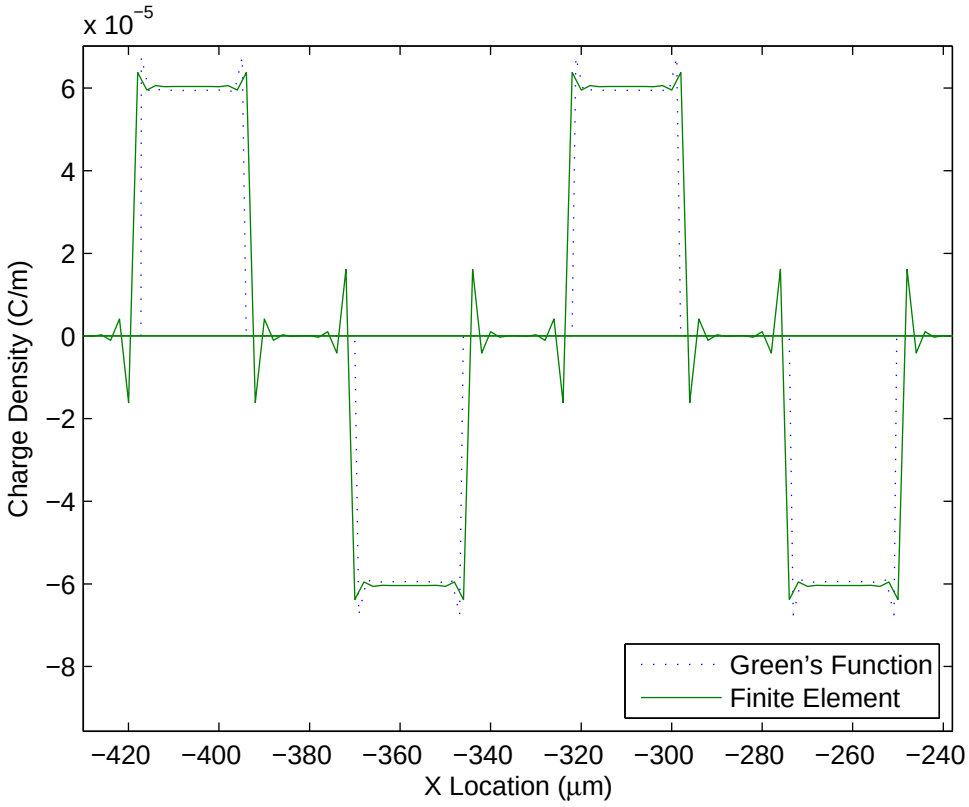


Figure 5.16: 2D FEM FPW Device - Input Electrode Electrostatic Analysis

To perform a comparison between the spectral domain Greens function and FEM results, charge must be integrated over the device surface. Charge neutrality states that the total charge across the device surface must equal zero. Table 5.4 indicates that despite the previously mentioned issues with the FEM, the electrostatic analysis appears to be converging to the theoretical solution of zero. Whilst increasing the nodal density increases accuracy, consideration must be taken into account of the computational

effort required to solve the problem. As the piezoelectric layer is bounded by a ground plane, the simulation can be simplified further by removing the $Si_3N_4$ and Al ground layers, provided that the bottom of the ZnO is electrically grounded. However, it was found that this approximation was invalid for the 3D structure as fringing effects need to be considered.

Table 5.4: Residual Charge vs. Node Density

| Node Density | Total Nodes | Residual Charge (C/m) |
|---|---|---|
| 1 node / 2.0µm | 9807 | $-2.94 \times 10^{-14}$ |
| 1 node / 1.0µm | 19607 | $1.97 \times 10^{-16}$ |
| 1 node / 0.6µm | 29407 | $2.57 \times 10^{-17}$ |
| Green's function | 52 | $0.00 \times 10^{0}$ |

To determine the static input capacitance of the transducer, a modified version of the ANSYS macro CMATRIX is used. Equally, the integral of the electrostatic charge density could be undertaken, however this process only provides the self-capacitance of the electrodes. By using the modified macro, the self and mutual capacitances of the electrodes can be calculated. In terms of modifications, the macro was edited to prevent the removal of nodal charge loads and the applied boundary conditions adjusted to apply a differential load voltage of $1V$. For this analysis, an IDT can be considered to be two capacitors connected in series with an voltage source, Figure 5.17, with the self-capacitances denoted $C_{11}$ and $C_{22}$ and a mutual capacitance $C_{12}$. In practical applications, the mutual capacitance is typically one to two orders of magnitude smaller than the self-capacitance and hence typically neglected. Table 5.5 lists the ANSYS generated capacitances for a variety of finger pair combinations per unit length. To obtain the actual capacitance of the device, the values in Table 5.5 must be multiplied by the IDT aperture. The simplified FPW structure in Figure 5.14 was used for this analysis. For comparative purposes, the equivalent capacitances derived from the spectral domain Green's function are also presented.

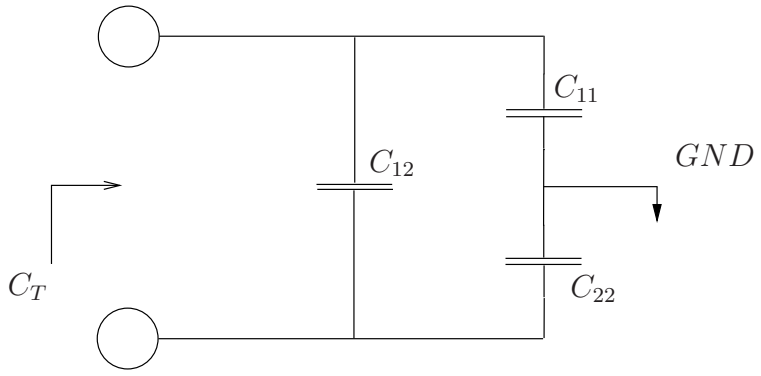


Figure 5.17: FPW Device FEM Equivalent Input Capacitance

Table 5.5: Static Capacitance for Varied Electrode Configurations (F / unit length)

| Electrode Pairs | $C_{12}$ | $C_{11} + C_{22}$ | $C_T$ | Greens Function |
|---|---|---|---|---|
| 1 | $9.86 \times 10^{-12}$ | $5.19 \times 10^{-10}$ | $5.29 \times 10^{-10}$ | $6.19 \times 10^{-10}$ |
| 2 | $2.89 \times 10^{-11}$ | $1.08 \times 10^{-9}$ | $1.11 \times 10^{-9}$ | $1.24 \times 10^{-9}$ |
| 3 | $4.84 \times 10^{-11}$ | $1.59 \times 10^{-9}$ | $1.64 \times 10^{-9}$ | $1.86 \times 10^{-9}$ |
| 4 | $6.80 \times 10^{-11}$ | $2.10 \times 10^{-9}$ | $2.17 \times 10^{-9}$ | $2.48 \times 10^{-9}$ |
| 8 | $1.46 \times 10^{-10}$ | $4.13 \times 10^{-9}$ | $4.28 \times 10^{-9}$ | $4.48 \times 10^{-9}$ |

### 5.4.5 2D FPW Device Displacement Profiles

Alternative numerical models presented in Section 3.3.2 indicated that a FPW device can support an infinite number of Lamb modes. At higher thickness-frequency products, where the dispersion curves begin to cross each other, Figure 3.3, it becomes quite difficult to differentiate between antisymmetric or symmetric modes. One technique is via the depth versus displacement profiles, which can be readily achieved by exporting the ANSYS degree of freedom solution files for further processing.

The analysis presented in Section 4.3.1 operated solely in the frequency domain and hence time independent. Conversely, a dynamic transient analysis by nature operates in the time domain. To determine the displacement profile of a given mode, the time domain simulation must be 'paused' at an appropriate point where the displacement is a maximum. A plane through the depth of the device at the $x$ origin, $224$µm from the furthermost edge of the first input electrode, was selected to evaluate the displacement

of two primary modes. A total of 21 nodes were selected through the device depth. As the distance to the reference plane and the frequency of the modes was known, an approximate time could be determined at which the mode of interest would be passing over the reference plane. For the antisymmetric mode, this corresponded to 72ns and 33ns for the symmetric mode. Figures 5.18 and 5.19 depict the absolute normalised displacement profiles for the primary antisymmetric and symmetric modes respectively. For simplicity, both graphs are normalised to the peak displacement in the propagation direction $x$. The piezoelectric surface of the device is indicated by a normalised thickness of 1.

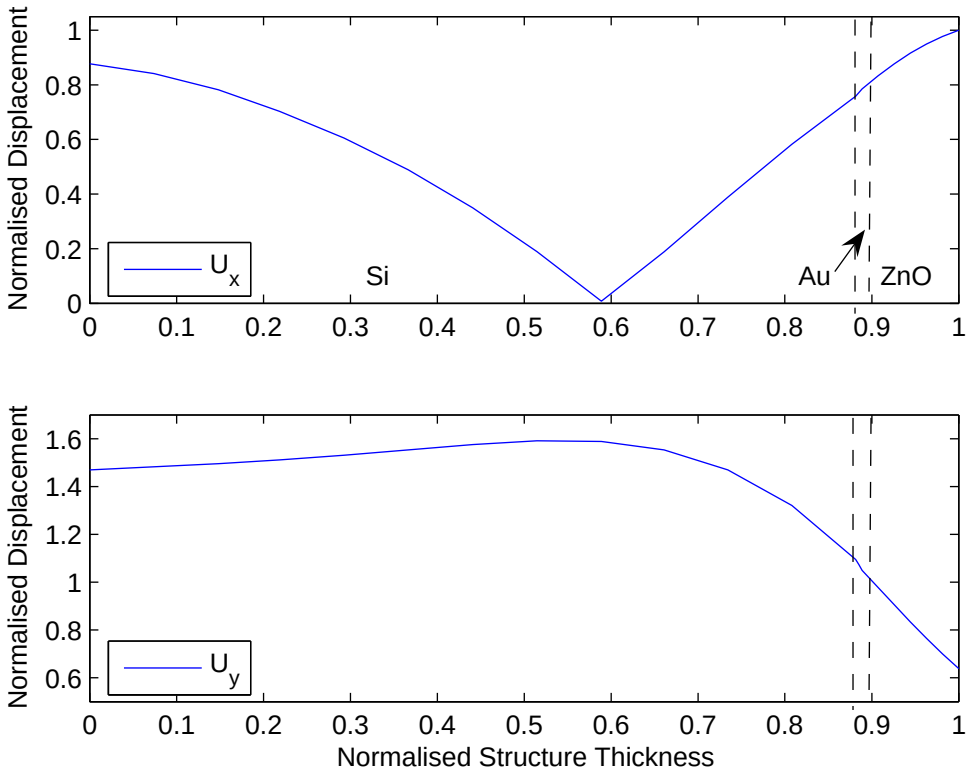


Figure 5.18: 2D FEM FPW Device - Primary Antisymmetric Mode Displacement Profile

In an isotropic material the longitudinal component of the antisymmetric displacement is a maximum at the plate edges and a minimum at the median. In contrast, Figure 5.18, the longitudinal displacement is not quite symmetrical about the centre of the plate. This is due to the multilayered structure used, where different stresses are distributed throughout the device thickness. However, the maximum longitudi-

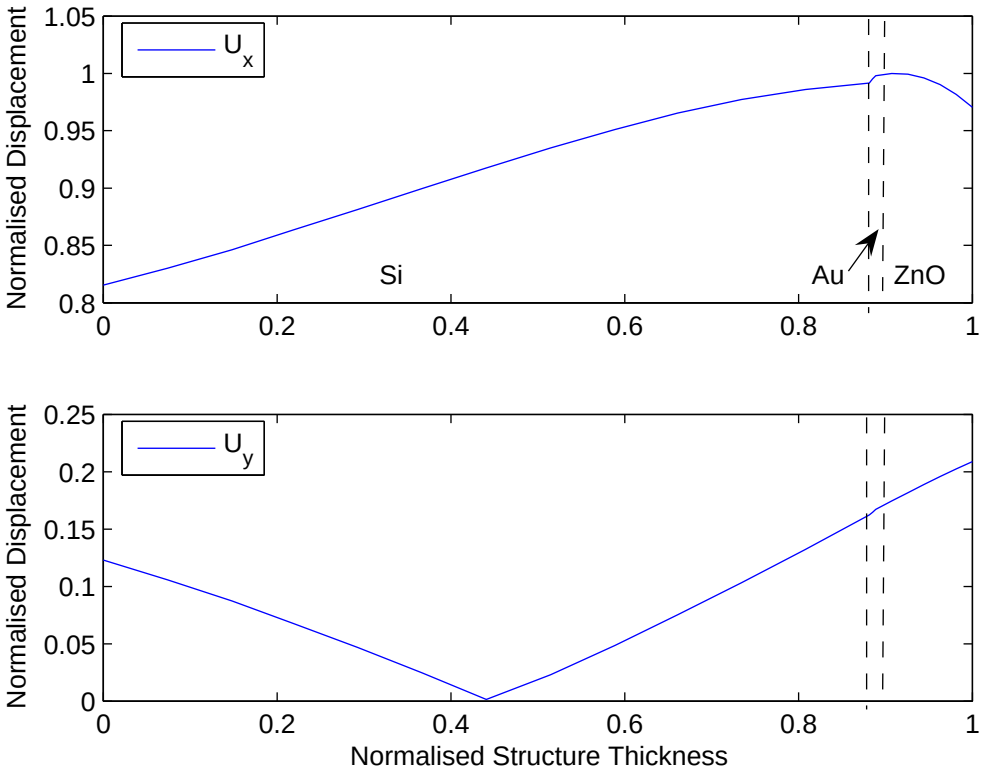


Figure 5.19: 2D FEM FPW Device - Primary Symmetric Mode Displacement Profile

nal displacement is as expected at the two plate surfaces. Derivative discontinuities can be seen at the various layer interfaces, verifying the presence of different stress fields within the structure. The transverse displacement is larger than the longitudinal displacement, and hence dominates the motion of the antisymmetric mode. This behaviour was illustrated in the analysis presented in Section 4.3.1, thereby verifying the FEM derived solutions. The larger displacement of the bottom side of the structure could be potentially advantageous for sensing applications in liquid media for two reasons. Firstly, sensitivity analysis presented in Section 4.3.2 indicates that higher mass sensitivity can be obtained when a larger displacement is present, and secondly the fabrication process creates a natural reservoir on the silicon side of the structure, thus shielding the sensitive IDTs from potentially corrosive substances. The mode type, either antisymmetric or symmetrical, can also be confirmed by the displacement profile presented. As a basic rule, if the $x$ displacement is greater at the device surface, and tends to zero at some point within the structure, then an antisymmetric mode is

assumed. Note that this process is valid for the first two primary modes.

Conversely, the longitudinal displacement is dominant for the first symmetric mode, Figure 5.19. At its maximum, the displacement of the transverse component is only $20\%$ of that in the longitudinal direction. In terms of liquid sensing applications, the relatively small displacement in the transverse direction would be dissipated in the target liquid. Similar to the antisymmetric mode, the symmetric mode is identified by its displacement profile. Although the absolute displacement is presented, a change of particle direction exists in the transverse displacement component between the two surfaces of the plate. If this change is identified, then it is assumed that a symmetric mode is present.

Once the displacements have been determined, mass sensitivity of the device can be calculated via perturbation theory [14]. This process assumes that the target analyte does not significantly alter the propagation characteristics of the device. To apply this approach to the FEM model also requires extraction of the acoustic power, which can be determined via the Poynting vector, however this is beyond the scope of this thesis.

### 5.4.6 Electromechanical Coupling Coefficient

Evaluation of the electromechanical coupling coefficient is essential to critically evaluate any acoustic wave device design. If the coupling coefficient is small, the acoustic response could be lost due to background noise or feedthrough effects. To evaluate $K^2$, several different techniques can be applied. The most commonly used technique is a modification of the electrical boundary conditions, placing an effective short circuit over the device surface. By altering the boundary conditions, the voltage on the piezoelectric surface is set to $0$V, whilst the charge remains unknown.

In ANSYS terms, a metalised boundary condition is obtained by coupling the voltage degree of freedom for all free piezoelectric surface nodes. The space between the IDTs is also completely metalised and hence set to $0V$. It should be noted that the ANSYS metalised surface coupled set is not the same as the ground plane set. Although the simulation can be easily modified to enforce metalised surface conditions, obtaining accurate results is not a simple task primarily due to the lack of spectral resolution. Coupling coefficients for the FPW in Figure 5.7 are approximately $0.59\%$ and $0.35\%$ for

the first antisymmetric and symmetric modes respectively as calculated via the stiffness matrix method. In terms of frequency, approximate shifts of $85$kHz and $123$kHz are expected between open and short circuit boundary conditions. Investigation of simulation parameters, to be discussed shortly, have shown that in order to achieve sufficient resolution to determine the change in operating frequency, a timestep of $1$ns, with a total of $5882$ substeps would be required. Due to resource limitations, a simulation with these parameters was not conducted, however a $758$ step metalised surface simulation was performed with a $1$ns timestep. Figure 5.20 illustrates the results of the metalised surface simulations.

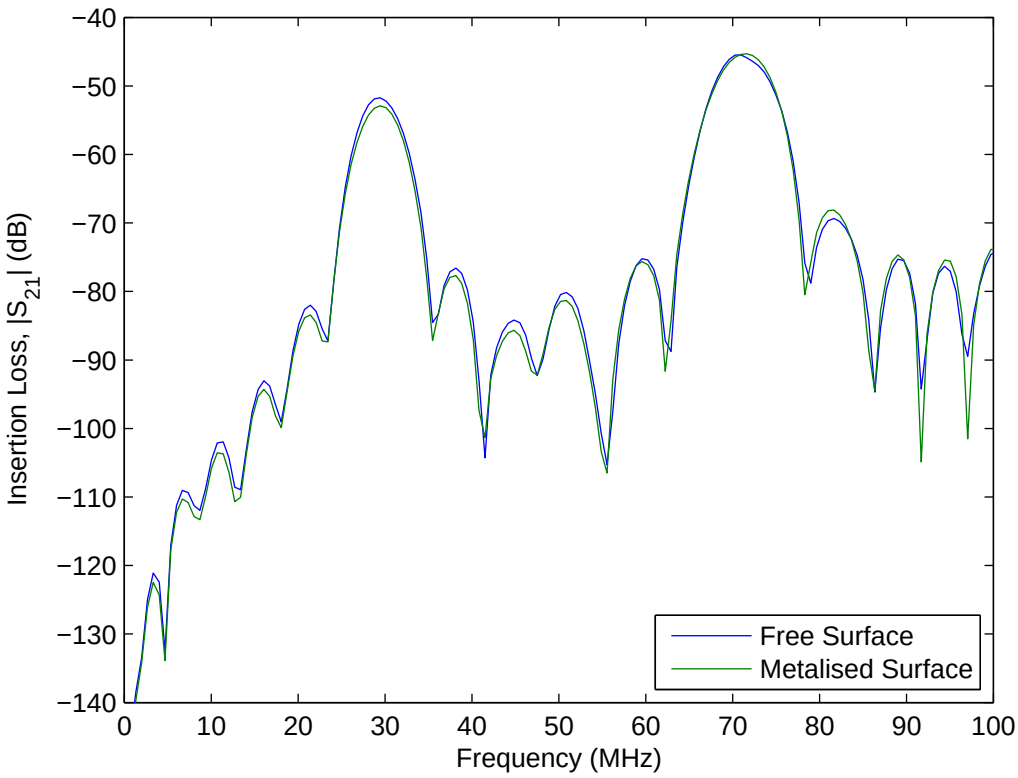


Figure 5.20: 2D FEM FPW Device - Metalised Surface Insertion Loss Characteristics

From Figure 5.20, it is not possible to accurately determine the shift in operating frequency due to the metalised boundary conditions. Upon closer inspection, the metalised frequencies are $29.46$ and $70.58$MHz for the antisymmetric and symmetric modes respectively. Under a metalised surface condition, the centre frequency of a mode should be reduced, which is shown not be the case with the symmetric mode. Thus,

for the developed simulation, the FEM is unable to accurately determine the metalised conditions. A potentially more appropriate method is the crossed-field model [1] which considers the device admittance characteristics rather than a visual identification of the metalised boundary condition frequency shift.

To determine $K^2$, it is necessary to know the device input admittance, $Y_{11}$. This calculation was previously obtained to determine the insertion loss characteristics of the device. From the crossed field model, $K^2$ is determined by equation 5.22. The electrode capacitance previously determined, Section 5.4.4, is used for this calculation. All other parameters are constants and do not depend on the FPW structure.

$$K^2_{A_0} = \frac{\mathrm{Re}\,(Y_{11})}{8 f_0 C_s N^2}, \tag{5.22}$$

where $N$ is the number of electrode pairs.

Figure 5.21 illustrates the simulated FPW input admittance characteristic, $Y_{11}$. Using equation 5.22, with $8$ electrode pairs and an aperture of $200$µm, the antisymmetric mode $K^2$ is evaluated at $0.55\%$.

Whilst the crossed-field model has been shown to work for the antisymmetric mode, there appears to be a slight discrepancy in the $K^2$ value for the symmetric mode. In both the spectral domain Green's function and ANSYS simulations, it was not possible to accurately determine the symmetric mode coupling coefficient from the device admittance characteristics. Further investigation of the Mason equivalent circuit used to derive the crossed-field model has shown that its application depends on the primary displacement of the acoustic wave. Investigation of the symmetric mode presented in Section 5.4.5 has shown that the primary motion is in the longitudinal direction. The crossed-field model assumes that a Rayleigh mode displacement occurs, and hence should not be used for the evaluation of the coupling for the symmetric mode. The alternative in-line model also does not accurately predict the symmetric mode coupling. Thus, the only effective solution to determine $K^2$ for the symmetric mode is by the shift in frequency caused by the metallisation of simulated FPW structure surface. In liquid density sensing applications, the symmetric mode is typically not used as it has a strong displacement component in the transverse direction, which is damped by the applied liquid.

In this section, it has only been possible to accurately determine the antisymmetric

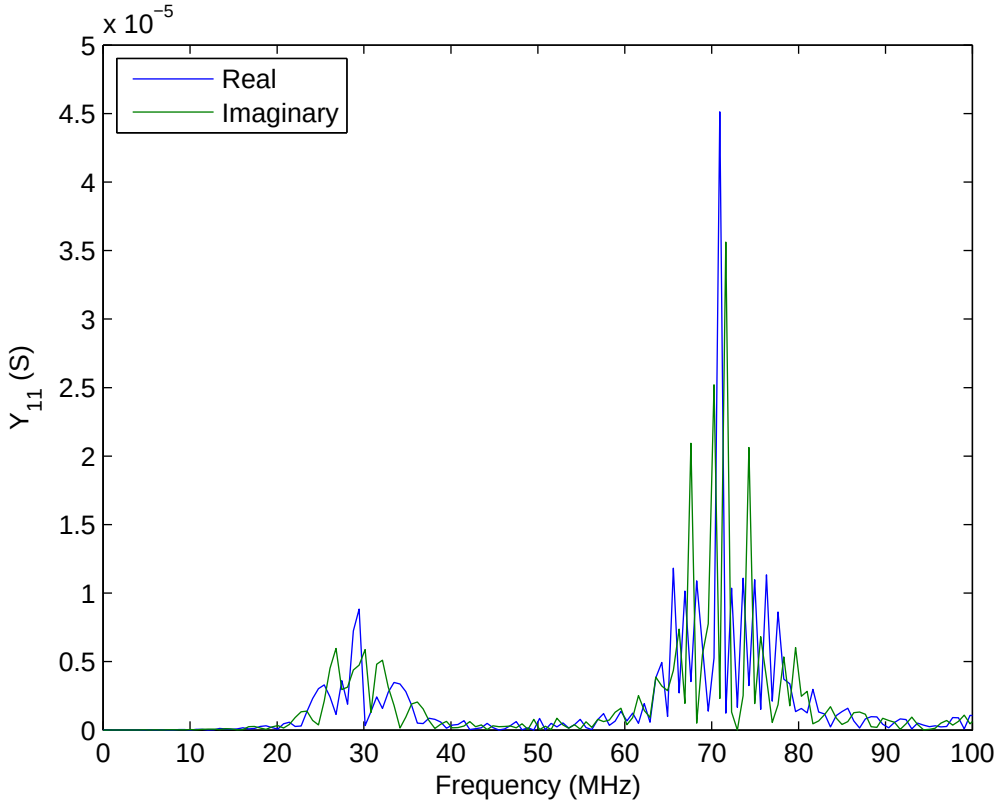


Figure 5.21: 2D FEM FPW Device - Input Admittance

coupling coefficient using the crossed-field model. If a stronger piezoelectric material, or an alternative configuration used, it may be possible to determine coupling coefficient via the metalised operating frequency shift. In other acoustic wave devices, coupling coefficients as high as $6\%$ are routinely obtained [141]. With such a large frequency shift, it would be a relatively simple task to obtain the value of $K^2$ by inspection.

## 5.5 FEM Parameter Modification

Although simplifications in terms of simulated structure geometry have been shown to improve the computation time of the FEM, there are several other user controllable parameters within ANSYS that can also be modified. Depending on the parameters, these can either reduce the computation time, or greatly increase it. This section examines three different ANSYS simulation parameters and their impact on the frequency

response characteristics of a FPW structure. This analysis also demonstrates the need for a careful and rigourous approach to applying the FEM when simulating an acoustic wave device. Throughout this study, the simplified charge model of Figure 5.14 is used.

### 5.5.1 Simulation Time

With regards to a transient analysis, simulation time dictates the virtual ANSYS time that the physical solution is calculated over. From the overall time and the stepping between successive calculations, known as a timestep, the total number of substeps is determined. In terms of an acoustic wave device, the simulation time will determine the distance travelled by the propagating wave. Particular care must be taken when working with multiple acoustic modes as they propagate at different velocities. In these scenarios, the simulation time must be long enough to allow the lower order modes to pass a given reference point, however not too long as to bring about triple transit interference. In terms of the insertion loss characteristics, triple transit effects are undesirable and therefore simulation time should be selected to avoid these effects. Section 5.5.1.1 illustrates the effects of triple transit and suggests methods to reduce its influence.

For the results presented, the two primary modes propagate at $2828.2$ and $6813.1$m/s respectively. The ANSYS simulation length is dictated by the time it takes for the lower velocity antisymmetric mode to travel from the furthermost input electrode to the last output electrode, an overall distance of $1888$µm. With the given velocities the antisymmetric mode would reach its destination at approximately $668$ns. To ensure that mode passes the last output electrode the simulation was extended to $758$ns. During the same period of time the higher velocity symmetric mode will propagate $5164$µm. Therefore, the simulated structure must be made sufficiently large that over the given period of time the symmetric mode has not reflected from the simulation boundaries and impinged for a second time on the output electrodes. The round trip distance for the simulated device presented is $5550$µm, thus the reflected symmetric mode should not influence the insertion loss characteristics. It should be noted that this analysis focuses directly on the first two primary modes and refections will still be preset from various higher order modes.

One issue with modelling a FPW device is the relatively high aspect ratio of the structure. That is, the device may be up to 100 or more times larger in the propagation direction than in the thickness of the layers. Using the theory from Section 3.3.2, the thinner the device, the larger the frequency separation of the two primary modes, corresponding to vastly different velocities. In these cases, it may not be possible to make the structure large enough to negate the reflected symmetric mode.

Figure 5.22 illustrates the change in insertion loss characteristics due to modification of the overall simulation length. Simulation time was varied between 200 and 758ns, with the timestep set to a constant 1ns. In terms of frequency, all simulations correctly resolved the first two primary modes. Although the centre frequencies are correct, there appears to be a logical change in insertion loss value. With a shorter simulation time, less of the acoustic wave passes over the receiving electrode, and thus its relative amplitude will be decreased in comparison to higher frequency modes.

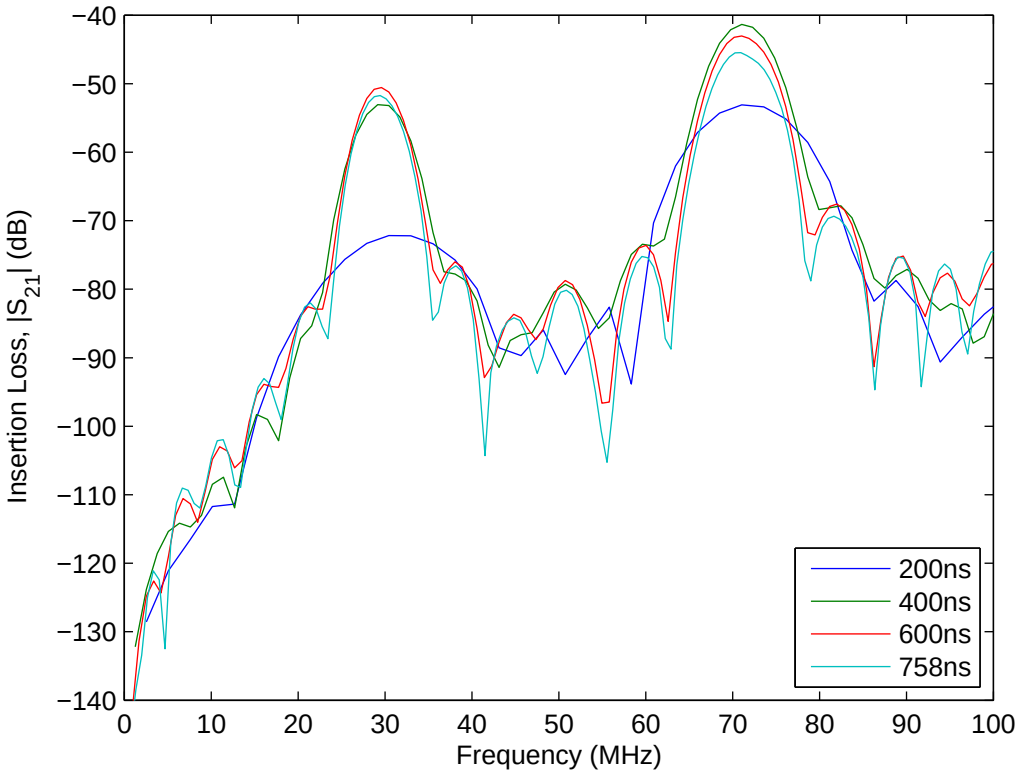


Figure 5.22: 2D FEM FPW Device - Simulation Length Modification

Although not visually apparent in Figure 5.22, the modification of simulation length

has changed the spectral resolution of the results. This is quite an important result as a link can now be established between the minimum frequency resolution and its relationship to the time domain FEM simulation. Table 5.6 describes the spectral resolution of the various simulations as well as the calculated change in insertion loss.

Table 5.6: FEM Simulation Length vs. Insertion Loss and Spectral Resolution.

| Simulation Length | $A_0 s_{21}$ (dB) | $S_0 s_{21}$ (dB) | Frequency Resolution $f_{res}$ (MHz) |
|---|---|---|---|
| 200ns | $-72.16$ | $-53.09$ | 2.50 |
| 400ns | $-53.05$ | $-41.35$ | 1.25 |
| 600ns | $-50.55$ | $-43.03$ | 0.833 |
| 758ns | $-51.75$ | $-45.46$ | 0.6596 |

By inspection the frequency resolution can be seen to obey equation 5.23. Thus, to improve the frequency domain resolution, either a smaller timestep is required, or the number of substeps increased. Either parameter will increase the computational time, but only a smaller timestep will provide beneficial results. If the simulation time was increased, the higher order modes would cover a greater distance and be reflected at the simulated device boundaries, causing triple transit interference. With a smaller timestep the acoustic wave travels the same distance and, provided the simulated structure is of appropriate length, will not degrade the results.

$$f_{res} = \frac{1}{2nt_s}, \tag{5.23}$$

where $n$ is the number of substeps and $t_s$ is the simulation step time.

The insertion loss values in Table 5.6 do not appear to follow a pattern as the simulation time is changed. To confirm that the solution had correctly converged, the insertion loss was compared against the spectral Green's function model, where excellent agreement was obtained.

#### 5.5.1.1 Triple Transit Interference

Triple transit interference is an undesirable effect brought about by the reflection of an acoustic wave at physical device boundaries. In practice, the reflected wave is usually

at a reduced amplitude and causes a small degradation in performance of the device [1]. A difficulty with the ANSYS simulation package is that it is not possible to include damping or infinite elements that can be used in conjunction with a piezoelectric transient analysis. In a pure acoustic problem, where the wave is caused by a localised change in pressure, a 2D infinite boundary can be simulated using the *Fluid129* element. The author did attempt to incorporate this into the presented simulations, however the ANSYS package would not commence the solution phase due to a mismatch of boundary conditions.

To determine the impact of triple transit, either the total simulation runtime should be increased to allow for reflections, or the simulated device boundaries shortened whilst keeping the overall simulation time constant. It was decided to reduce the simulated device length as this procedure requires less computational effort. The $x$ dimension of the 2D FPW structure in Figure 5.14 was reduced to $2800$µm with all other values left constant. In order to visualise the effect of triple transit interference, the displacement degree of freedom was animated over time. Figure 5.5.1.1 provides an exaggerated snapshot of the FPW displacement as the two primary modes reach the physical boundaries of the device. Once the modes reached the boundaries, both were reflected and travel towards the output IDT for a second time.

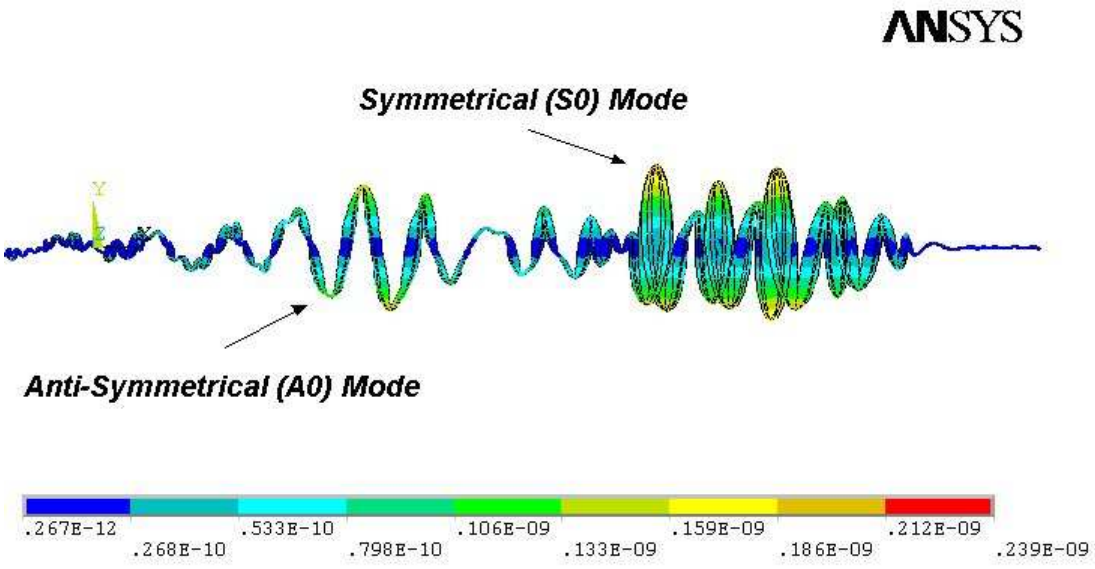


Figure 5.23: 2D FEM FPW Device - ANSYS Mode Displacement

Figure 5.24 illustrates the quite profound change in insertion loss characteristics due to a reduction in simulated FPW device boundaries. The centre frequencies of the two primary modes are significantly obscured, making it difficult to obtain an accurate measure of operating frequency. It can also be seen that the bandwidth of the modes has been reduced, thus the centre frequencies could not be determined by this method either.

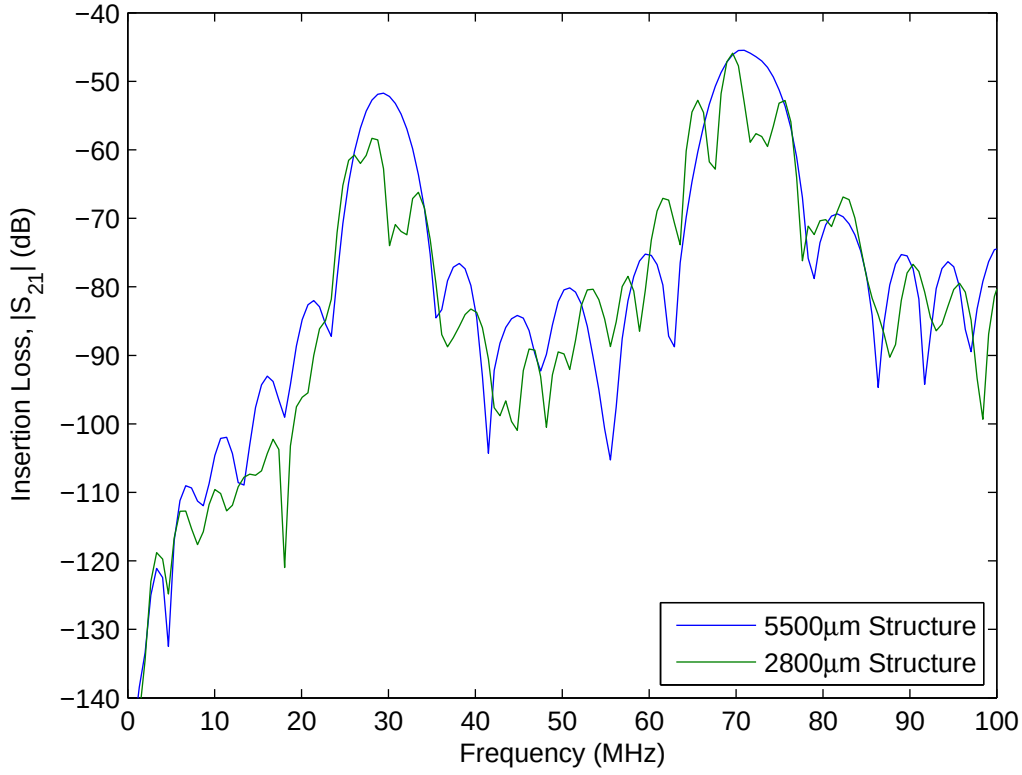


Figure 5.24: 2D FEM FPW Device - Insertion Loss Characteristic with Triple Transit Influence

To reduce the effect of triple transit, several simulations were conducted that focused on the modification of the material parameters at the boundaries of the device. Initially it was believed that a fictional material could be constructed that exhibited low shear and longitudinal velocities, determined by equations 5.24a and 5.24b. Silicon material properties were used as the basis for the fictional damping material and the density modified with the stiffness constants held constant. The simulated FPW device was modified to $4$ electrode pairs, silicon thickness altered to $12.0$µm and the gold

layer increased to $0.3$µm, with corresponding centre frequencies of $17.85$ and $67.28$MHz for the antisymmetric and symmetric modes respectively.

$$v_s = \sqrt{\frac{c_{44}}{\rho}} \tag{5.24a}$$

$$v_l = \sqrt{\frac{c_{11}}{\rho}} \tag{5.24b}$$

The undamped structure $x$ dimension was reduced to $3568$µm. Damping material was placed at the simulated device boundaries and extended for a further $1000$µm, resulting in an overall length of $5568$µm. The piezoelectric and ground plane layers were also placed on the damping material. To confirm that this method, an initial simulation was completed that set the density of the damping material identical to that of silicon. This result was compared against another structure that did not include the damping material, however was the same length, where the insertion loss characteristics proved to be identical. Once it has been established that the technique was viable, the density of the fictional material was modified according to Table 5.7. The shear and longitudinal velocities are also presented for comparative purposes.

Table 5.7: Fictional FEM Damping Material Densities and Velocities.

| Density ($\rho$) | $v_l$ (m/s) | $v_s$ (m/s) |
|---|---|---|
| 2332 | 8729.4 | 5840.9 |
| 4664 | 5960.5 | 4130.2 |
| 9892 | 4092.8 | 2836.0 |
| 18584 | 2986.0 | 2069.1 |

Figure 5.25 illustrates the insertion loss characteristics of the device with the addition of a fictional damping material. The antisymmetric mode has been resolved correctly, but the higher velocity symmetric mode has not. The displacement degree of freedom for all modes was animated over time, and it could clearly be seen that the symmetric mode did indeed propagate to the end of the structure. In comparison to Figure 5.24, the symmetric mode appears to show characteristics of triple transit interference. To confirm the nature of the reflection, the displacement about the point where the silicon joined the damping material was animated. As the symmetric mode

reached this interface, part of the wave was reflected back towards the output IDT, thus providing characteristics very similar to triple transit interference. It is also apparent from Figure 5.25 that the higher the density of the damping material, the greater the reflected energy. This correlates with a greater mismatch in material properties, hence more 'energy' is reflected.

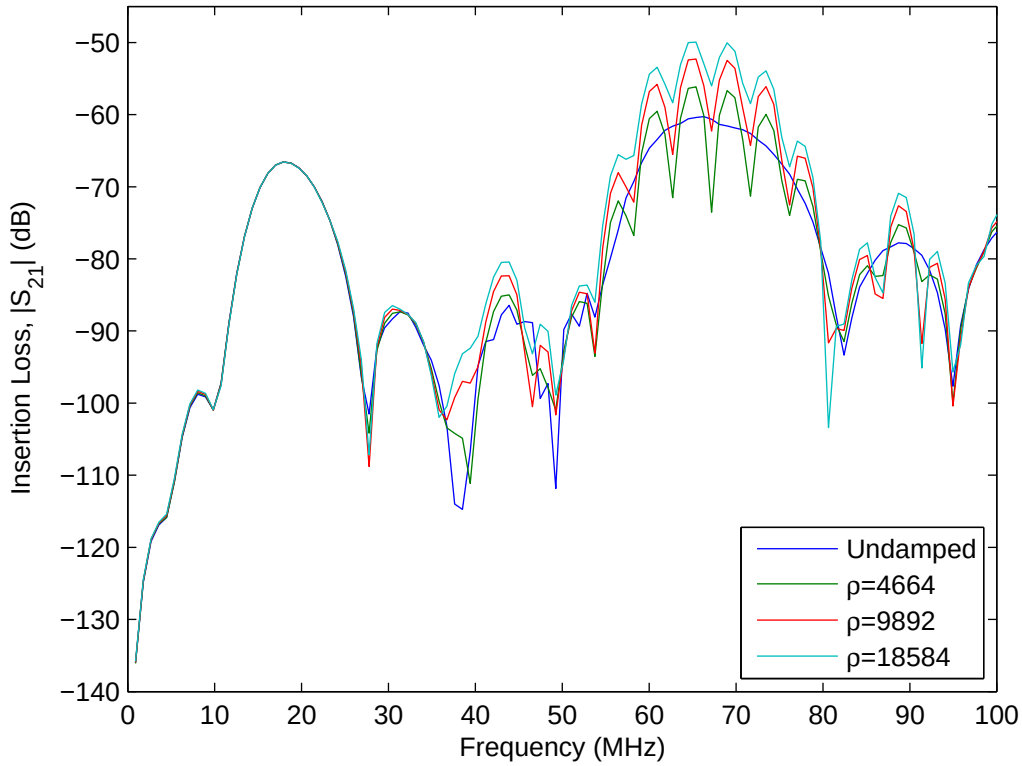


Figure 5.25: 2D FEM FPW Device - Damping Material Simulation

Although numerous simulations have been undertaken, the author has not been able to find a suitable technique to simulate an infinite boundary that can be used in a piezoelectric analysis. The most appropriate solution has been to extend the simulated structure boundaries to prevent the higher velocity modes from reaching the output IDT a second time.

### 5.5.2 Simulation Timestep

The second time based parameter that can be modified is simulation timestep. Recall that a transient analysis consists of a series of static solutions, where the simulation

timestep sets the spacing between subsequent analyses. If the timestep is set too large small changes in the solution may be overlooked, however care should be taken as not set a too fine timestep as this will greatly increase the computational resources required. Where possible, the overall simulation time was kept constant at $758$ns and the timestep varied between $1$ and $5$ns. As the timestep and the overall number of substeps are naturally related, an increase in timestep results in a corresponding reduction in the number of simulation substeps. Figure 5.26 illustrates the insertion loss characteristics of the simulated FPW device of Figure 5.14 with respect to the modified timesteps. The excitation function, equation 5.19 was also redefined to match the width of the timestep under consideration.

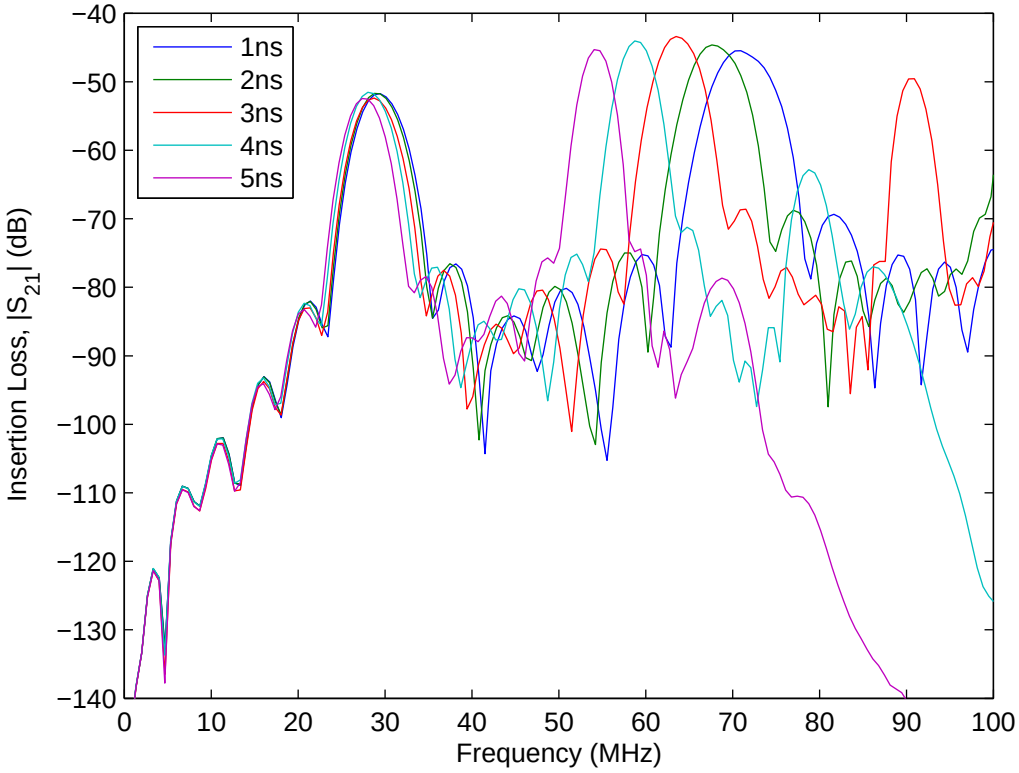


Figure 5.26: 2D FEM FPW Device - Timestep Modification

To quantify the change in device frequency response, the deviation in centre frequency for the two primary modes was tabulated, Table 5.8. The deviation in frequency is referenced to the spectral domain Green's function centre frequencies. Also indicated is the simulation timestep and total number of substeps.

Table 5.8: FEM Node Density vs. Primary Mode Centre Frequencies.

| Timestep | $f_{A_0}$(MHz) | $\triangle f_{A_0}$ (MHz) | $A_0s_{21}$(dB) | $f_{S_0}$(MHz) | $\triangle f_{S_0}$ (MHz) | $S_0s_{21}$(dB) |
|---|---|---|---|---|---|---|
| 1ns | 29.46 | - | $-51.75$ | 70.97 | - | $-45.46$ |
| 2ns | 28.79 | $-0.67$ | $-51.69$ | 67.62 | $-3.35$ | $-44.62$ |
| 3ns | 28.75 | $-0.71$ | $-52.38$ | 63.52 | $-7.45$ | $-43.39$ |
| 4ns | 28.05 | $-1.41$ | $-51.53$ | 58.76 | $-12.21$ | $-44.05$ |
| 5ns | 27.38 | $-2.09$ | $-52.43$ | 54.09 | $-16.88$ | $-45.31$ |

From Figure 5.26, an increase in the timestep significantly varies the insertion loss characteristics of the simulated device. The antisymmetric mode has typically been resolved within $7\%$ of its nominal value, however the symmetric mode is greatly shifted towards the lower end of the spectrum with a maximum deviation of $23.8\%$. As well as a reduction in centre frequency, the bandwidth of the mode is reduced by approximately the same value. Visually, the modification of the timestep causes 'frequency compression', where the higher frequencies are compressed, or shifted to lower frequency bands [142]. Investigation of the frequency shift associated with the symmetric mode indicates a linear dependence on the timestep, with a relatively consistent insertion loss value. Due to the limited spectral resolution it is not possible to determine the dependence of timestep of the antisymmetric mode, but it appears that it would also be linear. Further analysis of the 3ns simulation illustrates a mode at approximately $90.5$MHz. This is not a true mode, but rather an artifact of the post-processing stage.

Although the centre frequency of the modes has clearly shifted, the spectral resolution between all simulations is identical. Thus the shift in response is not brought about by a lack of spectral resolution, but rather the inability of the FEM to accurately determine the device response for a given timestep.

Modification of the timestep also influences the maximum resolvable frequency determined by the FFT used in the post-processing of the FEM results. In frequency terms, the sample points are inversely proportional to the timestep used, thus an increase in timestep is analogous to a reduction of the sample rate. From basic signal

processing, a reduction in the sample rate and the total number of data points results in a corresponding reduction in maximum frequency. Within the bounds of this study, it is apparent that the deviation in results presented is caused by an insufficient timestep rather than the lack of FFT data.

To confirm that the solution had converged, a final simulation was conducted with a timestep of $0.5$ns and the response compared to the $1$ns simulation. No measurable change in frequency response over the range of interest could be determined.

### 5.5.3 Node Density

The final parameter investigated was node density. Of all parameters discussed, node density can set the most constraints on the FEM simulation. For an optimum solution, particularly when dealing with rapidly changing field variables, the more nodes in a structure, typically the more accurate the solution. Nodal limits are typically set by the purchased licence, so a tradeoff must be made between solution accuracy and the cost to obtain the results. As previously mentioned, the research licence purchased by the author's university had an upper node limit of $128,000$, for which nodal densities were investigated up to this limit.

From the electrostatic analysis of the 2D simulations, it has been seen that an increase of nodes is beneficial to theoretical convergence. To examine the effect of nodal densities in a transient analysis, the number of nodes in the $y$-direction was kept constant, while the number in the propagation direction, $x$, were varied. As a metric, the point where the insertion loss deviated from the $1$ node / $2.0$µm structure, termed the maximum resolvable frequency, was used. Figure 5.27 illustrates the change in insertion loss characteristics for the simulated 2D FPW device when adjusting the nodal densities.

The deviation in response due to a change in nodal densities is far less than those found by modifying the timestep. With the exception of the last simulation, $1$ node per $8.0$µm, the centre frequencies and insertion loss values of the two primary modes have been resolved.

To further determine the impact of the nodal densities, a FPW device was simulated with uneven spacing in the $x$-direction. This technique has been used by several other

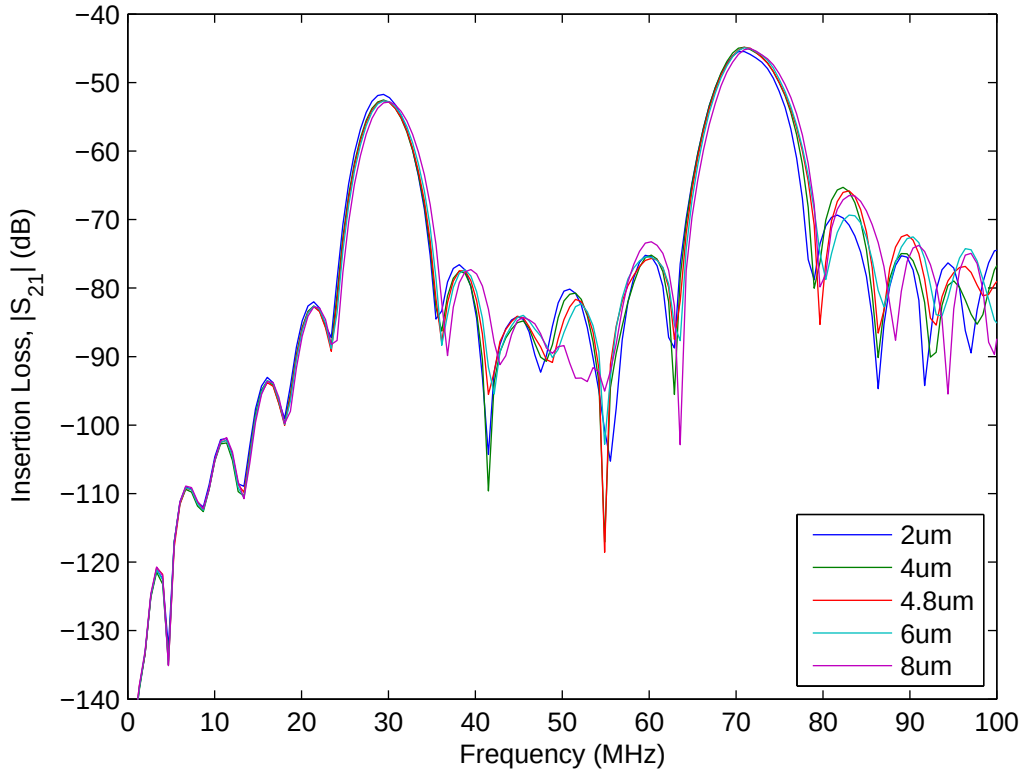


Figure 5.27: 2D FEM FPW Device - Node Density Modification

researchers, particularly when working with SAW structures [7]. For a FPW device, it was found that this approach leads to erroneous results.

## 5.6 FEM Simulated FPW Device Verification

Before the FEM is accepted as an effective tool for the analysis of acoustic wave devices, it must be verified against more traditional analysis techniques. In particular, this section provides a comparison between the results obtained via the novel FEM techniques presented and the spectral domain Green's function introduced in Chapter 4.

Basic electrical characteristics, such as capacitance and admittance, developed throughout this chapter, have demonstrated excellent agreement between the two models. The piezoelectric coupling coefficient has shown reasonable agreement for the antisymmetric mode, but a small discrepancy exists for the higher velocity symmetric mode.

Table 5.9: FEM Node Density vs. Primary Mode Centre Frequencies.

| Node Density | $f_{A0}$(MHz) | $\triangle$ $f_{A0}$ (MHz) | $f_{S0}$(MHz) | $\triangle$ $f_{S0}$ (MHz) | $f_{max}$(MHz) |
|---|---|---|---|---|---|
| 1 node / 2.0µm | 29.46 | - | 70.97 | - | - |
| 1 node / 4.0µm | 29.46 | 0.00 | 70.97 | 0.00 | 79.00 |
| 1 node / 4.8µm | 29.46 | 0.00 | 70.97 | 0.00 | 77.80 |
| 1 node / 6.0µm | 29.46 | 0.00 | 70.98 | 0.01 | 68.90 |
| 1 node / 8.0µm | 30.13 | $-0.67$ | 71.64 | $+0.67$ | 30.38 |

In terms of liquid density sensing applications, the antisymmetric mode is primarily used and as such the deviation in the symmetric mode value of $K^2$ is deemed irrelevant. Potentially more important than the basic electrical parameters presented is the overall performance of the device across a wide frequency range. Insertion loss characteristics are used as a metric to evaluate relative performance and accuracy of both techniques, Figure 5.28. For the spectral domain Green's function analysis, the same number of electrodes are used, with $8$ spatial divisions representing one electrode. In comparison, the FEM simulated device contained $13$ nodes per electrode. Although the same number of divisions could be used for the spectral domain Green's function analysis, the solution had successfully converged and hence the extra computational load was not necessary.

In terms of centre frequencies, the spectral Green's function model calculates the antisymmetric mode at $29.06$MHz, and the symmetric mode at $71.21$MHz. In comparison with the FEM model, the antisymmetric mode deviates by approximately $0.4$MHz and small shift of $0.24$MHz is found for the symmetric mode. The minor deviations in response can be attributed to the FEM simulation frequency resolution. Recall that for the FEM simulations the frequency stepping is approximately $0.67$MHz, thus the centre frequencies may not exactly coincide. Excellent agreement has been obtained between the FEM simulations and the spectral domain Green's function results for sidelobe values throughout the regime of interest.

The insertion loss values at the centre frequencies also appear to be well matched. For $A_0$, the insertion loss magnitude is $51.75$ and $51.27$dB for the FEM and spectral

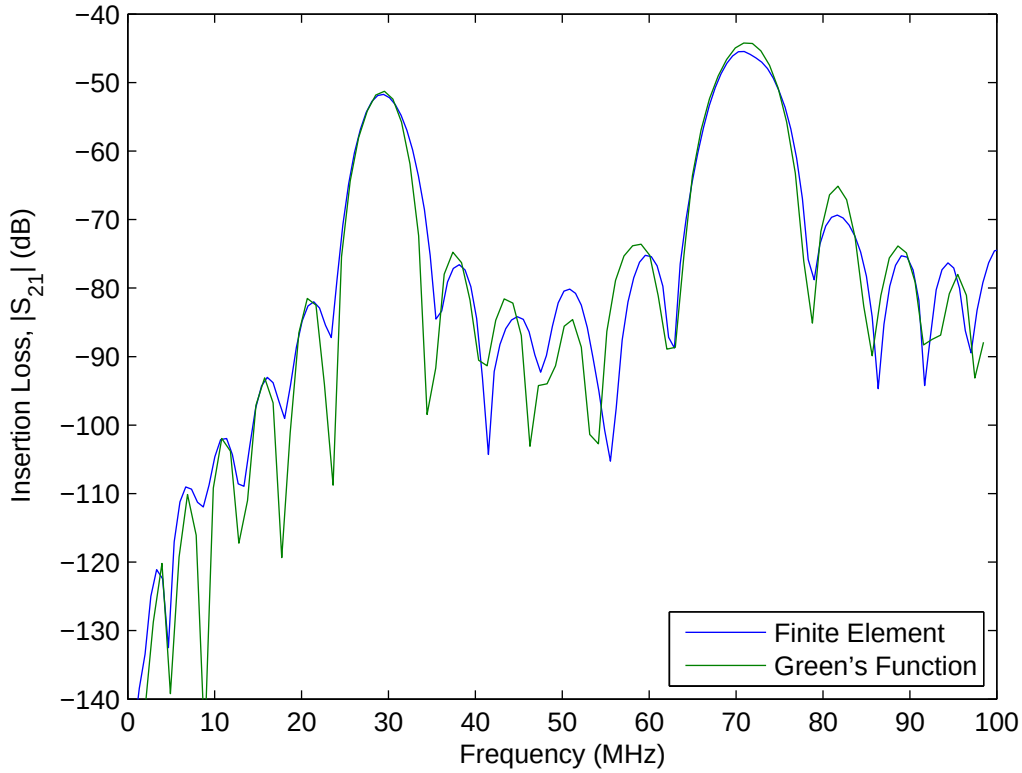


Figure 5.28: 2D FEM FPW Device - Simulation Verification

domain Green's function models respectively. Likewise, the symmetric mode predicts insertion loss values of $45.46$ and $44.24$dB for the two modelling techniques. The slight variations are certainly acceptable, as variances in the manufacturing process will have a greater impact than the slight differences in modelling techniques.

It was also envisaged to compare the two techniques described here against a device fabricated by the author. Unfortunately the fabrication process is still being developed and as such a comparison can not be drawn. However, the spectral domain Green's function has been verified against another devices in literature where excellent agreement has been obtained. Between the agreement with the FEM and spectral domain Green's function, it is deemed that the FEM technique can successfully simulate multilayered FPW devices.

Throughout this analysis, the insertion loss characteristics were used to determine the centre frequencies of the transducer. Equally valid is $Y_{21}$, the short circuit, forward-transfer admittance parameter. An example of these results can be found in the authors

published work [143]. Note that the incorrect axis label was used in Figure 2 and should read $Y_{21}$.

## 5.7 Limitations of the FEM

In the realm of this study, the FEM has successfully been applied to determine key electrical and mechanical parameters of a wide variety of multilayered FPW devices. Whilst the use of the FEM ultimately isolates the designer from the device physics, greatly simplifying the design process, care must be taken to ensure that solutions are feasible and provide meaningful results. A comprehensive understanding of the analysis tool and its limitations is essential to the successful completion of any engineering problem. The associated benefits of the FEM are numerous, such as geometry independent analysis and ease of use, however limitations also exist. This section discusses such limitations and how a simulation should be structured to minimise their influence.

The FEM assumes that fields, whether electrical or structural, vary slowly between nodes. In the case of IDT, where the charge density becomes singular at the electrode edge, the FEM miscalculates and the charge appears to have inverted polarity at these locations. A potential cause of the problem is the shape function used to approximate the solution. For the Plane13 element used, a linear interpolation model is assumed. To improve the solution at the electrode edge a higher order element, such as *Plane223* could be utilised. Whilst the solution would be more accurate, the resulting extra nodes would significantly increase the computational requirements. The author has investigated the use of uneven node spacing across the device surface and has found that the results are vastly different than from fixed spacing. Thus, to increase the number of nodes at the electrode edges, more nodes would be required across the complete device.

To accurately determine the behaviour of a FPW device, prior knowledge about the structure is required. For example, if the velocities of the first two primary modes are miscalculated, then due to incorrect device dimensions triple transit may occur, or the acoustic wave may not reach the output transducer over the given simulation time. A free application is available that uses the methods describe in Chapter 3 to deter-

mine the approximate velocities, and hence overcome this problem. Once the software was well understood, a solution can be found within minutes, therefore starting point issues are of little concern.

Highlighted throughout this chapter is the high computational requirements of the FEM package ANSYS. The author has had limited experience with other FEM tools, however believes that this is characteristic of the solution method. All results presented were calculated on a $2.66$GHz Pentium $4$ workstation with $2$GB of RAM and $160$GB of storage. Even with a significant amount of computing power, the complete solution for the FPW plate structure discussed in Section 5.4.3 took approximately $6$ hours to calculate, with a further $2.75$ hours to extract the results. The spectral domain Green's function approach presented in Chapter 4 is certainly a more efficient technique, however the same time, if not more, must be invested to develop an appropriate solution for complex geometries. The benefit of the FEM is its ability to discretise the problem and thus is very capable of solving complex structures.

Model verification plays a significant rile in any FEM analysis. In terms of a FPW device, the basic device has been verified using the spectral Green's function method which is sufficient verification for all other simulations presented. The verification does not have to be as in-depth as that presented in Section 5.6, and may be as simple as confirming the centre frequencies of the device against the methods in Chapters 3 and 4. When verifying the model, care must be taken to ensure that the alternative technique also makes the same assumptions about the given fields. For example, with the exception of the 3D FPW device simulation presented, all techniques within this thesis assume that the displacement in the $z$ plane is insignificant when compared against other directions. If this was not the case, then model verification would most probably fail. It should also be noted that verification can be as simple as the solution lies within an acceptable bounds when compared against another solution method.

Further to verification issues, simulation parameters can cause inaccuracies and convergence issues. It was shown in Section 5.5.2 that a too large timestep causes a shift in the centre frequency of the symmetric mode. Subsequently another simulation was developed that had a smaller timestep to confirm that the previous simulation had successfully converged. Whilst a smaller timestep is desirable, a tradeoff must be

made between the computational resources available and the time required to obtain a solution. It is suggested that in the preliminary stages of analysing an acoustic wave device using the package ANSYS, that simulation parameters are at least doubled to ensure that the suitable convergence has been reached.

Contrary to most other transducer analysis techniques, the FEM operates in the time domain, therefore a conversion to the frequency domain is required before usable data can be obtained. A major issue when converting between the two domains is equivalent representation of the data. Although the timestep and overall simulation time can be specified, the corresponding conversion to the frequency domain is not as well defined. Through experimentation, it has been found that frequency resolution can be defined by equation 5.23, however it is most beneficial to specify the frequency resolution for comparative purposes.

During the course of this study, the author has been in contact with several researchers regarding the use of ANSYS for the analysis of acoustic wave devices. A key issue has been the ability to determine variation in response brought about by changes in surface boundary conditions. Primarily, the difficulties lie in the lack of frequency domain resolution, particularly when adding small loads to the surface. One particular group [18] assumed that the introduction of an analyte causes a sensitive layer to swell, thus increasing the effective area covered by the sensitive film. While a perfectly valid assumption, is can be quite difficult to measure changes in surface geometry in-situ, thus it is quite difficult to correctly model the changes in structure. In this approach, it is assumed that the sensitive layer changes homogenously, which may not be the case due to defects in the film.

A significant issue when modelling a FPW device is its high aspect ratio. That is, the device simulated has a quite small thickness in comparison to its overall length. This can cause errors in the FEM calculations due to excessively large deformations of the elements.

## 5.8 Conclusion

In this chapter a novel FEM based approach to the analysis of multilayered FPW structures has been presented. The author has successfully combined the FEM with modi-

fied SAW analysis techniques to determine key electrical and mechanical performance parameters of various FPW structures. In particular, the author has demonstrated the ability of this novel approach to evaluate essential parameters such as admittance, particle displacement profiles and the primary antisymmetric mode electromechanical coupling coefficient. Furthermore, the results obtained have been verified using more conventional modelling techniques such as the stiffness matrix method and spectral domain Green's function where excellent agreement has been obtained.

A thorough discussion of simulation parameters has been undertaken, highlighting the need for careful consideration of device structure and features when using the FEM for this type of analysis. From the presented results, a series of modelling guidelines have been established which, to the best of the author's knowledge, can be applied to other acoustic wave devices. Advantages and limitations of the author's approach have been critically addressed and potential methods for increasing the reliability and accuracy of the FEM when used for this type of analysis has also been discussed.

Two different models were presented which illustrate the assumptions made when converting from a complex 3D structure to a much simpler 2D layout. An electrostatic analysis has shown that effect of electrode end effects, in both $x$ and $z$-directions. Several simplifications have been made ranging from the assumed form of the charge density in the $z$-plane to geometrical considerations and the impact on simulated device response has been presented.

The FEM has shown that it can simultaneously model various second-order phenomena, such as electromagnetic feedthrough, diffraction and triple transit, which are not easily accounted for using other more conventional analysis techniques. In particular, the effect of triple transit interference has been discussed and potential methods to reduce its influence discussed.

Using the knowledge gained from this chapter, the author's novel technique is further extended for the purpose of modelling liquid loaded FPW structures in Chapter 6.

# Chapter 6

# Modelling of FPW Devices for Liquid Media Applications

## 6.1 Introduction

This chapter investigates the use of Flexural Plate Wave devices for sensing applications in liquid media. FPW structures are well suited to sensing applications in liquid media for two main reasons. The first it based on their physical construction. During the etching process a natural reservoir is formed which can be used to contain the liquid. In other acoustic wave structures, liquid flow cells are typically attached to the substrate, thus affecting propagation characteristics as well as increasing fabrication cost. The second advantage of FPW structures is the relatively low phase velocity of the primary antisymmetric mode. If the phase velocity of this mode is below that of the liquid medium compressional velocity, the acoustic energy is confined to the plate, rather than dispersing into the surrounding medium.

Section 6.2 describes the required modifications to the stiffness matrix method discussed in Chapter 4 to incorporate an additional liquid layer. Using this approach, the liquid layer is approximated as a semi-infinite, similar to the techniques used to analyse SAW structures. The viscous properties of the liquid layer are described by complex, frequency dependent, material parameters.

This section also examines the displacement profiles for a liquid loaded FPW device, revealing a tightly coupled surface wave, known as a Scholte mode. This particu-

lar mode is typically deemed responsible for the ability of FPW structures to measure changes in liquid parameters. The presence of this mode is highly dependent on the overall thickness of the structure. It will also be seen that once the thickness of the FPW structure increases beyond a given threshold, the primary antisymmetric mode is no longer confined to the structure and begins to radiate energy into the surrounding medium. This will be explained with the aid of the particle displacement profiles for an acoustically thick structure. The particle displacement profiles for the symmetric mode will also be examined revealing how this mode can be used for sensing applications in liquid media.

Section 6.3 presents the author's novel approach to the analysis of liquid loaded FPW devices using the FEM. It will be shown the techniques developed by the author are more suitable to calculating the liquid loaded frequency response characteristics of multilayered FPW structures when compared against the commonly used spectral Green's function. A study is also undertaken on the FEM optimum node density and assumed liquid thickness to minimise computation time as well as ensure that the calculated results are consistent and accurate. A brief introduction into the additional elements and theory behind the use of the FEM in conjunction with liquid loaded structures will also be given.

Section 6.4 investigates the ability of FPW structures to detect changes in density and viscosity of liquid media. It will be shown that the primary antisymmetric mode is well suited for density measurements, whereas the symmetric mode can be applied to viscosity sensing. As both of these modes can be excited simultaneously, a FPW device can theoretically be employed to measure both of these parameters using one structure. An investigation is also undertaken on the application of alternative piezoelectric layers, where is found that aluminium nitride, which is a higher velocity material than the commonly used zinc oxide, provides significantly higher sensitivity towards density, viscosity and additional mass. Mass sensitivity will also be explored, where it is shown that under liquid loading, the sensitivity of the symmetric mode remains relatively unchanged.

Finally, Section 6.5 concludes the theoretical analysis of liquid loaded FPW structures with a preliminary discussion on the author's attempts to fabricate a functional

device. It is envisaged that the FPW device presented can be used as further verification of the author's novel approach to the analysis of FPW structures.

## 6.2 Modification of the Stiffness Matrix Method for Liquid Media

As was highlighted in Chapter 4, the stiffness matrix method can be applied to lossy media. In this section, the necessary modifications are presented, allowing the technique to be applied to multilayered FPW structures in contact with an additional liquid layer.

During the fabrication process of a FPW device a natural reservoir is formed, which for the author's design measures approximately $300$µm in depth, corresponding to approximately $3\lambda$. Recall that for a Rayleigh mode, the acoustic energy is confined to $1-2$ wavelengths from the surface. Therefore, in the FPW device case, the liquid is analogous to a semi-infinite substrate allowing the complete structure to be modelled similar to a SAW device. By expressing the liquid layer as semi-infinite, the number of free mechanical surfaces is reduced to one. Although this study is concerned with the use of a FPW device in contact with water, the same process can be applied to determine the viscoelastic properties of other materials by analysing the change in phase velocity as well as attenuation of the propagating wave [144].

To incorporate viscous loading either the wavenumber component, $k_x$, or the angular frequency, $\omega$, must become complex, equation 6.1.

$$\omega^{fluid} = \omega^{unloaded} + j\omega^{damping} \tag{6.1a}$$

$$k_x^{fluid} = \beta - j\chi, \tag{6.1b}$$

where $\beta$ and $\chi$ represent the real and imaginary components of the wavenumber for the liquid loaded FPW structure. The phase velocity of the structure is still determined from the real component of the wavenumber, ie. $v_p = \omega/\mathrm{Re}\left(k_x^{fluid}\right)$.

Depending on the solution required, either expression in equation 6.1 is applied. As before, if the frequency term is held constant, such as when determining the insertion loss characteristics, the complex wavenumber is scanned. Conversely, to determine

the frequency shift due to modification of the liquid density, the frequency component becomes complex with the wavenumber purely real.

Several analytical models exist to determine the influence of liquid loading on the operating parameters of acoustic wave devices [145, 146]. Many of these models are severely limited as they assume that the device consists of a single isotropic layer, or can be effectively modelled as a simple harmonic oscillator. In the authors implementation of the stiffness matrix method, multilayered FPW structures can be analysed with relative ease. It will be shown in Section 6.4 that significant differences exist in terms of density and viscosity sensitivity between single layer devices comprised of isotropic materials and multilayered structures which validate this approach.

### 6.2.1 Stress / Strain Relationship for Liquid Media

In Section 3.2, the basic constitutive equations for stress and strain were developed for solid media. Here a similar technique is employed to describe the properties of a liquid by the same parameters allowing many analogies to be drawn from the solid material case. By describing the properties of a liquid in terms of material stiffness matrices the effects of viscous loading on wave propagation can be studied without the need to greatly modify the solution procedure. This will allow the liquid media to be inserted within the structure stack as simply another layer.

In developing the equivalent material properties for liquid media, it is assumed that the fluid is non-conductive and exhibits Newtonian properties. That is, the stress and strain are linearly related analogous to Hooke's Law, equation 3.8. In a simple liquid, such as water, isotropic material properties are assumed [147]. For most cases this is sufficient, but for biomedical applications, where long chains of molecules may align to a preferred orientation, anisotropic material properties can be applied [148]. By assuming isotropic material properties, the material stiffness matrix for a liquid can be fully described by two frequency dependent terms, $c_{11}$ and $c_{44}$. Similarly, the liquid dielectric matrix contains the same terms on the main diagonal. Naturally, as with a solid isotropic material, the piezoelectric matrix is also zero.

Consider the liquid loaded FPW structure depicted in Figure 6.1. For convenience the added liquid layer is placed on the upper surface of the structure. Calculations

performed in Chapter 4 indicate that there is a marginal difference in mass sensitivity for the primary $A_0$ mode if this side of the structure is subjected to the liquid layer. Due to the physical construction of the device, the Si side is preferred as a natural reservoir exists to contain the target liquid. Secondly, the sensitive IDTs are isolated from potentially corrosive analytes, thus negating the need for a further passivation layer which is known to reduce the overall device sensitivity.

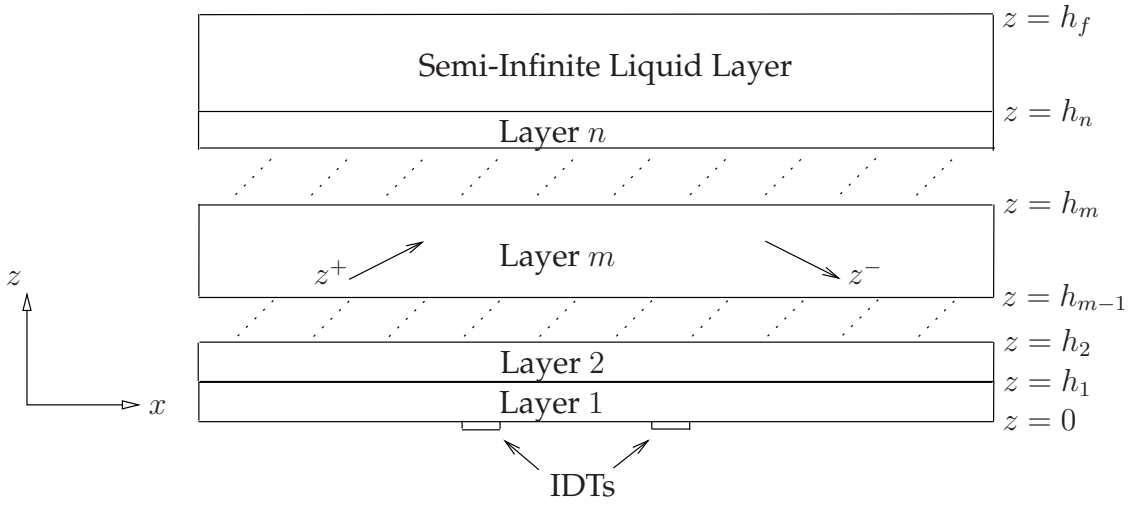


Figure 6.1: Liquid Loaded Multilayered FPW Device Coordinate System

Assume that a wave is propagating through the solid in the positive $x$ direction. The liquid molecules located at the fluid-solid interface, $z = h_n$, will move faster than those at the upper surface $z = h_f$ and will cause a drag force on the lower molecules. This allows a viscosity stress tensor to be defined as [149]:

$$T_{ij} = -P\delta_{ij} + \Pi_{ij}, \tag{6.2}$$

where $P$ is the hydrostatic pressure, $\delta_{ij}$ is the Kronecker delta and $\Pi_{ij}$ is a second rank tensor that describes the shear stress components.

If the liquid remains at rest or is under uniform motion, then the $\Pi_{ij}$ terms in equation 6.2 are zero and the resulting stress is simply the hydrostatic pressure. Similarly, if viscosity effects are ignored, then the total stress is simply due to the hydrostatic case [150]. As with solid structures, in the liquid acoustic approximation, which states that the change in localised pressure is far less than the static pressure, all second order

stress terms are ignored, thereby allowing the condensed stress tensor to be written as:

$$T_{ij} = \begin{bmatrix} -P + \eta^{'}\left(\nabla_s \cdot \mathbf{v}\right) + 2\eta\left(\frac{\partial v_x}{\partial x}\right) & \eta\left[\frac{\partial v_x}{\partial y} + \frac{\partial v_y}{\partial x}\right] & \eta\left[\frac{\partial v_x}{\partial z} + \frac{\partial v_z}{\partial x}\right] \\ \eta\left[\frac{\partial v_x}{\partial y} + \frac{\partial v_y}{\partial x}\right] & -P + \eta^{'}\left(\nabla_s \cdot \mathbf{v}\right) + 2\eta\left(\frac{\partial v_y}{\partial y}\right) & \eta\left[\frac{\partial v_y}{\partial z} + \frac{\partial v_z}{\partial y}\right] \\ \eta\left[\frac{\partial v_x}{\partial z} + \frac{\partial v_z}{\partial x}\right] & \eta\left[\frac{\partial v_y}{\partial z} + \frac{\partial v_z}{\partial y}\right] & -P + \eta^{'}\left(\nabla_s \cdot \mathbf{v}\right) + 2\eta\left(\frac{\partial v_z}{\partial z}\right) \end{bmatrix}, \tag{6.3}$$

where $\eta$ is the first coefficient of, or shear, viscosity and $\eta^{'}$ is the second.
The terms in equation 6.3 are a function of velocity rather than displacement for the solid case. A simple conversion can be applied, equation 3.11a, allowing the displacement vector to be used instead. Following the approach in [104], equation 6.3 is written in vector form as:

$$T_{ijkl} = K\left(\nabla_s \cdot \mathbf{u}\right)\delta_{ij}\delta_{kl} + \eta^{'}\frac{d}{dt}\left(\nabla_s \cdot \mathbf{u}\right)\delta_{ij}\delta_{kl} + \eta\frac{d}{dt}\left(\nabla_s \cdot \mathbf{u}\right)\left(\delta_{ik}\delta_{jl} + \delta_{il}\delta_{ij}\right), \tag{6.4}$$

where the substitution [74]:

$$P = -K\mathbf{S} = -K\left(\nabla_s \cdot \mathbf{u}\right), \tag{6.5}$$

has been made. The term $K$ is the fluid bulk modulus of elasticity.

### 6.2.2 Modification of Material Properties

Analogous to Hooke's Law, equation 3.8, the coefficients in equation 6.4 can be treated similarly to the material stiffness matrix, $c_{ijkl}$. Assuming isotropic material properties, the individual components of the fluid stiffness matrix are written as:

$$c_{ijkl} = K\delta_{ij}\delta_{kl} + \eta^{'}j\omega\delta_{ij}\delta_{kl} + \eta j\omega\left(\delta_{ik}\delta_{jl} + \delta_{il}\delta_{jk}\right), \tag{6.6}$$

which is seen to coincide with the material parameters for an isotropic thin film [74]. By modifying the material properties to correspond to the liquid case, no significant changes are required to the basic solution path. The $\Gamma_{ik}$ matrices, equation 3.20, are identical with the exception of the imaginary terms. A boundary determinant scan can still be used to define the operating point of any given structure, however it is necessary to include a secondary scan that finds the imaginary component of the solution, which represents the attenuation of the acoustic wave.

In the Navier-Stokes approximation [149], the second coefficient of viscosity, $\eta^{'}$, is related to the first, $\eta$, by:

$$\eta^{'} = \frac{-2\eta}{3}, \tag{6.7}$$

which allows the isotropic liquid stiffness matrix to be fully described by:

$$c_{11} = K + \frac{4j\omega\eta}{3} \tag{6.8a}$$

$$c_{12} = K - \frac{2j\omega\eta}{3} \tag{6.8b}$$

$$c_{44} = j\omega\eta \tag{6.8c}$$

It can be seen that the resulting shear stress component, $c_{44}$ is purely imaginary, corresponding to the inability of a non-viscous liquid to support shear stress.

### 6.2.3 Boundary Conditions for Liquid Loaded FPW Devices

To accurately determine the influence of liquid loading on a FPW device, it is necessary to examine the boundary conditions at the fluid-solid interface (FSI) as well as at the corresponding free liquid surface. Considering the FSI, both the normal and tangential velocity components must be continuous across the liquid and solid materials. Enforcing the continuity of the tangential velocity is known as the no-slip condition [148]. In formulating equation 6.7, which is based on the acoustic approximation of the Navier-Stokes equations, the no-slip condition is enforced at the FSI. Furthermore, the acoustic approximation assumes the liquid is incompressible and neglects temperature gradients[148].

A Newtonian fluid does not support shear stress, and hence only the term, $T_{zz}$ should be continuous[151]. The other two normal stress terms, $T_{xz}$ and $T_{yx}$ should be zero in the liquid, but clearly non-zero within the FPW structure. If the electrical properties of the fluid are considered, then the dielectric displacement, $D_z$, is continuous between the fluid and the solid. By appropriately modifying the components of the material stiffness matrix, equation 6.8, the mentioned interfacial boundary conditions are automatically satisfied by the recursive calculation of the overall stiffness matrix, $\mathrm{K^T}$.

In developing the solution for the liquid loaded FPW, the additional liquid layer has been approximated as semi-infinite. Under these conditions, identical to the SAW case,

it is assumed that the semi-infinite material is sufficiently thick that no contributions exist from the essential field variables at the liquid-gas, or liquid-vacuum, interface. From the discussion of boundary conditions, it is apparent that with minor modifications, the stiffness matrix method can be successfully applied to determine the effect of liquid loading on a FPW structure. The first modification, where the added liquid layer is described in terms of complex material parameters, has already been discussed. A further simplification can be made to the stiffness matrix method to determine the influence of the additional liquid layer, whilst retaining many of the numerical solution techniques used to solve piezoelectric wave propagation problem for an unloaded FPW device. In the presented approach, the liquid loaded structure can be considered to consist of a multilayered FPW device of finite thickness coupled with a semi-infinite substrate.

The analysis performed in Chapters 3 and 4 indicated that the wave propagation problem for an unloaded FPW structure can be described by eight partial modes, each consisting of eight individual components, resulting in a global stiffness matrix of size $8\times8$. Under the assumption that a liquid loaded FPW can be fully described by approximating the liquid layer as semi-infinite [152], the global stiffness matrix is reduced to a $4 \times 4$ matrix. As previously mentioned, in formulating the liquid loaded FPW device global stiffness matrix, it is beneficial to split the analysis in two, with the individual sections considering the semi-infinite and layered FPW structure respectively.

In a semi-infinite medium, where it is assumed that there is no interaction from the lower surface of the substrate [87], the stiffness matrix can be described by considering only the normal stress and displacement at the upper surface as:

$$\mathbf{T}\left(z+h\right) = \mathrm{K}_{11}^{\mathrm{S}}\mathbf{U}\left(z+h\right) \tag{6.9}$$

The term $\mathrm{K}_{11}^{\mathrm{S}}$ can be calculated by considering the four partial modes, identified by the scalar component of the complex Poynting vector, that decay with depth into the liquid media via:

$$\mathrm{K}_{11}^{\mathrm{S}} = \left[\mathrm{D}^{-}\left(\mathrm{P}^{-}\right)^{-1}\right], \tag{6.10}$$

where from Chapter 4, $\mathrm{D}^{-}$ and $\mathrm{P}^{-}$ represent the general displacement and stress components. Care must be taken with the assigned direction of the partial mode compo-

nents as the coordinate system has been reversed from that of the unloaded FPW in Chapters 3 and 4.

Calculation of the stiffness matrix for the multilayered FPW structure is slightly different to that in Chapter 4 due to the change in coordinate system. In this case, the piezoelectric surface of the FPW is at the bottom of the layer stack, rather than the top, requiring the terminal boundary conditions to be subsequently modified. The recursive algorithm in equation 4.10 is still applied, however the subscripts $M-1$ and $m$ must be interchanged. The resulting stiffness matrix, denoted $\mathrm{K^N}$, can then be combined with the semi-infinite component and the global stiffness matrix evaluated via the application of:

$$\mathrm{K^T} = \mathrm{K^N_{11}} + \mathrm{K^N_{12}} \left(\mathrm{K^S_{11}} - \mathrm{K^N_{22}}\right)^{-1} \mathrm{K^N_{21}}. \tag{6.11}$$

Similar to the unloaded device case, either the effective permittivity function or the determinant of the global stiffness matrix, $\mathrm{K^T}$, can be used to find a numerical solution for the piezoelectric wave propagation problem. In the author's implementation, a boundary determinant scan is used as this is the most compatible with the computational processes developed in Chapter 4. In terms of the generalised Green's function, the piezoelectric wave propagation problem can be fully described by:

$$\begin{bmatrix} \mathbf{u_l} \\ \varphi_l \end{bmatrix} = \begin{bmatrix} \mathrm{K^f_S} & \mathrm{K^{fe}_S} \\ \mathrm{K^{ef}_S} & K^e_S - \theta \end{bmatrix}^{-1} \begin{bmatrix} \boldsymbol{\sigma_l} \\ \gamma_l \end{bmatrix}, \tag{6.12}$$

Equation 6.12 is then rearranged to determine the open-circuit and short-circuit terminal boundary conditions, equations 6.13a and 6.13b respectively.

$$\textit{Open-Circuit}: \ \det \begin{vmatrix} \mathrm{K^f_S} & \mathrm{K^{fe}_S} \\ \mathrm{K^{ef}_S} & K^e_S - \theta \end{vmatrix} = 0 \tag{6.13a}$$

$$\textit{Short-Circuit}: \ \det \begin{vmatrix} \mathrm{K^f_S} + \frac{\mathrm{K^{fe}_S} + \mathrm{K^{ef}_S}}{K^e_S - \theta} & -\frac{\mathrm{K^{fe}_S}}{K^e_S - \theta} \\ \frac{\mathrm{K^{ef}_S}}{K^e_S - \theta} & -\frac{1}{K^e_S - \theta} \end{vmatrix} = 0 \tag{6.13b}$$

As the material properties for the liquid layer contain complex terms, it is necessary to slightly modify the boundary determinant scan procedure to identify the local minima corresponding to a propagating wave. A minimum of two determinant scans must be performed per solution iteration. Any real component can be set, be it frequency

or wavenumber, and the other variable determined. For example, if the frequency is set to a finite real value, then in a lossy medium, the complex wavenumber must be determined. In the author's implementation the real component is set and then the imaginary evaluated. In the next solution phase, the imaginary component is then fixed, while the subsequent real value is re-evaluated. This process is continued until a specific convergence criterion is met. Several other techniques, such as the Newton-Raphson and Regula Falsi methods have also been used to determine the complex parameters with varying levels of success [15]. Although these techniques can potentially determine the solution more efficiently than the simple scheme utilised, they are potentially not as robust and require careful boundaries to ensure that the calculated solution has not widely deviated from the correct value. To determine the insertion loss characteristics of a fluid loaded FPW device, the frequency term is set as the real variable and then the complex wavenumber determined. The phase velocity of the propagating modes is still given by the real part of the wavenumber, whereas the imaginary component represents attenuation, which is typically measured in dB/wavelength, and given by [1]:

$$\alpha = 40\pi \log_{10}(e) \frac{\mathrm{Im}(k_x)}{\mathrm{Re}(k_x)} \tag{6.14}$$

### 6.2.4 Liquid Loaded FPW Device Analysis

To evaluate the influence of liquid loading on a FPW device an alternative structure was defined consisting of a $12$µm Si, $0.3$µm Au and $3.0$µm ZnO layers. The added liquid layer, in this case water, was simulated as semi-infinite. Due to the frequency dependent nature of the added liquid layer the material stiffness constants were re-calculated during every solution iteration, however their initial values are listed in Appendix C. In this implementation the electrode period was fixed at $96$µm, identical to the device studied in Chapter 5, and the corresponding complex frequency determined. Figure 6.2 presents the real component of an open-circuit boundary determinant scan for the liquid loaded structure.

Analysis of Figure 6.2 indicates that the phase velocity for the first two primary modes, under liquid loading, is approximately $1324.7$ and $6335.2$m/s for the $A_0$ and $S_0$ modes respectively. For the equivalent unloaded structure, the velocity of the two

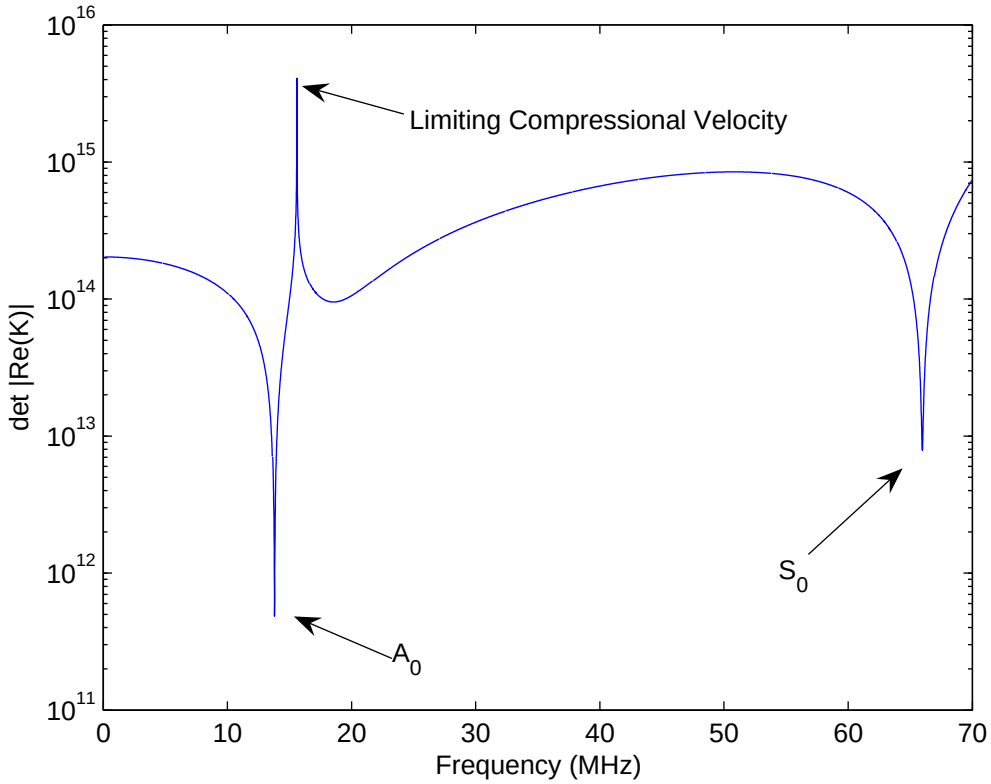


Figure 6.2: Liquid Loaded Determinant Scan - Open Circuit Boundary Conditions

modes is to $1653.3$ and $6330.9$m/s respectively. An important feature, not found in the unloaded case, can also be seen in the boundary determinant scan of Figure 6.2. Whereas guided modes are described by the solution of equation 6.13a approaching zero, a maximum is found at a frequency of approximately $15$MHz, corresponding to the compressional velocity of the liquid layer. This appears to be limiting phase velocity of the primary $A_0$ mode in the liquid loaded case. To further examine this phenomenon, the dispersion characteristics of the liquid loaded FPW structure are presented in Figure 6.3 as a function of Si thickness. As a reference the unloaded FPW device dispersion characteristics are included as well as the compressional velocity of the added liquid layer at $1435$m/s.

Under the liquid loading condition, the dispersion characteristics are virtually identical for the primary $S_0$ mode. A maximum deviation of $4$m/s is found across the complete Si thickness range. As will be discussed shortly, the limited change in $S_0$ is caused by the dominant particle displacement being in the longitudinal direction rather than

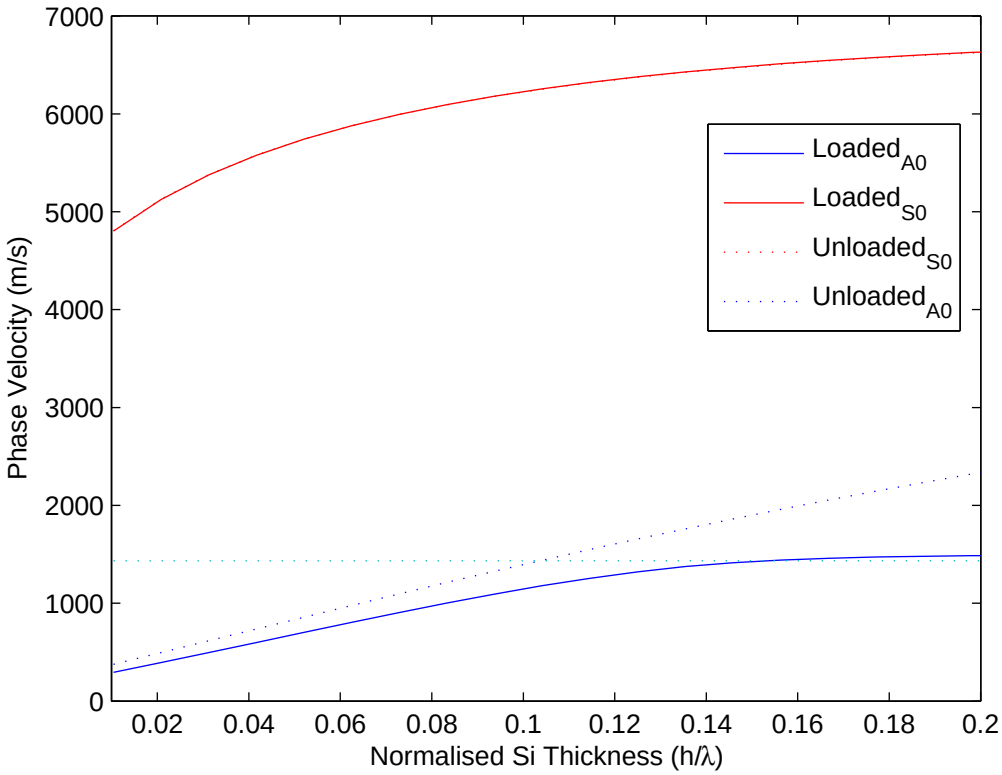


Figure 6.3: Liquid Loaded Phase Velocity - Normalised Layer Thickness

the transverse for the $A_0$ mode. As suspected, the characteristics for the low phase velocity $A_0$ mode vary significantly, particularly as the thickness of the underlying Si layer is increased. The phase velocity of the $A_0$ mode asymptotically approaches that of the compressional velocity of the liquid layer, which is often termed a Scholte mode[8]. In an inviscid material this mode is lossless and is typically attributed to the acoustic mode applied in most FPW device sensing experiments in liquid media. Figure 6.4 depicts the attenuation of the primary two modes as a function of Si thickness. Under the liquid loaded assumption, the term Scholte mode is used to describe the behaviour of the $A_0$ mode.

Due to the viscous nature of the liquid, the Scholte mode shows a slight frequency dependent attenuation. In the presented structure, the attenuation appears to be a maximum in the low thickness region corresponding to a smaller phase velocity, with the attenuation decreasing as the structure becomes thicker. As a comparison, a typical Love mode SAW device constructed on a ST-cut quartz substrate used for sensing

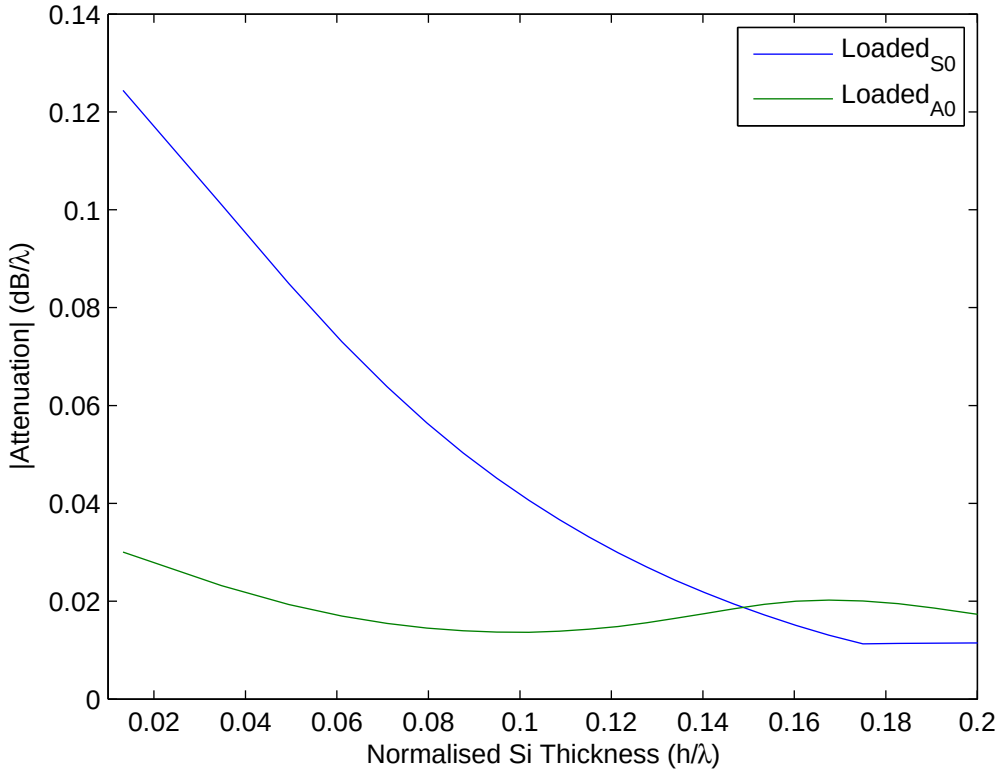


Figure 6.4: Liquid Loaded Primary Mode Attenuation

applications in liquid media, operating at $123.5$MHz, exhibits attenuation on the order of $0.014$ dB/$\lambda$ [153]. The low attenuation is caused by the predominant displacement in the structure being in the $y$, or shear, direction. Although these types of structures can be used for sensing applications in liquid media, they are not as sensitive as FPW structures and also require significantly more elaborate processing electronics due to their relatively high frequency. For higher order modes, which are not of interest here, attenuations in the order of $800$dB/cm have been reported for the second antisymmetric mode[8]. Examination of the unloaded higher order mode FPW particle displacement profiles, Table 4.2, indicates that the transverse and longitudinal components are comparable which coupled with the high phase velocity, causes significant amounts of energy to be dissipated into the surrounding medium and hence these modes are typically not used for sensing applications in liquid media.

Figures 6.5 and 6.6 depict the particle displacement profiles within the liquid loaded FPW structure for the $A_0$ and $S_0$ modes respectively. As a reference, the unloaded pro-

files are also included as indicated by the term 'Free'. The underlying Si membrane was fixed at $20.0$µm corresponding to unloaded and loaded antisymmetric and symmetric phase velocities of $2398.9$ and $6601$m/s and $1489.1$ and $6607.8$m/s respectively. Figures 6.5 and 6.6 have been normalised to the maximum longitudinal displacement for each respective mode in the unloaded condition.

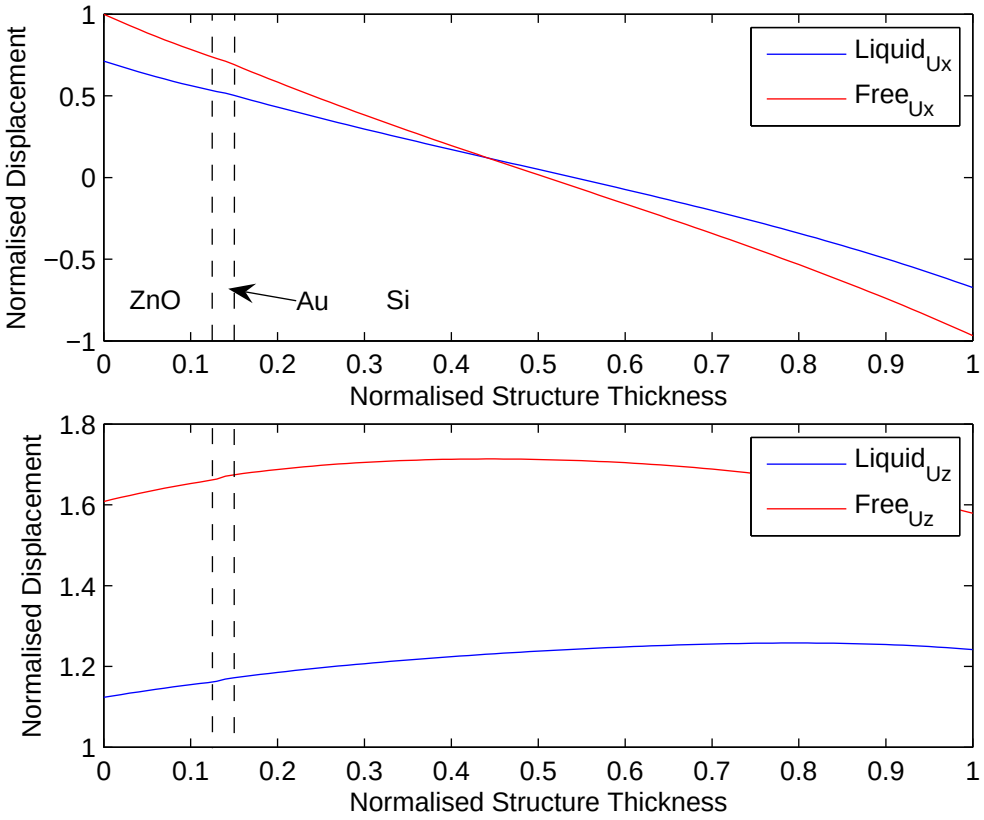


Figure 6.5: Liquid Loaded Primary Antisymmetric Mode Displacement Profile

From Figure 6.5 the transverse displacement in the liquid loaded condition is still dominant, however the position of the local maximum has shifted towards the fluid-solid interface, indicated by a normalised structure thickness of $1$. Whereas in the unloaded condition, the displacement at the piezoelectric free surface is slightly larger than at the Si surface, the converse is true for the loaded case. A slightly higher displacement at the FSI is beneficial for sensing applications. A reduction in peak displacement of $26.7\%$ is observed for the transverse component, where the corresponding reduction in phase velocity is $36.3\%$. The characteristics of the longitudinal component remain virtually unchanged, with the exception of a slight reduction in amplitude.

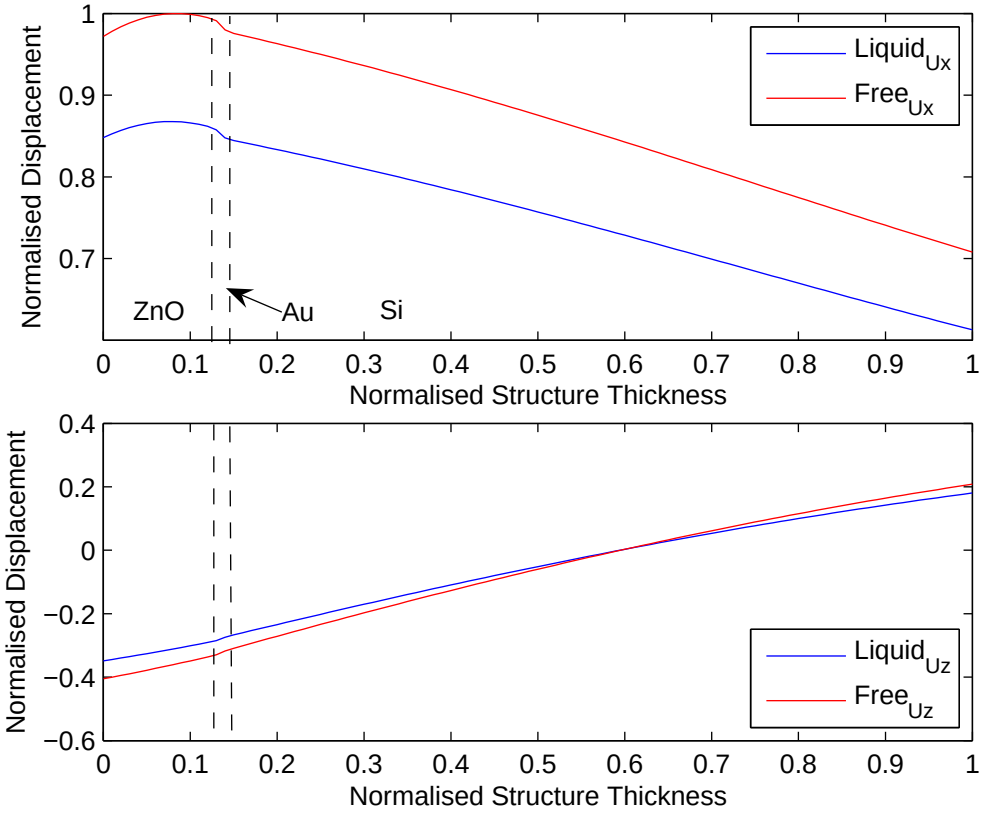


Figure 6.6: Liquid Loaded Primary Symmetric Mode Displacement Profile

Conversely, the transverse component of the $S_0$ mode, although significantly less than the longitudinal displacement, virtually remains unchanged in the liquid loaded case. The liquid loading is therefore shown not to significantly load the transverse particle displacement of the structure, which will be used to explain the limited change in mass sensitivity for the $S_0$ mode. The longitudinal component of $S_0$ shows a reduction in particle displacement of approximately $13.2\%$, however the general characteristics of remain unchanged.

The same identification process discussed in Chapter 4 can still be used to identify the $A_0$ and $S_0$ modes in the liquid loaded case. The particle displacement profiles were also considered with an similar structure with a Si thickness of $2.0$µm. In this case, as expected, there was insignificant change in the displacement profiles.

It is also instructive to evaluate the displacement profiles within the added liquid layer. Although the stiffness matrix method has been modified to consider the liquid layer as semi-infinite, a reference thickness of $350$µm is used to determine the particle

displacement profiles within the liquid. Typically, velocity fields are used to describe the motion within a liquid medium [154], however for consistency with the underlying solid structure and the analysis performed so far, particle displacement will be used instead. Initially, a separate model was defined, the same as presented in Section 3.3.2, consisting of a $2.0$µm Si, $0.4$µm Al and a $0.6$µm ZnO piezoelectric guiding layers. The added fluid in the case was water. This structure allows the particle displacement to be determined before the primary $A_0$ mode begins to behave as a Scholte mode, where the displacement and attenuation profiles vary significantly. Also included is an alternative FPW device with a Si thickness of $20$µm to demonstrate the unique behaviour of liquid loaded FPW structures as the resonant frequency is increased. Figure 6.7 depicts the real component of the particle displacement profiles for the $A_0$ mode for both structures. The particle profiles have been normalised to the respective maximum longitudinal displacement values within the $2.0$µm Si simulated structure.

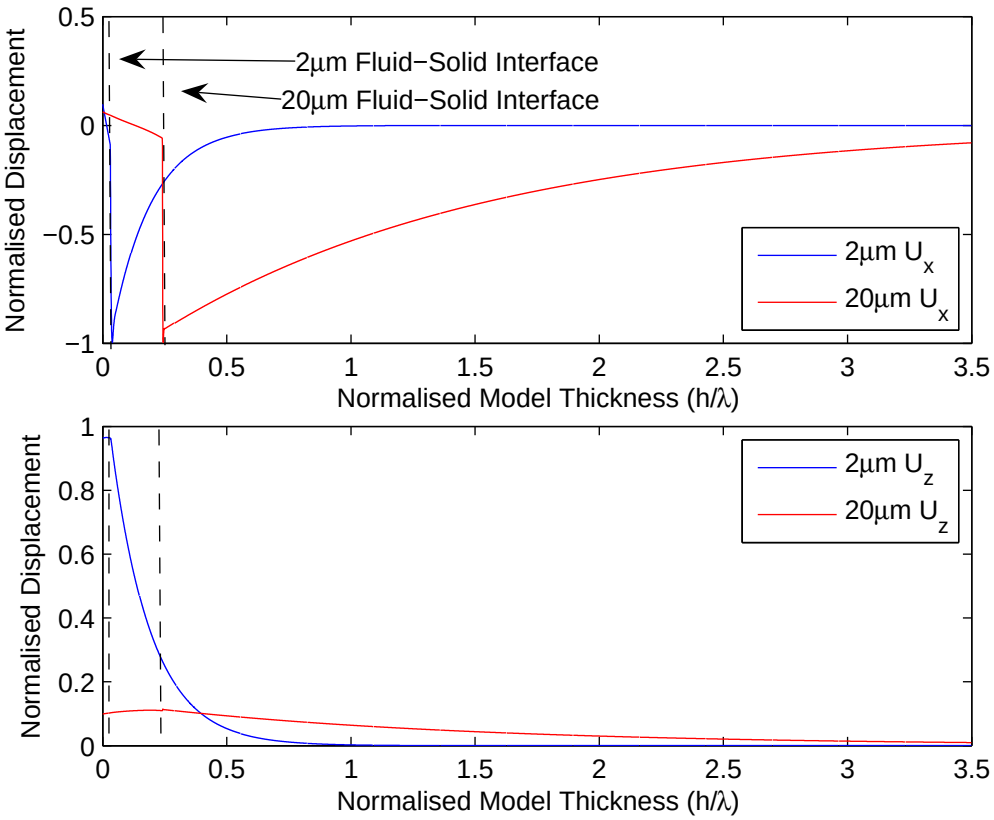


Figure 6.7: Liquid Loaded Primary Antisymmetric Mode Displacement Comparison

Considering the displacement profile of the $A_0$ mode in Figure 6.7, it can be seen

that the maximum displacement for the longitudinal component is in the liquid, rather than within the FPW structure. The local maximum, which occurs at a small distance from the fluid-solid interface illustrates the tightly-coupled surface wave component, even in the case of the lower frequency $2.0$µm structure. The evanescent decay length, which defines the depth where the energy within the target fluid drops to a value of $1/e$ of its peak value, can be obtained in both the transverse and longitudinal directions by considering the real component of the displacement profiles. An analytical expression exists for isotropic materials, and is given by [13]:

$$\delta_e = \frac{\lambda}{2\pi}\left[1 - \left(\frac{v_p}{v_f}\right)^2\right]^{\frac{1}{2}}, \tag{6.15}$$

where $v_f$ represents the compressional velocity of the target fluid.

One issue associated with equation 6.15 is that it can only be applied where the phase velocity of the propagating mode is less than the compressional velocity of the liquid. By applying the techniques introduced here, the decay length can be determined for arbitrary structures. From Figure 6.7, the actual transverse decay length is $15.98$ and $127$µm for the $2.0$ and $20.0$µm structures respectively. If the absolute value of the square root in equation 6.15 is taken, theoretical decay lengths of $15.73$ and $21.32$µm are obtained for the $2.0$ and $20$µm structures respectively. As expected, the decay length is incorrectly calculated for the thicker structure, thus illustrating the benefit of the author's approach. For biosensing applications a small evanescent decay length is necessary to sense the molecules of interest which are typically within $50$nm of the device surface [8].

The transverse displacement component of $A_0$ demonstrates significantly different characteristics than the longitudinal component for both simulated structures. Considering the $2.0$µm structure, the peak displacement is seen to be within the FPW structure rather than within the liquid. The transverse displacement then decays within the liquid, with a majority of the energy contained within one wavelength of the FPW device surface, a characteristic typical of SAW structures. However, once the Si thickness is increased to $20$µm, the behaviour of the $A_0$ mode varies significantly. Figure 6.8 provides an enlarged view of the fluid-solid interface for the $20$µm Si structure, allowing the existence and behaviour of Scholte mode to be highlighted. For simplicity, the dis-

placements have been individually scaled to highlight the characteristics of the mode. The solid interface exists at a normalised wavelength of $0.2427$.

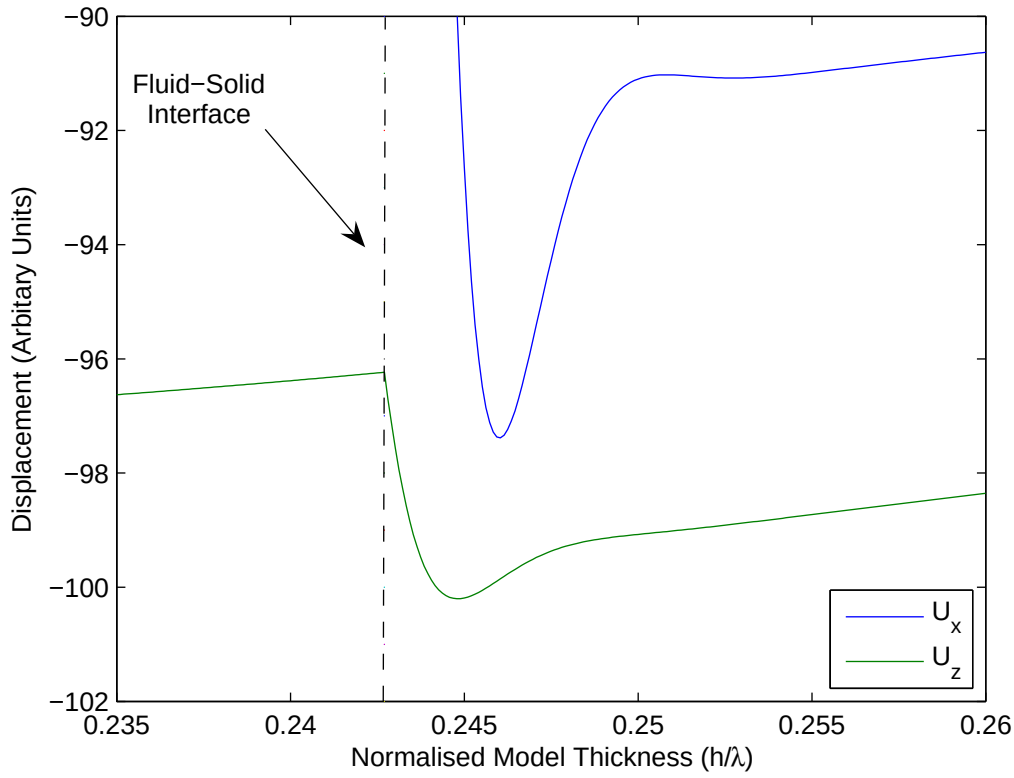


Figure 6.8: Liquid Loaded FPW Device - Scholte Mode Displacement Profile

A Scholte mode is identified by a wave that decays with distance from the fluid-solid interface. Two wave components are typically present, however due to the forced displacement within the FPW, the wave decay into the solid structure is not as obvious. Firstly, considering the longitudinal component of the Scholte mode, an abrupt increase in displacement is observed at the fluid-solid interface, which represents the one of the evanescent waves. The longitudinal maximum is not at the FSI, rather it is shifted to a fraction of a wavelength within the liquid. Interestingly, other examples presented in literature [74], shows that the peak of the longitudinal component, at least when considering solid structures is within the material with lower density, unlike the presented FPW case. Also, as the added water layer is a lossy material, the acoustic wave decays slowly with depth, rather than within one to two wavelengths as shown in the solid case in literature.

The transverse displacement, apart from being significantly smaller in magnitude than the longitudinal component, also exhibits a local maximum within the liquid medium. This behaviour is also shown for the solid case in [74], however as with the longitudinal component, the peak transverse component is in the liquid, rather than the solid. Note that the transverse displacement direction has been inverted to allow a direct comparison between the two components.

Under the liquid loading assumptions, the first symmetric mode causes a compressional wave to be established in both the longitudinal and transverse directions, Figure 6.9. This is true in both simulated structures, however more prevalent in the thicker $20$µm Si FPW device. Unlike the lower velocity $A_0$ mode, there appears to be insignificant acoustic coupling at the device surface. It can also be seen that the transverse component is still dominant, whereas in the $2.0$µm structure the longitudinal and transverse components are of approximately the same magnitude within the liquid.

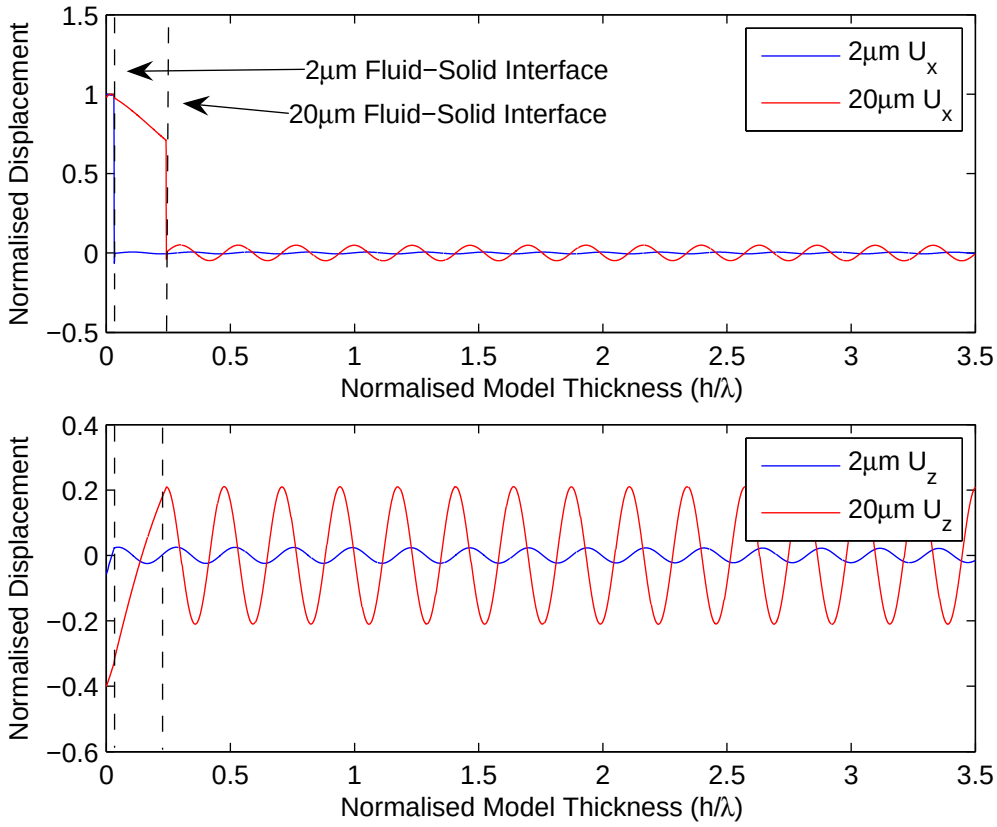


Figure 6.9: Liquid Loaded Primary Symmetric Mode Displacement Comparison

## 6.3 FEM Simulation Modification

Chapter 5 has demonstrated that the FEM is capable of evaluating the electrical and displacement characteristics of a multilayered FPW structure. As FPW devices are typically employed for sensing applications in liquids, the FEM techniques developed by the author must also be able to determine the device response when subjected to such media. This section presents a novel approach to determine the liquid loaded characteristics of a FPW device. In particular, the FEM derived frequency response characteristics are determined and compared against the equivalent spectral domain Green's function results. It will be shown that the FEM is certainly a viable tool when working with liquid loaded structures mainly due to the ability to visualise the interaction between the liquid media and the solid FPW structure.

### 6.3.1 Additional Elements

In constructing the FEM simulation of a FPW device in Chapter 5, a single element type, *Plane13*, was used throughout the complete structure. This particular element was configured to utilise two displacement and one electrical degrees of freedom. To accurately model a liquid loaded FPW device, additional elements are required that can be used in conjunction with Plane13. Although seemingly a trivial issue, care must be taken when using ANSYS that the correct nodal loads can be transferred between two different element types. Secondly, the selected element must be capable of modelling the fluid-solid interface. Two elements were initially considered, *Fluid29* and *Fluid79*, with slight differences in capabilities. Fluid29 will accept pressure loads, whereas Fluid79 directly incorporates the displacement degree of freedom, thus making the element more suitable for this type of analysis. Alternatively, if a pressure load were required, a script can be written to manually calculate the structural displacement of an element and then map this as a pressure field on the liquid. However, this process is often time consuming and must be repeated until an equilibrium is reached before the next timestep can be evaluated. In using Fluid79, it is assumed that the liquid is contained, thus it is necessary to set displacement boundary conditions on the external interfaces. By using a constrained fluid, net flow effects are negated, therefore the

response generated would be typical of directly placing a drop of liquid on the surface and allowing it to settle rather than pumping it in via microfluidic channels.

Fluid79 consists of four nodes per element with two structure degrees of freedom. Material properties are entered in terms of density, viscosity and compressional velocity. The element shares the same interpolation functions as the structural Plane13 element. Due to product limitations within the FEM package the simulated structure is inverted such that the fluid-solid interface coincides with $y = 0$.

Unlike the technique presented in Section 6.2, the FEM initially assumes that the liquid is incompressible and inviscid. This allows the Navier-Stokes equations to be greatly simplified and converted to a diagonalised form. To represent the losses in the liquid layer a coupling matrix is used. A similar process can be used to evaluate thermal expansion effects, however this is beyond the scope of this thesis. In the liquid-structural problem, three different equations must be considered. Firstly, the effect of the liquid on the structural component of the solution is considered. Note that in the FEM package, the term fluid is used to represent a liquid layer, thus in this section, the two terms are interchangeable.

In Chapter 5, it was shown that the solution to the unloaded FPW device problem is described by equation 5.17. This particular solution incorporated the piezoelectric component of the problem by considering the electrical load vector as well as the piezoelectric and dielectric constants. The particular problem had two displacement degrees of freedom and one electrical. In the fluid coupled solution the influence of the liquid loading must be determined on the structural component of equation 5.17. It is assumed that the added fluid is non-conductive and added on the Si side of the structure. To demonstrate the effect of fluid loading, consider the structural component of the FEM simulations, equation 5.15, which is repeated here:

$$\mathrm{M}\ddot{\mathbf{u}} + \mathrm{C}\dot{\mathbf{u}} + \mathrm{K}\mathbf{u} = \mathbf{F(t)}, \tag{6.16}$$

To incorporate the liquid loading effect on the structure an additional fluid coupling mass matrix, $\mathrm{R}$, is included. Although the effect of the fluid coupling matrix is applied throughout the entire structure, it depends primarily on the fluid-solid interface. With the inclusion of the liquid loading effects, the modified structural relationship becomes

[136]:

$$\mathrm{M}\ddot{\mathbf{u}} + \mathrm{C}\dot{\mathbf{u}} + \mathrm{K}\mathbf{u} - \mathrm{R}\mathbf{P} = \mathbf{F}(\mathbf{t}), \tag{6.17}$$

where the fluid coupling mass matrix is given by:

$$\mathrm{R} = \int_S \mathrm{N}\mathrm{n}^T \mathrm{N}'^T \, d\,(S) \tag{6.18}$$

Note, Table 6.1 lists the parameters used in the analysis of the FSI equations. In the FEM package, the FSI must be correctly flagged during the construction of the model. It was found that the interface must be set once the model had been meshed. If loads, whether structural of electrical were applied, then it was not possible to correctly set the flag.

At the FSI, another set of equations must be considered. Again, negating the piezoelectric and dielectric influence, and analogous to the purely solid case, the motion of the nodes at the interface can be described in terms of both pressure and displacement via the application of:

$$\begin{bmatrix} \mathrm{M} & 0 \\ \mathrm{M}^{\mathrm{fs}} & \mathrm{M}^{\mathrm{p}} \end{bmatrix} \begin{bmatrix} \ddot{\mathbf{u}} \\ \ddot{\mathbf{P}} \end{bmatrix} + \begin{bmatrix} \mathrm{C} & 0 \\ 0 & \mathrm{C}^{\mathrm{p}} \end{bmatrix} \begin{bmatrix} \dot{\mathbf{u}} \\ \dot{\mathbf{P}} \end{bmatrix} + \begin{bmatrix} \mathrm{K} & \mathrm{K}^{\mathrm{fs}} \\ 0 & \mathrm{K}^{\mathrm{p}} \end{bmatrix} \begin{bmatrix} \mathbf{u} \\ \mathbf{P} \end{bmatrix} = \begin{bmatrix} \mathbf{F} \\ \mathbf{0} \end{bmatrix} \tag{6.19}$$

Equation 6.19 implies that the nodes at the interface contain both displacement and pressure degrees of freedom, evidencing the need to correctly set the FSI flag. The superscript $P$ indicates terms related to the additional liquid layer. The parameters of equation 6.19 can be found in Table 6.1. Similar to the development of the stiffness matrix method for liquid media, the FEM treats the added fluid layer as a structure allowing direct integration to the previously developed techniques and procedures.

The interaction between the solid and liquid layer can be seen in the off diagonal terms of equation 6.19, in particular the terms $M^{fs}$ and $K^{fs}$. The first of these parameters $M^{fs}$ is the mass interaction from the liquid to the structure as indicated by the sign. Conversely, $K_s$ acts from the structure to the liquid.

The final component to be considered is the motion of the liquid away from the fluid-solid interface. Assuming that the liquid is inviscid, incompressible, no mean flow exists and the mean density and pressure are constant, the discretised wave equation is given by:

$$\mathrm{M}^{\mathrm{P}}\ddot{\mathbf{P}} + \mathrm{K}^{\mathrm{P}}\mathbf{P} + \rho_0 \mathrm{R}^{\mathrm{T}}\ddot{\mathbf{u}}, \tag{6.20}$$

Table 6.1: FEM Fluid-Structural Equation Parameters

| Parameter | Description |
|---|---|
| $\mathrm{M^P} = \frac{1}{c^2}\int_{vol} \mathrm{N}\mathrm{N}^T \, d_{vol}$ | Fluid Mass Matrix |
| $\mathrm{K^P} = \int_{vol} \mathrm{B}^T\mathrm{B} \, d_{vol}$ | Fluid Stiffness Matrix |
| $\mathrm{R^T} = \int_S \mathrm{N}'\mathrm{N}^T\mathrm{n} \, d\,(S)$ | Transpose of Coupling Mass Matrix |
| $\mathrm{M^{fs}} = \rho_0 \mathrm{R}^T$ | Fluid-Structure Coupling Mass Matrix |
| $\mathrm{K^{fs}} = -\mathrm{R}$ | Fluid Coupling Mass Matrix |
| $\mathrm{C^P} = \frac{\beta}{c}\int_S \mathrm{N}\mathrm{N}^T \, d\,(S)$ | Fluid Damping Matrix |
| $\mathrm{N}$ | Finite Element Pressure Shape Function |
| $\mathrm{N}'$ | Finite Element Structural Shape Function |
| $S$ | Fluid-Structure Interface |
| $\beta$ | Boundary Adsorption Coefficient |
| $c$ | Compressional Velocity of Fluid |
| $\rho_0$ | Fluid Density |

with the parameters given in Table 6.1. However, this equation does not take into account the inherent losses at the fluid-structure interface. To include these effects, a damping term is added to equation 6.20. Note that this approach does not take into account other losses away from the interface. The damping term takes on the same form as for the solid elements, which greatly simplifies the solution process. After incorporating the losses due to the interface, the motion within the liquid can be described by to solution of:

$$\mathrm{M^P}\ddot{\mathbf{P}} + \mathrm{C}\dot{\mathbf{u}} + \mathrm{K^P}\mathbf{P} + \rho_0\mathrm{R^T}\ddot{\mathbf{u}} = 0, \tag{6.21}$$

where the terms in equation 6.21 are given in Table 6.1. The solution to the liquid loaded FPW device is obtained from the simultaneous consideration of equations 6.17, 6.19 and 6.21.

Up to this point, the liquid loaded FPW device FEM analysis has assumed that the structure is fabricated from ideal isotropic materials and thus piezoelectric and dielectric effects have been neglected. However, to achieve a usable solution these effects must be taken into consideration during the solution phase. As illustrated, a strong

coupling matrix is used to evaluate the interaction between the added liquid load and the FPW device. In the purely structural solution of Chapter 5, the coupling matrices considered the influence of the electrical parameters on the displacement and vice-versa, resulting in a $2 \times 2$ effective coupling matrix. Here, piezoelectric, pressure and displacement effects must be considered, increasing the problem dimension, which naturally increases the computation time.

In the preceding analysis it was assumed that the added liquid layer was contained within a vessel, which leads to the necessary FEM boundary conditions. With reference to Figure 6.10, and considering the alternative coordinate system used by ANSYS, it is assumed that $x$-displacement is zero at the external edges of the vessel. The end points of the FPW structure were also clamped to ensure that the liquid and FPW device were correctly coupled. The same electrical boundary conditions were set as in the transient analysis performed in Section 5.3.1.

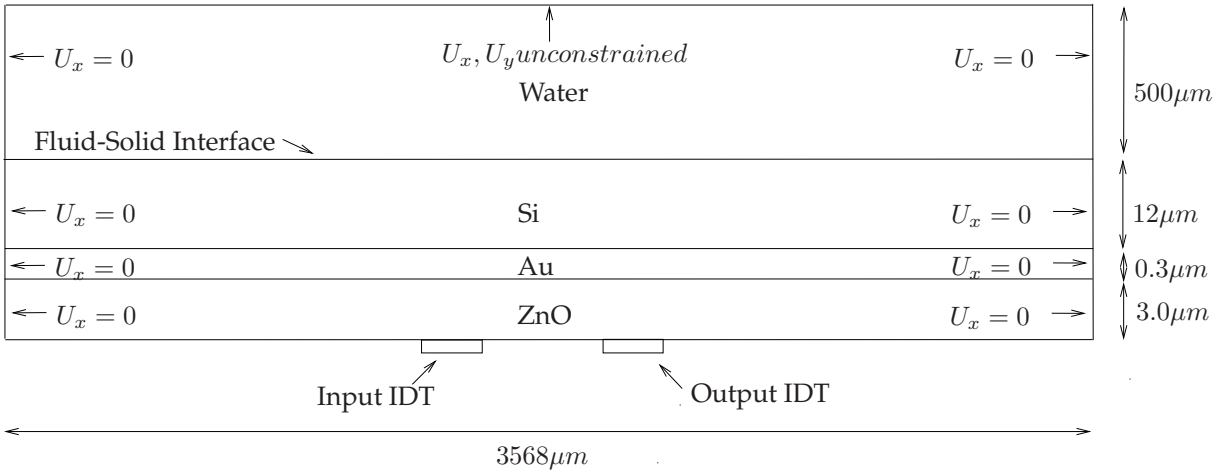


Figure 6.10: Simulated 2D FEM Liquid Loaded FPW Device

To evaluate the effect of liquid loading on the FPW device, a FEM simulation was performed with a structure consisting of $12$µm Si, $0.3$µm Au and $3.0$µm ZnO piezoelectric layers. Using the design process of Chapter 5, the simulated structure length was set at $3568$µm. Four electrode pairs were defined with a period of $96$µm corresponding to a unloaded phase velocity of $1661.7$ and $6337.2$m/s for $A_0$ and $S_0$ respectively. The thickness of the added liquid layer was varied between $100$ and $500$µm which brought about mixed effects on both the displacement profiles and frequency domain characteristics of the structure, which will be investigated momentarily. In the $x$- direction, node

densities were kept constant for all models at one node per $4$µm. In the $y$-dimension, $6$, $2$ and $3$ nodes were used in the Si, Au and ZnO layers respectively. For continuity between the alternative liquid height simulations, this layer was defined with one node per $5$µm in $y$. The nodal $x$-spacing within the liquid layer was consistent with the solid structure. With the available ANSYS licence, the FPW device had to be reduced to $4$ electrode pairs to accommodate for the necessary nodes to adequately model the liquid layer.

As a reference an identical unloaded FPW structure, with a total length of $6880$µm, was simulated for the same number of timesteps as the liquid loaded structure. The length of the structure was selected to minimise triple-transit interference. The frequency domain characteristics obtained from this simulation were used to compare against the liquid loaded FPW structure. As has been shown in Chapter 5, the FEM is capable of accurately determining the insertion loss characteristics of an unloaded FPW structure when compared against the more computationally efficient spectral domain Green's function. However, in the case of a liquid loaded FPW device, the spectral domain Green's function approach requires significant modification and thus in its current form is not suitable for the frequency domain analysis of a liquid loaded FPW device. This hypothesis was also confirmed against the reported behaviour of various liquid loaded FPW structures available in literature. Therefore, the results calculated from the FEM will serve as a benchmark for the analysis of a liquid loaded FPW device. To the best of the author's knowledge, this is the first time that the FEM and associated techniques have been used to determine the frequency domain characteristics of a multilayered liquid loaded FPW structure.

A dynamic transient analysis was performed, utilising an equation 5.19 as an excitation source. The timestep was set at $1$ns and the simulation performed for a total of $558$ substeps, corresponding to a frequency resolution of $0.896$MHz. Application of the stiffness matrix method to the same structure reveals a liquid loaded phase velocity of $1324.9$ and $6335.2$m/s for $A_0$ and $S_0$ respectively. Before considering the frequency domain characteristics of the structure, it is intuitive to consider the displacement profiles. Figure 6.11 presents a contour plot of the displacement at various timesteps within the composite structure with an added liquid layer thickness of $500$µm.

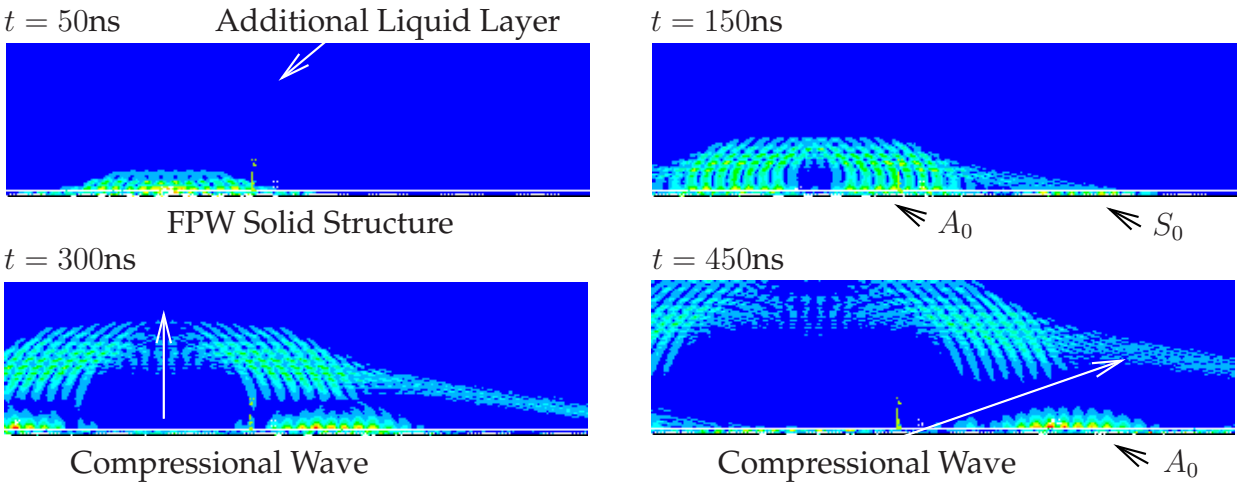


Figure 6.11: 2D FEM Liquid Loaded FPW Device Displacement Profile

From the FEM displacement contour plots, Figure 6.11, the behaviour of the primary acoustic modes under liquid loading can be clearly seen. Considering the plot when $t = 150$ns, the $S_0$ mode can be clearly identified propagating along the solid FPW structure, however there appears to be very little energy dispersed into the liquid media in comparison to $A_0$. It will be shown later in this section, that even though the velocity of the $A_0$ mode is below that of the compressional velocity of the liquid, there is an increase in insertion loss, which indicates that some of the acoustic energy is lost to the liquid layer. This can be particularly evidenced at $t = 300$ns, where a compressional wave has been established within the liquid layer which appears to have a similar phase velocity to the $A_0$ mode. It is not until $t = 450$ns that the effect of the $S_0$ mode on the liquid can be identified. The displacement in the liquid layer is significantly smaller than that caused by the $A_0$ mode, which will also be shown to correspond to a smaller deviation in insertion loss for the $S_0$ mode.

### 6.3.2 Frequency Response of a Liquid Loaded FPW Device

Of more importance than the displacement profiles are the frequency domain characteristics of a liquid loaded FPW device. Using the same approach developed in Chapter 5, the forward transmission coefficient, $S_{21}$, can be obtained for the liquid loaded FPW device. Figure 6.12 presents the frequency response characteristics for the simulated structure with an added $500\mu$m water layer. As a reference, the FEM derived

characteristics are also included from the unloaded test structure.

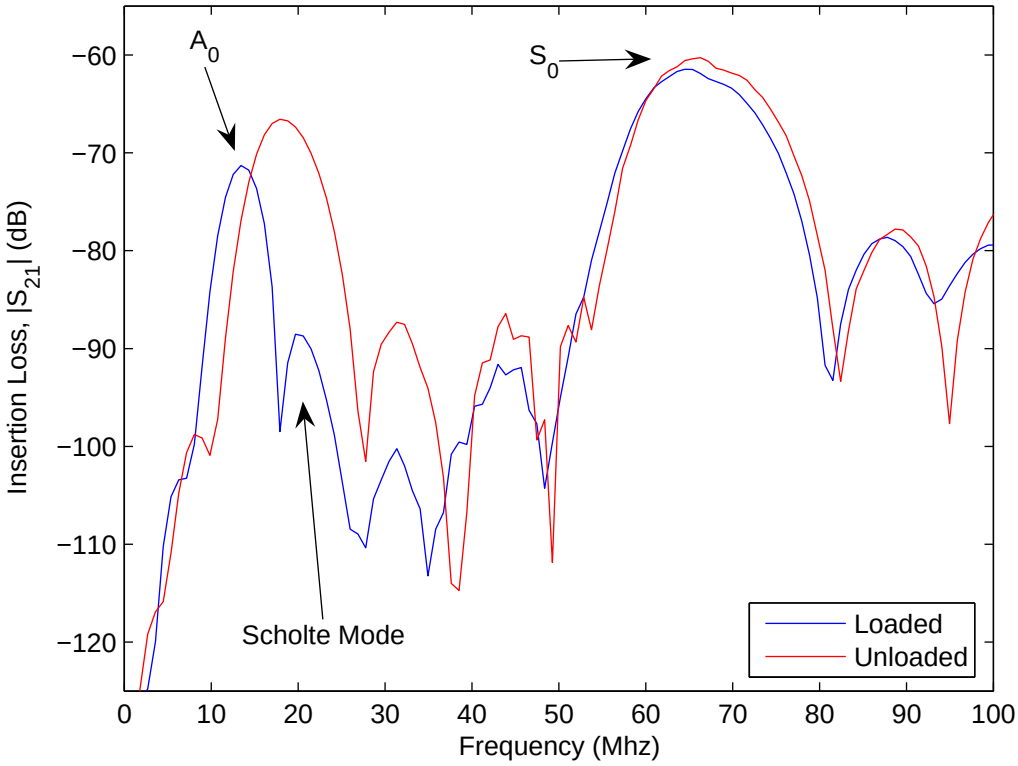


Figure 6.12: 2D Liquid Loaded FEM FPW Device - Insertion Loss Characteristics

From Figure 6.12, due to the influence of the Scholte mode, the spectral characteristics of the liquid loaded structure are vastly different from the unloaded case. Based on the stiffness matrix method of Chapter 4, the $A_0$ mode centre frequency is reduced to approximately $13.80$MHz, whereas the $S_0$ mode remains relatively unchanged at $65.98$MHz which is also shown in Figure 6.12. However, another peak appears quite close to $A_0$ which appears to be the Scholte mode. This mode appears at approximately $18.75$MHz and can be seen to interfere with $A_0$. In comparison to the unloaded case, the insertion loss of the $A_0$ mode is increased by approximately $4.74$dB, where for the $S_0$ mode, the loss is increased by $1.18$dB. Using the spectral domain Green's function approach of Chapter 4, there is a difference in insertion loss characteristics, with values of $-59.7$ and $-58.9$dB for $A_0$ and $S_0$ respectively. In this particular FEM simulation the calculated insertion loss value for $A_0$ and $S_0$ is $-71.3$dB and $-61.5$dB respectively. The calculated insertion loss values for the spectral domain Green's function simulation are

above the unloaded case for the equivalent FEM simulations, and thus is deemed that the spectral domain Green's function, at least in its current implementation, is unsuitable for calculating the insertion loss characteristics of a liquid loaded FPW structure. The FEM simulations were further verified by examining the behaviour of FPW devices studied in literature [6, 13, 147], where it was shown that the FEM simulations are more correct.The inability of the spectral domain Green's function to accurately resolve the spectral characteristics of a liquid loaded FPW will be further illustrated in the next simulation.

Although identifiable from Figure 6.12, the influence of the Scholte mode can be more readily determined by considering the two dimensional FEM FPW device used in Chapter 5. Here, the same structure dimensions were used, however an additional $600\mu$m liquid layer was incorporated. Due to reflections at the upper liquid boundary and the end of the simulated structure, the insertion loss characteristics contain a slight distortion, similar to the triple transit reflections seen in Chapter 5. As was discussed, these reflections can be minimised by extending the model boundaries, however this was not possible given the licence limitation of the FEM package available to the author. Figure 6.13 depicts the insertion loss characteristics of the two dimensional FEM liquid loaded FPW structure. Also included is the calculated insertion loss characteristics of the same structure via the spectral domain Green's function.

From Figure 6.13 it is once again clearly apparent that the spectral domain Green's function of Chapter 4 is unsuitable to determine the frequency characteristics of a liquid loaded FPW structure. The Scholte mode has been correctly resolved using the spectral Green's function, however the insertion loss values for the two primary modes are vastly different. The cause of the problem with the spectral domain Green's function lies with the calculation of $G_s^{FPW}(x)$, equation 4.37, which represents the guided mode component of the Green's function. Due to the highly dispersive nature of liquid loaded structure, this term is inaccurate and therefore the insertion loss characteristic becomes invalid. As the added liquid layer has been modelled as a semi-infinite, the SAW approximation for $G_s$, equation 4.35 was applied, however again due to the highly dispersive nature of the structure also provided unusable results. It is therefore concluded that the author's novel application of the FEM to determine the spectral

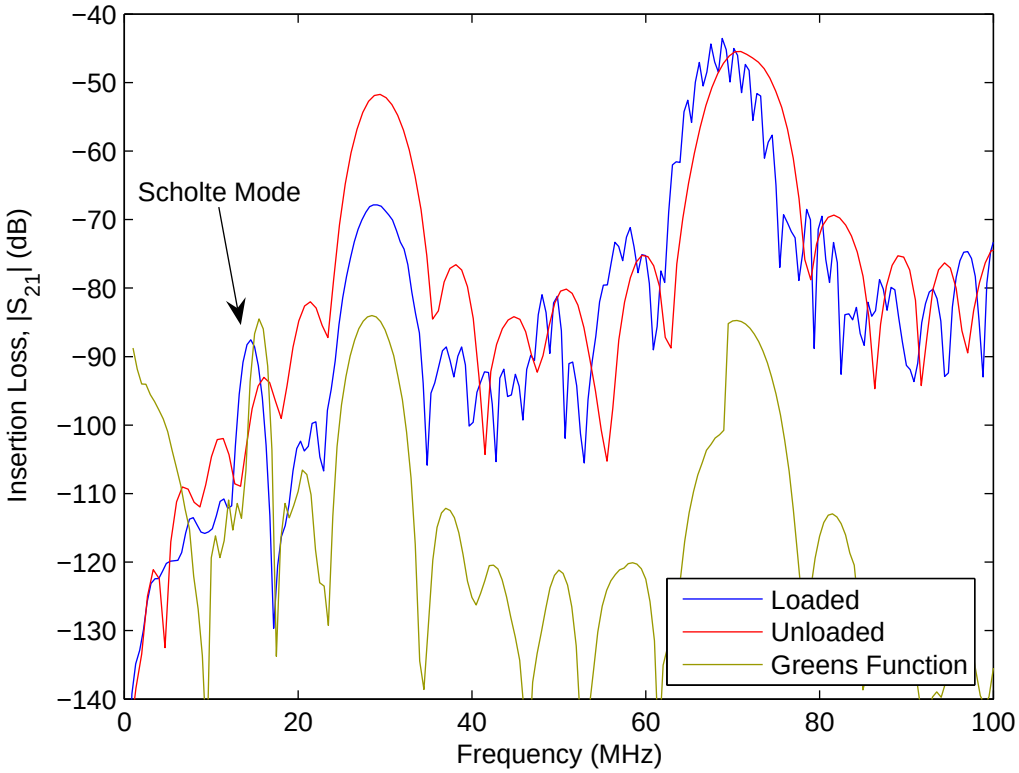


Figure 6.13: Liquid Loaded FPW Device - Insertion Loss Characteristics Comparison

characteristics of a liquid loaded FPW is highly appropriate.

Considering the FEM derived insertion loss characteristics of Figure 6.13, it can be seen that the $S_0$ mode is largely unaffected by the addition of the liquid layer. This has been confirmed through various experiments in literature [13]. A slight frequency shift of $1.93$MHz was found with the insertion loss remaining relatively unchanged. As expected, there is significant variation in the insertion loss of the $A_0$ mode which is caused by the energy of the mode radiating into the surrounding liquid media. Under liquid loading, the $A_0$ insertion loss changes from $-51.75$ to $-67.85$dB, a decrease of $16.10$dB. A small shift in frequency is also found, however it is believed that this is caused by the frequency resolution increase of the FEM simulation as the number of substeps, and hence simulation time, was increased to allow the Scholte mode to be identified. To confirm that the energy of the $A_0$ mode is radiated into the surrounding liquid, a FFT was taken of the nodal displacement degree of freedom $100$µm above the FPW surface within the liquid media. The resulting calculation can be found in Figure

6.14. Figure 6.14 indicates that the $A_0$ mode is radiated into the surrounding liquid

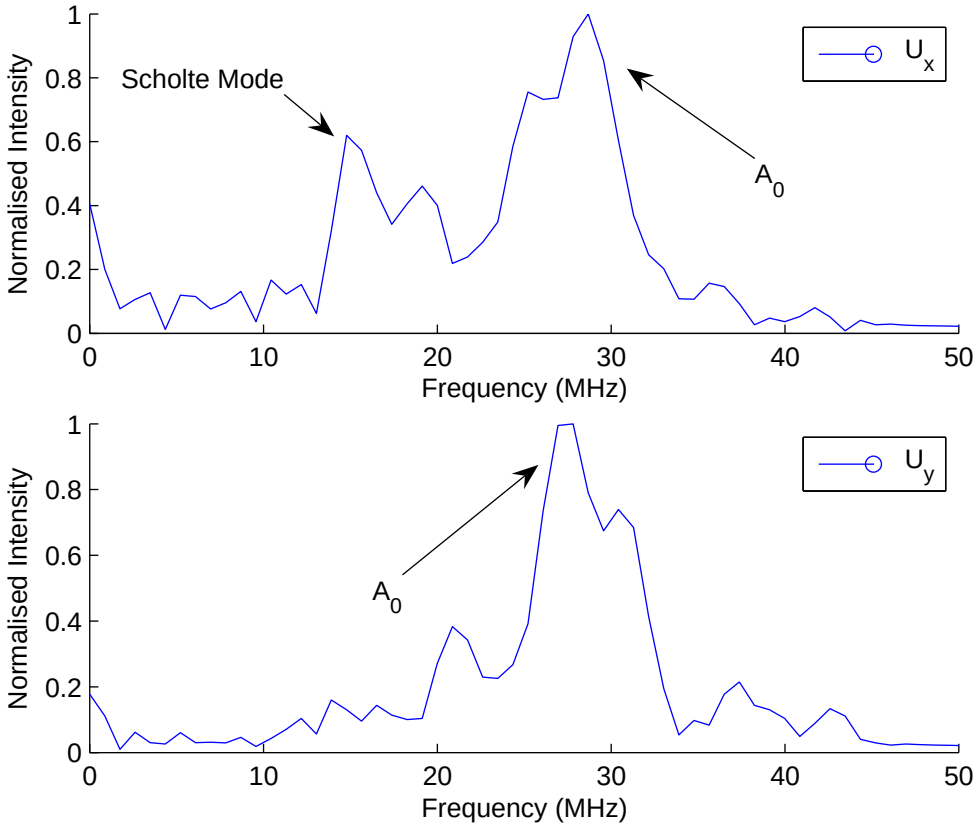


Figure 6.14: 2D Liquid Loaded FEM FPW Device - Displacement Spectral Content

with both longitudinal and transverse components. There appears to be insignificant displacement components in the Fourier Transform for the $S_0$ mode, indicating that the majority of the motion within the liquid is caused by the radiation of $A_0$. Interestingly, there appears to be a longitudinal displacement component corresponding to the Scholte mode.

A study was also undertaken on the effect of the added liquid layer thickness on the frequency domain characteristics of the simulated FPW device. In presenting the stiffness matrix method for liquid media, the added layer was approximated as a semi-infinite, however in the available FEM package this was not possible. Similar to Chapter 5 it was found that an infinite fluid element, although designed to be used in conjunction with Fluid79, is not compatible with the piezoelectric coupled-field analysis undertaken. Therefore it was necessary to model the added liquid as a finite height layer. The previously presented 12µm Si structure was used for this series of simula-

tions, with the node densities kept constant at $1$ node per $5$µm within the added liquid layer. Figure 6.15 illustrates the effect on the frequency domain of varying the liquid thickness between $100$ and $500$µm.

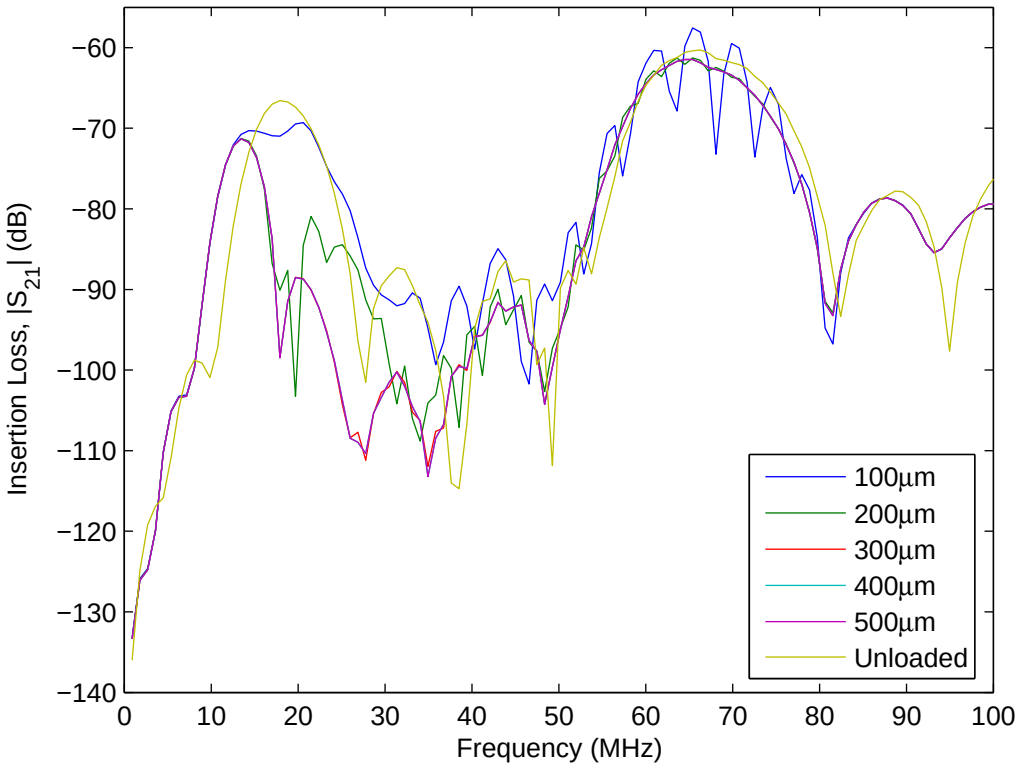


Figure 6.15: 2D Liquid Loaded FEM FPW Device - Alternative Liquid Thicknesses

Considering the $100$µm case, it can be seen that a significant amount of ripple is present at the frequency corresponding to the $S_0$ mode. This is caused by the compressional wave within the liquid being reflected at the simulation boundaries and repeatedly impinging on the FPW structure. This phenomenon is similar to triple transit interference discussed in Section 5.5.1.1 except that this particular example occurs in the transverse direction rather than longitudinal. The insertion loss value for both $A_0$ and $S_0$ modes is slightly different from the $500$µm liquid layer structure, however the centre frequency of the $S_0$ mode is correct. The $A_0$ mode shape is completely distorted and the Scholte mode has not been sufficiently resolved. The next liquid layer thickness of $200$µm correctly resolves the $A_0$ and $S_0$ modes in terms of frequency as well as insertion loss magnitudes. The Scholte mode is still not identified and only a small amount of ripple

appears on the insertion loss characteristic at higher frequencies. It is not until the liquid height is at, or beyond, $300$µm that all modes of interest are correctly identified. If the displacement degree of freedom is animated, it can be clearly seen that the transverse component of the compressional wave does not reach the structure once it has been reflected at the simulated device boundaries. Thus, as a guideline, when evaluating the frequency domain characteristics of a liquid loaded FPW device, the additional thickness of the liquid layer should be, as a minimum, at least $1.5$ times the IDT edge-to-edge spacing. In this particular series of simulations, the IDT edge-to-edge spacing is $200$µm, which translates to a liquid thickness of $300$µm.

Another series of simulations was developed to examine the effect of the $y$-direction node spacing within the added liquid layer. The node spacing within the solid FPW structure was held constant, whilst the liquid layer node spacing was varied between one node per $5$µm and one node per $50$µm, with an overall added liquid layer thickness of $500$µm. Figure 6.16 illustrates the effect on the frequency domain characteristics as the node densities are altered.

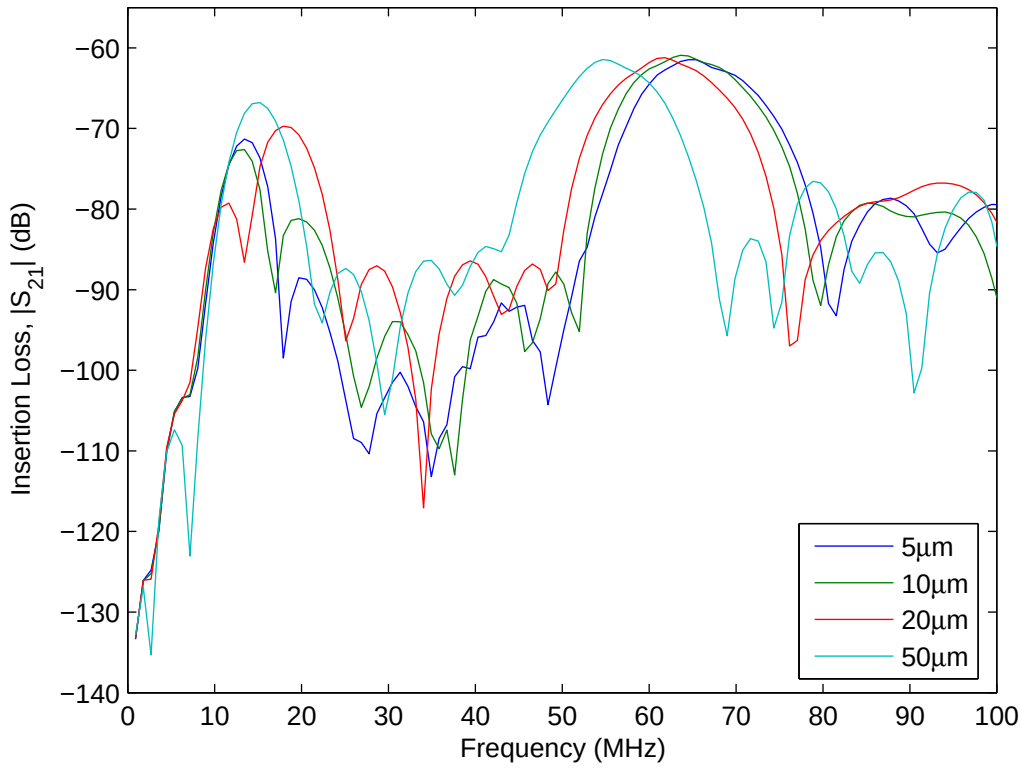


Figure 6.16: 2D Liquid Loaded FEM FPW Device - Liquid Layer Node Spacing

Unlike the purely structural simulations of Section 5.5.3, a reduction in the number of nodes in the $y$-direction is shown to have a significant effect on the insertion loss characteristics. In particular, once the nodal spacing is beyond $\lambda/2$, the resolved frequency for $A_0$ and $S_0$ are $15.2$ and $54.6$MHz respectively, which typically indicates, at least in an unloaded structure, that the overall thickness of the FPW has increased. Also, in the $50$µm node spacing simulations, the Scholte mode can no longer be identified. With the exception of the $1$ node per $5$µm structure, a reduction in the number of nodes causes the insertion loss characteristics to be poorly resolved. To confirm that the $1$ node per $5$µm simulation was correct, another simulation was performed at half the spacing where it was found that the insertion loss characteristics did not noticeably change. It is believed that the inaccuracies of the FEM are caused by the inability of the element shape functions to effectively describe the displacement degree of freedom within the element. As a result, it appears that a portion of the acoustic wave is reflected towards the solid FPW structure at the element interface thus distorting the frequency domain characteristics.

To confirm this hypothesis, a final simulation was undertaken to determine the influence of variable node spacing within the liquid layer. The fluid layer thickness was fixed at $300$µm with variable node spacing in the $y$-direction. The same overall number of nodes was used, with a larger density at the fluid-solid interface than at the upper boundary of the liquid layer. The spacing ratio was set at $3.2$, with $60$ nodes in the $y$-direction of the liquid layer. As expected, the frequency domain characteristics did not exhibit ripple caused by reflections at the elemental boundaries, however the insertion loss of the Scholte mode decreased by approximately $4$dB. As the characteristics of the Scholte mode depend on the FSI, it is concluded that constant spacing must be used within the liquid layer.

## 6.4 FPW Device Performance in Liquid Media

It has been shown in Section 4.3.2, that a FPW device can potentially have a higher mass sensitivity than other acoustic wave devices. In liquid media, typically devices containing a dominant shear component, such as QCM's and Love mode structures are employed [155, 156]. As an ideal inviscid liquid does not support shear waves

the acoustic energy is confined to the device rather than radiated into the surrounding medium [155]. Clearly, a FPW structure is unique as with its longitudinal and transverse motion, it has successfully been applied to sensing applications in liquid media [6]. This section examines the use of an ideal FPW device for density, viscosity and mass sensing applications. The stiffness matrix approach presented earlier in this chapter is also slightly modified to calculate the density and viscosity sensitivity of a FPW where both sides of the structure have been loaded with alternative fluids.

Several techniques have been developed in literature to describe the effect of liquid loading on similar acoustic wave devices. In equivalent circuit models, the influence of the added liquid media is modelled as a resistor and inductor in series. If mass loading is considered, an additional inductor is added [157]. In the author's implementation mass sensitivity is calculated at the fluid-solid interface by considering the area density of the average stored energy as was done for the unloaded structure in Chapter 4. This technique is based on a perturbation approach and therefore is only applicable when the added mass layer within the fluid does not greatly affect the wave propagation characteristics, which is typically the case in biomedical applications [158]. An alternative approach was also considered where a mass layer was added to the surface as in [21], where good agreement was achieved.

One associated problem with other acoustic wave devices is the inability to differentiate between density and viscosity effects. Currently a SH-SAW can be used to concurrently determine the effects due to density, viscosity, relative permittivity and conductivity [159], however in the case of a SAW structure, typically a multichannel array is required to differentiate between these effects. To obtain such a measurement three channel arrays are used, each with different mechanical and electrical boundary conditions [160]. It will be shown through the techniques developed by the author that a multilayered FPW structure is theoretically capable of differentiating between density and viscosity effects [13]. The numerical techniques developed by the author are quite powerful as they allow the evaluation of multilayered devices, where most examples in literature are for the much simpler single layer structures [158].

In the following analysis, the sensitivity to changes in density and viscosity will be presented in terms of simple measurement parameters such as frequency and at-

tenuation. With the exception of the density-viscosity product solutions presented in Section 6.4.2, this analysis is concerned with relative changes in density and viscosity of $-1\%$ and $11\%$ respectively. However, recall that for water, the examined deviation in viscosity can be brought about by a change in temperature of less than $5°$C.

### 6.4.1 Density Sensitivity

It has been shown, both via the FEM and stiffness matrix methods, that due to the relatively low phase velocity and particle displacement profile of the $A_0$ mode, that a FPW device is well suited to sensing applications in liquid media. In this section, an analysis is performed on the use of a FPW structure for density sensing applications. For this analysis water is used as the ambient medium, and the change in frequency and attenuation determined as a function of a change in liquid density.

To investigate the density sensitivity of a FPW device, the model presented in Section 3.3.2 will be used. To reiterate, this structure comprises of a $2.0$µm Si, $0.4$µm Al and $0.6$µm ZnO layers with a wavelength of $100$µm. The liquid layer was modelled on the back of the Si layer, thus neglecting the conductivity of the medium. Using the techniques described in Section 6.2.3, the liquid loaded centre frequencies of the $A_0$ and $S_0$ modes are $2.15$ and $65.28$MHz, corresponding to velocities of $214.6$ and $6527.7$m/s respectively. A preliminary investigation of density sensitivity was conducted at a fixed structure thickness, where the density was varied $\pm 1\%$ from its centre value of $997$kg/m$^3$. Over this range, it was found that the change in phase velocity was linear with both positive and negative variations in density. For the presented structure, the maximum shift in operational frequency, with a $1\%$ change in density was $-6.873$kHz and $-619.34$Hz for the $A_0$ and $S_0$ modes respectively, corresponding to a fractional change in frequency of $-3.1967 \times 10^{-3}$ and $-9.49 \times 10^{-6}$.

In evaluating the density sensitivity of a FPW, the wavelength is fixed, whilst the complex frequency is determined. However, to investigate the effect of liquid density on the attenuation, the frequency must be fixed and the corresponding complex wavenumber determined. Therefore, all calculations relating to density sensitivity were performed twice, with the real component of frequency used to determine the attenuation. Using this process, a change in attenuation of $8.68 \times 10^{-5}$ and $-5.072 \times$

$10^{-4}$dB/$\lambda$ was found for $A_0$ and $S_0$ respectively for a density deviation of $1\%$. The typical spacing between IDTs for a FPW device is approximately $2500$µm, therefore the theoretical measurable change in attenuation over this distance would correspond to $2.17 \times 10^{-3}$ and $-1.27 \times 10^{-2}$dB respectively. Accurate measurement of attenuation can be difficult [155], and thus for density measurements, changes in phase velocity are typically more suitable [145, 157].

Of more interest is the change in resonant frequency of the FPW structure as a function of underlying Si thickness. In this analysis the thickness of the Si layer is varied, whilst all other layers remain constant. Figure 6.17 depicts the change in resonant frequency for the first two primary modes as the density of the liquid medium is decreased by $1\%$. Figure 6.17 is generated by calculating the variation in resonant frequency between the theoretical liquid density and a corresponding $1\%$ reduction. A negative frequency shift indicates an increase in resonant frequency.

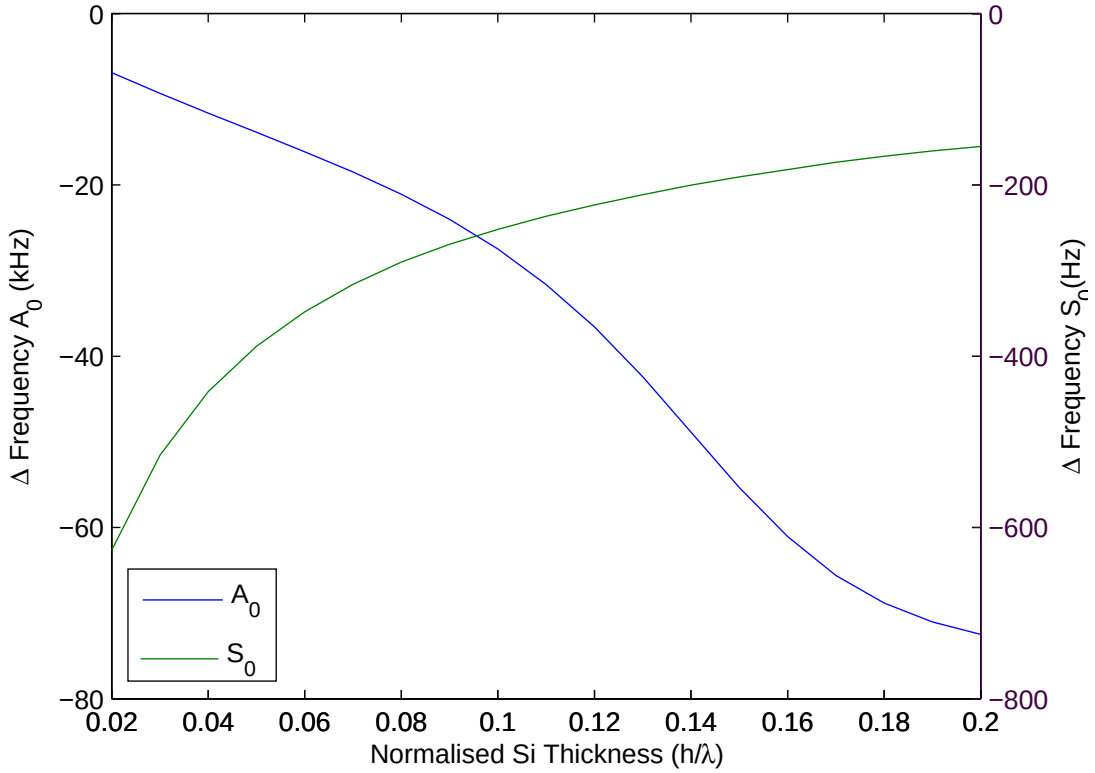


Figure 6.17: Liquid Density Modification and Si Thickness Frequency Shift

From Figure 6.17, it can be clearly observed that $A_0$ is highly sensitive to changes in

liquid density. As a function of centre frequency, a maximum shift of $-0.49\%$ is found at a Si thickness of $20$µm. At this point the phase velocity of the mode is beyond the compressional velocity of the liquid medium and energy is radiated into the surrounding environment. For density sensing applications, the Si thickness should be selected to ensure the phase velocity of the mode is below that of the compressional velocity of the liquid. In this particular structure a Si thickness below $15.3$µm would minimise the acoustic energy being dispersed into the surrounding medium. If operating at the prescribed thickness, a relative change in frequency of $-0.41\%$ would be obtained. Although not shown here, at the maximum desired thickness, the attenuation of $A_0$ has increased by a factor of three, however this is still too small to be used to detect changes in density.

With respect to $S_0$, a relatively small frequency shift is observed in comparison to $A_0$. This is due to the mainly longitudinal particle motion as was discussed in Section 4.3.1. Similar to the mass sensitivity to be discussed shortly, the shift in resonant frequency when subjected to a change in density is a maximum in the low frequency-thickness limit. At this point, the phase velocity of the $S_0$ mode is at a maximum. In terms of frequency, a maximum deviation of $625$Hz is calculated at a Si thickness of $2.0$µm, which corresponds to a previously discussed fractional deviation of $-9.49 \times 10^{-6}$. In many practical applications, a variation of $625$Hz could be attributed to system noise, therefore reinforcing the concept that $S_0$ is unsuitable for liquid media density sensing applications.

An analysis was also performed on potential methods to increase the observed change in resonant frequency of the presented FPW structure when subjected to a $1\%$ reduction in density. Using the premise of Section 4.3.2 an alternative piezoelectric layer was selected, in this case AlN. The ZnO layer was replaced with AlN layer of identical thickness and the change in resonant frequency recalculated as a function of underlying Si thickness. For comparative purposes, a purely Si structure with identical overall dimensions was also investigated. Although a far simpler structure to fabricate, it is necessary to use an external means to excite the acoustic waves such as bonded transducers or laser excitation, which would not only increase the size of the device, but also greatly increase its complexity. Figure 6.18 illustrates the change in $A_0$

resonant frequency as a function of Si thickness for all three cases.

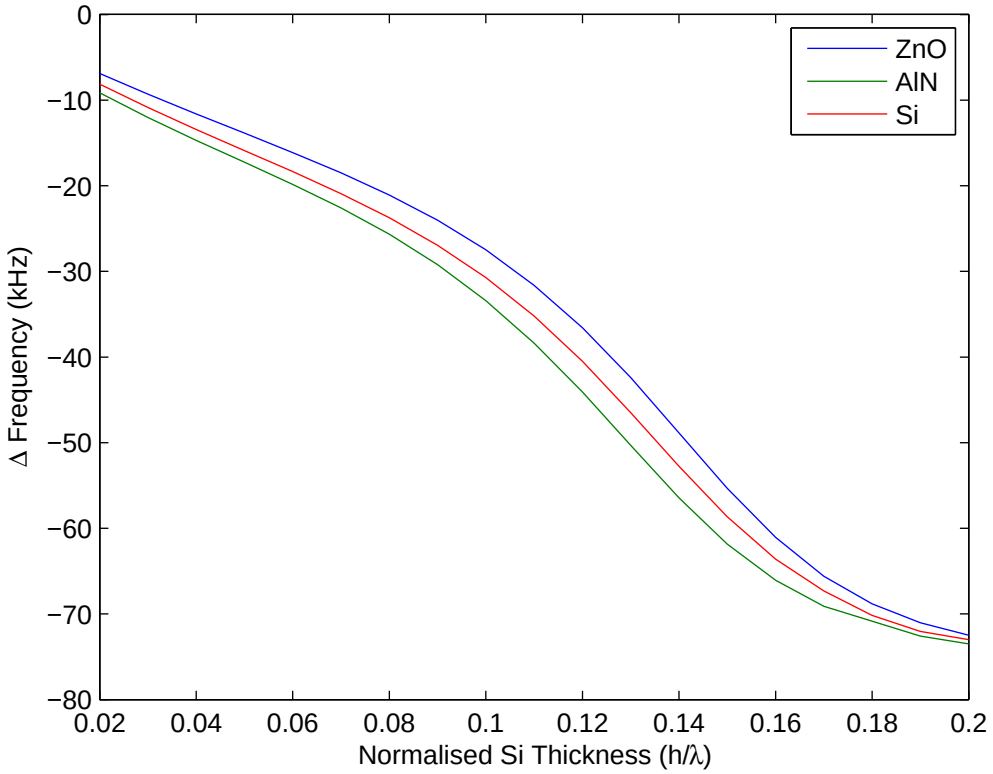


Figure 6.18: Primary Antisymmetric Mode Variation in Resonant Frequency - ZnO, AlN and Si Layers

As was found in the purely structural analysis of Chapter 4 the FPW device with an AlN piezoelectric layer has a higher sensitivity towards density. This is caused by the increase in velocity, and hence the frequency of $A_0$ for a given thickness. At an underlying Si thickness of 2µm the ZnO, AlN and Si structures exhibit frequency shifts of $0.342\%$, $0.321\%$ and $0.351\%$ respectively. Therefore, the addition of the higher velocity AlN layer slightly increases the ability of the FPW device to sense changes in density. However, it appears that the Si structure offers the highest density sensitivity, but the associated difficulty to excite the acoustic wave must be considered before this type of device is employed. Also of note is the change in resonant frequency of Figure 6.18 when compared against other simplified isotropic models [145]. In such models, the resonant frequency variation appears is linear with layer thickness when subjected to changes in liquid density. It is believed that the author's approach, which takes into

account the anisotropic nature of the materials and the frequency dependence of the added liquid layer provides a more realistic view of the physical phenomena.

A final simulation was performed to evaluate the effect of alternative guiding layers on the change in resonant frequency of $S_0$. As was found previously, the deviation in centre frequency caused by a slightly reduction in density is negligible when compared to the resonant frequency of the structure. Figure 6.19 illustrates the calculated deviation in frequency as a function of Si layer thickness. The maximum frequency shift is observed when the supporting Si thickness is at a minimum, which is opposite to $A_0$. It also appears that the density sensitivity of the AlN and single isotropic layer structures are approximately equal for $S_0$.

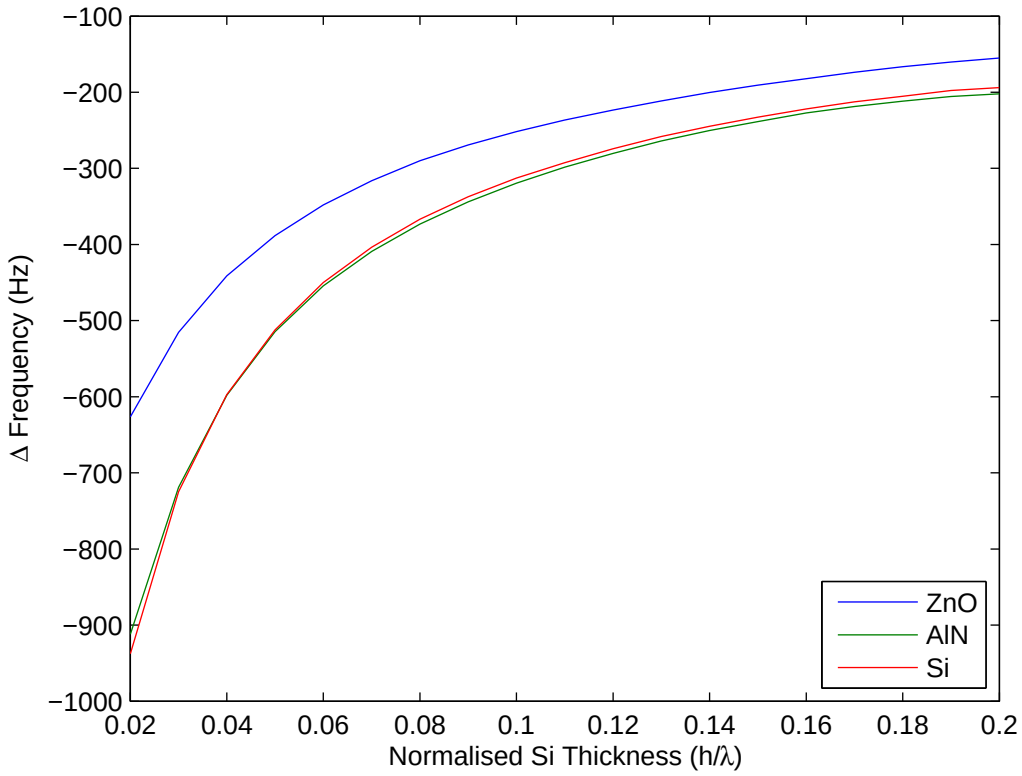


Figure 6.19: Primary Symmetric Mode Variation in Resonant Frequency - ZnO, AlN and Si Layers

### 6.4.2 Viscosity Sensitivity

Viscosity sensing is of great interest in the automotive industry, particularly in the areas of engine oil quality monitoring. In [161] a thickness shear mode resonator operating at $6$MHz was used determine the appropriate intervals to change the oil, allowing both cost and environmental savings. Whilst at low temperatures engine oil is a relatively viscous material, over the course of its normal use the viscosity can change by several orders of magnitude. With such a large change in viscosity, it is a relative straight forward task to detect the quality of the oil. However, for small values, such as those seen by slight changes in liquid temperature, the task of measuring liquid viscosity can be quite difficult. For a single isotropic layer FPW structure it is well known that the attenuation of the acoustic mode is caused by changes in the liquid viscosity [162]. In a multilayered structure, as will be shown, the combination of frequency and attenuation can be used to detect changes in the liquid viscosity. Throughout these series of simulations, unless explicitly stated, the density of the liquid medium was kept constant, whilst the first coefficient of viscosity, $\eta$, was modified.

As the viscosity of the media increases, a trapping effect can occur where the fluid acts as a deposited mass on the surface which resonates at the centre frequencies of the structure. If the thickness of the entrained fluid layer is larger than the evanescent decay length, equation 6.15, then the layer can cause substantial changes in resonant frequency. It has been shown that for a TSM resonator, the frequency deviation, although initially caused by the increase in viscosity, is dependent on the entrained liquid density [157]. For long term measurements, the highly temperature dependent nature of viscosity also requires some form of in-situ heating / cooling to ensure that results are consistent. To measure the temperature of the liquid, a meandering line resistor is typically used.

Both frequency and attenuation shifts were used to identify slight changes in liquid viscosity for the presented FPW structure. Throughout these experiments, water was used as the additional liquid layer. The viscosity was increased by $11\%$, corresponding to $5^{\circ}$C temperature reduction [148], and the shift in frequency and attenuation determined. Through the application of equation 6.14 the change in attenuation can be obtained. Figure 6.20 depicts the variation in attenuation for the presented structure.

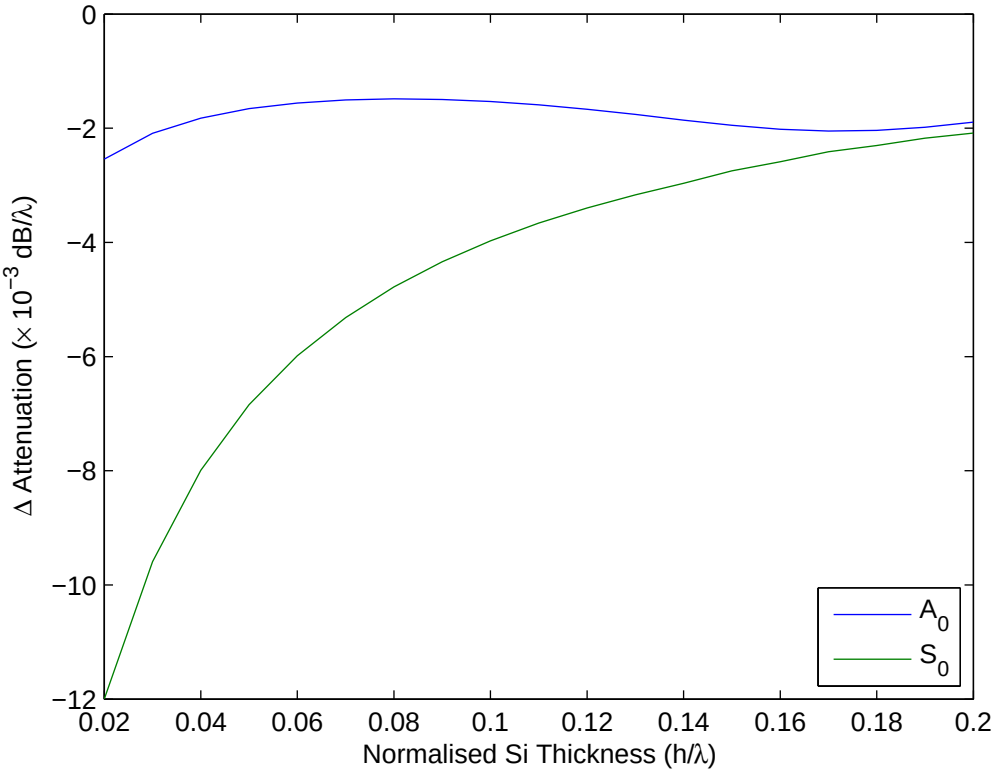


Figure 6.20: Liquid Viscosity Modification and Si Thickness Attenuation Shift

With reference to Figure 6.20 a negative value indicates that the increase in viscosity causes a corresponding increase in attenuation. For $S_0$ a thicker overall structure provides a higher deviation in relative attenuation, however the actual attenuation is decreased. The variation in actual attenuation appears to follow a $1/$thickness trend. A thicker structure allows more energy to be confined to the device rather than being lost due to viscous loading [13]. However, with respect to the $A_0$ mode, the maximum shift in attenuation is found for a Si thickness of $8$µm, corresponding to variation of $-1.48 \times 10^{-3}$dB$/\lambda$. Thus in terms of attenuation, for the presented structure the $S_0$ mode appears to provide better sensitivity towards small changes in viscosity than the $A_0$ mode.

In an attempt to improve the viscosity sensitivity of the presented FPW structure, alternative piezoelectric layers were investigated. A comparison was performed between structures having ZnO, AlN and a purely isotropic layers. Figures 6.21 and 6.22 illustrate the effect of different layers for the $A_0$ and $S_0$ modes respectively.

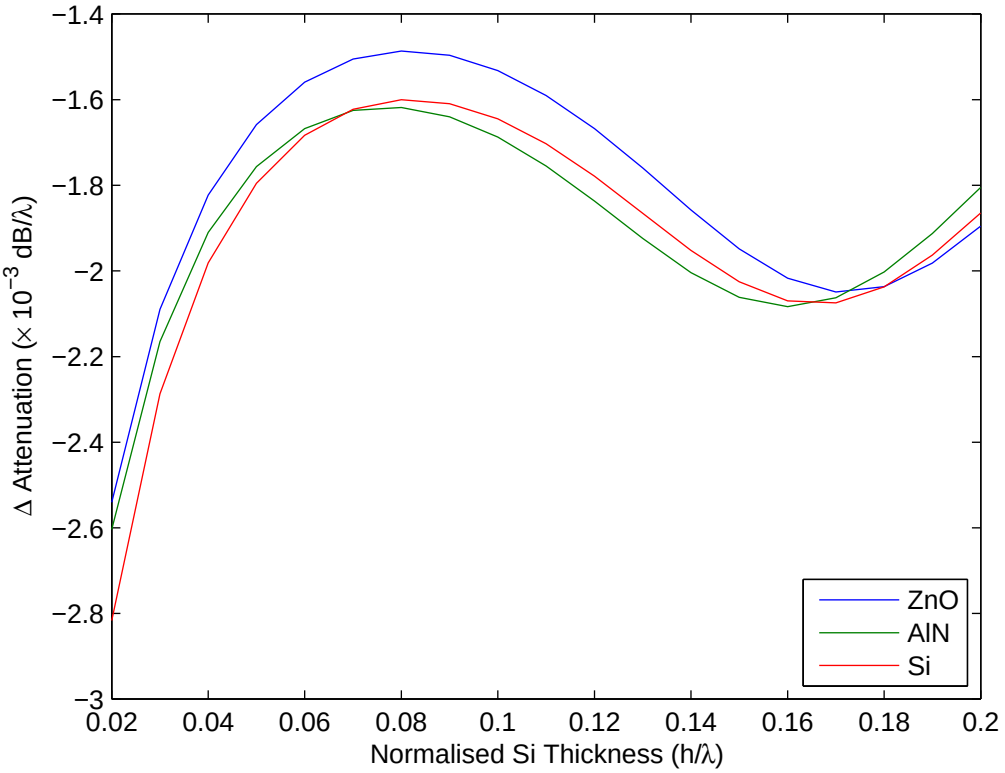


Figure 6.21: Primary Antisymmetric Mode Variation in Attenuation - ZnO, AlN and Si Layers

From Figures 6.21 and 6.22 it can be confirmed that the largest variation in attenuation for all three structures is at the lowest Si thickness. Similar to density, it appears that a FPW device comprised of a single isotropic Si layer provides the largest measurable variation. Considering $A_0$, the local minimum at an Si thickness of $16-18$µm is caused by the acoustic mode being converted to a Scholte mode. As this mode is tightly coupled to the FPW surface, the attenuation is expected to be quite small. In comparison to $A_0$, the $S_0$ mode, although having a larger phase velocity and hence frequency, has significantly higher attenuation for small Si thicknesses.

The author also decided to investigate the variation in resonant frequency caused by modification of the viscosity to examine whether this could also be used as a suitable measurand. A maximum frequency shift for $A_0$ of $-712$Hz was obtained at a Si thickness of $16$µm, corresponding to a fractional shift of $5.01 \times 10^{-5}$. At the same thickness, the variation in resonant frequency when considering density is approximately

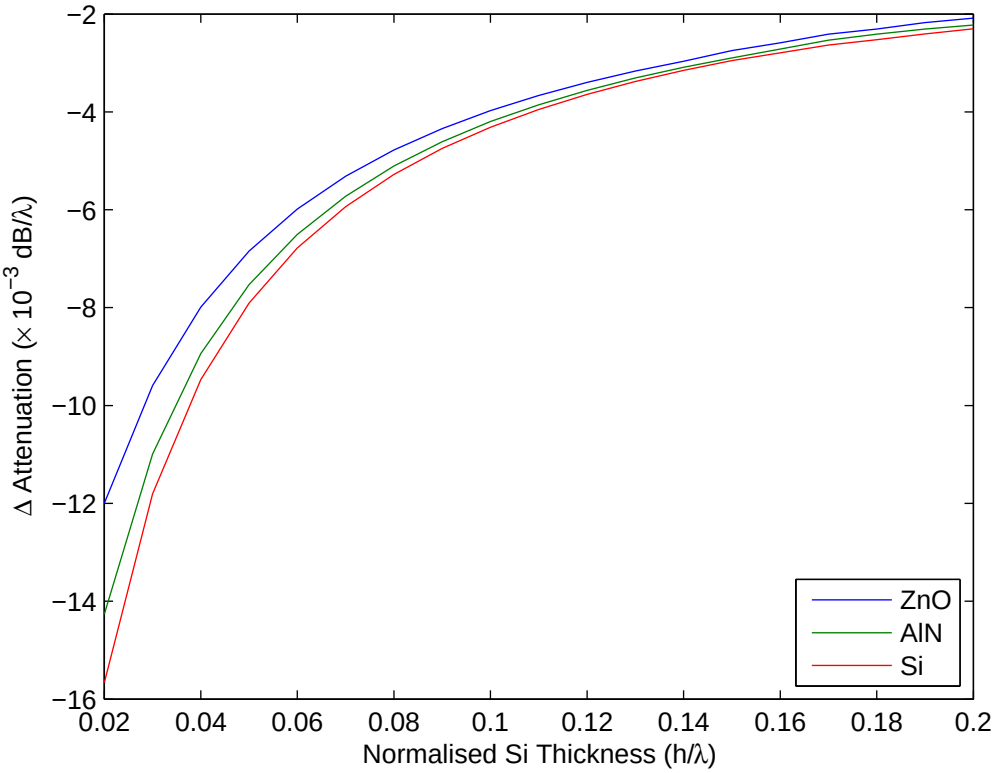


Figure 6.22: Primary Symmetric Mode Variation in Attenuation - ZnO, AlN and Si Layers

$4.30 \times 10^{-3}$. Thus, it appears that the $A_0$ mode is more suited to density sensing applications and is only marginally affected by changes in liquid viscosity. This will be further illustrated when considering the density-viscosity products later in this section.

Figure 6.23 illustrates the change in $S_0$ frequency for alternative layer configurations as a function of underlying Si thickness. In the low thickness limit, for the ZnO piezoelectric layer, a frequency shift of $-6.874$kHz is observed, corresponding to a fractional frequency deviation of $1.05 \times 10^{-4}$. In comparison to the density sensing simulations performed earlier in this section, for a $1\%$ change in density, a maximum frequency shift of approximately $626.38$Hz was observed. Therefore, in comparison with the viscosity sensing results, which clearly indicate a larger deviation in frequency, the combination of frequency and attenuation can be used to determine the viscosity in a given liquid medium. For the same thickness, an increase in frequency deviation of $2.3$kHz is obtained by using AlN rather than ZnO as a piezoelectric layer. It is also

interesting to note that if a thicker structure were desired, then either ZnO, AlN could be used as a guiding layer with only slight differences in frequency variation.

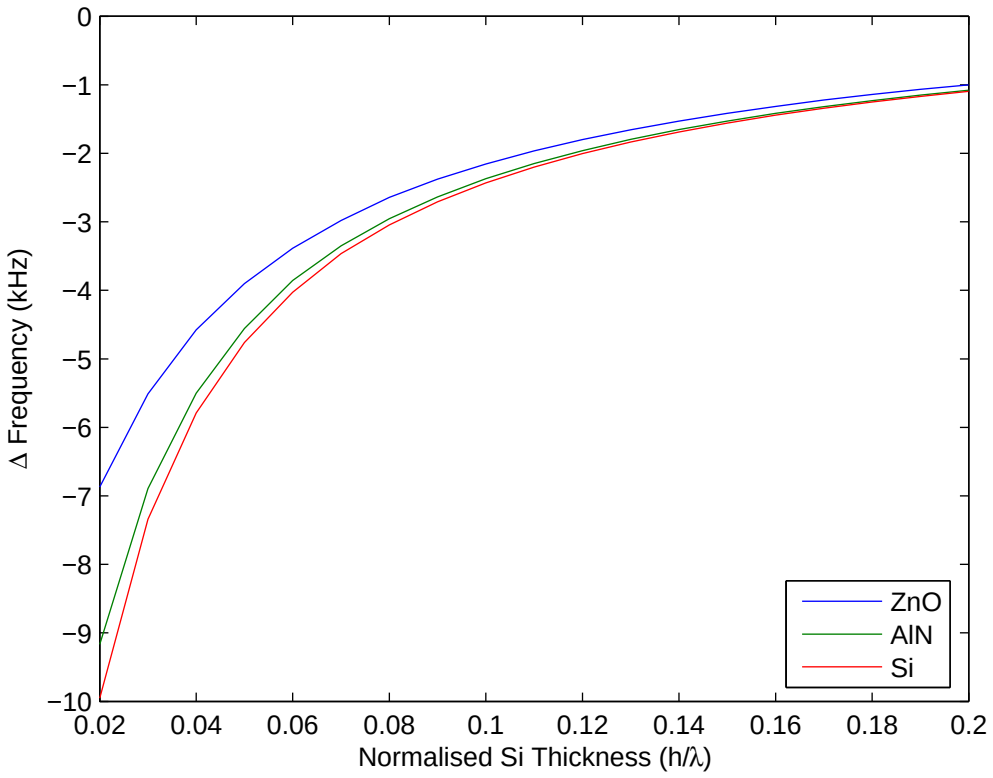


Figure 6.23: Primary Symmetric Mode - Viscosity Influence on Resonant Frequency

One associated issue with using SH-SAW and QCM acoustic wave sensors to measure liquid parameters is their inability to differentiate between density and viscosity effects [155]. In many cases a sensor array is used, where several acoustic wave structures are created with different electrical and mechanical boundary conditions. The information obtained from these structures, whether it be attenuation or frequency data, is then combined allowing the parameters of the liquid to be evaluated. A problem with this type of approach is that costs are typically increased, making the technology prohibitive when compared against other methods. A relatively recent study [157] has shown that a smooth-surfaced TSM resonator is incapable of discriminating between liquid density and viscosity. This can be rectified by creating a textured device which entraps the liquid at the device surface, however requiring extra fabrication steps. Love mode SAW structures also suffer from the same inability to discern liquid

media parameters from a single structure [157].

Unlike SAW and TSM structures, a multilayered FPW is theoretically capable of differentiating between density and viscosity effects. Although briefly illustrated when considering viscosity effects, the true ability of a FPW structure to theoretically discriminate between density and viscosity can be seen by evaluating the change in resonant frequency as a function of the density-viscosity product. Figure 6.24 presents the density-viscosity product for $A_0$ and Figure 6.25 depicts the same information for $S_0$. In these figures, the density was held constant whilst the viscosity range modified, and vice-versa. The square root of the density-viscosity product was varied between $0.1$ and $2$ $\sqrt{kgPam^{-3}s^{-1}}$ and is plotted against the change in resonant frequency. For this analysis, the $2.0$µm Si structure is used with a piezoelectric ZnO layer.

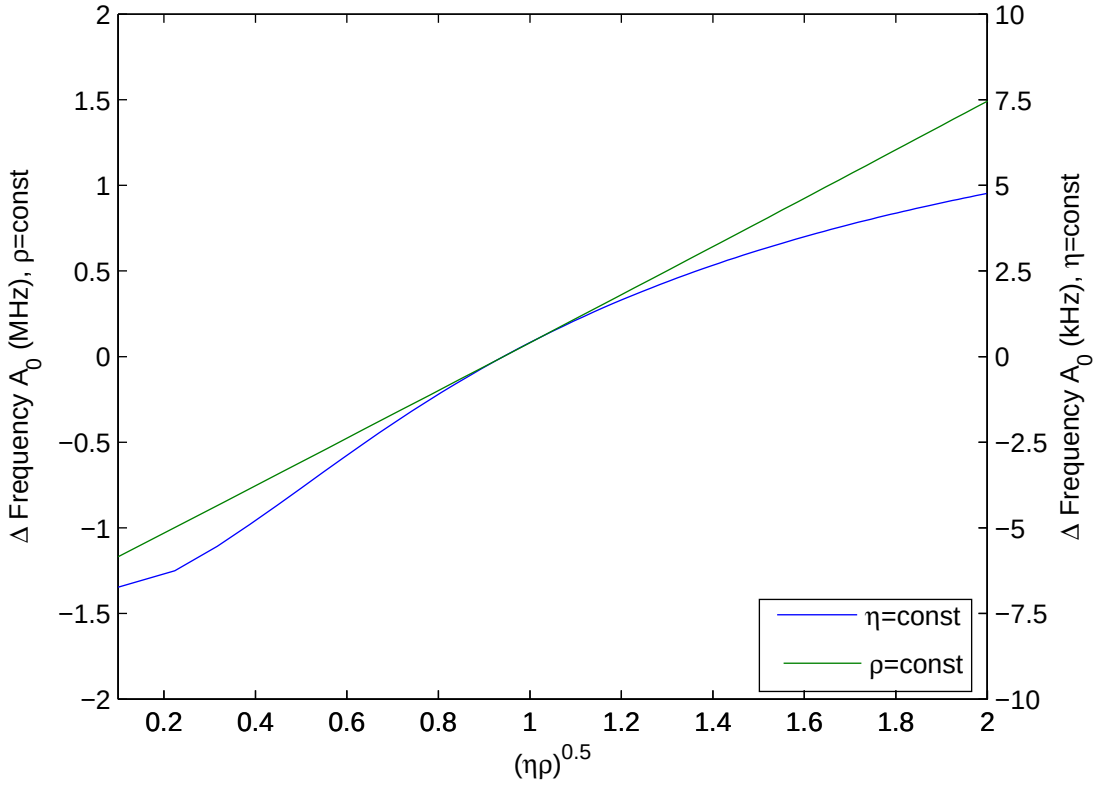


Figure 6.24: Primary Antisymmetric Mode - (Density $\times$ Viscosity)$^{0.5}$

Considering Figure 6.24, it can be immediately seen that there is a noticeable difference in resonant frequency variation between constant density and constant viscosity simulations. The $A_0$ mode appears to have a far higher sensitivity towards changes in

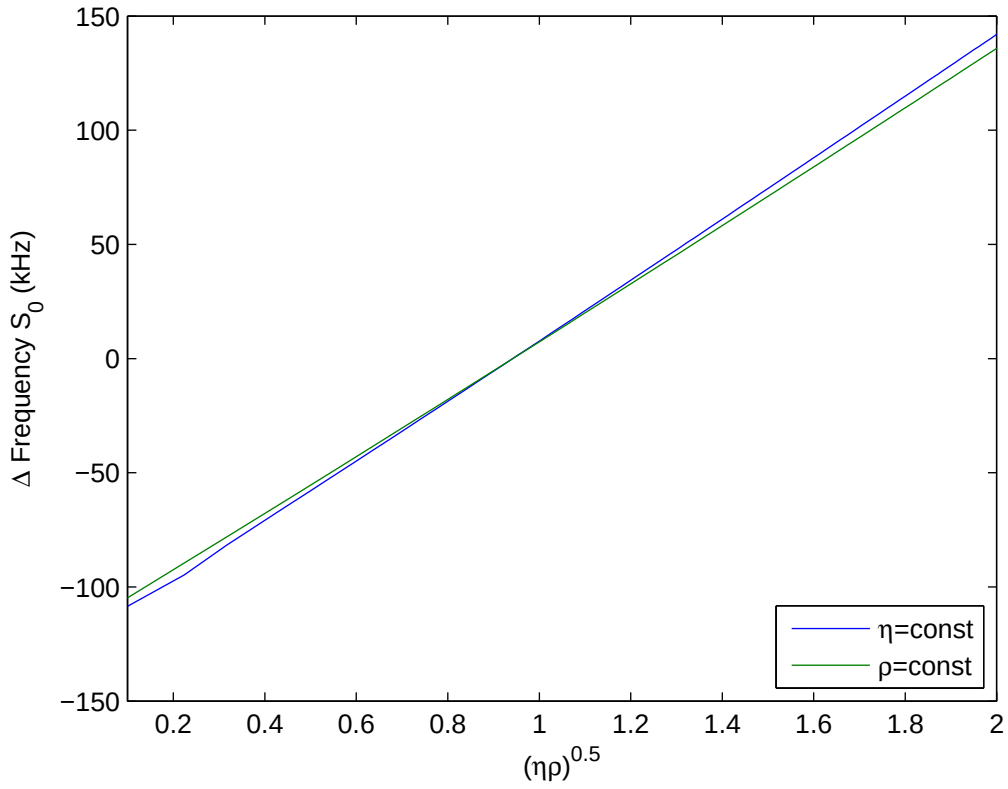


Figure 6.25: Primary Symmetric Mode - (Density $\times$ Viscosity)$^{0.5}$

density rather than viscosity. Frequency shifts of up to $1.42$MHz are obtained for density modification (constant viscosity), whereas when the viscosity is varied (constant density), the maximum deviation in resonant frequency is approximately $-5.85$kHz for the same density-viscosity product. As a percentage of centre frequency, the maximum deviation for $A_0$ is $40\%$ reinforcing that $A_0$ is better suited for density sensing applications than viscosity sensing.

In comparison, the $S_0$ mode shows a relatively linear dependence on the square root of the density-viscosity product. However, as previously mentioned, if the $S_0$ mode were to be used for sensing applications in liquid media, it would also be necessary to examine the attenuation component as well.

### 6.4.3 Differential Measurements

A key advantage of using a FPW device in liquid media sensing applications is the ability to shield the sensitive IDTs and piezoelectric layer from the liquid media. As

the device is constructed with a metallic ground plane between the Si and piezoelectric layers, the electrical influence of the liquid can also be ignored. However, if so desired, both sides of the FPW can be used for differential measurements. Using this approach a reference liquid is placed on one side of the structure whilst the other surface contains the liquid media under test. Using this approach there are additional concerns with delivering the liquid to both surfaces of the structure simultaneously, which typically requires the inclusion of a flow-cell which will also effect the propagation of the acoustic wave.

It was found in the previous sections that $A_0$ is well suited to measuring changes in density, whereas $S_0$ is better for detecting changes in viscosity, provided both frequency and attenuation are considered. Figure 6.26 illustrates the change in resonant frequency of the $A_0$ mode when both sides of the structure are loaded with a water layer, with one side having $1\%$ reduction in density. As a reference, the frequency deviation for a single sided liquid loaded structure is included, indicated by the 'S' prefix.

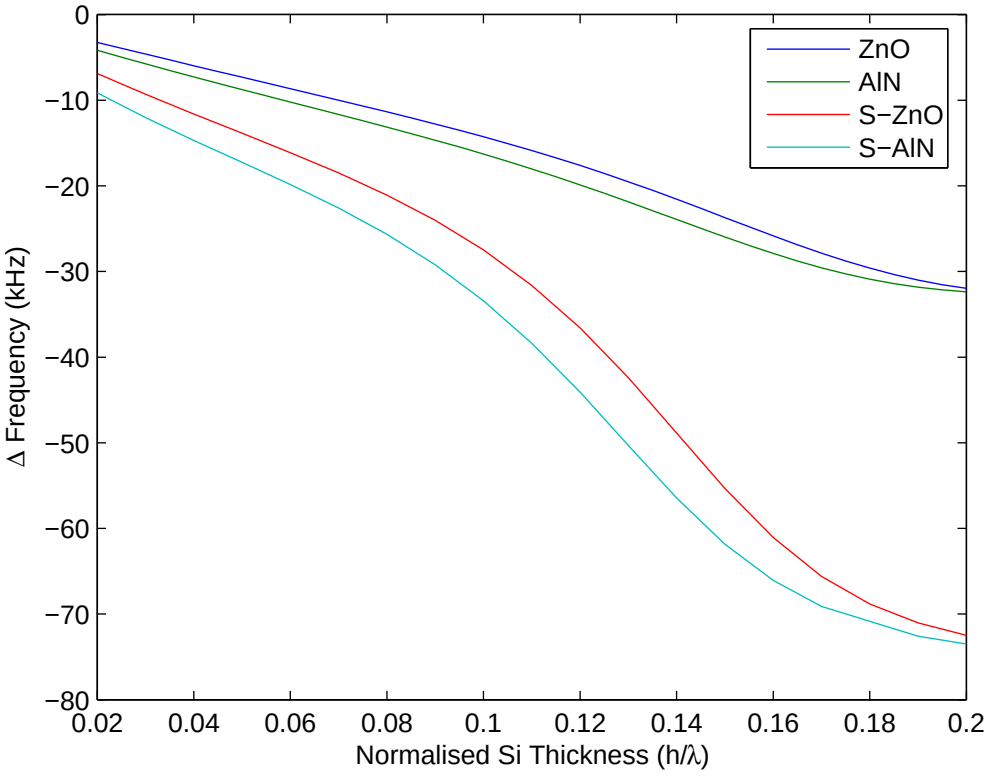


Figure 6.26: Primary Antisymmetric Mode - Density Reference Liquid Sensitivity

In this configuration the ability of the FPW device to detect changes in density is greatly reduced. Recall for a liquid loaded FPW structure the dominant displacement component is in the transverse direction. When both sides of the structure are loaded this motion becomes highly damped. The frequency deviation is less than half across the range of Si thicknesses of interest. Even with the addition of alternative piezoelectric layers, the FPW density sensitivity is reduced. Therefore, for density sensing applications, the delivery of the liquid media on one side of the structure provides the highest measurable frequency deviation.

For the $S_0$ mode, the frequency variation under the dual liquid layers does not vary significantly. Again, by considering the displacement profiles, this can be simply explained. The primary displacement for $S_0$ is in the longitudinal direction, and as it has been shown that density mainly affects the transverse components, such as those in $A_0$, the frequency shift is minimal.

Interestingly, when both sides of the structure are loaded and the viscosity varied between the two liquid layers, the $A_0$ mode becomes more sensitive to viscosity changes than $S_0$. In reality, the variation in attenuation for $S_0$ is reduced from $-1.2 \times 10^{-2}$ to $1.9 \times 10^{-3}$dB/$\lambda$. However, as shown in Figure 6.27, the attenuation for $A_0$ is increased from $-2.54$dB/$\lambda$ to $6.64$dB/$\lambda$. Also of note is the sign change in attenuation shift between single and dual layer configurations. Therefore, if the structure is loaded on both sides, then $A_0$ provides a far greater measure of changes in viscosity. Considering the particle displacements, as the $A_0$ displacement is mainly transverse, the addition of another liquid layer greatly damps the motion, causing larger variations in attenuation.

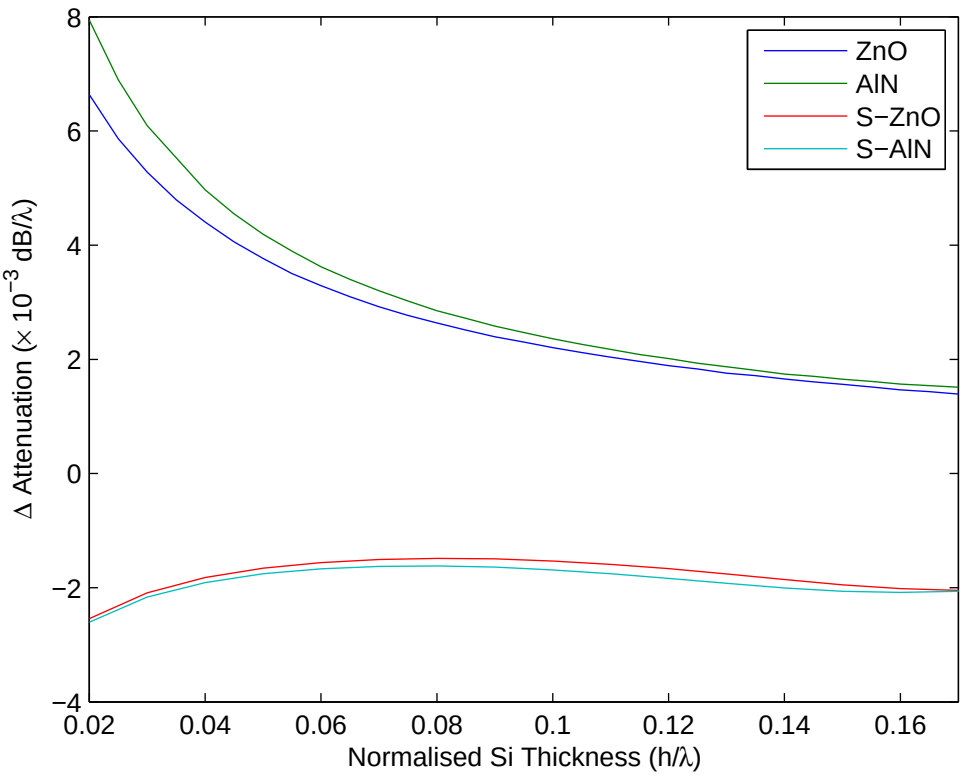


Figure 6.27: Primary Antisymmetric Mode - Viscosity Reference Liquid Sensitivity

### 6.4.4 Mass Sensitivity

For biosensing applications the ability of the FPW structure to detect an added mass within the liquid medium is of prime importance. The calculation of the mass sensitivity of a liquid loaded FPW is based on the perturbation approach, where it is assumed that the added mass does not significantly effect the wave propagation throughout the structure. It is also assumed that the attached mass layer does not induce shear stresses in the liquid, and thus the liquid layer can still be modelled as a Newtonian fluid.

Two approaches were used to evaluate the mass sensitivity of a liquid loaded FPW device. The first was based on the surface particle displacement presented in Chapter 4, allowing the sensitivity to be calculated at the fluid-solid interface. The second approach involved placing a fictional mass on the surface and then determining the corresponding change in frequency. Good agreement was achieved between the two different techniques. In the following analysis, the mass sensitivity calculations are based on the perturbation approach presented in Chapter 4. The simulated FPW structure is identical to that studied in Section 4.3.2 to allow a direct comparison to be made.

Figure 6.28 presents the mass sensitivity of a liquid loaded FPW as a function of underlying Si thickness. As a reference, the sensitivity is also presented for the unloaded case discussed in Chapter 4 indicated by the 'Ul' prefix. From Figure 6.28 it can be seen that the mass sensitivity of the $A_0$ mode is significantly reduced in the presence of an additional liquid medium. In comparison to the unloaded scenario, in the low thickness limit, the mass sensitivity is reduced by approximately $268\text{cm}^2/\text{g}$. This is caused by a reduction of the particle velocity at the fluid-solid interface caused by the addition of the lossy liquid layer. However, when compared to other acoustic wave sensors that can be used in liquid media [163], the calculated sensitivity is still quite high. The $S_0$ mode shows only a slight reduction in mass sensitivity when used in liquid media. This is due to the relatively high frequency of operation, coupled with the dominant particle displacement being in the longitudinal direction. A negligible reduction of $6\ \text{cm}^2/\text{g}$ is found for the $S_0$ mode when operating in liquid media. As was found in Chapter 4, by replacing the ZnO piezoelectric layer with AlN, the sensitivity of the device, even when operating in liquid media, increases by $15.4\%$ and $26.7\%$ for $A_0$ and $S_0$ respectively.

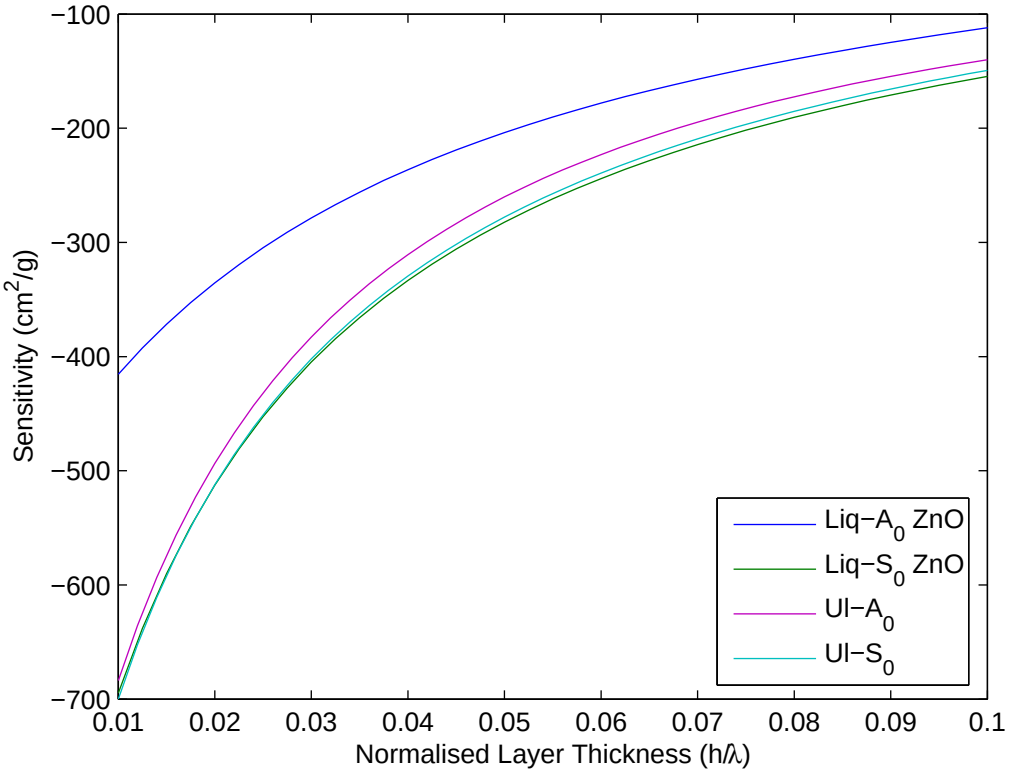


Figure 6.28: Liquid Loaded FPW Device - Mass Sensitivity

## 6.5 Device Fabrication

To confirm many of the analysis techniques and results presented in this thesis, the author has begun fabrication of a multilayered FPW structure with a layout similar to that of Figure 2.1. Many of the materials listed in Figure 2.1 were not available to the author and as such appropriate substitutions have been made. At the time of writing, the author had successfully formed a 24µm Si membrane on which all other layers will be deposited. Although the thickness of the structure is above ideal for liquid media sensing applications, the fabricated structure is consistent with that used for the FEM analysis demonstrated in Chapter 5.

The fabrication of the thin membrane, which defines the active area of the device, relies on the successful deposition of an appropriate mask material whilst the bulk silicon is chemically etched. Several different materials were considered, ranging from r.f. sputtered $Si_3N_4$ and $SiO_2$, to spin coated polymers. Microscopic examination of the sputtered films indicated numerous pinhole defects which would ultimately allow

the etchant to reach the underlying substrate in incorrect regions. The deposition conditions for the films were continuously altered, however no viable solution could be found. To alleviate the Si masking issue, a thermally grown $SiO_2$ was used. The thermally deposited $SiO_2$ provided a far superior etch mask, although the process took significantly longer to complete. A 4-inch silicon substrate was quartered and placed in an oxidation furnace for $6$ hours, at a temperature of $1050°$C, with an oxygen background flowing at 1l/m, resulting in a native oxide layer of $1.22$µm. The thickness of the layer was determined by placing a photoresist mask on the sample and etching a section of $SiO_2$ in a buffered hydrofluoric acid ($HF:NH_4F:H_2O$, 3ml:6g:10ml) solution. Once an appropriate etch mask was found a rectangular section, measuring approximately $9 \times 3$mm, was photolithographically patterned and opened on the backside of the sample to define the membrane area of the FPW device.

To etch the Si sample, $45\%$ Potassium Hydroxide (KOH) in water was used. Both materials, Si and $SiO_2$, are known to be chemically attacked in KOH, however depending on the quality, thermally grown $SiO_2$ is etched at a rate up to ten times less than Si [164]. An approximate etch depth of $320$µm was required, thus the mask layer alone would be insufficient to resist the etch for the required depth. To ensure that the $SiO_2$ film would last the length of the silicon etch, a stainless steel sample holder was fabricated. It consisted of two $316$ stainless steel plates with two teflon (PTFE) gaskets to hold the samples in place. A section was removed from the top stainless steel and teflon gaskets to allow the etchant to gain access to the previously exposed rectangular section of the Si samples.

The etch rate of Si in KOH is a well studied process [165] and is known to be a nonlinear function of temperature as well as KOH concentration. Several experiments were conducted, each with varying degrees of success. Initially it was believed that a fast etch rate would be favourable as the mask layer would have to withstand less time in the heated etch solution. A temperature of $90°$C was used, which etched the complete Si in less than three hours. The resulting thin membrane appeared to be quite rough, even to the naked eye, which is unsuitable for acoustic wave propagation. The surrounding mask layer was also totally removed, which caused several unwanted pits in the silicon. In light of these results, it was decided to etch the Si at a lower

temperature. The author then attempted to etch the wafer at $70$°C, where excellent results were obtained. The membrane was etched to a thickness of $24$µm over a $12$ hour, $45$ minute period, undertaken over two days. The etch solution was not replaced, nor stirred and gave an approximate rate of $26.26$µm/hr. Around the cutout in the stainless steel the etch mask had been totally removed, however remained on the backside of the wafer. After decontamination of the sample, the remaining $SiO_2$ was removed in the aforementioned buffered hydrofluoric acid solution.

Once the membrane of the structure was created, a decision had to be made with regards to the metallic ground plane and piezoelectric guiding layer. A reactive d.c. sputtering system was designed, developed and commissioned by the author to deposit the aluminium ground plane as well as the essential piezoelectric aluminium nitride layer. Although the author had previous experience with other piezoelectric materials such as zinc oxide, the selected materials could be deposited in one system without breaking the vacuum seal, thereby limiting contamination by manual handling of the samples.

The sputtering system developed by the author consists of a stainless steel chamber, integrated substrate heater, two mass flow controllers and a MDX $10$KW d.c. power supply. A base vacuum of $8.7 \times 10^{-7}$ Torr was achieved using an Edwards Diffstak diffusion pump. As these types of pumps can not be safely used at sputtering pressures, a secondary Alcatel $5081$ turbomolecular pump was used to maintain sputtering pressure. The system was continually loaded with a 4-inch diameter $99.999\%$ pure aluminium target that was liquid cooled during the sputtering process. A custom built substrate heater was fabricated, capable of maintaining sustained temperatures of $600$°C. For operation at these temperatures a secondary cooling loop was integrated into the chamber sidewalls. Two variable power circular electromagnets were used form the sputtering magnetron, which in turn increased the number of secondary electrons, lowered the deposition pressure and in turn increased the yield [166]. The electromagnet current was fixed during the deposition process. It was found that a higher magnetic field was required to initiate the plasma, with the field being reduced to a specified value during the deposition process. The influence of the electromagnet voltage and currents has been studied, however is beyond the scope of this preliminary

discussion. In this configuration, the target to substrate height was fixed at approximately 11cm. Table 6.2 indicates the basic d.c. sputtering parameters for the Al and AlN thin films:

Table 6.2: FPW Thin Films - Deposition Conditions

| Parameter | Al | AlN |
|---|---|---|
| Magnetron Power (W) | 120 | 120 |
| Magnetron Voltage (V) | 417 | 305 |
| Inner DC Electromagnet Voltage (V) | 9.7 | 10.4 |
| Inner DC Electromagnet Current (A) | 1.2 | 1.2 |
| Outer DC Electromagnet Voltage (V) | 7.9 | 10.3 |
| Outer DC Electromagnet Current (A) | 6.8 | 1.0 |
| Sputtering Gas | Ar | 40% Ar, $N_2$ balance |
| Sputtering Pressure (Torr) | $1.5 \times 10^{-2}$ | $1.0 \times 10^{-2}$ |
| Deposition Time (min) | 10 | 120 |
| Deposition Rate (μm/hr) | 1.35 | 0.516 |
| Substrate Temperature | 22°C | 350°C |

A four point probe measurement technique [167] was applied to the Al thin films to determine their quality. A sheet resistivity of 25.79μΩcm was obtained, 9.5 times larger than the standard thin film value [167], however still suitable for the electrical ground plane. The adhesion of the Al thin film was determined by a simple adhesive tape test. Here, a thin piece of adhesive tape was placed over the deposited film, pressed down, and then removed. If the film is also removed with the tape, then the adhesion is deemed to be insufficient. Due to the sputtering process, where electrons are accelerated towards the substrate, the deposited Al thin film was not removed, further indicating a high quality film.

To determine the quality of the AlN thin film, several different techniques were employed. For the AlN to be piezoelectric, the film should be c-axis orientated [168]. As the film could not be directly viewed via a Scanning Electron Microscope (SEM), an Atomic Force Microscope (AFM) was used. Figure 6.29 depicts a 1μm square scan of

the deposited AlN film. It can be seen that a majority of the grains are aligned perpendicular to the substrate surface, thereby confirming the c-axis orientation of the film. Furthermore, the AFM was used to determine the piezoelectric properties of the film using a recently developed technique, of which the results have been accepted for publication in an international journal in late 2007. The piezoelectric properties of thin films until recently have been evaluated using a piezoresponse force microscope. This is typically a very costly machine, and thus an alternative approach was required. In the author's approach, a standard AFM can be used to evaluate the piezoelectric properties without modification of the instrument. A planar sandwich structure is fabricated, where a bottom Al electrode is deposited on a Si substrate. The film under test is then deposited, followed by an upper Al electrode. A low frequency alternating voltage is then applied to the top and bottom electrodes which in a piezoelectric material causes a slight deformation. The AFM is operated in contact mode, with the non-conductive tip placed on the upper electrode. The scan area is set to zero, which causes the tip to continuously measure the same point. The transverse displacement of the tip corresponds to the applied voltage and frequency, and hence the piezoelectric coefficient $d_{33}$ can be directly obtained. The resulting scan image includes a series of bright and dark bands which represent the change in tip height as a function of time. For the deposited AlN thin film, an average displacement of $0.44$nm was obtained, corresponding to a value of $2.132$pm/V for $d_{33}$, therefore further proving that the deposited film is piezoelectric. The validity of the measurement technique has also been confirmed using a PLZT thin film.

Furthermore, an X-ray Photoelectron Spectroscopy (XPS) analysis was performed on the film to identify its composition. A depth profile was performed, where throughout the thickness of the film, a relatively constant atomic ratio of aluminium to nitrogen of $41.8 : 43.3$ was obtained, indicating good stoichiometry. The remaining materials in the sample were carbon and oxygen. It is believed that the process gas line had been opened to atmosphere hence causing the abnormally high oxygen concentration.

The final step in the fabrication process is the deposition of the electrodes to form the interdigital transducers. A chromium photolithographic mask has been developed by the author, however at the time of writing, the author had not successfully patterned

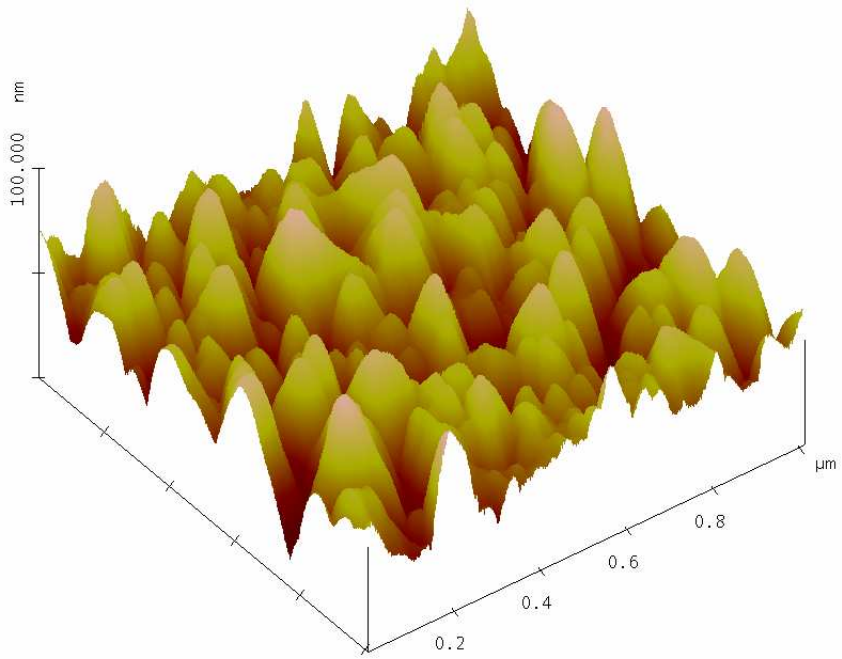


Figure 6.29: AlN Thin Film - AFM Results

the structure onto the FPW membrane. The mask consists of various FPW designs, however the most promising design consists of $25$ input and output electrode pairs, with an edge to edge spacing of $2500$µm, corresponding to $25\lambda$. The acoustic aperture was set at $3000$µm. It is envisaged that a FPW device will be successfully fabricated by December 2007 as the author continues at RMIT University in a post-doctorial research position.

## 6.6 Conclusion

In this chapter modelling of FPW devices for sensing applications in liquid media has been discussed. The additional liquid layer has been described in terms of complex, frequency dependent, material properties. It was found that a liquid layer can be approximated as a semi-infinite layer thereby reducing the electrical and mechanical boundary conditions of the wave propagation problem. Modifications have been sub-

sequently made to the stiffness matrix method, where is has been shown that via the incorporation of a complex wavenumber, or frequency, the wave propagation problem is lossy media can be simply calculated.

Using the modified stiffness matrix method, it has been shown that a tightly coupled interface wave, known as a Scholte mode, exists for a FPW structure which is attributed to being responsible for most liquid density sensing results. The displacement profiles for a liquid loaded FPW structure have also been evaluated, where it was found that beyond a critical thickness the energy of the low velocity $A_0$ mode disperses into the surrounding medium. It was also found that $S_0$ is responsible for establishing a compressional wave within the liquid which could potentially be used for liquid pumping and delivery.

The frequency domain characteristics of a multilayered FPW device have been presented using the author's novel approach based on the FEM. The author's techniques were compared against the widely accepted spectral domain Green's function, where it was found that this technique, at least in its current implementation, is not capable of accurately determining the frequency characteristics of the structure. The necessary modifications to the spectral domain Green's function are quite involved, whereas by using the author's approach, liquid loading of a FPW can be applied by simply adding an additional layer. A series of guidelines have been developed on the use of the FEM when considering liquid loaded structures, and to the best of the authors knowledge is the first time such discussions have been presented.

The use of both primary antisymmetric and symmetric modes has been considered for sensing applications in liquid media. It was found that $A_0$ is well suited to density sensing applications, whereas $S_0$ can be used for viscosity measurements. Using a dual band frequency measurement system, the parameters of both modes can be obtained simultaneously, thereby requiring only a single structure to evaluate liquid density and viscosity. The mass sensitivity for a FPW device operating in liquid media, which is of prime importance for biosensing applications, has been discussed. It was found that in the presence of a liquid medium the sensitivity of the primary antisymmetric mode was reduced by approximately $268\text{cm}^2/\text{g}$, however when compared to other acoustic wave devices, this value is still relatively high. The mass sensitivity of the symmet-

ric mode remains largely unaffected by the presence of a liquid due to its dominant longitudinal particle displacement.

A brief introduction has also been given on the author's attempts to fabricate a functional FPW device. The silicon masking and etching process has been described, from which the author has successfully fabricated a Si membrane with a thickness of approximately $24\mu$m. Furthermore, preliminary XPS characterisation and the unique application of an AFM have shown that the deposited AlN thin films are stoichiometric, c-axis orientated and hence piezoelectric. Optimal deposition parameters for both Al and AlN thin films, for the d.c. sputtering system designed and commissioned by author, have been described allowing these materials to be utilised in the future fabrication of FPW structures, as well as other acoustic wave devices.

# Chapter 7

# Conclusion and Future Work

In this thesis, a novel approach to the analysis of Flexural Plate Wave devices for sensing applications was presented. The author has successfully demonstrated a novel simulation and evaluation technique of FPW devices based on the convergence of the Finite Element method with classical SAW analysis methods and related procedures. It was shown that the technique demonstrated by the author can accurately and efficiently evaluate key electrical and mechanical characteristics of complex multilayered FPW devices when compared to more conventional, routinely applied, approaches. Further to meeting the key objectives of the author's research, several major achievements were obtained, including:

- Development of a novel analysis technique for the simulation and evaluation of multilayered FPW devices based on the convergence of the FEM with classical analysis techniques and related procedures typically applied to SAW structures. The necessary modifications to SAW device analysis techniques to suit FPW structures have been fully described and implemented by the author through careful consideration of the underlying principals and assumptions.

- Development of a three dimensional FEM simulation for the analysis of multilayered FPW structures. Two alternative simulation procedures, the first comprising of an electrostatic analysis and the second based on a dynamic transient analysis, have shown that the approach demonstrated by the author is capable of simultaneously evaluating various second-order effects such as electromagnetic

feedthrough and diffraction. These effects typically have to be considered individually by other analysis techniques. The three dimensional dynamic transient analysis further illustrated that the shear particle displacement of a FPW device can be assumed to be zero, therefore suggesting that a less computationally intensive two dimensional model is appropriate to simulate the structure.

- Comprehensive development and evaluation of a two dimensional FEM simulation procedure for the analysis of multilayered FPW structures. Various FPW structures have been simulated, with and without the underlying silicon support structure, which is typically neglected with other, more conventional, modelling techniques. It was shown that the support structure causes a measurable shift in both resonant frequency and attenuation of the first two primary acoustic modes, thereby providing a significantly more realistic representation of a physical FPW structure. Various signal processing techniques have been considered to improve the frequency domain resolution of the FEM results. A clear link has been established between the FEM simulation parameters and the calculated frequency response, which allows a desired resolution to be obtained.

- To obtain the FPW device frequency domain characteristics, the author employed a two dimensional dynamic transient FEM analysis. A modified impulse function was applied to the input IDT and the corresponding charge evaluated simultaneously on the input and output transducers over the complete simulation time. By carefully modifying SAW analysis techniques to suit FPW structures, the complete device admittance characteristics were calculated from the FEM results. This data was then converted to the more commonly used scattering parameters, allowing the insertion loss to be evaluated. By employing a modified impulse function, the complete frequency domain response can be obtained concurrently, without the need to apply discrete frequencies as previously done by other researchers. Furthermore, other researchers have typically utilised a modal analysis to determine the behaviour of FPW structures. This type of analysis does not take into account the excitation source, nor the piezoelectric nature of the device. The technique demonstrated by the author fully accounts for both the electrical influence of the IDTs as well as the anisotropic and piezoelectric proper-

ties of the individual layers. Although this study focused on the analysis of FPW structures, the author believes the developed technique can equally be applied to other acoustic wave devices.

- Key electrical and mechanical parameters of various FPW devices have been determined by the application of the author's novel approach based on the FEM. In particular, input capacitance, primary antisymmetric mode electromechanical coupling coefficient, admittance and hence insertion loss, have all been evaluated, where excellent agreement has been obtained when compared against other more conventional techniques. The technique demonstrated by the author has been verified by the application of both the stiffness matrix method and the widely accepted spectral domain Green's function. Via the stiffness matrix method, basic device parameters such as electromechanical coupling coefficient were calculated, whilst the spectral domain Green's function was applied to verify the FEM derived frequency response characteristics. A study was also conducted on the various FEM simulation parameters and their influence on the frequency response of a FPW device considered, allowing the author to develop a series of guidelines for the use of this technique for modelling acoustic wave devices in both liquid and gas media.

- A detailed description of the necessary additions to both the Stiffness Matrix method and FEM has been given to allow these techniques to be applied to liquid loaded FPW structures. For the FEM it was found that an additional dedicated fluid element could be used, whereas the stiffness matrix method required significant modification. A discussion was also given on the appropriate boundary conditions and assumed thicknesses for liquid media. In particular, the stiffness matrix method modelled the liquid layer as semi-infinite, whereas an optimum layer thickness of $1.5$ times the IDT edge-to-edge distance was found for the FEM simulations. The frequency domain characteristics of a liquid loaded FPW structure was presented using the author's approach and compared against a spectral domain Green's function, where it was found that the FEM provided more correct results when compared to experimental results available in literature.

- To further promote the use of the presented FEM based approach for the analysis of multilayered FPW structures, the author has developed a series of detailed modelling guidelines outlining the influence of the FEM simulation parameters. To the best of the author's knowledge, this is the first time that a critical discussion of these parameters has been presented when applied to acoustic wave structures. In particular, the influence of node density, simulation time, simulated structure length and timestep has been critically examined for an FPW device operating in gas media. Furthermore, the effect of node density and assumed liquid thickness has been discussed for a liquid loaded FPW device.

- Density, viscosity and mass sensitivity of multilayered FPW structures in liquid media has been discussed and compared against commonly quoted isotropic equivalents. To the best of the author's knowledge, this is the first time that theoretical density, viscosity and mass sensing results have been calculated for a multilayered FPW structure. Evaluation of the density-viscosity product has shown that a single FPW structure has the potential to discriminate between these two parameters. Guidelines, such as substitution of materials, to increase the density, viscosity and mass sensitivity of an FPW structure have been presented. It was found that replacement of the ZnO piezoelectric layer with another higher velocity piezoelectric material, AlN, resulted in an increase in all three quoted sensitivities.

- A critical review of modelling techniques has been presented and their suitability to the analysis of FPW structures has been discussed. Of the considered techniques, it was found that none of the existing approaches could simultaneously determine key electrical and mechanical properties. Three conventional modelling techniques were considered to verify the author's novel approach. The first technique, the transmission matrix method, was used to determine the basic properties of a FPW structures such as phase velocity and electromechanical coupling coefficient. Although relatively straightforward to implement, the technique suffered from numerical instability when applied to large frequency-thickness products and lossy material parameters, which are characteristic of liquid loaded structures. A replacement technique, the stiffness matrix method was

then considered. This particular technique was used in conjunction with a spectral domain Green's function to determine the complete frequency response characteristics of a FPW structure in the gas phase. The required modifications to these two techniques to suit FPW devices was also discussed and implemented. These techniques were also employed to verify the author's approach to the analysis of FPW structures based on the FEM.

- Particle displacement profiles for multilayered FPW structures have been discussed and compared against isotropic equivalents. It was found that the displacement in composite piezoelectric structures can no longer be segregated into purely antisymmetric or symmetric due to the differences in the material properties throughout the device. A simple computational technique was also developed to identify the predominant displacement in higher order modes near the cut-off region. When placed in contact with a liquid, a tightly coupled surface wave, known as a Scholte mode, was identified which exhibited a phase velocity approximately equal to the compressional velocity of the liquid. This mode is typically deemed responsible for most liquid sensing results presented in literature.

- A d.c. reactive sputtering system was also designed, developed and commissioned by the author. The system is capable of depositing both aluminium and piezoelectric aluminium nitride required for the realisation of the discussed FPW structures. Preliminary characterisation of the AlN films indicate good stoichiometry, with the piezoelectric properties evaluated by the unique application of an Atomic Force Microscope of which the results have been accepted for publication in an international journal.

In addition to the aforementioned major achievements, the author has also published four papers in international conference journals of which have been included within this thesis. The author's list of publications are:

- G. I. Matthews, S. J. Ippolito, W. Wlodarski, and K. Kalantar-zadeh, "Electrical parameter extraction of a Flexural Plate Wave device using the Finite Element Method," *Proc. IEEE Ultrason. Symp.*, pp. 1136–1139, 2006.

- G. I. Matthews, S. J. Ippolito, K. Kalantar-zadeh, W. Wlodarski, and A. S. Holland, "Finite Element Modelling of Flexural Plate devices," *Conference on Optoelectronic and Microelectronic Materials and Devices, (COMMAD)*, pp. 145–148, 2004.

- A. S. Holland, G. K. Reeves, G. I. Matthews, and P. W. Leech, "Finite Element Modeling of misalignment in interconnect vias," *Conference on Optoelectronic and Microelectronic Materials and Devices, (COMMAD)*, pp. 307–310, 2004.

- S. J. Ippolito, K. Kalantar-zadeh, W. Wlodarski, and G. I. Matthews, "The study of ZnO/XY $LiNbO_3$ layered SAW devices for sensing applications," *IEEE Sensors*, vol. 1, pp. 539–542, Oct. 2003.

- S. Sriram, M. Bhaskaran, K. T. Short, G. I. Matthews, and A. S. Holland, "Piezoelectric response characterization using atomic force microscopy with standard contact-mode imaging," *Micron*, In Press.

In addition to the four published conference journal articles, the author presented his novel approach to FPW analysis at the 2006 IEEE Ultrasonics Symposium, October 3-6, Vancouver, Canada.

The remainder of this chapter summarises the work conducted by the author during the course of this PhD program. Section 7.1 provides an overview of the author's work in the analysis of FPW structures for sensing applications. The author's suggestions for future work are discussed in Section 7.2.

## 7.1 Thesis Overview

This thesis was devoted to modelling Flexural Plate Wave devices for sensing applications in both gas and liquid media. Chapter 2 provided a critical review of four widely used acoustic wave devices which can equally be applied to such tasks. Key performance parameters were discussed for each device and when possible experimental mass sensitivities quoted. It was shown that FPW structures are well suited to sensing applications in liquid media due to their low phase velocity and therefore low resonant frequency. The phase velocity of the primary two acoustic modes was shown to be a function of both device membrane thickness and thin-film materials employed. By

carefully designing the FPW device, the velocity of the primary antisymmetric mode can be configured to be below that of the compressional velocity of a liquid medium, therefore confining the acoustic energy to the device thereby potentially enhancing sensitivity. Examples were given of FPW device performance parameters, where it was illustrated that these structures can exhibit mass sensitivities up to $31$ times greater than widely used QCM devices, whilst operating a approximately the same frequency.

Chapter 2 also provided an insight into various modelling techniques for the analysis of acoustic wave devices. The first series of techniques discussed focused on the evaluation of basic device parameters such as phase velocity and electromechanical coupling coefficient, whilst the second was concerned with FPW device frequency domain characteristics. A brief discussion was held on classical analysis techniques, such as the potential method, to obtain basic properties for single layer structures comprised of isotropic materials. It was found that such techniques could not be sufficiently modified for the author's purpose. To alleviate this issue, two alternative approaches, the transmission and stiffness matrix methods, were considered. The inherent instability of the transmission matrix method was highlighted, however the cause of this inaccuracy was discussed in detail later in Chapter 3. Noting the instability of the transmission matrix method, particularly when applied to liquid loaded structures, the stiffness matrix method was considered to solve the piezoelectric wave propagation problem. The stiffness matrix method was shown to be based on the reformulation of the transmission matrix method and was further demonstrated to be inherently stable. The full details of its implementation, particularly when analysing FPW structures, was discussed in Chapter 4.

The remainder of Chapter 2 considered conventional modelling techniques that could be applied to evaluate the frequency domain characteristics of FPW devices. It was found that a spectral domain Green's function appeared to be the most promising, however the approach required slight modifications to operate with FPW devices. The last technique introduced in Chapter 2, the Finite Element Method, formed the basis of the author's novel approach to the analysis of FPW devices. A discussion of other researcher's work was given, where it was found that current approaches are based on the modal analysis of FPW structures, which ignores both the excita-

tion source and the piezoelectric properties of the materials employed. Furthermore, existing models employed individual gates across the device membrane thickness to excite the acoustic modes, rather than IDTs as utilised by the author. The author's approach extended on current FEM models by considering the piezoelectric nature of the FPW structure and allowing the complete frequency response to be obtained during a single simulation. The author has also further illustrated that the demonstrated technique is capable of simultaneously modelling various second-order effects such as diffraction,electromagnetic feedthrough and triple transit, which can typically not be achieved using other accepted techniques.

Chapter 3 presented the commonly applied Transmission Matrix method and its application to solving the piezoelectric wave propagation problem for multilayered FPW structures. A brief review of stress, strain and piezoelectric constitutive equations was also given. The limiting assumptions for the transmission matrix method were described. Even though the transmission matrix method suffered from an inherent instability due to exponentially increasing partial mode wavenumbers, the method served as a basic process to evaluate boundary conditions, dispersion characteristics as well as electromechanical coupling coefficients. The instability of the transmission matrix was discussed in detail, where examples were given for FPW structures large frequency-thickness products and also complex material parameters. Due to the aforementioned numerical instability the transmission matrix method was found unsuitable for analysis of liquid loaded FPW structures.

Chapter 4 presented the recently developed Stiffness Matrix method which served as a replacement for the transmission matrix method. The technique is known to be inherently stable for large frequency-thickness produces as well as for structures consisting of complex material parameters. Based on this method, particle displacement profiles and mass sensitivity of multilayered FPW devices were calculated and compared against simpler, commonly quoted single layer structures. Using the parameters obtained from the stiffness matrix method, the frequency domain characteristics of a FPW device was determined via a spectral domain Green's function. The necessary modifications to the spectral domain Green's function to suit an FPW structure were also discussed and implemented by the author. The combination of the stiffness matrix

method and the spectral domain Green's function served as a verification method for the author's novel approach to FPW device analysis presented in Chapter 5.

The author's novel approach to the analysis of FPW devices, based on the convergence of FEM with modified SAW analysis techniques and procedures, was presented in Chapter 5. In this chapter, both three and two dimensional simulations were conducted of various FPW structures. Initially a three dimensional simulation was developed to determine the electrostatic charge density and particle displacement profiles of a multilayered FPW device. It was shown that the electrostatic charge density is not constant along the electrode depth, which is a simplifying assumption made by most other numerical techniques. The presented electrostatic analysis also illustrated the capability of the FEM to accurately model second-order effects such as electromagnetic feedthrough and diffraction. To further gain an understanding of wave propagation in a FPW structure, particle displacement profiles for a three dimensional device were also presented. Here, it was shown that the shear displacement is several orders of magnitude smaller than that of the transverse and longitudinal components, therefore suggesting that a two dimensional approximation can be used to determine the frequency domain characteristics of a FPW device.

Based on the three dimensional FPW device FEM results, a two dimensional FEM FPW device was simulated. Several different structures were simulated, including devices where the underlying silicon support was included, which is often neglected by other modelling techniques. With the inclusion of the silicon support structure a measurable shift, in both the resonant frequency and insertion loss was found, thereby providing a more realistic representation of a physical FPW device. To allow the frequency domain characteristics of a FPW device to be calculated, several post-processing techniques were applied to convert the FEM simulation output into a more usable form typically used within the Ultrasonics community. In particular, the charge on the input and output IDTs was evaluated which allowed key electrical parameters, such as electromechanical coupling coefficient, input capacitance and admittance to be calculated. To the best of the author's knowledge, this is the first time that essential performance parameters have been determined for a FPW structure using the commercial FEM package ANSYS 8.0. In terms of mechanical properties, the particle displacement

profiles were evaluated for the primary antisymmetric and symmetric modes. The influence of the FEM package simulation parameters, such as node density, timestep and simulation time were considered, which has resulted in a set of guidelines for modelling FPW devices based on the author's novel technique. To the best of the author's knowledge, the demonstrated technique could equally be applied to other acoustic wave structures.

Chapter 6 considered the use of FPW devices for sensing applications in liquid media. Necessary additions to both the stiffness matrix method and FEM were discussed to allow both techniques to be used for the analysis of liquid loaded FPW structures. For the stiffness matrix method, the additional liquid layer was modelled as a semi-infinite, which allowed many parallels to be drawn from established SAW analysis techniques. The addition of a liquid layer required significant modification of the stiffness matrix method, whereas for the FEM simulations, a dedicated fluid element was added to the upper surface of the FPW device. To evaluate the frequency domain characteristics of the liquid loaded FPW structure, the spectral domain Green's function presented in Chapter 4 was applied and compared against the novel approach developed by the author. It was found that the FEM simulation provided more reliable results than the spectral domain Green's function in its current implementation, when compared to devices presented in literature. The boundary conditions for a liquid loaded FPW structure were considered, which allowed the particle displacement profiles to be subsequently evaluated. An analysis was undertaken on the tightly coupled surface wave, commonly termed a Scholte mode, which is often deemed responsible for most sensing results in liquid media. The performance of a FPW structure in liquid media was also discussed, based on the displacement profiles. The primary antisymmetric mode, when subjected to liquid media, although being mainly transverse in nature, is confined to the FPW membrane due to its low phase velocity when compared to the compressional velocity of the applied liquid. As mentioned throughout this thesis, the phase velocity of this mode is partially determined by the ratio of acoustic wavelength to the membrane thickness, therefore the structure can be tailored to an appropriate liquid media sensing application. As the primary antisymmetric mode displacement is transverse in nature, this particular mode was found to be well

suited to both density sensing applications. Conversely, for viscosity sensing applications, the primary symmetric mode can be applied provided both resonant frequency and attenuation are measured. Furthermore, evaluation of the density-viscosity product illustrated that a FPW structure has the potential to differentiate between these two parameters. An in depth discussion was also held on the ability of FPW structures to be used for mass sensing applications in liquid media, where it was shown that the sensitivity of the $S_0$ mode is largely unaffected by the presence of the liquid, whereas for the $A_0$ mode the sensitivity is greatly reduced. Chapter 6 concluded with a brief discussion of the author's attempt to fabricate a functional FPW device. Preliminary material characterisation has shown that the deposited AlN thin film are stoichiometric, c-axis orientated and hence piezoelectric.

## 7.2 Future Work

The work undertaken in this thesis has focused on the modelling of FPW devices for both gas and liquid media sensing applications. Throughout its development, several assumptions were made to simplify the analysis. In this section, suggestions are made to further develop and improve the techniques demonstrated by the author. Future suggested work, particularly in the area of FEM analysis of acoustic wave structures, is as follows:

- **Electrode Influence.** In all FEM simulations performed, the IDT electrodes were simulated by coupling the electric potential for a given group of nodes. Thus, by employing this approximation, the electrodes were assumed to be infinitely thin therefore ignoring mass loading effects. In FPW devices where the electrode metallisation can be a substantial percentage of the overall membrane thickness, the mass loading effect should be considered. Further to the mass loading effect, regeneration and reflections occur at the electrode locations, which can potentially distort the spectral characteristics. It was also assumed that the electrodes were infinitely conductive, which is an assumption made by most other simulation techniques. The author believes that this effect could be included by an additional coupling matrix, similar to that used for the fluid-solid interface prob-

lem.

- **FEM Material Parameters** Another potential area for improvement relates to the parameters used to define the structural and electrical behaviour of the material models used during the FEM simulations. In the FEM simulations conducted, materials were described by basic parameters such as density, stiffness, dielectric and piezoelectric matrices. Further improvement of the FEM package is required to incorporate material parameters such as resistivity, impurity doping levels and thermal characteristics.

- **FEM Simulated Sensitive Layers.** In the developed FEM simulations, additional sensitive layers were not added to the FPW structure. A wide range of potential sensitive layers exist, ranging from metal oxide thin films to functional polymer biolayers, each with unique geometries. In newly developed nanomaterials, such as ZnO nanorods, the additional layer can no longer be assumed to be a homogenous solid, rather clusters of randomly aligned structures. Improvement of the FEM simulation software is required before these types of layers can be accurately modelled.

- **FEM Liquid Flow.** In Chapter 6, it was assumed that the additional liquid layer was constrained within a vessel, therefore no net flow existed. For typical sensing applications in liquid media, the analyte under consideration is pumped in through a series of microfluidic channels and hence the static assumption becomes invalid. Using a FLOWTRAN based technique, it may be possible to include the influence of liquid flow for the analysis of liquid loaded FPW structures using the FEM. At the time of writing, the FEM software was unable to conduct a piezoelectric/liquid flow based analysis, however this may have been rectified in later releases of the software.

- **Imperfect Interfaces.**The FEM simulations have also assumed that all layers are homogenous and the interface between layers is ideal, whereas in reality this is not the case. Lattice defects cause mismatch of the films at the interface which in turn can produce attenuation of the propagating acoustic modes. These effects could be incorporated into the FEM simulations in a similar manner as employed

in the stiffness matrix method, where a fictional lossy material is added between the actual physical layers. Although a viable solution, the added layer would be quite thin and thus there could be potential issues with the automated meshing processes. A superior approach would be the inclusion of a loss parameter at the layer interfaces, however this was not available in the FEM package used by the author.

- **High Aspect Ratio Devices.** Another difficulty when modelling micron size structures is the relatively high aspect ratios. The commercial FEM software employed was not specifically designed for the analysis of thin film structures, thus potential issues could have arisen when forming the element mesh. In particular, it was not possible to determine the mass sensitivity of the structure by the addition of a fictional layer, whose thickness is typically less than $1 \times 10^{-12}$m. The author did attempt to add a $0.1$µm mass layer, however meshing errors were generated by the FEM package. Therefore, to obtain mass sensitivity directly from the FEM software, the same approach used in Section 4.3.2 could be employed.

- **Spectral Domain Green's Function for Liquid Media Analysis.** It was also shown in Chapter 6 that the spectral domain Green's function, at least in its current form, was unable to accurately determine the insertion loss characteristics of a liquid loaded FPW structure. It is believed that this inaccuracy is caused by the evaluation of the piezoelectric coupling value $G_{FPW}$. A further study is required to confirm the source of the error, however this is beyond the scope of this thesis. Once rectified, the modified technique could be compared to the FEM approach used by the author.

- **Influence of Electrical Ground Plane.** Throughout the presented analysis of FPW devices using both the transmission and stiffness matrix methods, the influence of the electrical ground plane was ignored. When compared against the results obtained via the FEM, no significant deviation was found, however for correctness the electrical properties of the layer should be included in the calculation of the mode phase velocities and wavenumbers.

- **FPW Device Fabrication and further FEM Result Verification** In this thesis, the

author has successfully demonstrated a novel approach to the analysis of FPW devices based on the convergence of the FEM with classical SAW analysis techniques and related procedures. Excellent agreement has been obtained when compared to more conventional modelling techniques such as the stiffness matrix method and the spectral domain Green's function. However, to further verify the author's approach, a functional FPW device should be fabricated to experimentally confirm the calculated results. Although preliminary materials characterisation has shown that the deposited AlN is correctly orientated further work is required to reduce the intrinsic stress within the film to reduce buckling of the FPW device membrane. The author believes that modification of the deposition parameters should alleviate this issue. Once rectified, the IDTs can be patterned via a lift-off technique to realise a functional FPW device.

# Appendix A

# FPW Device Transmission Matrix Boundary Conditions

Based on the parameters of Table 3.2 the four alternative boundary conditions can be obtained for the Transmission Matrix method. This section provides the essential boundary determinants used to solve the piezoelectric wave propagation problem for a multilayered FPW structure.

Recall from equation 3.26, the wave propagation problem can be described in terms of the $8 \times 8$ transmission matrix, and the state vector $\boldsymbol{\tau}$ as:

$$\begin{bmatrix} T_{13} \\ T_{23} \\ T_{33} \\ D_3 \\ v_1 \\ v_2 \\ v_3 \\ j\omega\varphi \end{bmatrix}_u = \begin{bmatrix} \phi_{11} & \phi_{12} & \phi_{13} & \phi_{14} & \phi_{15} & \phi_{16} & \phi_{17} & \phi_{18} \\ \phi_{21} & \phi_{22} & \phi_{23} & \phi_{24} & \phi_{25} & \phi_{26} & \phi_{27} & \phi_{28} \\ \phi_{31} & \phi_{32} & \phi_{33} & \phi_{34} & \phi_{35} & \phi_{36} & \phi_{37} & \phi_{38} \\ \phi_{41} & \phi_{42} & \phi_{43} & \phi_{44} & \phi_{45} & \phi_{46} & \phi_{47} & \phi_{48} \\ \phi_{51} & \phi_{52} & \phi_{53} & \phi_{54} & \phi_{55} & \phi_{56} & \phi_{57} & \phi_{58} \\ \phi_{61} & \phi_{62} & \phi_{63} & \phi_{64} & \phi_{65} & \phi_{66} & \phi_{67} & \phi_{68} \\ \phi_{71} & \phi_{72} & \phi_{73} & \phi_{74} & \phi_{75} & \phi_{76} & \phi_{77} & \phi_{78} \\ \phi_{81} & \phi_{82} & \phi_{83} & \phi_{84} & \phi_{85} & \phi_{86} & \phi_{87} & \phi_{88} \end{bmatrix} \begin{bmatrix} T_{13} \\ T_{23} \\ T_{33} \\ D_3 \\ v_1 \\ v_2 \\ v_3 \\ j\omega\varphi \end{bmatrix}_l \tag{A.1}$$

For the four unique electrical boundary conditions, equation A.1 in conjunction with Table 3.2 is used to form the appropriate equations. In all cases, the normal stress on both sides of the structure is assumed to be zero, $\mathbf{T_u^z} = \mathbf{T_l^z} = 0$, which greatly simplified the determinant. The remaining two boundary conditions are therefore based on the assumed electrical state of the FPW structure.

**Bottom Surface (Layer 1) Open-Circuit, Top Surface (Layer n) Open-Circuit**

Under the conditions of zero normal stress at both external surfaces and open-circuit electrical conditions, equation A.1 can be written as:

$$\phi_{15} v_{1\,l} + \phi_{16} v_{2\,l} + \phi_{17} v_{3\,l} + \phi_{18} j\omega\varphi_l = 0 \tag{A.2a}$$

$$\phi_{25} v_{1\,l} + \phi_{26} v_{2\,l} + \phi_{27} v_{3\,l} + \phi_{28} j\omega\varphi_l = 0 \tag{A.2b}$$

$$\phi_{35} v_{1\,l} + \phi_{36} v_{2\,l} + \phi_{37} v_{3\,l} + \phi_{38} j\omega\varphi_l = 0 \tag{A.2c}$$

$$\phi_{45} v_{1\,l} + \phi_{46} v_{2\,l} + \phi_{47} v_{3\,l} + \phi_{48} j\omega\varphi_l = 0 \tag{A.2d}$$

ie. $D_3 = 0$, $\mathbf{T^z_u} = \mathbf{T^z_l} = 0$ leaving,

$$v_{1u} = \phi_{55} v_{1\,l} + \phi_{56} v_{2\,l} + \phi_{57} v_{3\,l} + \phi_{58} j\omega\varphi_l \tag{A.3a}$$

$$v_{2u} = \phi_{65} v_{1\,l} + \phi_{66} v_{2\,l} + \phi_{67} v_{3\,l} + \phi_{68} j\omega\varphi_l \tag{A.3b}$$

$$v_{3u} = \phi_{75} v_{1\,l} + \phi_{76} v_{2\,l} + \phi_{77} v_{3\,l} + \phi_{78} j\omega\varphi_l \tag{A.3c}$$

$$j\omega\varphi_u = \phi_{85} v_{1\,l} + \phi_{86} v_{2\,l} + \phi_{87} v_{3\,l} + \phi_{88} j\omega\varphi_l \tag{A.3d}$$

To satisfy equation A.3, the determinant of the coefficients in equation A.2 must be zero. Thus, for the both layers to be open-circuit, the following condition must be satisfied:

$$\det \begin{vmatrix} \phi_{15} & \phi_{16} & \phi_{17} & \phi_{18} \\ \phi_{25} & \phi_{26} & \phi_{27} & \phi_{28} \\ \phi_{35} & \phi_{36} & \phi_{37} & \phi_{38} \\ \phi_{45} & \phi_{46} & \phi_{47} & \phi_{48} \end{vmatrix} = 0 \tag{A.4}$$

**Bottom Surface (Layer 1) Open-Circuit, Top Surface (Layer n) Short-Circuit**

Under the conditions of zero normal stress at both external surfaces, with bottom surface open circuit whilst the top surface is short-circuit, it is convenient to switch the position of the dielectric displacement vector $D_3$ and the scalar potential, $j\omega\varphi$ in equation A.1 (interchange columns 8 and 4). This allows the same computational procedure to be utilised for all alternative boundary conditions. After substituting the appropriate boundary conditions, the modified version of equation A.1 can be written as:

$$\phi_{15}v_{1\,l} + \phi_{16}v_{2\,l} + \phi_{17}v_{3\,l} + \phi_{18}j\omega\varphi_l = 0 \tag{A.5a}$$

$$\phi_{25}v_{1\,l} + \phi_{26}v_{2\,l} + \phi_{27}v_{3\,l} + \phi_{28}j\omega\varphi_l = 0 \tag{A.5b}$$

$$\phi_{35}v_{1\,l} + \phi_{36}v_{2\,l} + \phi_{37}v_{3\,l} + \phi_{38}j\omega\varphi_l = 0 \tag{A.5c}$$

$$\phi_{85}v_{1\,l} + \phi_{86}v_{2\,l} + \phi_{87}v_{3\,l} + \phi_{88}j\omega\varphi_l = 0 \tag{A.5d}$$

ie. $j\omega\varphi_u = 0$, $\mathbf{T^z_u} = \mathbf{T^z_l} = 0$, $D_{3l} = 0$ leaving,

$$v_{1u} = \phi_{55}v_{1\,l} + \phi_{56}v_{2\,l} + \phi_{57}v_{3\,l} + \phi_{58}j\omega\varphi_l \tag{A.6a}$$

$$v_{2u} = \phi_{65}v_{1\,l} + \phi_{66}v_{2\,l} + \phi_{67}v_{3\,l} + \phi_{68}j\omega\varphi_l \tag{A.6b}$$

$$v_{3u} = \phi_{75}v_{1\,l} + \phi_{76}v_{2\,l} + \phi_{77}v_{3\,l} + \phi_{78}j\omega\varphi_l \tag{A.6c}$$

$$D_{3u} = \phi_{45}v_{1\,l} + \phi_{46}v_{2\,l} + \phi_{47}v_{3\,l} + \phi_{48}j\omega\varphi_l \tag{A.6d}$$

To satisfy equation A.6, the determinant of the coefficients in equation A.5 must be zero. Thus, for the bottom surface to be open-circuit and the upper surface to be electrically short, the following condition must be satisfied:

$$\det \begin{vmatrix} \phi_{15} & \phi_{16} & \phi_{17} & \phi_{18} \\ \phi_{25} & \phi_{26} & \phi_{27} & \phi_{28} \\ \phi_{35} & \phi_{36} & \phi_{37} & \phi_{38} \\ \phi_{85} & \phi_{86} & \phi_{87} & \phi_{88} \end{vmatrix} = 0 \tag{A.7}$$

**Bottom Surface (Layer 1) Short-Circuit, Top Surface (Layer n) Open-Circuit**

Under the conditions of zero normal stress at both external surfaces, with bottom surface short-circuit whilst the top surface is open-circuit, it is convenient to switch the position of the dielectric displacement vector $D_3^l$ and the scalar potential, $j\omega\varphi^l$ in equation A.1 (interchange rows 8 and 4). This allows the same computational procedure to be utilised for all alternative boundary conditions. After substituting the appropriate boundary conditions, the modified version of equation A.1 can be written as:

$$\phi_{15}v_{1\,l} + \phi_{16}v_{2\,l} + \phi_{17}v_{3\,l} + \phi_{14}D_{3\,l} = 0 \tag{A.8a}$$

$$\phi_{25}v_{1\,l} + \phi_{26}v_{2\,l} + \phi_{27}v_{3\,l} + \phi_{24}D_{3\,l} = 0 \tag{A.8b}$$

$$\phi_{35}v_{1\,l} + \phi_{36}v_{2\,l} + \phi_{37}v_{3\,l} + \phi_{34}D_{3\,l} = 0 \tag{A.8c}$$

$$\phi_{45}v_{1\,l} + \phi_{46}v_{2\,l} + \phi_{47}v_{3\,l} + \phi_{44}D_{3\,l} = 0 \tag{A.8d}$$

ie. $D_{3u} = 0$, $\mathbf{T^z_u} = \mathbf{T^z_l} = 0$, $j\omega\varphi_l = 0$ leaving,

$$v_{1u} = \phi_{55}v_{1\,l} + \phi_{56}v_{2\,l} + \phi_{57}v_{3\,l} + \phi_{54}D_{3\,l} \tag{A.9a}$$

$$v_{2u} = \phi_{65}v_{1\,l} + \phi_{66}v_{2\,l} + \phi_{67}v_{3\,l} + \phi_{64}D_{3\,l} \tag{A.9b}$$

$$v_{3u} = \phi_{75}v_{1\,l} + \phi_{76}v_{2\,l} + \phi_{77}v_{3\,l} + \phi_{74}D_{3\,l} \tag{A.9c}$$

$$j\omega\varphi_u = \phi_{85}v_{1\,l} + \phi_{86}v_{2\,l} + \phi_{87}v_{3\,l} + \phi_{84}D_{3\,l} \tag{A.9d}$$

To satisfy equation A.9, the determinant of the coefficients in equation A.8 must be zero. Thus, for the bottom surface to be short-circuit and the upper surface to be electrically open, the following condition must be satisfied:

$$\det \begin{vmatrix} \phi_{15} & \phi_{16} & \phi_{17} & \phi_{14} \\ \phi_{25} & \phi_{26} & \phi_{27} & \phi_{24} \\ \phi_{35} & \phi_{36} & \phi_{37} & \phi_{34} \\ \phi_{45} & \phi_{46} & \phi_{47} & \phi_{44} \end{vmatrix} = 0 \tag{A.10}$$

**Bottom Surface (Layer 1) Short-Circuit, Top Surface (Layer n) Short-Circuit**

Under the conditions of zero normal stress and electrical shorts at both external surfaces, it is convenient to switch the position of the dielectric displacement vector $D_{3l}, D_{3u}$ and the scalar potential, $j\omega\varphi_l, j\omega\varphi_u$ in equation A.1 (interchange rows 8 and 4, interchange columns 8 and 4). This allows the same computational procedure to be utilised for all alternative boundary conditions. After substituting the appropriate boundary conditions, the modified version of equation A.1 can be written as:

$$0 = \phi_{15} v_{1\,l} + \phi_{16} v_{2\,l} + \phi_{17} v_{3\,l} + \phi_{14} D_{3\,l} \tag{A.11a}$$

$$0 = \phi_{25} v_{1\,l} + \phi_{26} v_{2\,l} + \phi_{27} v_{3\,l} + \phi_{24} D_{3\,l} \tag{A.11b}$$

$$0 = \phi_{35} v_{1\,l} + \phi_{36} v_{2\,l} + \phi_{37} v_{3\,l} + \phi_{34} D_{3\,l} \tag{A.11c}$$

$$0 = \phi_{85} v_{1\,l} + \phi_{86} v_{2\,l} + \phi_{87} v_{3\,l} + \phi_{84} D_{3\,l} \tag{A.11d}$$

ie. $j\omega\varphi_l, j\omega\varphi_u = 0$, $\mathbf{T_u^z} = \mathbf{T_l^z} = 0$, leaving,

$$v_{1u} = \phi_{55} v_{1\,l} + \phi_{56} v_{2\,l} + \phi_{57} v_{3\,l} + \phi_{54} D_{3\,l} \tag{A.12a}$$

$$v_{2u} = \phi_{65} v_{1\,l} + \phi_{66} v_{2\,l} + \phi_{67} v_{3\,l} + \phi_{64} D_{3\,l} \tag{A.12b}$$

$$v_{3u} = \phi_{75} v_{1\,l} + \phi_{76} v_{2\,l} + \phi_{77} v_{3\,l} + \phi_{74} D_{3\,l} \tag{A.12c}$$

$$D_{3\,u} = \phi_{45} v_{1\,l} + \phi_{46} v_{2\,l} + \phi_{47} v_{3\,l} + \phi_{44} D_{3\,l} \tag{A.12d}$$

To satisfy equation A.9, the determinant of the coefficients in equation A.8 must be zero. Thus, for the both surfaces to be electrically short-circuit, the following condition must be satisfied:

$$\det \begin{vmatrix} \phi_{15} & \phi_{16} & \phi_{17} & \phi_{14} \\ \phi_{25} & \phi_{26} & \phi_{27} & \phi_{24} \\ \phi_{35} & \phi_{36} & \phi_{37} & \phi_{34} \\ \phi_{85} & \phi_{86} & \phi_{87} & \phi_{84} \end{vmatrix} = 0 \tag{A.13}$$

# Appendix B

# FPW Device Green's Function Boundary Conditions

Based on the parameters listed in Table 4.1 the piezoelectric wave propagation problem can be solved by considering the determinant of the generalised Green's function. This section illustrates the boundary scan determinants used to solve the wave propagation for the four distinct electrical boundary conditions of a FPW structure.

**Bottom Surface (Layer 1) Open-Circuit, Top Surface (Layer n) Open-Circuit**

*Assumed Boundary Conditions:*

$$\gamma_u = \gamma_l = 0 \tag{B.1a}$$

$$\boldsymbol{\sigma_u} = \boldsymbol{\sigma_l} = 0 \tag{B.1b}$$

$$\det \begin{vmatrix} \mathrm{K}_{11}^{\mathrm{f}} & \mathrm{K}_{11}^{\mathrm{fe}} & \mathrm{K}_{12}^{\mathrm{f}} & \mathrm{K}_{12}^{\mathrm{fe}} \\ -\mathrm{K}_{11}^{\mathrm{ef}} & \theta + K_{11}^{e} & -\mathrm{K}_{12}^{\mathrm{ef}} & -K_{12}^{e} \\ \mathrm{K}_{21}^{\mathrm{f}} & \mathrm{K}_{21}^{\mathrm{fe}} & \mathrm{K}_{22}^{\mathrm{f}} & \mathrm{K}_{22}^{\mathrm{fe}} \\ \mathrm{K}_{21}^{\mathrm{ef}} & K_{21}^{e} & \mathrm{K}_{22}^{\mathrm{ef}} & K_{22}^{e} - \theta \end{vmatrix} = 0 \tag{B.2}$$

**Bottom Surface (Layer 1) Short-Circuit, Top Surface (Layer n) Open-Circuit**

*Assumed Boundary Conditions:*

$$\varphi_l = 0 \tag{B.3a}$$

$$\gamma_u = 0 \tag{B.3b}$$

$$\boldsymbol{\sigma_u} = \boldsymbol{\sigma_l} = 0 \tag{B.3c}$$

$$\det \begin{vmatrix} \frac{\mathrm{K}_{11}^{\mathrm{fe}}\mathrm{K}_{11}^{\mathrm{ef}}}{\theta+K_{11}^{e}} + K_{11}^{f} & \frac{\mathrm{K}_{11}^{\mathrm{fe}}\mathrm{K}_{12}^{\mathrm{ef}}}{\theta+K_{11}^{e}} + \mathrm{K}_{12}^{\mathrm{f}} & \mathrm{K}_{12}^{\mathrm{fe}} - \frac{\mathrm{K}_{11}^{\mathrm{fe}}K_{12}^{e}}{\theta+K_{11}^{e}} & \frac{\mathrm{K}_{11}^{\mathrm{fe}}}{\theta+K_{11}^{e}} \\ \frac{\mathrm{K}_{11}^{\mathrm{ef}}}{\theta+K_{11}^{e}} & \frac{\mathrm{K}_{12}^{\mathrm{ef}}}{\theta+K_{11}^{e}} & \frac{\mathrm{K}_{12}^{\mathrm{e}}}{\theta+K_{11}^{e}} & \frac{1}{\theta+K_{11}^{e}} \\ \frac{\mathrm{K}_{21}^{\mathrm{fe}}\mathrm{K}_{11}^{\mathrm{ef}}}{\theta+K_{11}^{e}} + K_{21}^{f} & \frac{\mathrm{K}_{21}^{\mathrm{fe}}\mathrm{K}_{12}^{\mathrm{ef}}}{\theta+K_{11}^{e}} + \mathrm{K}_{22}^{\mathrm{f}} & \mathrm{K}_{22}^{\mathrm{fe}} + \frac{\mathrm{K}_{21}^{\mathrm{fe}}K_{12}^{e}}{\theta+K_{11}^{e}} & \frac{\mathrm{K}_{21}^{\mathrm{fe}}}{\theta+K_{11}^{e}} \\ \frac{\mathrm{K}_{21}^{\mathrm{e}}\mathrm{K}_{11}^{\mathrm{ef}}}{\theta+K_{11}^{e}} + \mathrm{K}_{21}^{\mathrm{ef}} & \frac{K_{21}^{e}\mathrm{K}_{12}^{\mathrm{ef}}}{\theta+K_{11}^{e}} + \mathrm{K}_{22}^{\mathrm{ef}} & (K_{22}^{e}-\theta) + \frac{K_{21}^{e}K_{12}^{e}}{\theta+K_{11}^{e}} & \frac{K21_{e}}{K11_{e}} \end{vmatrix} = 0 \tag{B.4}$$

**Bottom Surface (Layer 1) Open-Circuit, Top Surface (Layer n) Short-Circuit**

*Assumed Boundary Conditions:*

$$\gamma_l = 0 \tag{B.5a}$$

$$\varphi_u = 0 \tag{B.5b}$$

$$\boldsymbol{\sigma_u} = \boldsymbol{\sigma_l} = 0 \tag{B.5c}$$

$$\det \begin{vmatrix} \mathrm{K}_{11}^{\mathrm{f}} - \frac{\mathrm{K}_{12}^{\mathrm{f}}\mathrm{eK}_{21}^{\mathrm{ef}}}{K_{22}^{e}-\theta} & \mathrm{K}_{11}^{\mathrm{fe}} - \frac{\mathrm{K}_{12}^{\mathrm{fe}}K_{21}^{e}}{K_{22}^{e}-\theta} & \mathrm{K}_{12}^{\mathrm{f}} - \frac{\mathrm{K}_{12}^{\mathrm{fe}}\mathrm{K}_{22}^{\mathrm{ef}}}{K_{22}^{e}-\theta} & \frac{\mathrm{K}_{12}^{\mathrm{fe}}}{K_{22}^{e}-\theta} \\ -\mathrm{K}_{11}^{\mathrm{ef}} + \frac{K_{12}^{e}\mathrm{K}_{21}^{\mathrm{ef}}}{K_{22}^{e}-\theta} & (\theta+K_{11}^{e}) + \frac{K_{12}^{e}K_{21}^{e}}{K_{22}^{e}-\theta} & -\mathrm{K}_{12}^{\mathrm{ef}} + \frac{K_{12}^{e}\mathrm{K}_{22}^{\mathrm{ef}}}{K_{22}^{e}-\theta} & \frac{-K_{12}^{e}}{K_{22}^{e}-\theta} \\ \mathrm{K}_{21}^{\mathrm{f}} - \frac{\mathrm{K}_{22}^{\mathrm{fe}}\mathrm{K}_{21}^{\mathrm{ef}}}{K_{22}^{e}-\theta} & \mathrm{K}_{21}^{\mathrm{fe}} - \frac{\mathrm{K}_{22}^{\mathrm{fe}}K_{21}^{e}}{K_{22}^{e}-\theta} & \mathrm{K}_{22}^{\mathrm{f}} - \frac{\mathrm{K}_{22}^{\mathrm{fe}}\mathrm{K}_{22}^{\mathrm{ef}}}{K_{22}^{e}-\theta} & \frac{K_{22}^{fe}}{K_{22}^{e}-\theta} \\ \frac{-\mathrm{K}_{21}^{\mathrm{ef}}}{K_{22}^{e}-\theta} & \frac{-K_{21}^{e}}{K_{22}^{e}-\theta} & \frac{-\mathrm{K}_{22}^{\mathrm{ef}}}{K_{22}^{e}-\theta} & \frac{-K_{12}^{e}}{K_{22}^{e}-\theta} \end{vmatrix} = 0 \tag{B.6}$$

**Bottom Surface (Layer 1) Short-Circuit , Upper Surface (Layer n) Short-Circuit**

*Assumed Boundary Conditions:*

$$\varphi_u = \varphi_l = 0 \tag{B.7a}$$

$$\boldsymbol{\sigma_u} = \boldsymbol{\sigma_l} = 0 \tag{B.7b}$$

When both sides of a FPW are metalised, the boundary determinant is significantly more complex. To simplify the calculation procedure, the following substitutions are made:

$$\sigma_{\mathrm{u}}^{\mathrm{u_u}} = -\frac{K_{11}^{fe}}{\theta+K_{11}^{e}}(-\mathrm{K}_{11}^{\mathrm{ef}} - \frac{K_{12}^{e}(-K_{21}^{e}\mathrm{K}_{11}^{\mathrm{ef}} - \mathrm{K}_{21}^{\mathrm{ef}}(\theta+K_{11}^{e}))}{(\theta+K_{11}^{e})(K_{22}^{e}-\theta)+K_{21}^{e}K_{12}^{e}} + \mathrm{K}_{11}^{\mathrm{f}} + \frac{\mathrm{K}_{12}^{\mathrm{fe}}(-K_{21}^{e}\mathrm{K}_{11}^{\mathrm{ef}} - \mathrm{K}_{21}^{\mathrm{ef}}(\theta+K_{11}^{e}))}{(\theta+K_{11}^{e})(K_{22}^{e}-\theta)+K_{21}^{e}K_{12}^{e}} \tag{B.8a}$$

$$\sigma_{\mathrm{u}}^{\mathrm{u_l}} = \frac{\mathrm{K}_{12}^{\mathrm{fe}}(-K_{21}^{e}\mathrm{K}_{12}^{\mathrm{ef}} - \mathrm{K}_{22}^{\mathrm{ef}}(\theta+K_{11}^{e}))}{(\theta+K_{11}^{e})(K_{22}^{e}-\theta)+K_{21}^{e}K_{12^{e}}} - \frac{K_{11}^{fe}}{(\theta+K_{11}^{e})}(-\mathrm{K}_{12}^{\mathrm{ef}} - \frac{K_{12}^{e}(-K_{21}^{e}\mathrm{K}_{12}^{\mathrm{ef}} - \mathrm{K}_{22}^{\mathrm{ef}}(\theta+K_{11}^{e}))}{(\theta+K_{11}^{e})(K_{22}^{e}-\theta)+K_{21}^{e}K_{12}^{e}}) + \mathrm{K}_{12}^{\mathrm{f}} \tag{B.8b}$$

$$\sigma_{\mathrm{u}}^{\gamma_{\mathrm{u}}} = -\frac{\mathrm{K}_{12}^{\mathrm{fe}}K_{21}^{e}}{(\theta+K_{11}^{e})(K_{22}^{e}-\theta)+K_{21}^{e}K_{12}^{e}} - \frac{K_{11}^{fe}}{\theta+K_{11}^{e}}(-1 + \frac{K_{12}^{e}K_{21}^{e}}{(\theta+K_{11}^{e})(K_{22}^{e}-\theta)+K_{21}^{e}K_{12}^{e}}) \tag{B.8c}$$

$$\sigma_{\mathrm{u}}^{\gamma_{\mathrm{l}}} = \frac{\mathrm{K}_{12}^{\mathrm{fe}}(\theta+K_{11}^{e})}{(\theta+K_{11}^{e})(K_{22}^{e}-\theta)+K_{21}^{e}K_{12}^{e}} + \frac{K_{11}^{fe}K_{12}^{e}}{(\theta+K_{11}^{e})(K_{22}^{e}-\theta)+K_{21}^{e}K_{12}^{e}} \tag{B.8d}$$

$$\phi_{\mathrm{u}}^{\mathrm{u_u}} = -\frac{1}{\theta + K_{11}^e}(-\mathrm{K}_{11}^{\mathrm{ef}} - \frac{K_{12}^e(-K_{21}^e\mathrm{K}_{11}^{\mathrm{ef}} - \mathrm{K}_{21}^{\mathrm{ef}}(\theta + K_{11}^e))}{(\theta + K_{11}^e)(K_{22}^e - \theta) + K_{21}^e K_{12}^e}) \tag{B.9a}$$

$$\phi_{\mathrm{u}}^{\mathrm{u_l}} = -\frac{1}{\theta + K_{11}^e}(-\mathrm{K}_{12}^{\mathrm{ef}} - \frac{K_{12}^e(-K_{21}^e\mathrm{K}_{12}^{\mathrm{ef}} - \mathrm{K}_{22}^{\mathrm{ef}}(\theta + K_{11}^e))}{(\theta + K_{11}^e)(K_{22}^e - \theta) + K_{21}^e K_{12}^e} \tag{B.9b}$$

$$\phi_{u}^{\gamma_u} = -\frac{1}{\theta + K_{11}^e}(-1 + \frac{K_{12}^e K_{21}^e}{(\theta + K_{11}^e)(K_{22}^e - \theta) + K_{21}^e K_{12}^e}) \tag{B.9c}$$

$$\phi_{u}^{\gamma_l} = \frac{K_{12}^e}{(\theta + K_{11}^e)(K_{22}^e - \theta) + K_{21}^e K_{12}^e)} \tag{B.9d}$$

$$\sigma_{\mathrm{l}}^{\mathrm{u_u}} = -\frac{\mathrm{K}_{21}^{\mathrm{fe}}}{\theta + K_{11}^e}(-\mathrm{K}_{11}^{\mathrm{ef}} - \frac{K_{12}^e(K_{21}^e\mathrm{K}_{11}^{\mathrm{ef}} - \mathrm{K}_{21}^{\mathrm{ef}}(\theta + K_{11}^e))}{(\theta + K_{11}^e)(K_{22}^e - \theta) + K_{21}^e K_{12}^e}) + \mathrm{K}_{21}^{\mathrm{f}} + \frac{\mathrm{K}_{22}^{\mathrm{fe}}(-K_{21}^e\mathrm{K}_{11}^{\mathrm{ef}} - \mathrm{K}_{21}^{\mathrm{ef}}(\theta + K_{11}^e))}{(\theta + K_{11}^e)(K_{22}^e - \theta) + K_{21}^e K_{12}^e} \tag{B.10a}$$

$$\sigma_{\mathrm{l}}^{\mathrm{u_l}} = \frac{\mathrm{K}_{22}^{\mathrm{fe}}(-K_{21}^e\mathrm{K}_{12}^{\mathrm{ef}} - \mathrm{K}_{22}^{\mathrm{ef}}(\theta + K_{11}^e))}{(\theta + K_{11}^e)(K_{22}^e - \theta) + K_{21}^e K_{12}^e} - \frac{\mathrm{K}_{21}^{\mathrm{fe}}}{\theta + K_{11}^e}(-\mathrm{K}_{12}^{\mathrm{ef}} - \frac{K_{12}^e(-K_{21}^e\mathrm{K}_{12}^{\mathrm{ef}} - \mathrm{K}_{22}^{\mathrm{ef}}(\theta + K_{11}^e))}{(\theta + K_{11}^e)(K_{22}^e - \theta) + K_{21}^e K_{12}^e}) + \mathrm{K}_{22}^{\mathrm{f}} \tag{B.10b}$$

$$\sigma_{\mathrm{l}}^{\gamma_l} = \frac{\mathrm{K}_{22}^{\mathrm{fe}}(\theta + K_{11}^e)}{(\theta + K_{11}^e)(K_{22}^e - \theta) + K_{21}^e K_{12}^e} + \frac{\mathrm{K}_{21}^{\mathrm{fe}} K_{12}^e}{(\theta + K_{11}^e)(K_{22}^e - \theta) + K_{21}^e K_{12}^e} \tag{B.10c}$$

$$\sigma_{\mathrm{l}}^{\gamma_u} = -\frac{\mathrm{K}_{22}^{\mathrm{fe}} K_{21}^e}{(\theta + K_{11}^e)(K_{22} - \theta) + K_{21}^e K_{12}^e} - \frac{\mathrm{K}_{21}^{\mathrm{fe}}}{\theta + K_{11}^e}(-1 + \frac{K_{12}^e K_{21}^e}{(\theta + K_{11}^e)(K_{22}^e - \theta) + K_{21}^e K_{12}^e}) \tag{B.10d}$$

$$\phi_{\mathrm{l}}^{\mathrm{u_u}} = \frac{-K_{21}^e\mathrm{K}_{11}^{\mathrm{ef}} - \mathrm{K}_{21}^{\mathrm{ef}}(\theta + K_{11}^e)}{(\theta + K_{11}^e)(K_{22}^e - \theta) + K_{21}^e K_{12}^e} \tag{B.11a}$$

$$\phi_{\mathrm{l}}^{\mathrm{u_l}} = \frac{-K_{21}^e\mathrm{K}_{12}^{\mathrm{ef}} - \mathrm{K}_{22}^{\mathrm{ef}}(\theta + K_{11}^e)}{(\theta + K_{11}^e)(K_{22}^e - \theta) + K_{21}^e K_{12}^e} \tag{B.11b}$$

$$\phi_{l}^{\gamma_u} = \frac{-K_{21}^e}{(\theta + K_{11}^e)(K_{22}^e - \theta) + K_{21}^e K_{12}^e} \tag{B.11c}$$

$$\phi_{l}^{\gamma_l} = \frac{\theta + K_{11}^e}{(\theta + K_{11}^e)(K_{22}^e - \theta) + K_{21}^e K_{12}^e} \tag{B.11d}$$

Equations B.8 to B.11 are then used to form the boundary scan determinant matrix, equation B.12 which must be satisfied to identify a propagating mode.

$$\det \begin{vmatrix} \sigma_{\mathrm{u}}^{\mathrm{u_u}} & \sigma_{\mathrm{u}}^{\mathrm{u_l}} & \sigma_{\mathrm{u}}^{\gamma_u} & \sigma_{\mathrm{u}}^{\gamma_l} \\ \phi_{\mathrm{u}}^{\mathrm{u_u}} & \phi_{\mathrm{u}}^{\mathrm{u_l}} & \phi_{u}^{\gamma_u} & \phi_{u}^{\gamma_l} \\ \sigma_{\mathrm{l}}^{\mathrm{u_u}} & \sigma_{\mathrm{l}}^{\mathrm{u_l}} & \sigma_{\mathrm{l}}^{\mathrm{u_l}} & \sigma_{\mathrm{l}}^{\gamma_l} \\ \phi_{\mathrm{l}}^{\mathrm{u_u}} & \phi_{\mathrm{l}}^{\mathrm{u_l}} & \phi_{l}^{\gamma_u} & \phi_{l}^{\gamma_l} \end{vmatrix} = 0 \tag{B.12}$$

# Appendix C

# Material Properties

To enable the work undertaken by the author to be repeated, it is essential that all material constants are consistent. Table C.1 lists the material properties used for all simulations within this thesis. The constants are presented in the standard IEEE form, therefore in the case of anisotropic materials, must be rotated to the correct orientation. Only independent constants are listed, where complete relationships can be found in [102]. A '$-$' symbol indicates that constant is not independent, however this does not infer that it is zero. For piezoelectric materials, stiffness constants are evaluated at constant electric field, whilst the dielectric components are evaluated at constant strain.

Table C.1: Material constants - IEEE Standard

| Material | Source | Symmetry Class | Density ($kg/m^3$) | Stiffness ($10^{10}$ $N/m^2$) | | | | |
|---|---|---|---|---|---|---|---|---|
| | | | | $c_{11}^E$ | $c_{12}^E$ | $c_{13}^E$ | $c_{33}^E$ | $c_{44}^E$ |
| ZnO | [169] | 6mm | 5720 | 15.7 | 8.9 | 8.3 | 20.8 | 3.8 |
| AlN | [170] | 6mm | 3260 | 34.5 | 11.25 | 12.0 | 39.5 | 11.8 |
| Si | [102] | m3m | 2332 | 16.57 | 6.39 | - | - | 7.97 |
| Au | [102] | Isotropic | 19300 | 20.7 | - | - | - | 2.85 |
| Al | [102] | Isotropic | 2695 | 11.1 | - | - | - | 2.5 |
| $Si_3N_4$ | [171] | | 2700 | 16.0 | - | - | - | 5.5 |
| Water | [172] | Isotropic | 997 | $\kappa = 2.24\times10^9 N/m^2$, $\theta = 8.9\times10^{-4} Ns/m^2$ | | | | |

| Material | Piezoelectric Constants ($C/m^2$) | | | | Permittivity | |
|---|---|---|---|---|---|---|
| | $e_{15}$ | $e_{22}$ | $e_{31}$ | $e_{33}$ | $\varepsilon_{11}^S/\varepsilon_0$ | $\varepsilon_{33}^S/\varepsilon_0$ |
| ZnO | -0.48 | - | -0.573 | 1.32 | 8.55 | 10.2 |
| AlN | -0.48 | - | -0.58 | 1.55 | 8.0 | 9.5 |
| Si | 0 | | | | 11.7 | - |
| Au | 0 | | | | - | - |
| Al | 0 | | | | - | - |
| $Si_3N_4$ | 0 | | | | 7.5 | - |
| Water | 0 | | | | 80.36 | - |

# Bibliography

[1] C. K. Campbell, *Surface Acoustic Wave Devices for Mobile and Wireless Communications*, 1st ed. San Diego: Academic Press Inc, 1998.

[2] D. P. Morgan, *Studies in Electrical and Electronic Engineering 19, Surface-Wave Devices for Signal Processing*, paperback ed. Amsterdam: Elsevier Science Publishers, 1991, vol. 19.

[3] H. Wohltjen and R. Dessy, "Surface acoustic wave probe for chemical analysis. I. introduction and instrument description," *Analytical Chemistry*, vol. 51, no. 9, pp. 1458–1464, Aug. 1979.

[4] S. G. Joshi and Y. Jin, "Excitation of ultrasonic Lamb waves in piezoelectric plates," *J. Appl. Phys.*, vol. 69, no. 12, pp. 8018–8024, June 1991.

[5] M. J. Vellekoop, "Acoustic wave sensors and their technology," *Ultrasonics*, vol. 36, pp. 7–14, 1988.

[6] T. Laurent, F. O. Bastien, J. Pommier, A. Cachard, D. Remiens, and E. Cattan, "Lamb wave and plate mode in ZnO/silicon and AlN/silicon membrane - application to sensors able to operate in contact with liquid," *Sens. Act. B: Chem.*, vol. 87, pp. 26–37, 2000.

[7] S. J. Ippolito, "Investigation of multilayered surface acoustic wave devices for gas sensing applications," Ph.D. dissertation, RMIT University, July 2006.

[8] D. S. Ballantine, R. M. White, S. J. Martin, A. J. Ricco, E. T. Zellers, G. C. Frye, and H. Wohltjen, *Acoustic Wave Sensors: Theory, Design, and Physico-Chemical Applications*. San Diego: Academic Press, 1997.

[9] R. M. Moroney, R. M. White, and R. T. Howe, "Microtransport induced by ultrasonic Lamb waves," *Appl. Phys. Lett.*, vol. 59, no. 7, pp. 774–776, Aug. 1991.

[10] N. Tirole, A. Choujaa, D. Hauden, G. Martin, P. Blind, M. Mroelicher, J. C. Pommier, and A. Cachard, "Lamb wave pressure sensor using an AlN/Si structure," *Proc. IEEE Ultrason. Symp.*, pp. 371–374, 1993.

[11] M. Sato, T. Yamamoto, M. Takeuchi, and K. Yamanouchi, "Humidity sensitivity of Lamb waves on composite Polyimide/ZnO/$Si_3N_4$ structure," *Jpn. J. Appl. Phys., Part 1*, vol. 32, no. 5B, pp. 2380–2383, May 1993.

[12] J. Pepper, R. Noring, M. Klempner, B. Cunningham, A. Petrovich, R. Bousquet, C. Clapp, J. Brady, and B. Hugh, "Detection of proteins and intact microorganisms using microfabricated flexural plate silicon resonator arrays," *Sens. Act. B: Chem.*, vol. 96, pp. 565–575, 2003.

[13] B. A. Martin, S. W. Wenzel, and R. M. White, "Viscosity and density sensing with ultrasonic plate waves," *Sens. Act. A: Phys.*, vol. 21-23, pp. 704–708, 1990.

[14] S. W. Wenzel and R. M. White, "Analytic comparison of the sensitivities of bulk-wave, surface-wave, and flexural plate-wave ultrasonic gravimetric sensors," *Appl. Phys. Lett.*, vol. 54, no. 20, pp. 1976–1978, May 1989.

[15] M. J. S. Lowe, "Matrix techniques for modeling ultrasonic waves in multilayered media," *IEEE Trans. Ultrason., Ferroelect., Freq. Contr.*, vol. 42, no. 4, pp. 525–542, July 1995.

[16] A. R. Baghai-Wadji, H. Reichinger, H. Zidek, and C. Mecklenbräuker, "Green's function applications in SAW devices," *Proc. IEEE Ultrason. Symp.*, pp. 11–20, 1991.

[17] S. J. Ippolito, K. Kalantar-zadeh, D. A. Powell, and W. Wlodarski, "A Finite Element approach for 3-Dimensional simulation of layered acoustic wave transducers," *Optoelectronic and Microelectronic Materials and Devices, 2002 Conference on*, pp. 541–544, Dec. 2002.

[18] M. Z. Atashbar, B. J. Bazuin, M. Simpeh, and S. Krishnamurthy, "3D FE simulation of $H_2$ SAW gas sensor," *Sens. Act. B: Chem.*, vol. 111-112, pp. 213–218, 2005.

[19] A. R. Baghai-Wadji, O. Männer, and R. Ganß-Puchstein, "Analysis and measurement of transducer end radiation in saw filters on strongly coupled substrates," *IEEE Trans. Microwave Theory Tech.*, vol. 37, no. 1, pp. 150–158, Jan. 1989.

[20] E. L. Adler, "Bulk and surface acoustic waves in anisotropic solids," in *Advances in Surface Acoustic Wave Technology - Systems and Applications*, C. C. W. Ruppel and T. A. Fjeldly, Eds. Singapore: World Scientific Publishing, 2000, vol. 1, pp. 101–132.

[21] D. A. Powell, "Modelling of layered surface acoustic wave resonators for liquid media sensing applications," Ph.D. dissertation, RMIT University, May 2006.

[22] G. I. Matthews, *Vehicle Cabin Air Quality Monitor*, R. W. Brown, Ed. Melbourne, Australia: RMIT, 2005.

[23] H. Lamb, "On waves in an elastic plate," *Proc. R. Soc. A*, vol. 93, pp. 114–128, 1917.

[24] I. Viktorov, *Rayleigh and Lamb Waves - Physical Theory and Applications*, L. Balamuth, Ed. New York, United States: Plenum Press, 1967.

[25] S. W. Wenzel and R. M. White, "Silicon-based ultrasonic Lamb-wave multisensors," *Solid-State Sensor and Actuator Workshop, Technical Digest.*, pp. 27–30, 1988.

[26] R. M. White, P. J. Wicher, S. W. Wenzel, and E. T. Zellers, "Plate-mode ultrasonic oscillator sensors," *IEEE Trans. Ultrason., Ferroelect., Freq. Contr.*, vol. UFFC-34, no. 2, pp. 162–171, Mar. 1987.

[27] M. D. Billy, "Influence of the wetting and the angle of immersion on the generation of a Scholte wave : Experimental investigation," *Physics Letters*, vol. 96, no. 2, pp. 85–87, June 1983.

[28] B. J. Costello, B. A. Martin, and R. M. White, "Ultrasonic plate waves for biochemical measurements," *Proc. IEEE Ultrason. Symp.*, pp. 977–981, 1989.

[29] R. M. White, "Surface acoustic wave sensors," *Proc. IEEE Ultrason. Symp.*, pp. 490–494, 1985.

[30] S. J. Martin, M. A. Butler, J. J. Spates, W. K. Schubert, and M. Mitchell, "Magnetically-excited flexural plate wave resonator," *IEEE Trans. Ultrason., Ferroelect., Freq. Contr.*, vol. 45, no. 5, pp. 1381–1387, Sept. 1998.

[31] T. Giesler and J. U. Meyer, "Electrostatic excitation and capacitive detection of flexural plate-waves," *Sens. Act. A: Phys.*, vol. 36, pp. 113–119, 1993.

[32] D. N. Alleyne and P. Cawley, "The interaction of Lamb waves with defects," *IEEE Trans. Ultrason., Ferroelect., Freq. Contr.*, vol. 39, no. 3, pp. 381–397, May 1992.

[33] F. L. Degertekin, B. Honein, and B. T. Khuri-Yakub, "Efficient excitation and detection of Lamb waves for process monitoring and NDE," *Proc. IEEE Ultrason. Symp.*, pp. 787–790, 1995.

[34] D. Leduc, B. Morvan, P. Pareige, and J. Izbicki, "Measurement of the effects of rough surfaces on Lamb waves propagation," *NDT&E International*, no. 37, pp. 207–211, 2004.

[35] A. H. Nayfeh and D. E. Chimenti, "Propagation of guided waves in fluid-coupled plates of fiber-reinforced composite," *J. Acoust. Soc. Amer.*, vol. 83, no. 5, pp. 1736–1743, May 1988.

[36] A. Moreau, J. B. Ketterson, and B. Davis, "A new ultrasonic method for measuring elastic moduli in unsupported thin films: Application to Cu-Pd superlattices," *Appl. Phys. Lett.*, vol. 68, no. 4, pp. 1622–1628, Aug. 1990.

[37] S. J. Ippolito, K. Kalantar-zadeh, A. Trinchi, and W. Wlodarski, "Layered SAW nitrogen dioxide sensor with $WO_3$ selective layer," in *Proceedings of SPIE International Symposium on Microtechnolgoies for the New Millenium*, 2003.

[38] D. A. Powell, K. Kalantar-zadeh, S. Ippolito, and W. Wlodarski, "Comparison of conductometric gas sensitivity of surface acoustic wave modes in layered structures," *Sensor Letters*, vol. 3, no. 1, pp. 66–70, Mar. 2005.

[39] A. C. Fechete, S. J. Ippolito, K. Kalantar-zadeh, W. Wlodarski, A. S. Holland, K. Galatsis, G. Kiriakidis, N. Katsarakis, and M. Katharakis, "The study of $InO_x$ ZnO XZ $LiNbO_3$ layered SAW devices for ozone sensing," *Proc. IEEE Sensors*, pp. 1510–1513, 2004.

[40] Z. Wang, J. D. N. Cheeke, and C. K. Jen, "Pertubation method for analyzing mass sensitivity of planar multilayer acoustic sensors," *IEEE Trans. Ultrason., Ferroelect., Freq. Contr.*, vol. 43, no. 5, pp. 844–851, Sept. 1996.

[41] S. W. Wenzel and R. M. White, "A multisensor employing an ultrasonic Lamb-wave oscillator," vol. 35, no. 6, pp. 735–743, June 1988.

[42] D. S. Ballantine Jr. and H. Wohltjen, "Surface acoustic wave devices for chemical analysis," *Analytical Chemistry*, vol. 61, no. 11, pp. 704–715, June 1989.

[43] J. C. Pyun, H. Beutel, J. U. Meyer, and H. H. Ruf, "Development of a biosensor for E.Coli based on a fleuxral plate wave (FPW) transducer," *Biosensors and Bioelectronics*, vol. 13, pp. 839–845, 1998.

[44] J. D. N. Cheeke and Z. Wang, "Acoustic wave gas sensors," *Sens. Act. B: Chem.*, vol. 59, pp. 146–153, 1999.

[45] G. Z. Sauerbrey, *Phys.*, vol. 155, pp. 206–222, 1959.

[46] M. Thompson, G. K. Dhaliwal, C. L. Arthur, and G. S. Calabrese, "The potential of bulk acoustic wave devices as a liquid-phase immunosensor," *IEEE Trans. Ultrason., Ferroelect., Freq. Contr.*, no. 2, pp. 127–135, Mar. 1987.

[47] J. Schröder, R. Bomgräber, F. Euchelbaum, and P. Hauptmann, "Advanced interface electronics and methods for QCM," *Sens. Act. A: Phys.*, vol. 97-98, pp. 543–547, 2002.

[48] R. P. Buck, E. Lindner, W. Kutner, and G. Inzelt, "Piezoelectric chemical sensors," *Pure Appl. Chem.*, vol. 76, no. 6, pp. 1139–1160, 2004.

[49] H. Campanella, J. Esteve, J. Montserrat, A. Uranga, G. Abadal, N. Barniol, and A. Romano-Rodrigeuz, "Localized and distributed mass detectors with high sen-

sitivity based on thin-film bulk acoustic resonators," *Appl. Phys. Lett.*, vol. 89, pp. 33 507–1–33 507–3, July 2006.

[50] K. K. Kanazawa and J. G. Gordon II, "Frequency of a quartz microbalance in contact with liquid," *Analytical Chemistry*, vol. 57, pp. 1771–1772, 1985.

[51] L. Tessier, F. Patat, N. Schmitt, M. Lethiecq, Y. Frangin, and D. Guilloteau, "Significance of mass and viscous loads discrimination for an AT-quartz blood group immunosensor," *Sens. Act. B: Chem.*, vol. 18-19, pp. 698–703, 1994.

[52] S. J. Martin, G. C. Frye, A. J. Ricco, and S. D. Senturia, "Effect of surface roughness on the response of thickness-shear mode resonators in liquids," *Analytical Chemistry*, vol. 65, pp. 2910–2922, 1993.

[53] F. Shen, K. H. Lee, S. J. O'Shea, P. Lu, and T. Y. Ng, "Frequency interference between two quartz crystal microbalances," *IEEE Sensors*, vol. 3, no. 3, pp. 274–281, June 2003.

[54] R. M. White and F. W. Voltmer, "Direct piezoelectric coupling to surface elastic waves," *Appl. Phys. Lett.*, vol. 7, no. 12, pp. 314–316, 1965.

[55] S. W. Wenzel and R. M. White, "Silicon SAW devices and electromagnetic feedthrough," *Proc. IEEE Ultrason. Symp.*, pp. 297–301, 1988.

[56] E. Gatti, A. Palma, and E. Verona, "A surface acoustic wave voltage sensor," *Sens. Act.*, vol. 4, pp. 45–54, 1983.

[57] M. Penza and G. Cassano, "Relative humidity sensing by PVA-coated dual resonator SAW osciallator," *Sens. Act. B: Chem.*, vol. 68, pp. 300–306, 2000.

[58] K. Kalantar-zadeh, "Investigation of a Love mode acoustic wave transducer for bio-sensing applications," Ph.D. dissertation, RMIT University, Nov. 2001.

[59] A. J. Ricco, S. J. Martin, and T. E. Zipperian, "Surface acoustic wave gas sensor based on film conductivity changes," *Sens. Act.*, vol. 8, pp. 319–333, 1985.

[60] S. J. Ippolito, S. Kandasamy, K. Kalantar-zadeh, and W. Wlodarski, "Layered SAW hydrogen sensor with modifed tungsten trioxide selective layer," *Sens. Act. B: Chem.*, vol. 108, pp. 553–557, 2005.

[61] B. A. Auld, *Acoustic Fields and Waves in Solids*, 2nd ed. Florida: Krieger, 1990, vol. 2.

[62] Y. Kwon and Y. Roh, "Development of SH-SAW sensors for underwater measurement," *Ultrasonics*, vol. 42, pp. 409–411, 2004.

[63] J. Du, G. L. Harding, A. F. Collings, and P. R. Dencher, "An experimental study of Love-wave acoustic sensors operating in liquids," *Sens. Act. A: Phys.*, vol. 60, pp. 54–61, 1997.

[64] E. Gizeli, N. J. Goddard, C. R. Lowe, and A. C. Stevenson, "A Love plate biosensor utilising a polymer layer," *Sens. Act. B: Chem.*, vol. 6, pp. 131–137, 1992.

[65] E. Gizeli, F. Bender, A. Rasmusson, K. Saha, F. Josse, and R. Cernosek, "Sensitivity of the acoustic waveguide biosensor to protein binding as a function of the waveguide properties," *Biosensors and Bioelectronics*, vol. 18, pp. 1399–1406, 2003.

[66] O. Tamarin, C. Déjous, D. Rebière, J. Pistré, S. Comeau, D. Moynet, and J. Bezian, "Study of acoustic Love wave devices for real time bateriophage detection," *Sens. Act. B: Chem.*, vol. 91, pp. 275–284, 2003.

[67] K. M. Lakin, "Thin film resonator technology," *IEEE Trans. Ultrason., Ferroelect., Freq. Contr.*, vol. 52, no. 5, pp. 707–715, May 2005.

[68] G. Wingqvist, J. Bjurström, L. Liljeholm, V. Yantchev, and I. Katardjiev, "Shear mode AlN thin film electro-acoustic resonant sensor operating in viscous media," *Sens. Act. B: Chem.*, vol. 123, pp. 466–473, 2007.

[69] H. Zhang and E. S. Kim, "Vapor and liquid mass sensing by micromachined acoustic resonator," *J. Microelectromech. Syst.*, vol. 87, pp. 470–473, 2003.

[70] J. Bjurström, G. Wingqvist, V. Yantchev, and I. Katardjiev, "Design and fabrication of temperature compensated liquid FBAR sensors," *Proc. IEEE Ultrason. Symp.*, pp. 894–897, 2006.

[71] M. Benetti, D. Cannatà, F. DiPietrantonio, V. Foglietti, and E. Verona, "Microbalance chemical sensor based on thin-film bulk acoustic wave resonators," *Appl. Phys. Lett.*, vol. 87, pp. 173 504–1–173 504–3, 2005.

[72] J. Weber, W. M. Albers, J. Tuppurainen, M. Link, R. Gabl, W. Wersing, and M. Schreiter, "Shear mode FBARs as highly sensitive liquid biosensors," *Sens. Act. A: Phys.*, vol. 128, pp. 84–88, 2006.

[73] IEEE Standards Coordinating Committee 27 on Time and Frequency, *IEEE Standard Definitions of Physical Quantities for Fundamental Frequency and Time Metrology – Random Instabilites*. The Institute of Electrical and Electronics Engineers, 1999.

[74] J. D. N. Cheeke, *Fundamentals and Applications of Ultrasonics Waves*. Boca Raton, Florida: CRC Press, 2001.

[75] A. H. Fahmy and E. L. Adler, "Propagation of acoustic surface waves in multilayers: A matrix description," *J. Appl. Phys.*, vol. 22, no. 10, pp. 495–497, May 1973.

[76] E. L. Adler, "Matrix methods applied to acoustic waves in multilayers," *IEEE Trans. Ultrason., Ferroelect., Freq. Contr.*, vol. 37, no. 6, pp. 485–490, Nov. 1990.

[77] E. Adler, "SAW and Pseudo-SAW properties using matrix methods," *IEEE Trans. Ultrason., Ferroelect., Freq. Contr.*, vol. 41, no. 6, pp. 876–882, 1994.

[78] E. L. Adler, "Electromechanical coupling to Lamb and Shear-Horizontal modes in piezoelectric plates," *IEEE Trans. Ultrason., Ferroelect., Freq. Contr.*, vol. 36, no. 2, pp. 223–230, Mar. 1989.

[79] A. Tonning and K. A. Ingebrigsten, "Norwegian Institute of Technology ELAB report (unpublished)," no. TE-74.

[80] R. C. Y. Chin, G. W. Hedstrom, and L. Thigpen, "Matrix methods in synthetic seismograms," *Geophys. J. R. Astr. Soc.*, vol. 77, pp. 483–502, 1984.

[81] W. J. Rugh, *Linear System Theory*, 2nd ed. New Jersey, United States: Prentice Hall, 1996.

[82] M. Castaings and B. Hosten, "Delta operator technique to improve the Thomson-Haskell-method stability for propagation in multilayered anisotropic adsorbing plates," *J. Acoust. Soc. Amer.*, vol. 95, no. 4, pp. 1931–1941, Apr. 1994.

[83] A. K. Mal, "Wave propagation in layered composite laminates under periodic surface loads," vol. 10, pp. 257–266, 1988.

[84] L. Wang and S. I. Rokhlin, "Stable reformulation of transfer matrix method for wave propagation in layered anisotropic media," *Ultrasonics*, vol. 39, pp. 413–424, 2001.

[85] ——, "Recursive geometric integrators for wave propagation in a functionally graded multilayered elastic medium," *J. Mech. Phys. Solids*, vol. 52, pp. 2473–2506, 2004.

[86] Z. Gajic, S. Koskie, and C. Coumarbatch, "On the singularly peturbed matrix differential Riccati equation," *Proc. IEEE Decision and Control*, vol. 44, pp. 3638–3644, Dec. 2005.

[87] L. Wang and S. I. Rokhlin, "A compliance/stiffness matrix formulation of general Green's function and effective permittivity for piezoelectric multilayers," *IEEE Trans. Ultrason., Ferroelect., Freq. Contr.*, vol. 51, no. 4, pp. 453–463, Apr. 2004.

[88] R. H. Tancrell and M. G. Holland, "Acoustic surface wave filters," *Proc. IEEE*, vol. 59, no. 3, pp. 393–409, Mar. 1971.

[89] J. R. Pierce, "Coupling of modes of propagation," *J. Appl. Phys.*, vol. 25, no. 2, pp. 179–183, Feb. 1954.

[90] Y. Suzuki, H. Shimizu, M. Takeuchi, K. Nakamura, and A. Yamada, "Some studies on SAW resonators and multiple-mode filters," *Proc. IEEE Ultrason. Symp.*, pp. 297–302, 1976.

[91] H. A. Haus, "Modes in SAW grating resonators," *J. Appl. Phys.*, vol. 48, no. 12, pp. 4955–4961, Dec. 1977.

[92] V. P. Plessky, "Periodic Green's functions analysis of SAW and leaky SAW propagation in a periodic system of electrodes on a piezoelectric crystal," *IEEE Trans. Ultrason., Ferroelect., Freq. Contr.*, vol. 42, no. 2, pp. 280–293, Mar. 1995.

[93] D. P. Morgan, "Quasi-static analysis of generalized SAW transducers using the Green's function method," *IEEE Trans. Sonics and Ultrasonics*, vol. SU-27, no. 3, pp. 111–123, May 1980.

[94] R. F. Milsom, N. H. C. Reily, and M. Redwood, "Analysis of generation and detection of surface and bulk acoustic waves by interdigital transducers," *IEEE Trans. Sonics and Ultrasonics*, no. 3, pp. 147–166, May 1977.

[95] M. J. Turner, R. W. Clough, H. C. Martin, and L. J. Topp, "Stiffness and deflection analysis of complex structures," *Journal of the Aeronautical Sciences*, vol. 23, no. 9, Sept. 1956.

[96] Various. (2007) Xansys mailing list. [Online]. Available: http://www.xansys.org

[97] W. Friedrich, R. Lerch, K. Prestele, and R. Soldner, "Simulations of piezoelectric Lamb wave delay lines using a Finite Element Method," *IEEE Trans. Ultrason., Ferroelect., Freq. Contr.*, vol. 37, no. 2, pp. 248–254, May 1990.

[98] M. Koshiba, S. Karakida, and M. Suzuki, "Finite-Element analysis of Lamb wave scattering in an elastic plate waveguide," *IEEE Trans. Ultrason., Ferroelect., Freq. Contr.*, no. 1, pp. 18–25, Jan. 1984.

[99] N. Finger, G. Kovacs, J. Schöberl, and U. Langer, "Accurate FEM/BEM-simulation of surface acoustic wave filters," *Proc. IEEE Ultrason. Symp.*, pp. 1680–1685, 2003.

[100] G. Xu, "Finite Element analysis of second order effects on the frequency response of a SAW device," *Proc. IEEE Ultrason. Symp.*, pp. 187–190, 2000.

[101] E. L. Adler, J. K. Slaboszewicz, G. W. Farnell, and C. K. Jen, "PC software for SAW propagation in anisotropic multilayers," *IEEE Trans. Ultrason., Ferroelect., Freq. Contr.*, vol. 37, no. 2, pp. 215–223, May 1990.

[102] B. A. Auld, *Acoustic Fields and Waves in Solids*, 2nd ed. Florida: Krieger, 1990, vol. 1.

[103] S. G. Joshi and R. M. White, "Excitation and detectection of surface elastic waves in piezoelectric crystals," *J. Acoust. Soc. Amer.*, vol. 46, no. 1, pp. 17–27, 1969.

[104] A.-R. Baghai-Wadji, "Theory and applications of Green's functions," in *Advances in Surface Acoustic Wave Technology, Systems and Applications*, C. C. W. Ruppel and T. A. Fjeldly, Eds. Singapore: World Scientific Publishing, 2001, vol. 2, pp. 83–149.

[105] A. H. Fahmy and E. L. Adler, "Multilayer acoustic-surface-wave program," *Institution of Electrical Engineers*, vol. 122, no. 5, pp. 470–472, May 1975.

[106] K. M. Lakin, "Perturbation theory for electromagnetic coupling to elastic surface waves on piezoelectric substrates," *J. Appl. Phys.*, vol. 42, no. 3, pp. 899–906, 1971.

[107] W. H. Press, *Numerical Recipes in C++ - The Art of Scientific Computing*, 1st ed. New York: Cambridge University Press, 2002.

[108] A. J. Ricco, S. J. Martin, and T. E. Zipperian, "Surface acoustic wave gas sensor based on film conductivity changes," *Sens. Act.*, vol. 8, no. 4, pp. 319–333, Dec. 1985.

[109] G. Kovacs and A. Venema, "Theoretical comparison of sensitivities of acoustic Shear wave modes for (bio)chemical sensing in liquids," *Appl. Phys. Lett.*, vol. 61, no. 6, pp. 639–641, Aug. 1992.

[110] T. Pastureaud, V. Laude, and S. Ballandras, "Stable scattering-matrix method for surface acoustic waves in piezoelectric multilayers," *Appl. Phys. Lett.*, vol. 80, no. 14, pp. 2544–2546, Apr. 2002.

[111] N. T. Nguyen, R. W. Doering, A. Lal, and R. M. White, "Computational fluid dynamics modeling of flexural plate wave pumps," *Proc. IEEE Ultrason. Symp.*, pp. 431–434, 1998.

[112] V. Kecman, S. Bingulac, and Z. Gajic, "Eigenvector approach for order reduction of singularly perturbed linear-quadratic optimal control problems," *Automatica*, vol. 35, pp. 151–158, Jan. 1999.

[113] S. I. Rokhlin and L. Wang, "Stable recursive algorithm for elastic wave propagation in layered anisotropic media: Stiffness matrix method," *J. Acoust. Soc. Amer.*, vol. 112, no. 3, pp. 822–834, Sept. 2002.

[114] K. A. Ingebrigtsen, "Surface waves in piezoelectrics," *J. Appl. Phys.*, vol. 40, no. 7, pp. 2681–2686, June 1969.

[115] R. M. Moroney, R. M. White, and R. T. Howe, "Microtransport induced by ultrasonic Lamb waves," *Appl. Phys. Lett.*, vol. 59, pp. 774–776, June 1991.

[116] D. W. Galipeau, P. R. Story, K. A. Vetelino, and R. D. Mileham, "Surface acoustic wave microsensors and applications," *Smart Mater. Struct.*, vol. 6, pp. 658–667, 1997.

[117] Z. Wang, J. D. N. Cheeke, and C. K. Jen, "Perturbation method for analyzing mass sensitivity of planar multilayer acoustic sensors," *IEEE Trans. Ultrason., Ferroelect., Freq. Contr.*, vol. 43, no. 5, pp. 844–851, Sept. 1996.

[118] ——, "Unified approach to analyse mass sensitivities of acoustic gravimetric sensors," *Electronics Letters*, vol. 26, no. 18, pp. 1511–1513, Aug. 1990.

[119] J. P. Black, B. Chen, R. Quinn, M. Madou, and R. M. White, "Comparison of the performance of fleuxral plate wave and surface acoustic wave devices as the detector in a gas chromatograph," *Proc. IEEE Ultrason. Symp.*, pp. 435–440, 2000.

[120] S. G. Joshi and Y. Jin, "Lamb wave excitation in piezoelectric plates," *Proc. IEEE Ultrason. Symp.*, pp. 455–458, 1990.

[121] C. S. Hartmann and B. G. Secrest, "End effects in interdigital surface wave transducers," *Proc. IEEE Ultrason. Symp.*, pp. 413–416, 1972.

[122] W. R. Smith, H. M. Gerard, J. H. Collins, T. M. Reeder, and H. J. Shaw, "Analysis of interdigital surface wave transducers by use of an equivalent circuit model," *IEEE Trans. Microwave Theory Tech.*, vol. 17, no. 11, pp. 856–864, Nov. 1969.

[123] P. Denbigh, *System Analysis and Signal Processing*, 1st ed. Essex, England: Addison Wesley Longman Ltd, 1998.

[124] K. Bløtekjær, K. A. Ingebrigtsen, and H. Skeie, "A method for analyzing waves in structures consisting of metal strips on dispersive media," *IEEE Trans. Electron Devices*, vol. 20, no. 12, pp. 1133–1138, Dec. 1973.

[125] R. F. Milsom, J. Heighway, N. H. C. Reily, and M. Redwood, "Comparison of exact theoretical predictions and experimental results for interdigital transducers," *Proc. IEEE Ultrason. Symp.*, pp. 406–411, 1974.

[126] R. C. Peach, "A general approach to the electrostatic problem of the SAW interdigital transducer," *IEEE Trans. Sonics Ultrason.*, vol. 28, no. 2, pp. 96–105, Mar. 1981.

[127] A. R. Baghai-Wadji, S. Selberherr, and F. Seifert, "Rigorous 3D electrostatic field analysis of SAW transducers with closed-form formulae," *Proc. IEEE Ultrason. Symp.*, pp. 23–28, 1986.

[128] R. L. Boylestad, *Introductory Circuit Analysis*, 8th ed. New Jersey: Prentice-Hall International, 1997.

[129] R. S. Wagers, "Analysis of finite-width interdigital transducer excitation profiles," *IEEE Trans. Sonics and Ultrasonics*, no. 2, pp. 105–111, 1979.

[130] A. Farrar and A. T. Adams, "Computation of lumped microstrip capacities by matrix methods - rectangular sections and end effect," *IEEE Trans. Microwave Theory Tech.*, vol. MTT-19, pp. 495–497, May 1971.

[131] D. P. Morgan, "Admittance calculations for non-reflective SAW transducers," *Proc. IEEE Ultrason. Symp.*, pp. 131–134, 1996.

[132] C. S. Hartmann, S. Jen, M. A. Domalewski, and J. C. Andle, "Improved accuracy for determining SAW transducer capacitance and $K^2$," *Proc. IEEE Ultrason. Symp.*, pp. 161–167, 1987.

[133] G. Barron, "History and Development," in *What Every Engineer Should Know About Finite Element Analysis*, J. R. Brauer, Ed. New York: Marcel Dekker Inc, 1993, ch. 1, pp. 1–7.

[134] S. S. Rao, *The Finite Element In Engineering*, 4th ed. Burlington, MA: Elsevier Inc, 2005.

[135] S. Moaveni, *Finite Element Analysis - Theory and Applications With Ansys*, 2nd ed. Upper Saddle River, NJ: Pearson Education Inc, 2003.

[136] ANSYS Inc, *ANSYS 8.0 Online Help*. United States: SAS IP Inc, 2003.

[137] Computers and Structures Inc, "Dynamic analysis by numerical integration," *Journal of the Aeronautical Sciences*, vol. 23, no. 9, Sept. 1956.

[138] E. J. Danicki, "Electrostatics of interdigital transducers," *IEEE Trans. Ultrason., Ferroelect., Freq. Contr.*, vol. 51, no. 4, pp. 444–452, 2004.

[139] S. J. Ippolito, K. Kalantar-zadeh, D. A. Powell, and W. Wlodarski, "A 3-Dimensional Finite Element approach for simulating acoustic wave propagation in layered SAW devices," *Proc. IEEE Ultrason. Symp.*, pp. 303–306, 2003.

[140] The Mathworks Inc, *MATLAB 7.1 Online Help*. United States: The Mathworks Inc, 2005.

[141] G. Carlotti, D. Fioretto, G. Socino, and L. Palmieri, "Surface acoustic waves in c-axis inclined ZnO films," *Proc. IEEE Ultrason. Symp.*, pp. 449–453, 1990.

[142] M. Ross. (2000) Frequency compression hearing aids. [Online]. Available: http://www.hearingresearch.org/Dr.Ross/Freq_Comp_HAs.htm

[143] G. I. Matthews, S. J. Ippolito, W. Wlodarski, and K. Kalantar-zadeh, "Electrical parameter extraction of a flexural plate wave device using the Finite Element method," *Proc. IEEE Ultrason. Symp.*, pp. 1136–1139, 2006.

[144] C. Caliendo, D. Fioretto, G. Socino, and E. Verona, "Determination of viscoelastic constants of thin films by acoustic plate modes," *Proc. IEEE Ultrason. Symp.*, pp. 387–391, 1991.

[145] R. M. White and S. W. Wenzel, "Fluid loading of a Lamb wave sensor," *Appl. Phys. Lett.*, vol. 52, no. 20, pp. 1653–1655, May 1988.

[146] G. McHale, M. K. Banerjee, M. I. Newton, and V. V. Krylov, "Surface acoustic wave resonances in the spreading of viscous fluids," *Phys. Rev. B*, vol. 59, no. 12, pp. 8262–8270, Mar. 1999.

[147] M. S. Weinberg, C. E. Dubé, A. Petrovich, and A. M. Zapata, "Fluid damping in resonant flexural plate wave device," *J. Microelectromech. Syst.*, vol. 12, no. 5, pp. 567–576, Oct. 2003.

[148] G. K. Batchelor, *An Introduction to Fluid Dynamics*, 3rd ed. New York: Cambridge Mathematical Library, 2000.

[149] A. B. Bhatia, *Ultrasonic Absorption*. Oxford: Oxford University Press, 1967.

[150] S. Ballandras, A. Reinhardt, A. Khelif, M. Wilm, V. Laude, W. Daniau, V. Blondeau-Pâtissier, and W. Boireau, "Theoretical analysis of damping effects of SAW at solid/fluid interfaces," in *Proc. IEEE Freq. Cont. Symp.*, 2003, pp. 907–910.

[151] J. J. Campbell and W. R. Jones, "Propagation of surface waves at the boundary between a piezoelectric crystal and a fluid medium," *IEEE Trans. Sonics and Ultrasonics*, no. 2, pp. 71–76, Apr. 1970.

[152] M. Thompson and G. L. Hayward, "Mass response of the Thickness-Shear mode acoustic wave sensor in liquids as a central misleading dogma," *Proc. IEEE Freq. Cont. Symp.*, pp. 114–119, 1997.

[153] L. A. Francis, J. Friedt, R. D. Palma, C. Zhou, C. Bartic, A. Campitelli, and P. Bertrand, "Techniques to evaluate the mass sensitivity of Love mode surface acoustic wave biosensors," *Proc. IEEE Ultrason., Ferroelect., Freq. Contr. Symp.*, pp. 241–249, 2004.

[154] G. McHale, M. I. Newton, M. K. Banerjee, and J. A. Cowen, "Acoustic wave-liquid interactions," *Materials Science and Engineering: C*, vol. 12, pp. 17–22, 2000.

[155] F. Herrmann, D. Hahn, and S. Büttenbach, "Separation of density and viscosity influence on liquid-loaded surface of acoustic wave devices," *Appl. Phys. Lett.*, vol. 74, no. 22, pp. 3410–3412, May 1999.

[156] M. Rodahl and B. Kasemo, "On the measurement of thin liquid overlayers with the quartz-crystal microbalance," *Sens. Act. A: Phys.*, vol. 54, pp. 448–456, 1996.

[157] S. J. Martin, K. O. Wessendorf, C. T. Gebert, G. C. Frye, R. W. Cernosek, L. Casaus, and M. A. Mitchell, "Measuring liquid properties with smooth- and textured-surface resonators," *Proc. IEEE Freq. Cont. Symp.*, pp. 603–608, 1993.

[158] Z. Zhu, J. Li, and J. Wu, "A pertubation analysis of Lamb-wave sensors," *Ultrasonics*, vol. 33, no. 3, pp. 213–219, 1995.

[159] T. Oyama, J. Kondoh, and S. Shiokawa, "Measurement of particles in liquid using surface acoustic wave sensors," *Proc. IEEE Ultrason., Ferroelect., Freq. Contr. Symp.*, pp. 235–240, 2004.

[160] J. Kondoh, K. Saito, S. Shiokawa, and H. Suzuki, "Simultaneous measurements of liquid properties using multichannel Shear Horzitonal surface acoustic wave transducer," *Jpn. J. Appl. Phys., Part 1*, vol. 35, no. 5B, pp. 3093–3096, 1996.

[161] A. Agoston, C. Ötsch, and B. Jakoby, "Viscosity sensors for engine oil condition monitoring - application and interpretation of results," *Sens. Act. A: Phys.*, vol. 121, pp. 327–332, 2005.

[162] A. J. Ricco and S. J. Martin, "Acoustic wave viscosity sensor," *Appl. Phys. Lett.*, vol. 50, no. 21, pp. 1474–1476, May 1987.

[163] G. McHale, M. I. Newton, and F. Martin, "Theoretical mass, liquid and polymer sensitivity of acoustic wave sensors with viscoelastic guiding layers," *J. Appl. Phys.*, vol. 93, no. 1, pp. 675–690, Jan. 2003.

[164] H. Seidel, L. Csepregi, A. Heuberger, and H. Baumqärtel, "Anisotropic etching of crystalline silicon in alkaline solutions," *J. Electrochem. Soc.*, vol. 137, no. 11, pp. 3612–3632, Nov. 1990.

[165] M. J. Madou, *Fundamentals of microfabrication - The science of miniturization*, 2nd ed. Boca Raton, Florida, United States: CRC Press, 2002.

[166] K. Wasa and S. Hayakawa, *Handbook of sputter deposition technology - Principles, Technology and Applications*, 1st ed. New Jersey, United States: Noyles Publications, 1992.

[167] J. D. Plummer, M. D. Deal, and P. B. Griffin, *Silicon VLSI Technology: Fundamentals, Practice and Modeling*, 1st ed. New Jersey, United States: Prentice Hall Inc., 2000.

[168] M. Clement, L. Vergara, J. Sangrador, E. Iborra, and A. Sanz-Hervás, "SAW characteristics of AlN films sputtered on silicon substrates," *Ultrasonics*, vol. 42, pp. 403–407, 2004.

[169] G. Carlotti, G. Socino, A. Petri, and E. Verona, "Elastic constants of sputtered ZnO films," in *Proc. IEEE Ultrason. Symp.*, 1987, pp. 295–299.

[170] K. Tsubouchi, K. Sugai, and N. Mikoshiba, "AlN material constants evaluation and SAW properties on AlN/$Al_2O_3$ and AlN/Si," *Proc. IEEE Ultrason. Symp.*, pp. 375–380, 1981.

[171] F. S. Hickernell, H. D. Knuth, T. S. Hickernell, and L. Mang, "Surface acoustic wave propagation on piezoelectric substrates with thin-film PECVD silicon nitride," *Proc. IEEE Ultrason. Symp.*, pp. 530–536, 1995.

[172] S. Furukawa, T. Nomura, and T. Yasuda, "Theoretical study of leaky surface acoustic wave propagating on water/ZnO/glass structures," *J. Phys. D: Appl. Phys.*, vol. 21, pp. 216–218, 1988.